Electron-electron interaction effects in the optical and transport properties of 2D materials beyond graphene.

Tesi di perfezionamento in Nanoscienze

Academic Year 2020/2021

Pietro Novelli

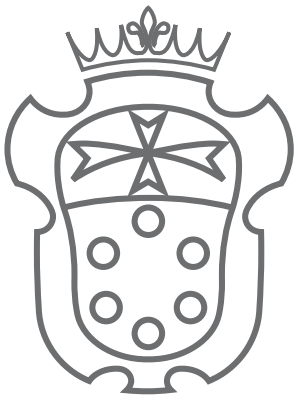

SCUOLA
NORMALE
SUPERIORE

Supervisors: Prof. M. Polini, Dr. F. Taddei

Acknowledgements

List of Publications

- P. Novelli, F. Taddei, A. K. Geim, and M. Polini
  Failure of Conductance Quantization in Two-Dimensional Topological Insulators-due to Nonmagnetic Impurities
  Phys. Rev. Lett **122**, 016601 (2019)

- N. C. H. Hesp, I. Torre, D. Rodan-Legrain, P. Novelli, Y. Cao, S. Carr, S. Fang, P. Stepanov, D. Barcons-Ruiz, H. Herzig-Sheinfux, K. Watanabe, T. Taniguchi, D. K. Efetov, E. Kaxiras, P. Jarillo-Herrero, M. Polini, and F. H. L. Koppens,
  Collective excitations in twisted bilayer graphene close to the magic angle
  arXiv:1910.07893 (under review, Nature Physics)

- P. Novelli, I. Torre, F. H. L. Koppens, F. Taddei, and M. Polini
  Optical and plasmonic properties of twisted bilayer graphene: Impact of interlayer tunneling asymmetry and ground-state charge inhomogeneity
  Phys. Rev. B **102**, 125403 (2020)

Abstract

This Thesis studies optical, plasmonic, and transport phenomena in two-dimensional materials. In particular, optical and plasmonic properties in twisted bilayer graphene are analyzed in the first part of the Thesis, whereas transport phenomena in two-dimensional topological insulators are left for the second part. A common element of the physical systems studied here are electron-electron interactions, whose presence is pivotal for many of the results presented.

The first Chapter of the manuscript is devoted to a review and critical analysis of the experimental results that motivated our work. Among these results, I emphasize recent experimental work carried out at ICFO on MIT samples on the plasmonic properties of twisted bilayer graphene whose theoretical interpretation was accomplished mostly thanks to the original theory presented in this Thesis. The first Chapter is also devoted to present some of the necessary theoretical concepts and tools forming the basis of this manuscript.

The second Chapter of the thesis presents a theory of twisted bilayer graphene, an atomically-thin heterostructure which in early 2018 was showed to host a plethora of exotic quantum phases of matter. This Chapter also includes a technical Section where the details of the numerical codes developed for our study of twisted bilayer graphene are thoroughly discussed. These numerical codes are planned to be fully released and openly available for the scientific community in the near future.

The third Chapter contains original results on the optical and plasmonic properties of twisted bilayer graphene. These results are obtained for a large variety of different parameter configurations, in the spirit of giving as much information as possible for a material (twisted bilayer graphene) whose actual physical properties are to a large extent still unknown. This Chapter is concluded by the presentation of preliminary results on the density-density response function of twisted bilayer graphene, which is essential to understand its dielectric properties, and hence how and how much the electron-electron interactions are screened.

The fourth Chapter is about the theory of two-dimensional topological insulators, a class of materials hosting very interesting transport phenomena that are related to to the topological nature of their non-interacting bands and eigenstates. A Section of this Chapter is also devoted to the theory of ballistic electron transport, which is essential to understand many properties of two-dimensional topological insulators.

In the fifth and last Chapter of the Thesis, we present an original result on the interplay between electron-electron interactions and localized defects in two-dimensional topological insulators. The theory presented in this Chapter provides a straightforward conceptual framework to explain experimental results on the transport properties of

two-dimensional topological insulators, especially those in atomically thin crystals, plagued by short-range edge disorder.

Contents

Acronyms

2D two-dimensional

2DTI two-dimensional topological insulator

BZ Brillouin zone

CNP charge neutrality point

DOS density of states

e-e electron-electron

hBN hxagonal Boron Nitride

BZ Brillouin zone

RPA random phase approximation

RTA relaxation time approximation

s-SNOM scattering-type scanning near-field optical microscopy

TBG twisted bilayer graphene

TDHF time dependent Hartree Fock

TMD transition metal dichalcogenide

1

Introduction to relevant theoretical and experimental facts

In this introductory Chapter we review the basic physical properties of the two-dimensional (2D) materials studied in the Thesis. Starting from the relevant experimental observations, we will highlight the properties of graphene [1, 2], twisted bilayer graphene [3, 4, 5, 6], and two-dimensional topological insulators [7, 8]. The Chapter is organized as follows.

Sections 1.1.1 to 1.1.3 are dedicated to introduce graphene along with its salient transport, optical and plasmonic properties. The introduction to graphene and to its theoretical description is instrumental for the discussion of all the original work presented in this Thesis. Graphene, indeed, is the constituent material of twisted bilayer graphene, analysed in Chapter 2. Its optical and plasmonic properties can be compared to the results obtained in Chapter 3 for twisted bilayer graphene. The theoretical description of graphene is enriched in Chapter 4, where we introduce the Kane-Mele model of topological insulator, at the core of the results in Chapter 5. The latter concerns transport properties of topological materials. The description of graphene nanoribbons presented in the present Chapter 1 is a good starting point to introduce many important concepts concerning electronic transport in nanoscopic systems, discussed in Chapter 4.

Other relevant two-dimensional materials such as hexagonal Boron Nitride, transition metal dichalcogenides, and moiré superlattices are briefly presented in Sections 1.1.4 to 1.1.6. Hexagonal Boron Nitride is a material widely employed as dielectric substrate for graphene-based devices, and its inclusion in the theoretical models, as done in Chapter 3, is necessary if one wants to compare the theory to experiments. Transition metal dichalcogenides are two-dimensional materials which, among many physical properties, can be topologially non-trivial.

A review on the recent experiments on twisted bilayer graphene, which is a moiré

superlattice, is found in Section 1.2, whereas Section 1.3 is dedicated to the relevant experimental facts concerning two-dimensional topological materials.

1.1 Graphene and two-dimensional materials

Research on the physical properties of two-dimensional (2D) materials has become one of the most active and important areas in contemporary condensed matter physics. The interest on 2D materials started when graphene was isolated for the first time in 2004, by A. K. Geim and K. S. Novoselov [9], and expanded at incredible paces thereafter. In the last years the focus has shifted also to other 2D materials, and, more importantly, to combinations of them [10, 11]. It has been demonstrated that multiple layers of different 2D materials can be stacked one on top of the other to form complex structures which are held together by the Van der Waals forces between the different layers. These structures are therfore known as Van der Waals (VdW) heterostructures.

1.1.1 Graphene

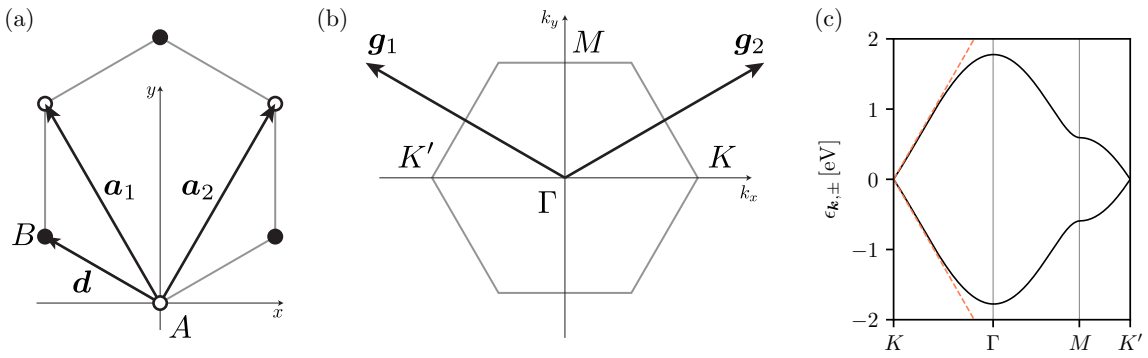

FIGURE 1.1: Panel (a): Lattice structure, primitive translation vectors and basis vectors of graphene. The carbon atoms are arranged on the sites of the A and B triangular sublattices. Panel (b): Brillouin zone of graphene and a basis of reciprocal lattice vector. Panel (c): tight-binding band structure of graphene along the high-symmetry path $K-\Gamma-M-K'$. The dashed red lines correspond to the low-energy bands obtained from the Dirac Hamiltonian Eq. (1.9).

Graphene, has been the first truly 2D material to be discovered and it is also, by far, the most studied among 2D materials. Graphene has remarkable electronic [1], optical [12, 13, 14], thermal [15] and mechanical properties [16]. At the atomic level, graphene is a single layer of Carbon atoms which, due to their sp^2 hybridization, occupy the sites of an hexagonal honeycomb lattice, as showed in Fig. 1.1. The honeycomb lattice is a composite structure, consisting of two triangular Bravais sub-lattices, often referred to as the A and B sublattices. The inter-atomic distance between Carbon atoms is $a_0 = 0.142\,\text{nm}$, and a possible choice of primitive translation vectors and basis

vectors is:

$$\boldsymbol{a}_1 = a\left(-\frac{1}{2}, \frac{\sqrt{3}}{2}\right), \qquad \boldsymbol{a}_2 = a\left(\frac{1}{2}, \frac{\sqrt{3}}{2}\right), \tag{1.1a}$$

$$\boldsymbol{d}_A = (0,0), \qquad \boldsymbol{d}_B = \frac{a}{\sqrt{3}}\left(-\frac{\sqrt{3}}{2}, \frac{1}{2}\right), \tag{1.1b}$$

where we have defined the Bravais lattice parameter $a \equiv a_0\sqrt{3} = 0.246\,\text{nm}$. The area of the unit cell is $\Omega_{\text{u.c.}} = \sqrt{3}a^2/2 \approx 0.051\,\text{nm}^2$. The reciprocal space geometry of graphene is defined by a basis of reciprocal translation vectors, which are obtained from the relation $\boldsymbol{g}_i \cdot \boldsymbol{a}_j = 2\pi\delta_{ij}$, implying

$$\boldsymbol{g}_1 = \frac{4\pi}{a\sqrt{3}}\left(-\frac{\sqrt{3}}{2}, \frac{1}{2}\right), \qquad \boldsymbol{g}_2 = \frac{4\pi}{a\sqrt{3}}\left(\frac{\sqrt{3}}{2}, \frac{1}{2}\right). \tag{1.2}$$

Most of graphene's electronic and optical properties arise from the peculiar energy dispersion of its π bands, i.e. the energy bands generated by the p_z orbital of the Carbon atoms [2, 17]. The π bands of graphene are so important because, in practice, they are the only bands crossed by the Fermi level, even under strong doping. For this reason we can disregard all the other bands when discussing transport or optical properties up to energies $\lessapprox 3\,\text{eV}$.

The π bands can be conveniently described within the semi-empirical tight-binding method [2, 18], starting from the two Bloch sums built from the p_z orbitals of the two carbon atoms in the primitive cell

$$\Phi_{A,B}(\boldsymbol{k}, \boldsymbol{r}) = \frac{1}{\sqrt{\mathcal{N}}}\sum_{\boldsymbol{a}_n} e^{i\boldsymbol{a}_n \cdot \boldsymbol{k}}\phi(\boldsymbol{r} - \boldsymbol{d}_{A,B} - \boldsymbol{a}_n), \tag{1.3}$$

where $\mathcal{N} = \mathcal{N}_1\mathcal{N}_2$ is the number of atoms in the system. We have assumed Born-von Karman cyclic boundary conditions on the electronic wavefunction $\Phi_{A,B}(\boldsymbol{k}, \boldsymbol{r}) = \Phi_{A,B}(\boldsymbol{k}, \boldsymbol{r} + \mathcal{N}_1\boldsymbol{a}_1) = \Phi_{A,B}(\boldsymbol{k}, \boldsymbol{r} + \mathcal{N}_2\boldsymbol{a}_2)$ and we have defined the vectors

$$\boldsymbol{a}_n \equiv n_1\boldsymbol{a}_1 + n_2\boldsymbol{a}_2 \;\text{ with } n \equiv (n_1, n_2) \in \mathbb{Z} \times \mathbb{Z}. \tag{1.4}$$

Assuming nearest neighbour interaction, no hopping processes within the same sublattice is present. Hopping occurs only between different sublattices, with hopping energy t. The tight-binding Hamiltonian on the basis functions Eq. (1.3) is therefore the 2×2 matrix

$$\mathcal{H}(\boldsymbol{k}) = t\begin{pmatrix} 0 & f(\boldsymbol{k}) \\ f^*(\boldsymbol{k}) & 0 \end{pmatrix}, \tag{1.5}$$

where

$$f(\boldsymbol{k}) = e^{i\boldsymbol{k}\cdot\boldsymbol{\delta}_1} + e^{i\boldsymbol{k}\cdot\boldsymbol{\delta}_2} + e^{i\boldsymbol{k}\cdot\boldsymbol{\delta}_3}, \tag{1.6}$$

and $\boldsymbol{\delta}_i$ with $i = 1, 2, 3$ are the vectors joining each site in the sublattice A to its nearest neighbours in the sublattice B

$$\boldsymbol{\delta}_1 = \frac{a}{\sqrt{3}}\left(\frac{\sqrt{3}}{2}, \frac{1}{2}\right), \qquad \boldsymbol{\delta}_2 = \frac{a}{\sqrt{3}}\left(-\frac{\sqrt{3}}{2}, \frac{1}{2}\right), \qquad \boldsymbol{\delta}_3 = \frac{a}{\sqrt{3}}(0, -1). \tag{1.7}$$

The diagonalization of the tight-binding Hamiltonian, Eq. (1.5), is straightforward and gives the following energy bands

$$\epsilon_{\boldsymbol{k},\pm} = \pm t|f(\boldsymbol{k})|, \tag{1.8}$$

plotted in Fig. 1.1.

Many of graphene's properties can be described also by an even simpler, low-energy, one-particle Hamiltonian obtained approximating the tight-binding Hamiltonian (1.5) near the K or K' point of the Brillouin Zone (BZ) (See Fig. 1.1). This approximation yields

$$\tilde{\mathcal{H}}(\boldsymbol{k},\zeta) = \frac{\sqrt{3}}{2}ta\begin{pmatrix} 0 & k_x - i\zeta k_y \\ k_x + i\zeta k_y & 0 \end{pmatrix} = \hbar v_{\mathrm{F}}\begin{pmatrix} 0 & k_x - i\zeta k_y \\ k_x + i\zeta k_y & 0 \end{pmatrix}, \tag{1.9}$$

where $\zeta = +1(-1)$ if the expansion is performed around the $K\,(K')$ point in the BZ and the Bloch wavevector $\boldsymbol{k}$ is now measured from the $K\,(K')$ point. We have also introduced the Fermi velocity v_{F} through the relation $v_{\mathrm{F}} = \sqrt{3}ta/(2\hbar) \approx 10^6\,\mathrm{m/s}$. The Fermi velocity is the effective velocity of low-energy electrons roaming in graphene. This approximate low-energy Hamiltonian is the massless Dirac Hamiltonian in (2+1) dimensions and has a linear energy spectrum

$$\tilde{\epsilon}_{\boldsymbol{k},\pm} = \pm\frac{\sqrt{3}}{2}ta|\boldsymbol{k}| = \hbar v_{\mathrm{F}}|\boldsymbol{k}|. \tag{1.10}$$

The low-energy electronic bands of graphene are reproduced in Fig. 1.1, dashed red lines in panel (c).

In pristine graphene the valence bands are completely occupied, the conduction bands are completely empty and the Fermi energy lies at the Dirac point. As in many other 2D conducting systems, however, graphene's carrier density can be tuned by means of electrical gating. The latter is usually impossible in 3D metals, because the external potential is screened by the free electrons on a lengthscale equal to the inverse of the Thomas-Fermi wavecector. If the carrier density n in graphene is modified by electron doping, the corresponding Fermi energy adjustment is given by the relation

$$E_{\mathrm{F}} = \mathrm{sign}(n)\hbar v_{\mathrm{F}}\sqrt{\pi|n|}. \tag{1.11}$$

In the low-energy limit, the Density Of States (DOS) is a linear function of the energy, given by the expression

$$N(\epsilon) = 2_s 2_\zeta \int \frac{d^2\boldsymbol{k}}{2\pi}\left[\delta(\epsilon - \tilde{\epsilon}_{\boldsymbol{k},+}) + \delta(\epsilon - \tilde{\epsilon}_{\boldsymbol{k},-})\right] = \frac{2|\epsilon|}{\pi}(\hbar v_{\mathrm{F}})^{-2}, \tag{1.12}$$

where 2_s and 2_ζ are the two-fold degenerecies of, respectively, the spin and valley degrees of freedom.

To conclude this brief survey on the basic electric properties of graphene we mention that the tight-binding model can be improved by relaxing the nearest-neighbour approximation, taking into account the next-nearest-neighbour hopping terms as well. This refinement of the theory yields two important consequences: firstly, the so called *trigonal warping*, which consists in an anisotropy of the energy dispersion around the Dirac points [19]. Second, in the next-nearest-neighbour approximation, the particle-hole symmetry is broken, so that $\epsilon_{\boldsymbol{k},+} \neq -\epsilon_{\boldsymbol{k},-}$.

1.1.2 Electron transport in graphene nanoribbons

A graphene nanoribbon is just a narrow (i.e. on the order of tens of nanometers) ribbon of graphene [20, 21]. Because of spatial confinement in the direction transverse to the ribbon, the electronic states of graphene nanoribbons are splitted in discrete subbands. In pristine nanoribbons the conduction and valence subbands may even be separated by an energy gap, in stark contrast to bulk graphene. The energy gap, however, scales as the inverse of the nanoribbon's width and goes to 0 for large widths, recovering the dispersion of bulk graphene. From a technological point of view, the existence of an energy gap in graphene nanoribbons makes them an ideal component of nanotransistors [22].

From a theoretical point of view, graphene nanoribbons can be described by calculating the electronic energy eigenstates analytically from the continuum model Eq. (1.10) of bulk graphene, with the appropriate boundary conditions. From these calculations it is possible to extract the energy gap between valence and conduction subbands. Furthermore, it is also possible to show that, in particular geometries, graphene nanoribbons host a pair of propagating states which are localized along the edges of the ribbon. In particular, if the nanoribbon is translationally invariant in the direction longitudinal to the ribbon, Bloch's theorem implies that a crystal wavevector k can be defined and, in general, one will have a dispersion relation $\epsilon_n(k)$, where n labels the subband index and k the crystal wavevector.

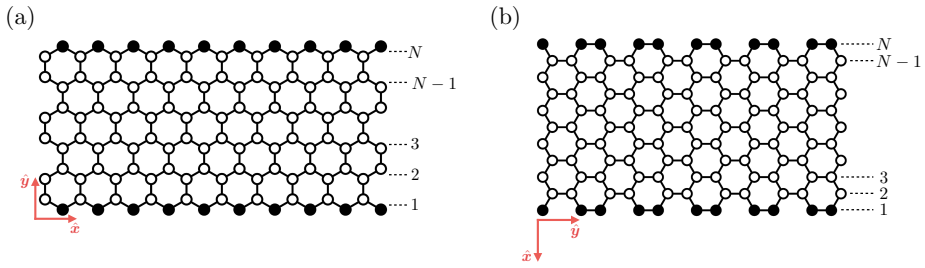

Figure 1.2: (a) Zigzag graphene nanoribbon extending along the $\hat{x}$ direction and confined along $\hat{y}$. (b) Armchair graphene nanoribbon extending along the $\hat{y}$ direction and confined along $\hat{x}$. In both panels the solid black sites are the edge of the nanoribbon.

Two important classes of translationally invariant graphene nanoribbons are commonly known as "armchair" and "zigzag", and are schematically represented in Fig. 1.2. The zigzag (armchair) configuration can be realised by cutting out a ribbon from an infinite sheet of graphene along a direction parallel (perpendicular) to one of the primitive translation vectors Eq. (1.1a). In both configurations the width of the ribbon is proportional to a single integer number N, denoting the number of dimer lines for armchair ribbons and the number of zigzag lines for zigzag ribbons. The energy spectrum of armchair and zigzag nanoribbons is showed in Fig. 1.3 for different sizes N of

the nanoribbon. For the armchair configuration [panel (b)] it is evident that both for $N = 10$ and $N = 12$, the valence subbands and the conduction subbands are separated by a gap, whereas the ribbon is metallic in the $N = 11$ case. More generally, whenever $N = 3M - 1$ with $M \in \mathbb{N}$, the armchair nanoribbons are metallic, and gapped otherwise. As anticipated, the energy gap in the armchair configuration turns out to be proportional to N^{-1}, and goes to 0 as the width of the nanoribbon increases. This is consistent with the fact that as the width of the nanoribbon increases we should recover the dispersion of bulk graphene Eq. (1.10). For the zigzag configuration, on the contrary, the highest valence band and the lowest conduction band are always degenerate at $k = \pm\pi$. It turns out that the degeneracy of the center bands at $k = \pm\pi$ does not originate from the intrinsic band structure of bulk graphene, and the corresponding wavefunctions are completely localized on the edge sites. These two special center bands get flatter as the width of the ribbon is increased, and their charge density distribution shows that the electronic states associated to them correspond to states localized on the zigzag edge. This edge states are quite fragile, and can be destroyed by a small amount of disorder disorder at the edge [23].

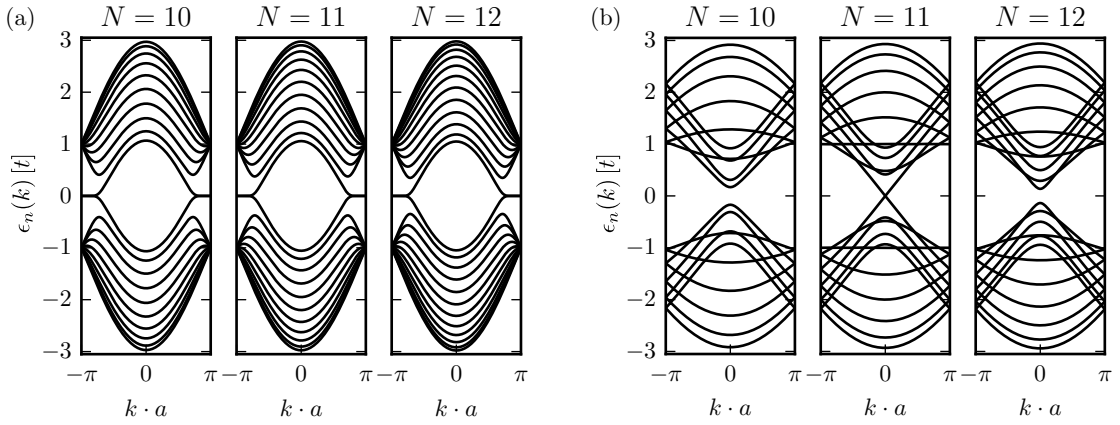

FIGURE 1.3: Panel (a): electronic states of zigzag graphene nanoribbons of different widths. Panel (b): electronic states of armchair graphene nanoribbons of different widths. The energies are in units of the next-neighbour hopping parameter t.

The presence of edge states in zigzag garaphene nanoribbons stems from the particular geometry of the ribbon itself, and it is quite sensitive to it. In Section 1.3, though, we are going to discuss 2D physical systems hosting edge states akin to the ones of zigzag nanoribboons which, however, are exceptionally insensitive to disorder. This insensitiveness to disorder is referred to as "topological protection", and it is a physical manifestation of the peculiar mathematical properties possessed by the Bloch wavefunctions of these materials.

Graphene nanoribbons are also an ideal platform to study electron transport in graphene-based materials. If an electrical potential gradient is enstablished along the graphene nanoribbon, a current flows in the ribbon itself. An interesting question to ask is how the current is related to the electrical potential gradient, and how their

relation depends on the physical properties of the ribbon. If the nanoribbon is free of defects, and the temperature is low enough so that scattering between electrons with other electrons or scattering between electrons and phonons can be ignored, then the nanoribbon it is said to be in the ballistic regime. A general theory of electron transport in the ballistic regime will be presented in Section 4.1. If the electrical potential drop V along the ribbon is much smaller than the Fermi energy, so that $eV \ll E_{\mathrm{F}}$, e being the elementary charge unit, it can be showed that the current along the ribbon is linearly proportional to the potential drop [24]

$$I = \frac{2e^2}{h}\mathcal{T}(E_{\mathrm{F}})V \ , \tag{1.13}$$

where h is the Planck constant, and $\mathcal{T}(\epsilon)$ is the transmission function calculated at energy ϵ. Roughly speaking, the transmission function at energy ϵ is the sum, for each of the subbands with energy lying between 0 and ϵ, of the probability that an electron in the n-th subband has to traverse the ribbon without being reflected [24]. In the case of graphene nanoribbons with zigzag or armchair edges, and in the ballistic regime, a good approximation is to assume that the probability is unity for each subband. This makes the transmission function to be just the number of subbands with energy less or equal to ϵ. This is generally true for clean materials where the electron-electron and electron-phonon scattering rates are suppressed (e.g. because of low temperature) and the scattering between different transport channels (i.e. different subbands in the case of graphene nanoribbons) is small as well: the transmission function is just the number of available transport channels up to energy ϵ [24].

To give a concrete example, we suppose to have an armchair graphene nanoribbon of width $w = (9N+1)a$ (a being the lattice parameter of graphene) with $N \in \mathbb{N}$ being the number of dimer lines, two sub-bands sequences are present [20, 21], whose minima are at energies

$$\epsilon_{n_+} = \pm\left|\pi\frac{\hbar v_{\mathrm{F}}}{w}(n+\frac{1}{3})\right|, \qquad n \geq 0 \tag{1.14a}$$

$$\epsilon_{n_-} = \pm\left|\pi\frac{\hbar v_{\mathrm{F}}}{w}(n-\frac{1}{3})\right|, \qquad n > 0 \tag{1.14b}$$

with $n \in \mathbb{N}$. Each subband is a transport channel, and upon defining $\delta = \pi\hbar v_{\mathrm{F}}/w$, the transmission function reads

$$\mathcal{T}(\epsilon) = \begin{cases} \left\lfloor \frac{|\epsilon|}{\delta} - \frac{1}{3} \right\rfloor + \left\lfloor \frac{|\epsilon|}{\delta} + \frac{1}{3} \right\rfloor + 1 & \text{if } \frac{\epsilon}{\delta} > \frac{1}{3}, \\ 0 & \text{otherwise.} \end{cases} \tag{1.15}$$

In the previous equation $\lfloor x \rfloor$ is the floor function, returning the largest integer smaller than x. It is also instructive to derive the large width limit of the conductance of a graphene nanoribbon. The conductance is defined as $G = I/V$ and from Eq. (1.13) we have

$$G = \frac{2e^2}{h}\mathcal{T}(E_{\mathrm{F}}). \tag{1.16}$$

The limit of large width is $w/\lambda_{\rm F} \to \infty$, where $\lambda_{\rm F} = hv_{\rm F}/E_{\rm F}$ is the Fermi wavelength. In Eq. (1.15), this limit yields

$$\lim_{w\to\infty} \mathcal{T}(\epsilon) \approx \frac{2w}{\pi\hbar v_{\rm F}}|\epsilon| \equiv \frac{2|\epsilon|}{\delta} \ . \tag{1.17}$$

Substituting the large widths limit of the transmission Eq. (1.17) into Eq. (1.16), and making use of the relation between the Fermi energy and the carrier density Eq. (1.11) one finds

$$G_{\rm Sharvin} = \frac{4e^2}{h} w \frac{\sqrt{\pi n}}{\pi} \ , \tag{1.18}$$

which is a well known formula by Sharvin for the conductance of graphene ribbons of width w [25].

With the appropriate boundary conditions, the electronic energies and states of graphene nanoribbons can be derived from the continuum model Hamiltonian Eq. (1.9). Combining the envelope functions $[\psi_A^+(\boldsymbol{r}), \psi_B^+(\boldsymbol{r})]$ and $[\psi_A^-(\boldsymbol{r}), \psi_B^-(\boldsymbol{r})]$, which multiply the states at the K and K' points into the vector $\Psi = [\psi_A^+(\boldsymbol{r}), \psi_B^+(\boldsymbol{r}), -\psi_A^-(\boldsymbol{r}), -\psi_B^-(\boldsymbol{r})]$, the Hamiltonian of the nanoribbon can be written thanks to Eq. (1.9) as

$$\mathcal{H}(\boldsymbol{k}) = \begin{pmatrix} \tilde{\mathcal{H}}(\boldsymbol{k},+) & 0 \\ 0 & -\tilde{\mathcal{H}}(\boldsymbol{k},-) \end{pmatrix} = \hbar v_{\rm F} \begin{pmatrix} 0 & k_x - ik_y & 0 & 0 \\ k_x + ik_y & 0 & 0 & 0 \\ 0 & 0 & 0 & -k_x - ik_y \\ 0 & 0 & -k_x + ik_y & 0 \end{pmatrix} . \tag{1.19}$$

Now, if the nanoribbon is confined in the direction $\hat{\alpha}$, then, k_α is not a good quantum number, because translational invariance is broken. In this case we need the momentum operator in its differential form $k_\alpha \to -i\partial_\alpha$. In this way, Eq. (1.19) becomes a system of partial differential equations, which are solved by imposing that the wavefunction should vanish at the edges. The solutions of such systems of differential equations are derived for the zigzag and armchair geometries e.g. in Ref. [21].

1.1.3 Graphene optics and plasmonics

The response of graphene to electromagnetic fields is described, in the long-wavelength limit, by the optical conductivity [2, 17] $\sigma(\omega) = \sigma_1(\omega) + i\sigma_2(\omega)$. At zero temperature and neglecting relaxation effects, the real and imaginary part of the optical conductivity of graphene reads [26, 27]

$$\sigma_1(\omega) = \frac{e^2}{h}\left\{2\pi|E_{\rm F}|\delta(\hbar\omega) + \frac{\pi}{2}\left[\Theta\left(\frac{\hbar\omega}{2|E_{\rm F}|} - 1\right) + \Theta\left(-\frac{\hbar\omega}{2|E_{\rm F}|} - 1\right)\right]\right\}, \tag{1.20a}$$

$$\sigma_2(\omega) = \frac{e^2}{h}\left\{\frac{2\pi|E_{\rm F}|}{\hbar\omega} + \frac{1}{2}\ln\left[\frac{2|E_{\rm F}| - \hbar\omega}{2|E_{\rm F}| + \hbar\omega}\right]\right\}, \tag{1.20b}$$

where $\Theta(\,\cdot\,)$ is the Heaviside step function. In both equations, the first term in the curly brackets is associated to intra-band transitions, while the second is related to inter-band transitions. The optical absorption is described by the real part of the conductivity

Eq. (1.20a), and in graphene takes place only at zero frequency (intra-band absorption) and at frequencies above $2|E_{\mathrm{F}}|/\hbar$ (inter-band absorption), due to Pauli blocking. It is interesting to note that the magnitude of the inter-band absorption is $\sigma_1^{\mathrm{inter}}(\omega) \equiv \pi e^2/(2h) = e^2/(4\hbar)$, depending only on universal constants. This amazing property of the response of graphene to electromagnetic fields is known as "universal optical conductivity" [2, 28]. Therefore, experiments on the light absorption of graphene as Ref. [29] can, literally, measure the fine structure constant $\alpha \equiv e^2/(hc)$.

Plasmons are high-frequency charge density oscillations occurring in many metals and doped semiconductors [17, 30, 31]. Plasmon excitations are sustained by the Coulomb interaction between electrons, and their physical origin can be understood as follows. When electrons move to screen an electric field, they tend to travel slightly too far, they are then pulled back toward the charge disturbance and overshoot again, setting up a weakly damped oscillation.

In ordinary three dimensional metals, like aluminum, copper or noble metals, plasmons have been well known from a long time [32], and various optical techniques were devised to probe them. An important way to probe plasmon excitations in ordinary materials is through electron energy-loss experiments [33]. In particular, in three dimensional materials, plasmons can be generated both in the bulk or in the surface of the material. More recently, plasmonic materials have established themselves as a versatile tool in many technological applications, ranging from biosensors [34] to laser waveguides [35] to quantum information [36].

The availability of truly 2D electron systems such as graphene, motivated a great deal of research about the properties and applications of surface plasmons [28]. Graphene plasmons, in particular, show very attractive features including extremely high localization, strong confinement, efficient and strong light–matter interactions, relatively long lifetimes, tunability and electrical controllability. In patterned graphene structures, plasmonic effects can enhance the optical absorpion of graphene from the $\approx 2.3\%$ value due to the normal inter-band optical processes, to nearly 100% [37, 38]. This can improve the efficiency of graphene based photodetectors and photovoltaic devices.

In this Section we give a brief introduction on graphene plasmonics and on the experimental techniques devised to probe plasmons in 2D materials. In particular we will focus on the experimental technique known as scattering-type scanning near field optical microscopy, as it is the most relevant technique for the plasmon experiments discussed in the next section.

The simplest theory of plasmons in graphene, considering only intraband processes, neglecting interband transitions, non-local, dissipative and retardation effects, yields the following dispersion relation [30]

$$\omega_{\mathrm{pl}}(q) = \sqrt{\frac{2e^2 q E_{\mathrm{F}}}{\hbar^2 \bar{\epsilon}}}. \tag{1.21}$$

In the latter, q is the in-plane plasmon wavevector, and $\bar{\epsilon}$ is the average dielectric constants of the media below and above graphene. This dispersion relation can be derived from a classical hydrodynamic approach. By considering the electrons roaming in graphene as an interacting liquid, the force attempting to restore equilibrium is provided primarily by a long-range electrostatic field. The plasmons are described

by the following linearized Euler equation of motion describing the deviation of the electron density from its average value, $\delta n(\boldsymbol{r}, t)$, and the associated current density $\boldsymbol{j}(\boldsymbol{r}, t)$

$$\partial_t \boldsymbol{j}(\boldsymbol{r}, t) = -\frac{E_\mathrm{F}}{\pi\hbar^2}\nabla_{\boldsymbol{r}} \int d^2\boldsymbol{r}' \frac{e^2}{\bar{\epsilon}|\boldsymbol{r}-\boldsymbol{r}'|}\delta n(\boldsymbol{r}', t). \tag{1.22}$$

By Fourier transforming the latter equation and using the continuity equation, Eq. (1.21) is readily obtained [28, 30].

The intraband plasmon described by the relation Eq. (1.21) has many interesting features. The scaling $\omega_\mathrm{pl}(q) \propto \sqrt{q}$ comes from the 2D geometry of the electron system [30], whereas the scaling $\omega_\mathrm{pl}(q) \propto E_\mathrm{F}^{1/2} \propto n^{1/4}$ is peculiar to the linear dispersion of the graphene electronic energy bands. In the range of wavevectors where Eq. (1.21) is valid, the compression of the surface plasmon wavelength relative to the excitation wavelength, i.e. the ratio between the plasmon wavelength λ_pl and the wavelength of a photon of the corresponding energy λ_0 is governed by the fine-structure constant α and can be strong because $\lambda_\mathrm{pl}/\lambda_0 \approx 2\alpha E_\mathrm{F}/(\bar{\epsilon}\hbar\omega) \sim \alpha$. This difference in wavelength is interesting from an applicational perspective, because it allows to reduce the size of optoelectronic components and to concentrate energy in small volumes, as done e.g. in Ref. [39], with a phase modulator with a footprint of only 350 nm operating on a wavelength of 10.6 μm. On the other hand, the direct excitation of plasmons using photons is forbidden because of wavevector mismatch.

Probing plasmons in near-field experiments. The s-SNOM technique.

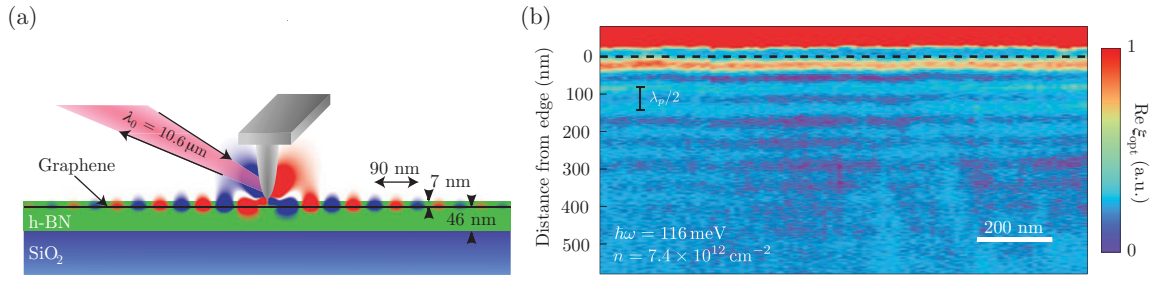

FIGURE 1.4: Panel (a): setup of the s-SNOM experiment for graphene encapsulated between hexagonal born nitride slabs. Panel (b): Optical signal of the s-SNOM experiment from a two-dimensional scan of the tip position near the graphene edge (dashed line). Edge-reflected plasmons appear as interference fringes. Figure adapted from Ref. [40].

A powerful technique to investigate plasmons propagating on the surface of a 2D material with sub-wavelength resolution is scattering-type Scanning Near-field Optical Microscopy (s-SNOM)[40, 41, 42, 43]. As showed in Fig 1.4, panel (a), in s-SNOM experiments a laser beam is focused on a metallized atomic force microscope tip. The momentum required to match the plasmon wavevector to the one of the incident photons is provided by the sharpnes of the tip, brought at the immediate vicinity of the

surface under study. The tip acts as an optical antenna that converts the incident light into a localized near field below the tip itself. The incident light is thus partly converted to plasmons, which propagate away from the tip as a circular wave. Plasmons return to the tip if they are reflected by edges or defects. Returning plasmons are partly converted to light and add to the out-scattered light field. Interferometric detection of the scattered light yields magnitude and phase as the complex-valued optical signal. Moving the s-SNOM tip across the sample allows to obtain a real-space image of the propagating plasmons like the one in panel (b) of Fig. 1.4, with a resolution limited only by the tip radius, and to measure their wavelength and decay length. The knowledge of the plasmon wavelength for a given frequency ω of the incident photons makes it possible to experimentally measure the plasmon dispersion relation, to be compared with the theoretical predictions, e.g. Eq. (1.21).

The radius of the tips used in the s-SNOM technique is tipically $\gtrapprox 10\,\mathrm{nm}$, so that plasmons with wavevectors $\lessapprox 0.1\,\mathrm{nm}^{-1} = 10^6\,\mathrm{cm}^{-1}$ are detectable by means of this technique.

1.1.4 Hexagonal Boron Nitride

Hexagonal Boron Nitride (hBN) is a layered material characterized by strong in-plane bonds and weak van der Waals interaction between layers, which can also be exfoliated to give flakes with atomically flat surfaces [44]. Very much like graphite, it consists of monolayers with hexagonal lattice structure. The two sublattices are occupied by Nitrogen and Boron atoms, which are held together through ionic bonds, making hBN a large gap insulator, with a gap $\approx 6\,\mathrm{eV}$. The lattice parameter of monolayer hBN is slightly larger than the one of graphene, with a mismatch of just $\approx 2\%$.

In this Thesis we will make use of the optical properties of hBN, which are described by the dynamical dielectric tensor

$$\epsilon(\omega) = \begin{pmatrix} \epsilon_x(\omega) & 0 & 0 \\ 0 & \epsilon_x(\omega) & 0 \\ 0 & 0 & \epsilon_z(\omega) \end{pmatrix} , \tag{1.23}$$

where $\epsilon_z(\omega)$ and $\epsilon_x(\omega)$ are the out-of-plane and in-plane dielectric permittivities of hBN. These have the following frequency dependence [45] ($i = x, z$)

$$\epsilon_i(\omega) = \epsilon_i(\infty) + \frac{s_i \hbar^2 \omega_i^2}{\hbar^2 \omega_i^2 - i\hbar^2 \gamma_i \omega - \hbar^2 \omega^2} , \tag{1.24}$$

with parameters given in Table 1.1. Note that with the parametrization (1.24) of the frequency dependence of the permittivities $\epsilon_i(\omega)$, we have the static dielectric constant of hBN $\sqrt{\epsilon_z(0)\epsilon_x(0)} = 4.9$.

Hexagonal boron nitride is, at the present time, one of most common dielectric substrates for graphene-based devices [47]. The reasons behind this choice are multiple. First, the surface of an exfoliated hBN flake is exceptionally flat, down to the atomic

Parameter	$i = x$	$i = z$
s_i	2.001	0.5262
$\epsilon_i(\infty)$	4.9	2.95
$\hbar\omega_i$ [meV]	168.6	94.2
$\hbar\gamma_i$ [meV]	0.87	0.25

TABLE 1.1: The parameters entering the bulk hBN dielectric functions in Eq. (1.23). These values have been extracted from Ref. [45].

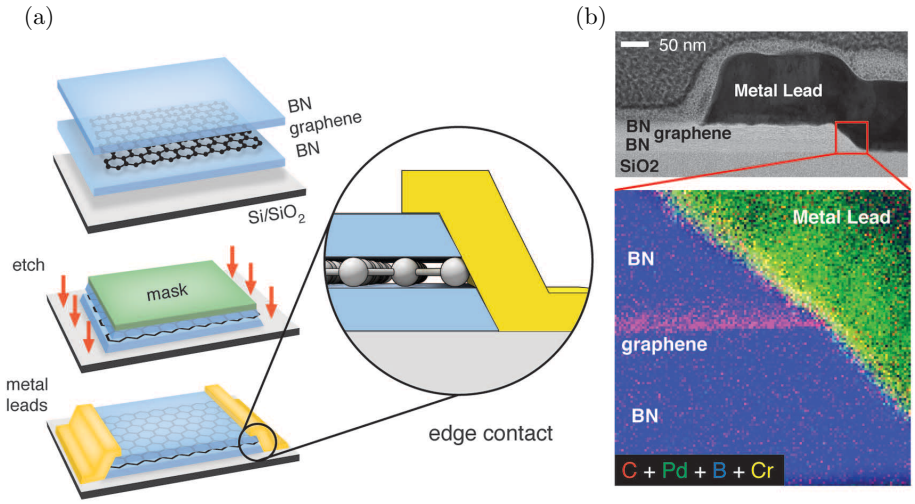

FIGURE 1.5: Encapsulation of graphene in hBN slabs, Figure adapted from Ref. [46].

level. Second, if the graphene-based device is encapsulated between two hBN crystals as showed in Fig. 1.5, contaminants and charged impurities cannot adhere to the graphene flake, screening it from environmental pollution. Third, the strong adhesion forces between graphene and hBN flakes, related to the closeness of their lattice parameters, makes graphene extremely flat and ripple free, quenching the out-of-plane oscillation modes, known as flexural phonons.

Devices of graphene encapsulated in hBN exhibit room-temperature ballistic transport well over a 1 μm distance and electronic mobilities exceeding values $10^5\,\mathrm{cm^2V^{-1}s^{-1}}$. At low temperetures, mobilities of $10^6\,\mathrm{cm^2V^{-1}s^{-1}}$ are reported, an order of magnitude higher than the devices realised with the first generation substrates such as silicon oxide (SiO_2).

1.1.5 Transition Metal Dichalcogenides

Transition Metal Dichalcogenides [49] (TMDs), are 2D materials formed by compounds of the type MX_2 , where M is a transition metal atom (such as Mo or W, Ti) and X is a chalcogenide (such as S, Se or Te). Each TMD consists in three separate layers: two external chalcogenide layers enclosing a central layer of the transition metal atoms. Any TMD can also exist in different structural phases, resulting from different coordinations

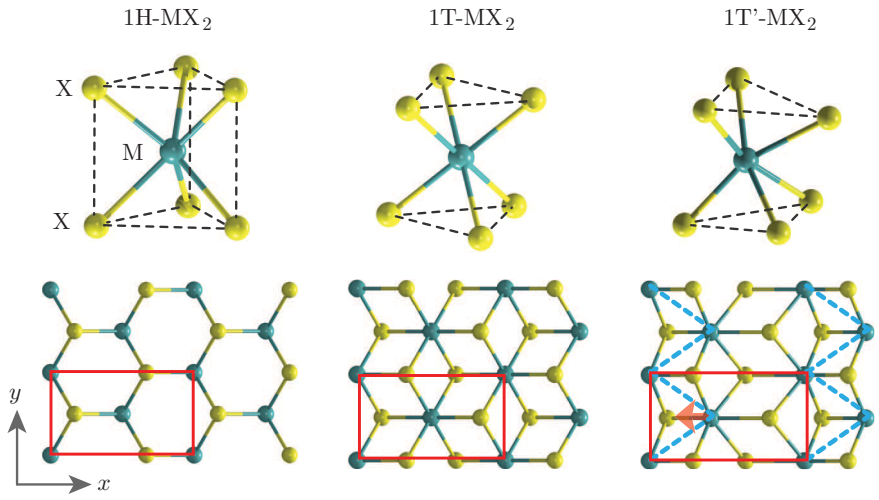

Figure 1.6: Structural phases of transition metal dichalcogenides. Figure adapted from Ref. [48].

of the transition metal atom with the other atoms in the unit cell of the TMD, as showed in Fig. 1.6.

Due to the diversity of the possible chemical compositions and structural phases, TMDs can be metallic, semiconducting or insulating. It has also been proved that certain TMDs host correlated or topological phases of matter [50]. Transition metal dichalcogenides can be exfoliated down to the monolayer and their electronic properties are strongly affected by the number of layers. For example, molybdenum disulfide (MoS_2) is an indirect bandgap semiconductor with negligible photoluminescence, but when the MoS_2 crystal is thinned to monolayer, a strong photoluminescence emerges, indicating an indirect to direct bandgap transition [51].

Recently, TMDs were also proposed as a platform to study topological phases of matter [48, 52, 53]. In particular, band structure calculations indicate that the two TMDs molybdenum ditelluride ($MoTe_2$) and tungsten ditelluride (WTe_2) can be intrinsic two-dimensional topological insulators. We defer the discussion of the experimental works concerning the topological properties of WTe_2 to Section 1.3.

1.1.6 Moiré superlattices

A moiré pattern is a large scale interference pattern occurring when two similar patterns are overlaid on top of each others. In 2D materials science moiré patterns are often found in Van der Waals heterostructures, where multiple layers of different 2D materials are superimposed one on top of the other, possibly with a relative twist angle. The large scale periodicity arising from the moiré interference pattern can be orders of magnitude higher than the lattice parameter of the underlying 2D materials, which is tipically few Angstroms. Heterostructures of this kind are often referred to as moiré superlattices. The electronic properties of moiré superlattices can be dramatically different with

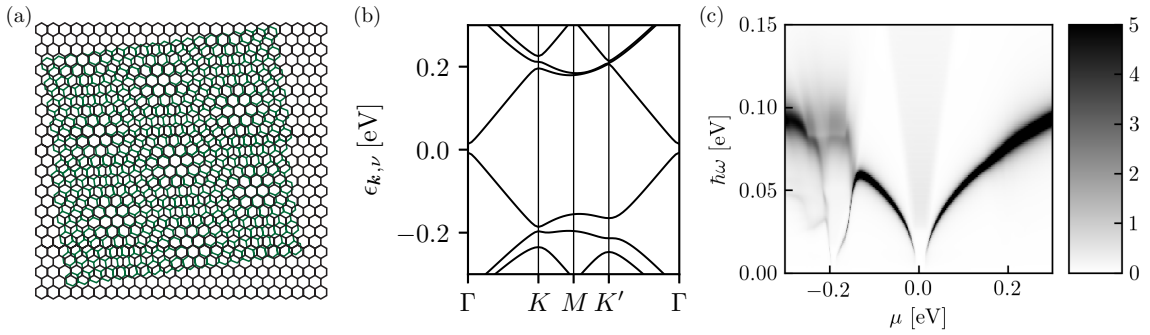

FIGURE 1.7: Panel (a): moiré pattern formed by two hexagonal lattices superimposed with a relative rotation angle. Panel (b): band structure of the moiré superlattice formed by a graphene-hBN heterostructure. Parameters taken as in Ref. [54]. Panel (c): loss function of the moiré superlattice formed by a graphene-hBN heterostructure. Collective electronic modes are excited with high probability in the darker region of the plot. Panel (a) adapted from Ref. [55]. Panel (c) adapted from Ref. [54].

respect to the properties of their constituent materials, and are the subject of numerous investigations in the condensed matter community. At the present time, arguably the two most important moiré superlattices are graphene-based. In particular, they are graphene stacked on top of an hBN layer, and twisted bilayer graphene. The latter is going to be throuroghuly invesigated in this Thesis, and we defer the presentation of its experimental and theoretical properties to Section 1.2 and Chapters 2 and 3.

Graphene stacked on top of hBN forms moiré superlattices which can be directly observed in atomically resolved topography experiments [56, 57]. The moiré superstructure is periodic over a triangular lattice, in contrast to the lattice structure of the underlying graphene and hBN, which is hexagonal (see Fig. 1.7(a)). Its lattice parameter λ is a combination of the lattice parameter of graphene a_{G}, the lattice parameter of hBN, a_{hBN}, and the relative rotation angle between the layers θ

$$\lambda = \frac{(1+\delta)a_{\mathrm{G}}}{\sqrt{2(1+\delta)(1-\cos(\theta))+\delta^2}}, \tag{1.25}$$

where $\delta = (a_{\mathrm{hBN}} - a_{\mathrm{G}})/a_{\mathrm{G}}$ is the fractional lattice mismatch between hBN and graphene [54, 58].

In Fig. 1.7(b) we show the band structure of the moiré superlattice formed by graphene stacked on top of hBN, for the case of perfect alignement, i.e. $\theta = 0$. The band structure is defined within the so-called "mini Brillouin zone", i.e. the Brillouin zone corresponding to the triangular moiré lattice of the graphene-hBN heterostructure. Compared to the band structure of monolayer graphene, Fig. 1.1(c), we can see that hBN introduces various interesting features. First, in contrast with graphene, the valence and conduction bands are separated by a small energy gap. This energy gap is the effect of the breaking of inversion simmetry of graphene by the hBN, which has different atoms in different sublattices. Second, at lower energies $\approx -0.2\,\mathrm{eV}$ another energy gap is opened, dividing a lower energy band with a noteworthy flat dispersion, clearly visible in the K-K' region of the path.

In Fig. 1.7(c) we show the so-called "loss function" corresponding to the energy bands of panel (b) as a function of the chemical potential μ. The energy loss function is proportional to the probability of exciting the 2D electron system by applying a perturbation of wavevector $\boldsymbol{q}$ and frequency ω. Its formal definition is given in Section 2.3.3. The darker lines in the loss function are associated to plasmon modes. For $\mu < 0$, the plasmon dispersion graphene on top of hBN is strongly different with respect to the basic analytical relationship scaling as $\sim \sqrt{q}$ given in Eq. (1.21).

1.2 Twisted Bilayer Graphene

In this Section we are going to review the most relevant experimental observations on Twisted Bilayer Graphene (TBG), a graphene-based moiré superlattice which in 2018 was showed to host insulating and superconducting states that are completely absent in a single graphene sheet. Twisted bilayer graphene [3, 4, 59, 60, 61, 62, 63, 64] is a system consisting of two graphene sheets stacked one on top of each other, with a relative rotation of the crystal axes quantified by the twist angle θ.

The energy spectrum of TBG is well described by a theory [3] which accounts for the long-range moiré modulations of the inter-layer tunneling amplitudes. At twist angles of $\approx 1^\circ$, the theory developed in Ref. [3] predicts the existence of a pair of remarkably flat energy bands, with a bandwidth of less than 20 meV, close to the charge neutrality point (CNP), where the Fermi level of an undoped sample lies. These bands exhibit a linear dispersion around the moiré Brillouin zone corners, with a twist-angle-dependent Fermi velocity $\hbar v_{\mathrm{F}}(\theta)$. The largest angle $\theta^\star$ satisfying $\hbar v_{\mathrm{F}}(\theta^\star) = 0$ is called the first *magic angle* (or simply *magic angle*) [3]. For systems with twist angles close to the magic one, the bandwidth of the flat bands reaches its minimum, ensuring a large density of states and strengthened electron-electron (e-e) interactions. Moreover, the strongly interacting electrons of TBG close to the magic angle are easy to control. That is because, at the magic angle, each flat band would contain only $\approx 10^{12}$ electrons per square centimiter. Electron densities of this order of magnitude can easily be tuned thanks to electronic gates by the experimentalists, avoiding the disruptive effects (e.g. structural distortion) of chemical doping on TBG systems.

In the magic angle regime ($\theta \sim 1.05^\circ$), a plethora of intriguing phenomena related to strong e-e interactions have been experimentally observed. Owing to the reduced kinetic energy, the flat band is susceptible to interaction effects, so that when the Fermi energy is brought within the band, interactions become dominant and the system can lower its energy through the formation of correlated electron phases. The experimental probes that have been used to explore the physics of TBG include electronic transport [5, 6, 65, 66, 67, 68], quantum capacitance [69], scanning tunneling microscopy, scanning tunneling spectroscopy [70, 71, 72, 73], scanning magnetometry [74] and scanning near-field optical microscopy [43].

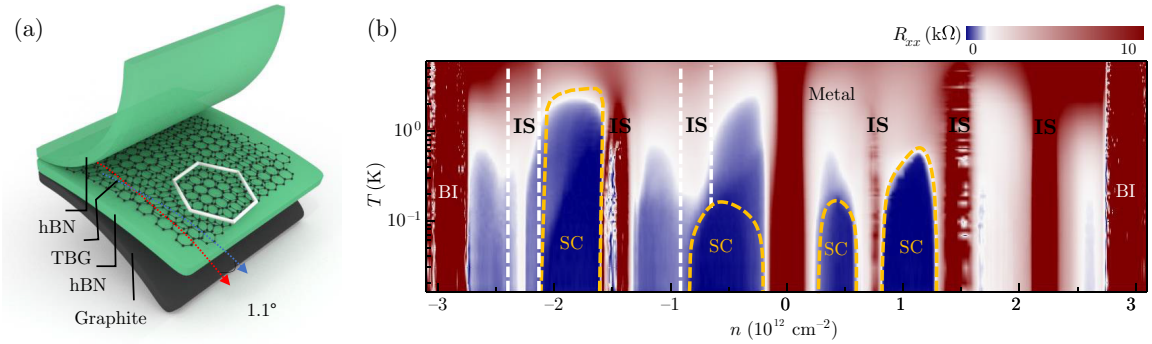

FIGURE 1.8: Panel (a): schematic of the setup used for transport experiments on twisted bilayer graphene. Panel (b): experimental phase diagram of twisted bilayer graphene with twist angle $\theta \approx 1.1°$. Acronyms in panel (b) have the following meanings. SC: SuperConductor. IS: Insulating State. BI: Band Insulator. Figure adapted from Ref. [66].

1.2.1 Transport and spectroscopic experiments on magic angle twisted bilayer graphene

Let us start by discussing the experimental findings on electronic transport in TBG. The transport experiments on TBG are usually conducted in devices as the one reproduced in Fig. 1.8(a), with TBG encapsulated between high quality dielectric materials such as hBN and placed on top of a metallic gate, in order to conveniently tune the electron density electrostatically. The works in Refs. [5] and [6] were the first to show the rich phase diagram (see e.g. Fig. 1.8(b)) of TBG samples with twist angle close to the magic angle. In particular, at electronic densities such that the valence (or conduction) flat band in magic angle TBG is half-filled, it is possible to observe insulating states. The emergence of these insulating states is not expected in the absence of electron-electron interactions and appears to be correlated with the narrow bandwidth near the first magic angle. Indeed, above 4 K, TBG behaves as a metal, exhibiting decreasing conductance with increasing temperature. A metal–insulator transition occurs at around 4 K. The conductance drops substantially from 4 K to 0.3 K, with the minimum value decreasing by 1.5 orders of magnitude. An Arrhenius fit yields a thermal activation gap of about 0.3 meV for these states. A plausible explanation for this gapped behaviour is the formation of a Mott-like insulator driven by Coulomb interactions between electrons in TBG.

At sligthly different electronic densities and for temperatures smaller than ≈ 2 K it is also possible to observe superconducting states, whose origin is still debated. The debate concerns the origin of the electronic pairing mechanism which allows superconductivity at the microscopic level. In most simple metals, the electronic pairing is mediated by phonons and any tendency of the electrons to form an insulating phase suppresses superconductivity, because fewer electrons are be available to pair. What makes magic angle TBG special in this scenario is simply that it has flat bands, which yield very high densities of states at a very low carrier density. A more exotic possibility is that the pairing of electrons in TBG superconducting states occurs between heavily interacting quasiparticles, which move in a correlated-electron environment

that locally favors an insulating state. This scenario might, in some systems, like the cuprates, allow superconductivity at much higher temperatures.

The findings of two recent experimental works suggest that the superconducting states in TBG arise from a conventional pairing scheme, i.e. the pairing is *not* mediated by e-e interactions, whereas the insulating states owe their origin to strong e-e interactions. In Ref. [75], the authors studied TBG samples with suppressed e-e interactions by changing its dielectric environment. Indeed, if the distance between TBG and a metallic layer is made smaller than the moiré unit cell size $\approx 15\,\text{nm}$, polarization charges screen out the Coulomb interactions on that scale. They found a strong suppression of the insulating states at half-filled flat bands when the metallic graphite screening layers (see Fig. 1.8(a)) were placed closer than 10 nm from the TBG plane, separated from it by insulating multilayers of hBN. On the other hand, rather than being weakened, superconductivity persisted in the absence of the insulating states, taking over the phase space vacated by them and spanning wide doping regions without interruption.

In Ref. [76], the authors investigated Van der Waals systems of the form hBN-TBG-WSe_2-hBN, i.e. heterostructures where TBG is encapsulated between hBN on one side and a single layer of tungsten diselenide (a TMD insulator with lattice parameter $\approx 0.353\,\text{nm}$) on the other. This choice was made because the typical high quality substrate used in TBG experiments is hBN, which, as discussed previously, has a lattice parameter very similar to the one of graphene. It turns out that relative alignment between the hBN and TBG is critical, because monolayer graphene aligned with hBN froms a moiré pattern with typical length scales $\approx 15\,\text{nm}$, the same of magic angle TBG. For example, a ferromagnetic state [67, 68] was observed in devices in which hBN aligns with TBG. However, in such devices the band structure of the flat bands is strongly altered, and superconductivity — typically observed when the hBN and TBG are misaligned — is absent. The Authors of Ref. [76] have studied four TBG–WSe_2 devices finding robust superconductivity in all the studied structures, even for twist angles fairly different from the magic angle. Although superconductivity persisted for all the twist angles considered, the insulating phases were shown to be quickly suppressed as the twist angle was reduced. For the smaller angle twist angle considered $\theta = 0.87°$, correlated insulating behaviour was heavily suppressed at all filling factors.

This corpus of experimental observations is in contrast with scenarios wherein superconductivity arises from a Mott-like insulating state as in high-temperature superconductors and are more consistent with phonon-only mediated superconductivity.

The presence of strong e-e interactions in TBG at Fermi energies within the flat bands was confirmed by scanning tunneling microscopy and scanning tunneling spectroscopy experiments such as the ones in Refs. [70, 71, 72, 73]. In these experiments it was possible to probe the local density of states of TBG at different Fermi energies. The local density of states gives informations on the quasiparticle spectra at the current Fermi energy, and it was showed that as long as the Fermi energy lies outside the flat bands, the quasiparticle spectrum can be adequately described by a single particle model of TBG. On the other hand, when the flat bands are partially filled, the local density of states of TBG develops many features which is not possible to explain within a simple single particle picture. In Ref. [72], for example, it was showed that

the experimental observations at Fermi energies lying in the flat bands are qualitatively reproduced by the numerical results obtained through exact diagonalization of the Hubbard model on small triangular clusters.

1.2.2 Collective excitations in twisted bilayer graphene close to the magic angle

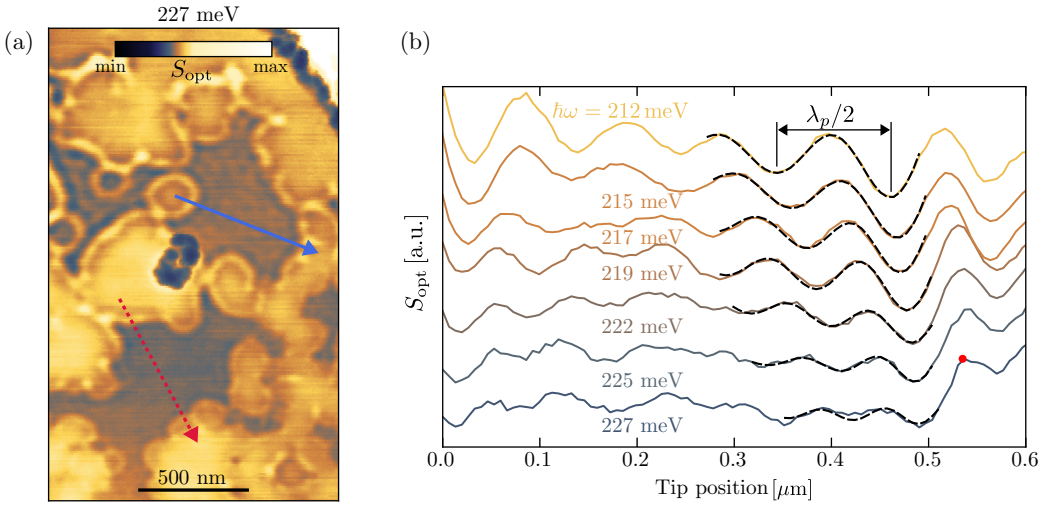

FIGURE 1.9: Panel (a): Near-field amplitude images of 1.35° twisted bilayer graphene at excitation energy $\hbar\omega = 227\,\text{meV}$. Solid and dashed arrows indicate linetraces associated to data in panel (b). Panel (b): Linetraces along the solid blue arrow in panel (a), visualizing the strong dependence of the plasmon wavelength on the excitation energy. Lines are vertically separated for clarity. From a fit (dashed lines) according to the model presented in Eq. (1.26), it is possible to extract the plasmon wavevector $q_1 = 2\pi/\lambda_p$. The red dot marks the position of the reflecting interface used in the fits. The Figure is adapted from Ref. [43].

The experimental works that we have just presented rely on techniques which are sensitive only to the static (very low frequency) response of the system. In systems where electron-electron (e-e) interactions play a dominant role, experimental techniques that probe the response to perturbations carrying a finite inplane wavevector $\boldsymbol{q}$ and angular frequency ω are expected to be rich sources of information. One of these techniques is the — already mentioned — scattering-type scanning near-field optical microscopy, or simply s-SNOM. In this Section we review the experimental observations of Ref. [43], where collective excitations in TBG close to the magic angle have been probed thanks to the s-SNOM technique. The theory developed in Chapter 3 of this Thesis has been used to interpret the experimental observations which we are about to present.

The experiment consists in s-SNOM measurements with mid-infrared light (free-space wavelength in the range $5\,\mu\text{m} < \lambda_0 < 11\,\mu\text{m}$) in ambient conditions $T = 300\,\text{K}$. As anticipated in Section 1.1.3, the first step of a s-SNOM experiment requires the

generation of a nanoscale light hotspot by focussing a laser beam on the apex of a sharp (apex radius $\approx 25\,\mathrm{nm}$) metallic atomic force microscope tip. This hotspot then interacts with the charge carriers and produces collective excitations that are reflected by interfaces, return to the tip, and are finally converted into a scattered field, which is measured by a photodetector. By scanning the tip position it is possible to acquire, simultaneously, a spatial map of the backscattered light intensity S_{opt} and the sample topography. Noise and far-field contributions to the optical signal were strongly reduced by locking to the third harmonic of the tapping frequency of the tip.

In Fig. 1.9(a), we display a typical near-field image of TBG with no gate voltage applied[1] and at twist angle $\theta = 1.35°$. The most evident feature is the presence of well-defined optically active areas where S_{opt} displays an oscillatory spatial behaviour. The latter has a characteristic period $\approx 80\,\mathrm{nm}$, about one order of magnitude larger than the moiré lattice parameter at that twist angle. The Authors attribute this oscillatory behaviour to the excitation of a propagating collective electronic mode. The fact that these interference patterns are observed in ungated TBG is in stark contrast with the intraband collective electronic excitations discussed in Section 1.1.3 of single-layer graphene, where high doping levels $> 10^{13}\,\mathrm{cm}^{-2}$ are required to propagate at the frequencies ω.

To get more insight into the nature of the collective excitations, their frequency dependence was probed by repeating the near-field measurements at different excitation energies. A dramatic change in the interference pattern is observed even for small variations in ω (and hence in λ_0), while the boundaries of the areas where the sample is optically active remain at a fixed position. This is a signature of the dispersive character of the propagating collective excitations that move in Fabry-Pérot-like cavities, due to reflecting interfaces.

The Authors extracted one-dimensional cuts of the measured S_{opt} along two specific lines (see arrows in Fig. 1.9(a)). The resulting profiles are shown in Fig. 1.9(b) as lines for a few representative photon energies. The oscillating signal is well fitted by the following expression, representing a tip-launched, tip-detected wave reflected at an interface:

$$S_{\mathrm{opt}}(x) = \mathrm{Re}\left[Ax^{-1/2}e^{2iqx}\right] + Bx. \tag{1.26}$$

Here, x is the tip position along the line cut, as measured from the interface, $A = A_1 + iA_2$ and $q = q_1 + iq_2$ are complex fit parameters, and B represents a linear background [40]. Note the factor of two in the exponential function that appears because the collective excitation makes a full round trip between the tip and the reflecting interface. The fitting procedure yields quantitative results for the real part q_1 of the wavevector q while the imaginary part q_2 has a larger error.

From the extracted values of $q_1(\omega)$ the Authors were able to construct a dispersion curve for the collective excitation as shown in Fig. 1.10(a). For energies above 200 meV, the dispersion is approximatively linear with a group velocity $v_s \approx 1.3 \times 10^6\,\mathrm{m/s}$, and crosses the $q_1 = 0$ point for $\hbar\Omega_{\mathrm{exp}} \approx 190\,\mathrm{meV}$. For lower energies, the typical discretization pattern of a finite size cavity appears (i.e. where the distance between

[1] At zero applied voltage, the experimentalists showed that their devices are close to charge neutrality.

the reflecting interfaces is comparable to the plasmon wavelength $2\pi/q_1$). Remarkably, the group velocity is larger than theoretically anticipated. See e.g. Ref. [77], where flat plasmonic bands were predicted, and the discussion below. As we will see, this points to a larger spectral weight in the optical transitions. Clearly, the observed nearly-linear dispersion, initiating from a finite energy $\hbar\Omega_{\text{exp}}$ for $q_1 = 0$, is very different from the typical Dirac plasmon dispersion of doped graphene discussed in Section 1.1.3

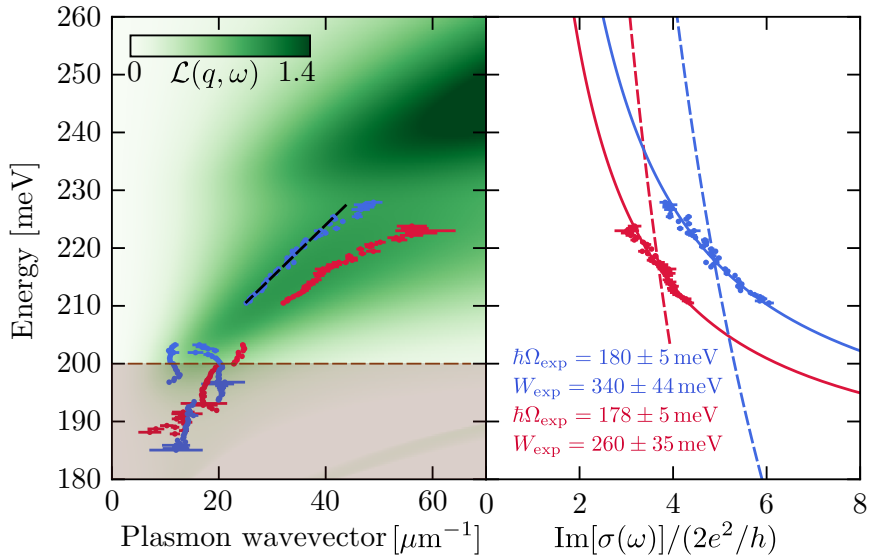

FIGURE 1.10: (Left Panel) Dispersion relation determined from fitting individual line-traces as the ones in Fig. 1.9(b) to a sinusoidal function (red points). The blue points are obtained in a similar way but from a slightly different location (solid blue arrow in Fig. 1.9(a)). The plasmon group velocity (black dashed line) is extracted thanks to a linear fit on the blue data points. The horizontal dashed line marks the threshold of the hBN reststrahlen band. The colorplot represents the loss function, calculated from the chirally-symmetric continuum model [78]. (Right Panel) Extracted values of the optical conductivity with the same colour coding as in the left panel. Dots represent experimental data, dashed lines are Drude fits, while solid lines are fits with resonant profiles. Figure adapted from Ref. [43]

To relate these observations to the electronic bands in the moiré superlattice, it is also convenient to extract the value of the optical conductivity $\sigma(\omega)$ for the optically active regions. In the local approximation, where the optical conductivity is taken to be independent of q and contributions from reciprocal lattice vectors are neglected, the longitudinal dielectric function [30] is given by[2] $\epsilon(q,\omega) = 1 + iqV_{q,\omega}\frac{\sigma(\omega)}{\omega}$ where $V_{q,\omega}$ is the 2D Fourier transform of the Coulomb potential, in which the effects of the optical response at frequency ω of the hBN crystal slab surrounding the TBG sample are included, as well with the finite thickness of the hBN slabs. Finite thickness effects are important close to the upper edge of the hBN reststrahlen band where the hBN in-plane permittivity vanishes and the out-of-plane decay length of the mode diverges (See

[2]This expression for the longitudinal dielectric function is a result of the random phase approximation. The random phase approximation will be introduced and discussed in Chapter 2.

Section 1.1.4). Neglecting the finite thickness of hBN would lead to a wrong dispersion relation, yielding a collective mode that does not enter the upper reststrahlen band. Collective modes can be found by solving $\epsilon(q,\omega)=0$. From the measured collective excitation dispersion, it is possible to find find the imaginary part $\mathrm{Im}\,[\sigma(\omega)]$ of the local conductivity, using the expression $\sigma(\omega)=i\omega/q^2V_{q,\omega}$ and neglecting the imaginary part of q.

The simplest possible fitting function, of the Drude form is

$$\mathrm{Im}[\sigma(\omega)]=\frac{4e^2}{h}\frac{W_0}{\hbar\omega}, \tag{1.27}$$

where W_0 is a fitting parameter with dimensions of energy. Using this expression yields $W_0\approx 1100\,\mathrm{meV}$ (that would correspond, for two uncoupled single-layer graphene sheets, to a Fermi energy $E_\mathrm{F}\approx 550\,\mathrm{meV}$ in each layer) and a very poor fit. This confirms that these experimental data data are not consistent with a regular intraband graphene Dirac plasmon. A much better fit (see Fig. 1.10(b)) is obtained by using the following resonant form

$$\mathrm{Im}\,[\sigma(\omega)]=\frac{4e^2}{h}W_\mathrm{exp}\frac{\hbar\omega}{\hbar\omega-\hbar\Omega_\mathrm{exp}}, \tag{1.28}$$

with W_exp and Ω_exp fitting parameters. Fitting this function yields $\hbar\Omega_\mathrm{exp}\approx 180\,\mathrm{meV}$ and a spectral weight $W_\mathrm{exp}\approx 300\,\mathrm{meV}$ for both presented datasets. The real part of the optical conductivity is recovered recalling that, because of causality, $\mathrm{Re}[\sigma(\omega)]$ and $\mathrm{Im}[\sigma(\omega)]$ are related by the Kramers-Kronig relations [30]. The theoretical justification for the resonant lineshape extracted from the experimental data and for the values of Ω_exp and W_exp depends on the details of the moiré electronic bands of TBG, whose theory will be presented in Chapters 2 and 3. A qualitative explaination of the origin of the resonant lineshape Eq. (1.28) follows by knowing that certain moiré energy bands of TBG — as calculated in Chapter 3 — show what is called "band nesting", which is the phenomenon of two electronic energy bands being parallel in the energy-wavevector space. In particular, band nesting in TBG occurs near the K point of the superlattice Brillouin zone. Close to the K point in TBG, different couples of bands — say ν and ν' — are such that $\nabla_{\boldsymbol{k}}\epsilon_{\boldsymbol{k}\nu}\approx\nabla_{\boldsymbol{k}}\epsilon_{\boldsymbol{k}\nu'}$ in a range of values of $\boldsymbol{k}$. In other words, the bands are parallel to each other for a wide range of crystal wavevectors $\boldsymbol{k}$. The joint density of states for these pairs of bands is large at the transition frequency and the resultant optical absorption spectrum $\mathrm{Re}\,[\sigma(\omega)]$ has a peak at a near frequency $\hbar\Omega_\mathrm{th}$. Now, the resonant lineshape introduced in Eq. (1.28) yields, through the Kramers-Kronig relations:

$$\mathrm{Re}\,[\sigma(\omega)]=\pi\frac{2e^2}{h}W_\mathrm{exp}\frac{\delta(\hbar\omega-\hbar\Omega_\mathrm{exp})+\delta(\hbar\omega+\hbar\Omega_\mathrm{exp})}{2}, \tag{1.29}$$

which evidently has two peaks at energies $\pm\hbar\Omega_\mathrm{exp}$. From this simple argument it follows that the resonant lineshape introduced empirically in Eqs. (1.28) and (1.29) represent the peak seen in the microscopically calculated (i.e. thanks to the theory developed in Chapter 2) optical conductivity $\sigma(\omega)$ at frequency $\hbar\Omega_\mathrm{th}$.

1.3 Transport in two-dimensional topological insulators

In this Section we introduce the concept of topological phase of matter by discussing its peculiar physical properties along with the experiments devised to probe such properties. Topological phases of matter exhibit unique experimental signatures which are insensitive to disorder and smooth variations in materials parameters. These properties do not change unless the system passes through a quantum phase transition, and can be understood as emerging from the peculiar topological structure of the electronic quantum state. Recently, topological phases have also gained a lot of appeal because of their potential practical applications: indeed, it has been proposed that a topological quantum computer could employ the 2D quasi-particles of a topological state called Fractional Quantum Hall state. A major advantage of a topological quantum computer over one using trapped quantum particles is that the former encodes information nonlocally and hence is less susceptible to local decoherence process [79, 80].

In this section we are going to give a review of different topological phases of matter from an experimental perspective, postponing a thorough theoretical tractation to Chapter 4. In particular, we are going to focus on two-dimensional insulating phases, i.e. phases where a bulk energy gap separates the highest occupied electronic states from the lowest empty states. In contrast to an ordinary insulator (often also called "trivial" insulator), the edge of a two dimensional insulator exhibiting topological properties, hosts conducting states. Among the topologically non-trivial insulating phases we can distinguish Chern insulators (and quantum Hall phases), arising when time-reversal symmetry is broken, and $\mathbb{Z}_2$ topological insulators (or quantum spin Hall phases), whose edge states are protected by time-reversal symmetry [7].

The question underlying the topological classification of insulators is whether all insulating phases are equivalent to each other, and in particular whether the ensembles of the valence bands of different insulators can be continuously transformed into each other without closing the energy gap. An informal argument explaining the origin of surface (or edge) states present in topological phases is as follows. The vacuum as well as most conventional insulating crystals are said to be topologically trivial. At the interface between such a standard insulator and a topological insulator, it is not possible for the band structure to interpolate continuously between a topological insulator and the vacuum without closing the gap. This forces the gap to close at this interface leading to metallic edge states of topological origin.

1.3.1 Quantum Hall effect and Chern insulators

A first example of a topologically non-trivial insulating state is the integer quantum Hall state [82], which occurs when electrons confined to two dimensions are placed in a strong magnetic field. The non-trivial topological properties of quantum Hall states, in practice, are observed in transport experiments. The latter is also true for the other topological materials considered in this Thesis. The quantum Hall effect was first

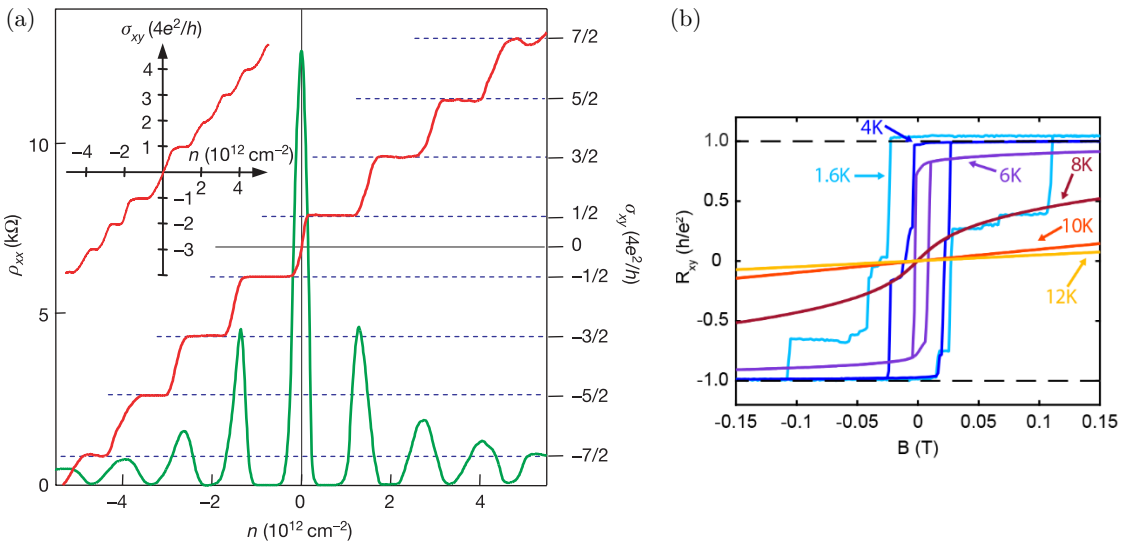

FIGURE 1.11: Panel (a): Hall conductivity σ_{xy} (red curve) and longitudinal resistivity ρ_{xx} (green curve) of graphene as a function of particle concentration at magnetic field $B = 14\,\mathrm{T}$ and temperature $T = 4\,\mathrm{K}$. $\sigma_{xy} = \pm 2e^2(2n+1)/h$ is calculated from the measured dependences of $\rho_{xy}(V_g)$ and $\rho_{xx}(V_g)$ as $\sigma_{xy}(V_g) = \rho_{xy}(V_g)/(\rho_{xy}^2(V_g) + \rho_{xx}^2(V_g))$. Inset: σ_{xy} in bilayer graphene, where the quantization sequence is normal and occurs at integer multiples of $4e^2/h$. Panel (b): Quantum anomalous Hall effect in the hysteresis loops for the Hall resistance of twisted bilayer graphene at various temperatures and at particle density $n = 2.37 \times 10^{12}\,\mathrm{cm}^{-2}$. At zero magneric field and low temperatures, the Hall resistance is $\pm h/e^2$. Panel (a) adapted from Ref. [81]. Panel (b) adapred from Ref. [68].

reported for the two-dimensional electron gas in the inversion layer of a silicon metal-oxide-semiconductor field-effect-transistor at temperature $T = 1.5\,\mathrm{K}$ and magnetic field $B = 18\,\mathrm{T}$ by Klaus von Klitzing [82] in 1980, and earned him the Nobel prize in 1985. The physical quantity of interest in the quantum Hall effect is the so-called Hall condictivity σ_{xy}, i.e. the ratio between the electric current density along $\hat{x}$ and the $\hat{y}$-component of the electric field in the sample. In Fig. 1.11(a), we show σ_{xy} for both monolayer graphene and bilayer graphene (inset). The Hall conductivity for two-dimensional materials in strong magnetic fields is quantized to integer values of the "conductance quantum" e^2/h. In particular, for a material with linearly dispersing bands such as graphene, $\sigma_{xy} = (n + 1/2)e^2/h$ with $n \in \mathbb{Z}$ and $n \neq 0$, whereas for a material with parabolic band dispersion, such as *aligned* bilayer graphene $\sigma_{xy} = ne^2/h$, with $n \in \mathbb{Z}$. The previous expressions for the Hall conductivity should be multiplied by the appropriate degeneracy factor g, if needed. The quantization of σ_{xy} has been measured to 1 part in 10^9, making it very appealing for metrological applications. This precision is a manifestation of the topological nature of σ_{xy}.

The non-vanishing Hall conductance σ_{xy} is due to the aforementioned edge states, which are *necessarily* present at the interface between a topological material and a trivial insulator. Indeed, it is known from the theory of ballistic transport (see Section 4.1) that each transport mode adds a factor of e^2/h to the conductivity. From this consideration it follows that the integer n of conductance quantums e^2/h to which σ_{xy}

is quantized in the quantum Hall effect is just the number of edge states in the system.

Insulating states with perfectly conducting edge modes are not exclusive to the case of quantum Hall effect. D. Haldane, in the 1988 work of Ref. [83] proposed a lattice model for a topologically non-trivial band insulator exhibiting the same edge behaviour as the quantum Hall states in absence of external magnetic field. Systems such as the one presented in Ref. [83] are called *Chern insulators*. The trick to obtain a topologically non-trivial lattice model is to break time-reversal symmetry by means of complex hopping parameters in the lattice model. In a way, the role that the magnetic field has in quantum Hall states is replaced by the complex hopping parameters in Chern insulators. In Fig. 1.11(b) we show the experimental observation of a Chern insulating state in twisted bilayer graphene aligned with the hBN substrated.

The perfect quantization of σ_{xy} in quantum Hall systems and Chern insulators can also be understood on more physical grounds by looking at the nature of the edge states themselves. It is indeed possible to show that the edge states of a quantum Hall system or Chern insulator are *chiral*, i.e. they can flow along the edge only in one of the two possible directions. In this way, an electron traversing the edge of the sample cannot be scattered in the direction opposite to his current motion simply because, due to the chirality of the edge mode, there are no available states for transport in the opposite direction.

1.3.2 Two-dimensional topological insulators

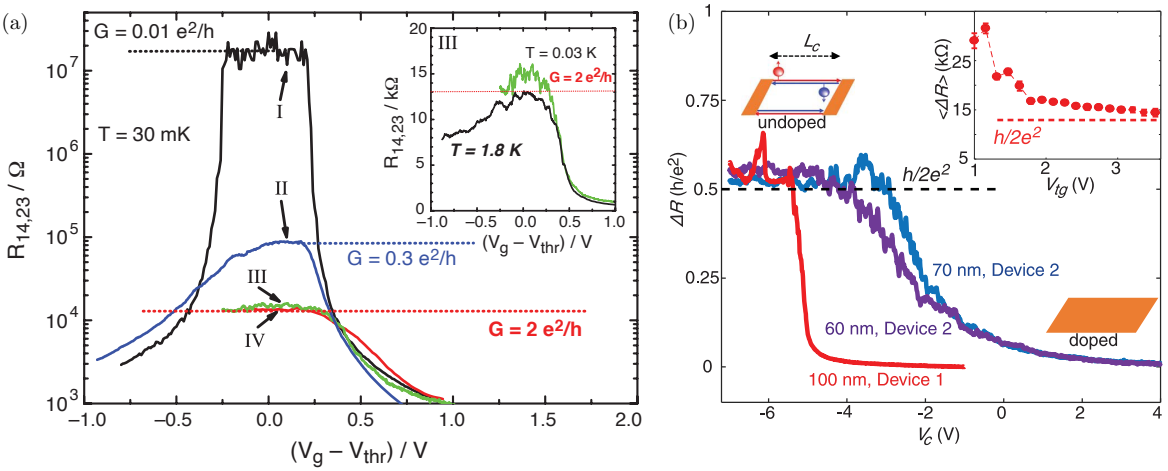

FIGURE 1.12: Panel (a): measures of non-local resistance as a function of the gating voltage in CdTe/HgTe/CdTe quantum wells of different width. Devices *III* and *IV* are in the topological regime, and the non-local resistance is roughly $h/(2e^2)$ (see inset). On the other hand, devices *I* and *II* are in the trivial insulating regime, showing much higher resistances. Panel (b): non-local resistance in WTe_2 crystals approaching the quantized value $h/(2e^2)$ expected in 2DTIs. Panel (a) adapted from Ref. [84]. Panel (b) adapted from Ref. [52].

Since the Hall conductivity σ_{xy} is odd under time-reversal symmetry, the topologically non-trivial states described above can only occur when the time-reversal symmetry is broken. However, the spin-orbit interaction allows a different topological class of insulating band structures when time-reversal symmetry is unbroken [85, 86]. The key to understand these new topological materials, called $\mathbb{Z}_2$ insulators, or simply Two Dimensional Topological Insulators (2DTIs) is to examine the role of time-reversal symmetry for spin 1/2 particles. This is going to be accomplished in Chapter 4, whereas this Section is devoted to a discussion of the experimental observations concerning $\mathbb{Z}_2$ topological insulators.

Very much like quantum Hall systems, 2DTIs are electron systems with a gap in the bulk density of states and conducting edge states. However, because of the unbroken time-reversal symmetry, and in contrast to quantum Hall systems, the edge states of 2DTIs display *helicity*, i.e. the electrons can flow in both directions, but particles with opposite spin polarization are forced to flow in opposite directions along the edge. Kramers theorem, which is valid when time-reversal symmetry is present, implies that in the absence of many-particle effects, Anderson disorder in a 2DTI cannot induce back-scattering at a 2DTI edge, yielding conductance quantization against elastic disorder [7, 8, 87, 88, 89, 90]. Evidence for the edge modes of 2DTIs has been reported in many systems, but the conductance quantization in such 2DTIs is far from being perfect like in the case of quantum Hall systems.

After the theoretical prediction in Ref. [88] that an appropriately enginereed semiconducting heterostructure of CdTe/HgTe/CdTe could be a 2DTI, the Authors of Ref. [84] reported evidence for an edge state state in this system. As shown in Fig. 1.12(a), the four-terminal resistances of micrometer-scale HgTe/CdTe samples in the 2DTI regime are approximately $2e^2/h$, i.e. the value expected for helical edge transport in the ballistic regime. In contrast, for a sample with a thickness of the HgTe layer of smaller than 6.3 nm, the critical thickness to have a 2DTI in this system, the resistance increases to the order of mega ohms, consistent with the insulating behavior expected for the topologically trivial regime. Further evidence for helical edge transport in HgTe quantum wells was obtained from non-local transport in micrometer-sized devices with various geometries [91, 92]. Even for micrometer-sized 2DTI samples, however, the quantisation of the edge conductance is much less precise than the quantum Hall effect. Another class of semiconducting heterostructures, InAs/GaSb quantum wells, were also predicted [93] to be 2DTI candidates. The evidence for edge transport in these systems were firstly reported in Ref. [94] and [95], despite the fact that the parallel bulk conduction had to be subtracted from the total conductanc. The Authors of Ref. [96] subsequently managed to use Si-doping to suppress the bulk conductivity and observed quantised edge channel conductance with a precision level of $\sim 1\%$.

Semiconducting heterostructures were extensively studied in the low-temperature regime (below 4 K) [84, 96] because of their small energy gap. For channel lengths L shorter than ~ 1 μm, fluctuations of the conductance around the quantized value $2e^2/h$ were observed as a function of the back gate voltage. For longer channels, even the average conductance was found to deviate from $2e^2/h$ and even totally suppressed [97], when the edge was perturbed by a scanning tip.

Another class of materials exhibiting 2DTIs signatures is atomically-thin TMDs

crystals such as WTe_2. ARPES experiments such as the one in Ref. [98] showed that a WTe_2 monolayer has a bulk energy gap of 55 meV, much larger than those in HgTe/CdTe and InAs/GaSb quantum wells. The existence of edge channels in WTe_2 monolayers has been confirmed thanks to transport measurements as the one in Ref. [52]. The resistance of WTe_2 samples with different channel lengths as a function of the gate voltage is showed in Fig. 1.12(b). Edge states in WTe_2 were also directly imaged thanks to microwave impedance microscopy in Ref. [53]. At the present day, monolayers of WTe_2 exhibit [52] conductance quantization up to 100 K, making them the 2DTIs existing at the highest temperatures up to date, though displaying quantization only in short channels ($L \lesssim 100$ nm).

2
Twisted Bilayer Graphene

This Chapter is dedicated to twisted bilayer graphene, a two-dimensional material which in recent years gained exceptional amounts of attention in the condensed matter community. The salient experimental observations on TBG have been presented in the introductory Chapter 1. This Chapter, on the other hand, is going to deal with the theoretical modeling of TBG.

Twisted bilayer graphene [3, 4, 59, 60, 61, 62, 63, 64] is a system consisting of two graphene sheets stacked one on top of each other, with a relative rotation of the crystal axes quantified by the twist angle θ. The physics of the two-dimensional electron system roaming in TBG with twist angles $\theta \lesssim 3^\circ$ is dominated by a triangular moiré pattern of periodicity $\approx a/\theta$[rad], where $a \approx 0.246$ nm is the lattice constant of monolayer graphene (see Section 1.1.1). In this case, the energy spectrum is well described by a continuum model [3] which accounts for the long-range moiré modulations of the inter-layer tunneling amplitudes.

At twist angles of $\approx 1^\circ$, the continuum model [3] predicts the existence of a pair of remarkably flat bands, with a bandwidth of less than 20 meV, close to the charge neutrality point (CNP), where the Fermi level of an undoped sample lies. These bands exhibit a linear dispersion around the moiré Brillouin zone corners, with a twist-angle-dependent Fermi velocity $\hbar v_{\mathrm{F}}(\theta)$. The largest angle $\theta^\star$ satisfying $\hbar v_{\mathrm{F}}(\theta^\star) = 0$ is called the first *magic angle* (or simply *magic angle*) [3]. For systems with twist angles close to the magic one, the bandwidth of the flat bands reaches its minimum, ensuring a large density of states and strengthened electron-electron (e-e) interactions.

Research on TBG is mostly focussed on the regime where the twist angle θ is close to the magic angle because of the interesting many-body effects arising in such systems. An exception to this trend worth mentioning, concerns investigations on the regime where the twist angle $\theta \approx 30^\circ$ [99, 100, 101, 102]. In this case, the overlaid hexagonal lattices are mapped onto a 12-fold rotationally symmetric quasicrystalline lattice without any translational symmetry. These systems are interesting because

of the interplay between the quasicrystalline order and the relativistic nature of the massless Dirac particles of graphene.

The theoretical description of TBG can be accomplished thanks to different models and approximations. Each of them is going to be thoroughly presented, along with its strengths and its weakeness, in Section 2.1 of the present Chapter. These models are going to be the starting point for any of our subsequent theoretical investigation of TBG. The next Sections of the Chapter are dedicated to review the Hartree theory (Section 2.2), and the linear response theory (Section 2.3) for translationally invariant systems. These analytical results are going to be applied to the case of TBG in Chapter 3. The Chapter is concluded by Section 2.4, where we present the numerical techniques and algorithms that we have used to develop the codes used to obtain many of our the results in Chapter 3.

2.1 Single particle theory of twisted bilayer graphene

In this Section we present two different ways to model TBG which are commonly used to calculate its electronic states. We will start with a tight-binding model describing the Carbon atoms in each of the graphene layers. From a conceptual point of view the tight-binding model is straightforward, as it models TBG down to the atomic scale. From a practical point of view, however, the tight-binding model may not be convenient at all, as the dimension of the problem to be solved explodes as the twist angle is reduced. For this reason, a low-energy continuum model is often preferred to the tight-binding model. The continuum model of TBG will be derived in Section 2.1.2, and describes the TBG by retaining only the long-wavelength components of the tight-binding model.

2.1.1 Tight binding model

The tight-binding model of TBG is the natural extension of the atomistic lattice model of graphene presented in Section 1.1.1. In this Thesis we will use the indexing notation $\ell = \pm 1$ for layer 1 and 2, respectively. Layer 1 is *always* assumed to be rotated by $\theta/2$ and layer 2 by $-\theta/2$ so their relative twist is θ. This can be accomplished by rotating graphene's primitive translation vectors and sub-lattice basis vectors with the 2×2 rotation matrix

$$R_\ell(\theta/2) = \cos(\theta/2)\mathbb{1}_{2\times 2} - i\sin(\ell\theta/2)\sigma_y \ . \tag{2.1}$$

Here and in the following, $\mathbb{1}_{2\times 2}$ is the identity matrix and σ_i with $i = \{x, y, z\}$ is the ordinary 2×2 i-th Pauli matrix. For convenience, we also copy the expression of graphene's primitive translation and basis vectors from Section 1.1.1

$$\boldsymbol{a}_1 = a\left(-\frac{1}{2}, \frac{\sqrt{3}}{2}\right), \qquad \boldsymbol{a}_2 = a\left(\frac{1}{2}, \frac{\sqrt{3}}{2}\right), \tag{2.2a}$$

$$\boldsymbol{d}_A = (0, 0), \qquad \boldsymbol{d}_B = \frac{a}{\sqrt{3}}\left(-\frac{\sqrt{3}}{2}, \frac{1}{2}\right), \tag{2.2b}$$

where $a \equiv a_0\sqrt{3} = 0.246\,\text{nm}$ is the lattice parameter of monolayer graphene. The atoms' positions in twisted bilayer graphene are therefore:

$$\boldsymbol{R}_{n,\ell,\tau} = n_1\tilde{\boldsymbol{a}}_{1,\ell} + n_2\tilde{\boldsymbol{a}}_{2,\ell} + \boldsymbol{d}_{\tau,\ell} \quad \text{with } n \equiv (n_1, n_2) \in \mathbb{Z}\times\mathbb{Z}\,, \tag{2.3}$$

where $\boldsymbol{d}_{\tau,\ell}$ is the basis vector of the sublattice τ in layer ℓ and the vectors $\tilde{\boldsymbol{a}}_{1/2,\ell}$ are primitive translation vectors of the graphene lattice in layer ℓ

$$\tilde{\boldsymbol{a}}_{1/2,\ell} = R_\ell(\theta/2)\cdot\boldsymbol{a}_{1/2}\,. \tag{2.4}$$

In this Thesis the basis vectors of the sublattice τ in layer ℓ are choiced according to the following convention

$$\boldsymbol{d}_{\tau,\ell} = \begin{cases} \frac{a}{\sqrt{3}}R_+(\theta/2)\left(-\frac{\sqrt{3}}{2},\frac{1}{2}\right)\,, & \text{if layer} = 1 \text{ and sub-lattice} = B\,. \\ -\frac{a}{\sqrt{3}}R_-(\theta/2)\left(-\frac{\sqrt{3}}{2},\frac{1}{2}\right)\,, & \text{if layer} = 2 \text{ and sub-lattice} = A\,. \\ \boldsymbol{0}\,, & \text{otherwise}\,. \end{cases} \tag{2.5}$$

The choice of the primitive translation vectors as in Eq. (2.4) and basis vectors as in Eq. (2.5) is such that in the limit $\theta \to 0$ one obtains AB-stacked bilayer graphene. In the following, sums over the index n appearing in Eq. (2.3) should be intended as

$$\sum_n [\,\cdots\,] = \sum_{n1,n2\in\mathbb{Z}} [\,\cdots\,]\,. \tag{2.6}$$

We now discuss under which conditions, i.e. for which twist angles θ, atoms arranged according to Eq. (2.3) form a translationally invariant structure. From Eqs. (2.4) and (2.5) it follows that at the origin a site of sub-lattice A for layer 1 exactly overlap with a site of sub-lattice B for layer 2 (AB-stacking). Now, a necessary and sufficient condition for translational invariance is the existence of a vector $\boldsymbol{t}$ such that at $\boldsymbol{t}$, again, an A site of layer 1 overlaps with a B site of layer 2. Different ways of derive the entire set of angles satisfying this condition were presented in literature [60, 61, 64]. In each of these works, the crystalline angles (i.e. the twist angles for which TBG is translationally invariant) are labelled by two integer indexes and due to the symmetry properties of graphene are defined just from 0 to $\pi/3$. Following the notation of Ref. [64], the crystalline angles are defined by the following relation

$$\theta_c(m,r) = \arccos\left(\frac{3m^2+3mr+r^2/2}{3m^2+3mr+r^2}\right), \tag{2.7}$$

m and r being positive *coprime* integer numbers. From the integers m and r descend all the information concerning the geometry of crystalline TBG. In particular, it is possible to show that the primitive translation vectors of the moiré superlattice of TBG at twist angle $\theta_c(m,r)$ are

$$\boldsymbol{t}_1 = \lambda_{\text{M}}\,(0,\,1)\,, \qquad \boldsymbol{t}_2 = \lambda_{\text{M}}\left(-\frac{\sqrt{3}}{2},\,\frac{1}{2}\right), \tag{2.8a}$$

where the moiré periodicity λ_{M} depends on the two coprime integers m and r appearing in Eq. (2.7) and on the graphene lattice parameter a as follows

$$\lambda_{\mathrm{M}} \equiv ar\sqrt{\frac{3}{\gcd(r,3)}\left[\left(\frac{m}{r}\right)^2+\frac{m}{r}+\frac{1}{3}\right]}. \tag{2.8b}$$

Here, $\gcd(x,y)$ is the greatest common divisor between the integers x and y.

As evident from the equations above, the symmetry of the moiré superlattice of TBG is triangular. To obtain the energy bands of TBG in the tight-binding approximation it is necessary to write down the Hamiltonian of the system and exploit Bloch's theorem to diagonalise it. We start by defining the localized atomic orbitals $|n,\ell,\tau\rangle$, which are centered at the point $\boldsymbol{R}_{n,\ell,\tau} = n_1\tilde{\boldsymbol{a}}_{1,\ell} + n_2\tilde{\boldsymbol{a}}_{2,\ell} + \boldsymbol{d}_{\tau,\ell}$ with $n \equiv (n_1,n_2) \in \mathbb{Z}\times\mathbb{Z}$. We are going to write the tight-binding Hamiltonian of TBG in a basis formed by the states $|n,\ell,\tau\rangle$, whose wavefunction is

$$\langle \boldsymbol{r}|n,\ell,\tau\rangle = \phi(\boldsymbol{r}-\boldsymbol{R}_{n,\ell,\tau}) \ , \tag{2.9}$$

where $\phi(\boldsymbol{r})$ is the wavefunction of a p_z orbital of the Carbon atom centered at the origin. The atomic orbitals are assumed to be orthogonalized according to

$$\langle n,\ell,\tau|n',\ell',\tau'\rangle = \delta_{n,n'}\delta_{\ell,\ell'}\delta_{\tau,\tau'} \ . \tag{2.10}$$

The Hamiltonian of TBG can be expressed as a sum of intra-layer and inter-layer contributions. We will write tha intra-layer Hamiltonian — the contribution accounting for every hopping process happening within the same layer, — in the two-center approximation, and retaining only the nearest-neighbour contributions, as done in Section 1.1.1 in the case of monolayer graphene. With these approximations in order, the intra-layer Hamiltonian of TBG in layer ℓ takes the form

$$\hat{H}^{(\ell)}_{\mathrm{intra}} = -t\sum_{\langle m,n\rangle}\sum_{\tau,\tau'}|m,\ell,\tau\rangle\langle n,\ell,\tau'|(1-\delta_{\tau,\tau'}) \ , \tag{2.11}$$

with the hopping t being given by

$$-t \equiv \int d\boldsymbol{r}\ \phi^*(\boldsymbol{r})V(\boldsymbol{r}-\boldsymbol{d}_{\tau,1})\phi(\boldsymbol{r}-\boldsymbol{d}_{\tau,1}) = \int d\boldsymbol{r}\ \phi^*(\boldsymbol{r})V(\boldsymbol{r}-\boldsymbol{d}_{\tau,2})\phi(\boldsymbol{r}-\boldsymbol{d}_{\tau,2}) \ , \tag{2.12}$$

and $V(\boldsymbol{r})$ being the spherically-symmetric potential of a Carbon atom centered at the origin. The sum over $\langle m,n\rangle$ runs over neighbouring orbitals, i.e. the states $|m,\ell,\tau\rangle$ and $|n,\ell,\tau'\rangle$ in Eq. (2.11) corresponding to neighbouring orbitals.

We now move on to discuss the inter-layer term, accounting for hopping processes between two different layers and schematically represented in Fig. 2.1. In the tight-binding framework we should describe the energy involved in the tunneling of electrons between orbitals in different layers. We require this energy to be dependent on the distance $\boldsymbol{r}$ between the two orbitals and on the sublattice index of the initial and final states ($\boldsymbol{\tau'}$ and $\boldsymbol{\tau}$, respectively), but not on the initial and final layers. The inter-layer

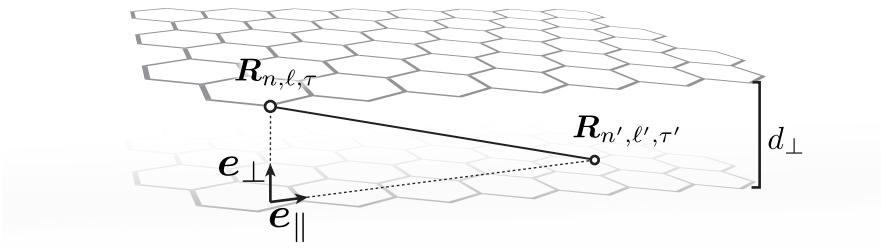

Figure 2.1: Schematic representation of the inter-layer hopping terms in the tight-binding model of twisted bilayer graphene.

tunneling energy will be denoted by the symbol $h_{\tau,\tau'}(\boldsymbol{r})$. An explicit form of $h_{\tau,\tau'}(\boldsymbol{r})$ can be obtained by approximating the transfer integrals between different orbitals $\phi(\boldsymbol{r})$ mediated by the spherically-symmetric atomic potential $V(\boldsymbol{r})$. An empirical form of the transfer integral between two p_z orbitals of Carbon atoms whose distance is $\boldsymbol{r}$ is given by the Slater-Koster approximation and is [103]

$$\tilde{h}(\boldsymbol{r}) = -t \exp\left(-\frac{\|\boldsymbol{r}\| - a/\sqrt{3}}{\lambda}\right) \frac{|\boldsymbol{r}\cdot\boldsymbol{e}_\parallel|^2}{\|\boldsymbol{r}\|^2} + t_\perp \exp\left(-\frac{\|\boldsymbol{r}\| - d_\perp}{\lambda}\right) \frac{|\boldsymbol{r}\cdot\boldsymbol{e}_\perp|^2}{\|\boldsymbol{r}\|^2}, \tag{2.13}$$

where $\lambda \approx 0.184a$ is a fitted parameter for the decay length of the hopping energy, $d_\perp = 1.36a$ is the distance between the two layers of graphene, $-t$ is the transfer integral already showed in Eq. (2.12), and $t_\perp$ is given by

$$t_\perp \equiv \int d\boldsymbol{r}\ \phi^*(\boldsymbol{r}) V(\boldsymbol{r} - \hat{\boldsymbol{e}}_z d_\perp)\phi(\boldsymbol{r} - \hat{\boldsymbol{e}}_z d_\perp), \tag{2.14}$$

i.e. $t_\perp$ is the transfer integral between two p_z orbitals which are one on top of the other at a distance $d_\perp$. In the literature, the integrals from which the hopping parameters $-t$ and $t_\perp$ are derived are also known as $V(pp\pi)$ and $V(pp\sigma)$, respectively (see e.g. Ref. [17], Chapter 5). Since the inter-layer hopping energy is exponentially decreasing as a function of $\|\boldsymbol{r}\|$, as showed in Eq. (2.13), hopping processes between atoms at distances $\|\boldsymbol{r}\| \gg \lambda$ can be safely neglected. The latter is a necessary approximation for numerical calculations. The numerical values used in this Thesis for the hopping energies t and $t_\perp$ are 2.7 eV and 0.48 eV, respectively [103].

In the Slater-Koster approximation which we have just discussed, the hopping energy between an orbital centered at $\boldsymbol{R}_{n,\ell,\tau}$ and an orbital centered at $\boldsymbol{R}_{n',\ell',\tau'}$ is

$$h_{\tau,\tau'}(\boldsymbol{R}_{n,\ell,\tau} - \boldsymbol{R}_{n',\ell',\tau'}) \equiv \tilde{h}(\boldsymbol{R}_{n,\ell,\tau} - \boldsymbol{R}_{n',\ell',\tau'}), \tag{2.15}$$

so that the inter-layer hopping term can be written as

$$\hat{H}^{(\ell,\ell')}_{\text{inter}} \equiv \sum_{n,n'} \sum_{\tau,\tau'} h_{\tau,\tau'}(\boldsymbol{R}_{n,\ell,\tau} - \boldsymbol{R}_{n',\ell',\tau'}) |n,\ell,\tau\rangle\langle n',\ell',\tau'|. \tag{2.16}$$

The full Hamiltonian of TBG is then given by summing intra-layer term Eq. (2.11) and inter-layer term Eq. (2.16) so that

$$\hat{H} = \sum_{\ell,\ell'} \hat{H}^{(\ell)}_{\text{intra}} + \hat{H}^{(\ell,\ell')}_{\text{inter}}. \tag{2.17}$$

We stress that the previous expression is valid in general, but if the twist angle θ is a crystalline angle, i.e. it belongs to the set spanned by Eq. (2.7), then the Hamiltonian Eq. (2.17) is translationally invariant.

For a translationally invariant Hamiltonian, one can define the primitive translation vectors $\boldsymbol{t}_1$ and $\boldsymbol{t}_2$, which in the case of TBG are given by Eqs. (2.8). Bloch's theorem assure that a translationally invariant Hamiltonian can be diagonalized in the basis of Bloch states. By taking the expectation value of Eq. (2.17) between the Bloch states, and using the definitions in Eqs. (2.11), (2.16), the orthogonalization conditions (2.10) and the translational invariance it is possible to obtain the matrix element of the TBG Hamiltonian in the basis of Bloch states, which is derived in full detail in Section 2.4.1 for the case of TBG. The matrix elements of the tight-binding Hamiltonian of TBG are used to numerically obtain the energy spectrum, as explained in Section 2.4.1. In any event, the physical informations of the tight-binding model of TBG are much more clearly seen in the formulation of Eqs. (2.11),(2.13) and (2.16).

It is important to stress that the tight-binding model of TBG is valid for *any* crystalline twist angle, i.e. for any twist angle which can be obtained by the relation in Eq. (2.7), and it is not restricted to small twist angles, as for the continuum model presented in the following Section. Furthermore, we now show that the crystalline angles are dense in the interval $[0, \pi/3)$, implying that the tight-binding model in principle can be used to describe arbitrarily well any twisting configuration.

By defining $x \equiv m/r$, Eq. (2.7) can be written as:

$$\theta_c(x) = \arccos\left(\frac{3x^2+3x+1/2}{3x^2+3x+1}\right) = \arccos \circ \left[\frac{3x^2+3x+1/2}{3x^2+3x+1}\right]. \tag{2.18}$$

Now, because the function $\left[\frac{3x^2+3x+1/2}{3x^2+3x+1}\right] : \mathbb{R}^+ \longrightarrow (1/2, 1]$ is invertible, as well as the function $\arccos : (1/2, 1] \longrightarrow [0, \pi/3)$, it follows that $\theta_c(x)$ is invertible. From the last consideration and because the set $\{x = m/r |\, m, r \text{ coprimes } \in \mathbb{N}\} = \mathbb{Q}^+$ is dense in $\mathbb{R}^+$, then we have that $\{\theta_c(x) |\, x \in \mathbb{Q}^+\}$ is dense in $[0, \pi/3)$. In physical terms this means that even if TBG is twisted by an angle θ not belonging to the set of crystalline angles, we can always find an *arbitrarily close* twist angle θ' which is in the set of crystalline angles. In other words, even if TBG is not in a translationally invariant configuration, it is anyway infinitesimally close to a periodic configuration. The tight-binding model of TBG can therefore describe virtually any twisting configuration. Despite this last observation, in practice it happens that the eigenvalue problem associated to the tight-binding model is often numerically intractable (see e.g. the discussion in Ref. [61] on the size of the unit cell for tight-binding TBG). For this reason the tight-binding model is often discarted in favour of the continuum model of TBG, which we now derive.

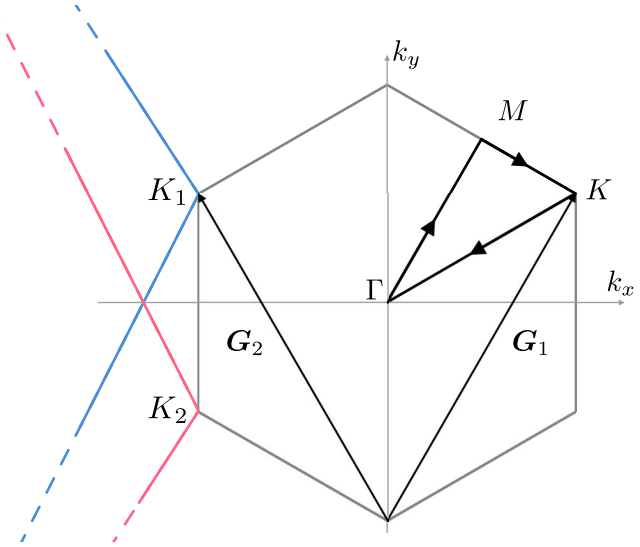

Figure 2.2: Moiré Brillouin zone of twisted bilayer graphene. The continuum model is a $\boldsymbol{k}\cdot\boldsymbol{p}$ expansion around the K_ℓ valley of layer ℓ. The blue (red) lines are edges of the Brillouin zone of layer 1 (2). The energy band structures shown in Figs. 3.1 and 3.7 are computed along the K-Γ-M-K path highlighted here.

2.1.2 Continuum model

In this Section we present a derivation of the continuum model [3, 104] used extensively in this Thesis to describe electrons roaming in the TBG moiré superlattice. The starting point to derive the continuum model are the tight-binding intra-layer Hamiltonian, Eq. (2.11), and inter-layer Hamiltonian, Eq. (2.16).

We start the derivation of the continuum model by introducing the Bloch sums of the localized atomic orbitals $|n,\ell,\tau\rangle$

$$|\boldsymbol{k},\ell,\tau\rangle = \frac{1}{\sqrt{\mathcal{N}}}\sum_n e^{i\boldsymbol{R}_{n,\ell,\tau}\cdot\boldsymbol{k}}|n,\ell,\tau\rangle\ . \tag{2.19}$$

At fixed layer ℓ and sub-lattice τ, Eq. (2.19) describes Bloch states with the periodicity of the Bravais lattice of Carbon atoms in the ℓ-th layer, and $\boldsymbol{k}$ belongs to the Brillouin Zone of the monolayer graphene in layer ℓ. These Bloch sums *do not diagonalize the TBG Hamiltonian*, and are are analogous to the ones used for the single layer case in Eq. (1.3).

Starting again with the intra-layer contribution we note that, at fixed layer index ℓ, the procedure to obtain the low-energy continuum intra-layer Hamiltonian from the tight-binding Hamiltonian Eq. (2.11) is described and explicitly carried out in Chapter 1 of Ref. [2], to which we refer. The core of this procedure is the calculation of the Taylor expansion of the matrix elements $\langle\boldsymbol{k},\ell,\tau|\hat{H}^{(\ell)}_{\text{intra}}|\boldsymbol{k},\ell,\tau'\rangle$ around $\boldsymbol{k}\approx\boldsymbol{k}^\ell_{\text{D}}$, with $\boldsymbol{k}^\ell_{\text{D}}$ being the position at which the Dirac cone of layer ℓ is centered. With the primitive translation vectors as in Eqs. (2.29), it is easy to verify (see also Fig. 1.1) that

$$\boldsymbol{k}^\ell_{\text{D}} = \frac{4\pi}{3a}R_\ell(\theta/2)\cdot(1,0)\,, \tag{2.20}$$

where $R_\ell(\,\cdot\,)$ is the rotation matrix defined in Eq. (2.1).

With the choice of primitive translation and basis vectors $\tilde{\boldsymbol{a}}_{1/2,\ell}$ and $\boldsymbol{d}_{\tau,\ell}$ as in Eq. (2.4), and Eq. (2.5) we have

$$\langle \boldsymbol{k}, \ell, \tau | \hat{H}^{(\ell)}_{\text{intra}} | \boldsymbol{k}, \ell, \tau' \rangle \approx \hbar v_{\text{F}} \left[R_\ell(-\theta/2)(\boldsymbol{k} - \boldsymbol{K}_\ell) \right] \cdot (-\sigma_x, \sigma_y). \tag{2.21}$$

Here, $(-\sigma_x, \sigma_y)$ is a vector of ordinary 2×2 Pauli matrices, $\hbar v_{\text{F}} = \sqrt{3}|t|a/(2\hbar) \simeq 0.87\times 10^6 \text{m/s}$ is the Fermi velocity of monolayer graphene—corresponding to the nearest-neighbor hopping energy of $|t| = 2.7\,\text{eV}$ adopted in the tight-binding model of graphene presented in the previous section—and $\boldsymbol{K}_\ell$ is the position of graphene's valley K_ℓ measured from the moiré Brillouin zone center Γ (see Fig. 2.2), i.e.

$$\boldsymbol{K}_{1,2} = \frac{8\pi}{3a} \sin\left(\frac{\theta}{2}\right) \left(\frac{\sqrt{3}}{2}, \pm\frac{1}{2} \right) \ . \tag{2.22}$$

We now move on to discuss the inter-layer Hamiltonian of the continuum model. In the tight-binding framework we have described the energy involved in the tunneling of electrons between orbitals in different layers in Eq (2.13) so that the inter-layer Hamiltonian is Eq. (2.16), reported here for convenience

$$\hat{H}^{(\ell,\ell')}_{\text{inter}} \equiv \sum_{n,n'} \sum_{\tau,\tau'} h_{\tau,\tau'}(\boldsymbol{R}_{n,\ell,\tau} - \boldsymbol{R}_{n',\ell',\tau'}) |n,\ell,\tau\rangle\langle n',\ell',\tau'|. \tag{2.23}$$

We now introduce the Fourier tranform of the inter-layer tunneling energy,

$$h_{\tau,\tau'}(\boldsymbol{q}) \equiv \int_A d\boldsymbol{r} e^{-i\boldsymbol{q}\,\cdot\,\boldsymbol{r}} h_{\tau,\tau'}(\boldsymbol{r}) \ , \tag{2.24a}$$

$$h_{\tau,\tau'}(\boldsymbol{r}) = \frac{1}{\mathcal{N}\Omega_{\text{u.c.}}} \sum_{\boldsymbol{q}} e^{i\boldsymbol{q}\,\cdot\,\boldsymbol{r}} h_{\tau,\tau'}(\boldsymbol{q}) \ , \tag{2.24b}$$

where the integral is performed over the area A of the 2D system and $\Omega_{\text{u.c.}}$ is the area of graphene's unit cell. We also recall the well known identity

$$\frac{1}{\mathcal{N}} \sum_{n_1,n_2\in\mathbb{Z}} e^{i(\boldsymbol{q}-\boldsymbol{k})\,\cdot\,(n_1\tilde{\boldsymbol{a}}_{1,\ell} + n_2\tilde{\boldsymbol{a}}_{2,\ell})} = \sum_{\boldsymbol{G}^\ell} \delta_{\boldsymbol{q}-\boldsymbol{k},\boldsymbol{G}^\ell} \ , \tag{2.25}$$

where $\boldsymbol{G}^\ell$ is an integer linear combination of the reciprocal lattice vectors corresponding to the primitive vectors of graphene $\tilde{\boldsymbol{a}}_{1,\ell}$ and $\tilde{\boldsymbol{a}}_{2,\ell}$, defined in Eq. (2.2). With the help of previous equations and recalling that the orbitals are centered at positions $\boldsymbol{R}_{n,\ell,\tau} = n_1\tilde{\boldsymbol{a}}_{1,\ell} + n_2\tilde{\boldsymbol{a}}_{2,\ell} + \boldsymbol{d}_{\tau,\ell}$, we can express the matrix element $\langle \boldsymbol{p}, \ell, \tau | \hat{H}^{(\ell,\ell')}_{\text{inter}} | \boldsymbol{k}, \ell', \tau' \rangle$

in the following form [105]:

$$\begin{aligned}\langle \boldsymbol{p},\ell,\tau|\hat{H}^{(\ell,\ell')}_{\text{inter}}|\boldsymbol{k},\ell',\tau'\rangle &= \frac{1}{\mathcal{N}^2\Omega_{\text{u.c.}}}\sum_{n,n'}\sum_{\boldsymbol{q}} e^{i(\boldsymbol{q}-\boldsymbol{p})\,\cdot\,\boldsymbol{R}_{n,\ell,\tau}} e^{i(\boldsymbol{k}-\boldsymbol{q})\,\cdot\,\boldsymbol{R}_{n',\ell',\tau'}} h_{\tau,\tau'}(\boldsymbol{q}) = \\ &= \frac{1}{\Omega_{\text{u.c.}}}\sum_{\boldsymbol{q}}\sum_{\boldsymbol{G}^\ell}\sum_{\boldsymbol{G}^{\ell'}} \delta_{\boldsymbol{q}-\boldsymbol{p},\boldsymbol{G}^\ell}\delta_{\boldsymbol{k}-\boldsymbol{q},\boldsymbol{G}^{\ell'}} e^{i(\boldsymbol{q}-\boldsymbol{p})\,\cdot\,\boldsymbol{d}_{\tau,\ell}} e^{i(\boldsymbol{k}-\boldsymbol{q})\,\cdot\,\boldsymbol{d}_{\tau',\ell'}} h_{\tau,\tau'}(\boldsymbol{q}) = \\ &= \frac{1}{\Omega_{\text{u.c.}}}\sum_{\boldsymbol{G}^\ell}\sum_{\boldsymbol{G}^{\ell'}} \delta_{\boldsymbol{k}-\boldsymbol{G}^{\ell'},\boldsymbol{p}+\boldsymbol{G}^\ell} e^{i\boldsymbol{G}^\ell\,\cdot\,\boldsymbol{d}_{\tau,\ell}} e^{i\boldsymbol{G}^{\ell'}\,\cdot\,\boldsymbol{d}_{\tau',\ell'}} h_{\tau,\tau'}(\boldsymbol{p}+\boldsymbol{G}^\ell) = \\ &= \frac{1}{\Omega_{\text{u.c.}}}\sum_{\boldsymbol{G}^\ell}\sum_{\boldsymbol{G}^{\ell'}} \delta_{\boldsymbol{k}+\boldsymbol{G}^{\ell'},\boldsymbol{p}+\boldsymbol{G}^\ell} e^{i(\boldsymbol{G}^\ell\,\cdot\,\boldsymbol{d}_{\tau,\ell}-\boldsymbol{G}^{\ell'}\,\cdot\,\boldsymbol{d}_{\tau',\ell'})} h_{\tau,\tau'}(\boldsymbol{p}+\boldsymbol{G}^\ell)\ .\end{aligned} \tag{2.26}$$

The matrix elements of the inter-layer Hamiltonian in the Bloch basis are thus expressed as a sum over the reciprocal lattice vectors of monolayer graphene $\boldsymbol{G}^\ell$ and $\boldsymbol{G}^{\ell'}$ of a phase factor $e^{i(\boldsymbol{G}^\ell\,\cdot\,\boldsymbol{d}_{\tau,\ell}-\boldsymbol{G}^{\ell'}\,\cdot\,\boldsymbol{d}_{\tau',\ell'})}$ multiplied by the Fourier transform of the inter-layer potential $h_{\tau,\tau'}(\boldsymbol{p}+\boldsymbol{G}^\ell)$. A drastic simplification can be performed [3], by truncating the (infinite) sums over reciprocal lattice vectors in the previous equations. The truncation is justified as long as the inter-layer potential $h_{\tau,\tau'}(\boldsymbol{p}+\boldsymbol{G}^\ell)$ is small enough. In practice it is possible to show [3] that when the twist angle θ is small enough, for a low-energy description of TBG only a very small number of reciprocal lattice vectors can be retained. We now recall that a basis of reciprocal lattice vectors for the monolayer graphene $\{\tilde{\boldsymbol{g}}_{1,\ell},\tilde{\boldsymbol{g}}_{2,\ell}\}$ in layer ℓ is defined via the usual relation $\tilde{\boldsymbol{a}}_{i,\ell}\cdot\tilde{\boldsymbol{g}}_{j,\ell}=2\pi\delta_{ij}$. The Authors of Ref. [3] showed that for small twist angles it is sufficient to truncate the sums over $\boldsymbol{G}^\ell$ and $\boldsymbol{G}^{\ell'}$ in Eq. (2.26) to the following three terms

- $\boldsymbol{G}^\ell=\boldsymbol{G}^{\ell'}=\boldsymbol{0}$,
- $\boldsymbol{G}^\ell=\tilde{\boldsymbol{g}}_{1,\ell}$ and $\boldsymbol{G}^{\ell'}=\tilde{\boldsymbol{g}}_{1,\ell'}$,
- $\boldsymbol{G}^\ell=-\tilde{\boldsymbol{g}}_{2,\ell}$ and $\boldsymbol{G}^{\ell'}=-\tilde{\boldsymbol{g}}_{2,\ell'}$.

This truncation defines the phase factors $e^{i(\boldsymbol{G}^\ell\,\cdot\,\boldsymbol{d}_{\tau,\ell}-\boldsymbol{G}^{\ell'}\,\cdot\,\boldsymbol{d}_{\tau',\ell'})}$ and values of $h_{\tau,\tau'}(\boldsymbol{p}+\boldsymbol{G}^\ell)$ used in the continuum approximation of TBG. To be quantitative, a last piece of information needed is the analytical form of the inter-layer tunneling potential $h_{\tau,\tau'}(\boldsymbol{p}+\boldsymbol{G}^\ell)$. This can be derived from Eq. (2.13), but it turns out that the details of the inter-layer hoppings are actually quite irrelevant. Since the continuum model is an approximation around $\boldsymbol{p}\approx\boldsymbol{k}^\ell_{\text{D}}$, with $\boldsymbol{k}^\ell_{\text{D}}$ as in Eq. (2.20), one can make the identification $h_{\tau,\tau'}(\boldsymbol{k}^\ell_{\text{D}}+\boldsymbol{G}^\ell)\approx h_{\tau,\tau'}(\boldsymbol{p}+\boldsymbol{G}^\ell)$, so that the continuum model is controlled by two effective parameters u_1 and u_0, defined as

$$u_0\equiv h_{\tau,\tau}(\boldsymbol{k}^\ell_{\text{D}}+\boldsymbol{G}^\ell)=h_{\tau,\tau}(\boldsymbol{k}^\ell_{\text{D}}), \tag{2.27a}$$

$$u_1\equiv h_{\tau,\tau'}(\boldsymbol{k}^\ell_{\text{D}}+\boldsymbol{G}^\ell)=h_{\tau,\tau'}(\boldsymbol{k}^\ell_{\text{D}})\quad \tau\neq\tau', \tag{2.27b}$$

where the second equality in both of the previous equations holds true because the vectors $\boldsymbol{G}^{\ell}$ retained in the summation satisfy that property. This implies that instead of the full analytical form of $h_{\tau,\tau'}(\boldsymbol{r})$ one just needs a tiny number of characteristic energy scales. These can be obtained both through tight-binding approximations such as Eq. (2.13) or the one in Ref. [104] of or density functional calculations [106]. Replacing the definitions in Eqs. (2.27) and (2.5) into the truncated sum yields directly

$$\begin{aligned}\hat{H}^{(\ell,\ell')}_{\text{inter}} \approx \sum_{\boldsymbol{k}} &\begin{pmatrix} u_0 & u_1 \\ u_1 & u_0 \end{pmatrix} \otimes |\boldsymbol{k},\ell\rangle\langle\boldsymbol{k},\ell'| + \\ &e^{-i\frac{2\pi}{3}} \begin{pmatrix} u_0 & u_1 e^{i\frac{2\pi}{3}} \\ u_1 e^{-i\frac{2\pi}{3}} & u_0 \end{pmatrix} \otimes |\boldsymbol{k}+\boldsymbol{G}_1,\ell\rangle\langle\boldsymbol{k},\ell'| + \\ &e^{i\frac{2\pi}{3}} \begin{pmatrix} u_0 & u_1 e^{-i\frac{2\pi}{3}} \\ u_1 e^{i\frac{2\pi}{3}} & u_0 \end{pmatrix} \otimes |\boldsymbol{k}+\boldsymbol{G}_2,\ell\rangle\langle\boldsymbol{k},\ell'|\end{aligned} \tag{2.28}$$

where the 2×2 matrices account for sub-lattice degreees of freedom, and u_1 and u_0 are the inter- and intra-sublattice hopping energies, respectively. Finally, we have introduced the vectors $\{\boldsymbol{G}_1,\boldsymbol{G}_2\}$, which are a basis for the primitive vectors of the moiré reciprocal lattice defined by the continuum model,

$$\boldsymbol{G}_{1,2} = \pm(\tilde{\boldsymbol{g}}_{1/2,2} - \tilde{\boldsymbol{g}}_{1/2,1}) = \frac{8\pi}{a\sqrt{3}} \sin\left(\frac{\theta}{2}\right) \left(\pm\frac{1}{2}, \frac{\sqrt{3}}{2}\right) \ . \tag{2.29}$$

Thanks to the intra-layer and inter-layer contributions in Eqs. (2.21) and (2.28), and exploiting the Bloch states Eq. (2.19) to switch to the real-space representation, we can write the continuum Hamiltonian of TBG as

$$\hat{H}_0 = \begin{pmatrix} \hat{H}^{(1)} & \hat{U} \\ \hat{U}^{\dagger} & \hat{H}^{(2)} \end{pmatrix} \ , \tag{2.30}$$

where we have defined

$$\hat{H}^{(\ell)} = v_{\text{F}} \left[R_{\ell}(\theta/2)(\hat{\boldsymbol{p}} - \hbar\boldsymbol{K}_{\ell})\right] \cdot (\sigma_x, \sigma_y) \ , \tag{2.31}$$

and

$$\begin{aligned}\hat{U} = &\begin{pmatrix} u_0 & u_1 \\ u_1 & u_0 \end{pmatrix} + e^{-i\frac{2\pi}{3} + i\boldsymbol{G}_1\cdot\hat{\boldsymbol{r}}} \begin{pmatrix} u_0 & u_1 e^{i\frac{2\pi}{3}} \\ u_1 e^{-i\frac{2\pi}{3}} & u_0 \end{pmatrix} + \\ &+ e^{i\frac{2\pi}{3} + i\boldsymbol{G}_2\cdot\hat{\boldsymbol{r}}} \begin{pmatrix} u_0 & u_1 e^{-i\frac{2\pi}{3}} \\ u_1 e^{i\frac{2\pi}{3}} & u_0 \end{pmatrix} \ .\end{aligned} \tag{2.32}$$

Here, $\hat{\boldsymbol{r}}$ and $\hat{\boldsymbol{p}}$ are the position and momentum operators, respectively.

It is interesting to compare the moiré lattice defined in the tight-binding model of TBG, which is summarised in Eqs. (2.8) and the one defined by the continuum model, whose periodicity can be extracted by Eq. (2.29).

Both the continuum and the tight-binding models of TBG describe electrons roaming in a triangular moiré superlattice, whose periodicity is

$$\lambda_{\mathrm{M}}^{\mathrm{tb}} = ar\sqrt{\frac{3}{\gcd(r,3)}\left[\left(\frac{m}{r}\right)^2 + \frac{m}{r} + \frac{1}{3}\right]}, \tag{2.33a}$$

for the tight-binding model, and

$$\lambda_{\mathrm{M}}^{\mathrm{c}} = \frac{a}{2\sin\left(\frac{\theta}{2}\right)} \tag{2.33b}$$

for the continuum model.

Scanning tunneling microscopy experiments [70, 71, 72, 73] on TBG find structures with periodicity consistent with the relation $\approx \lambda_{\mathrm{M}}^{\mathrm{c}} = \frac{a}{2\sin\left(\frac{\theta}{2}\right)}$.

Now, by using the trigonometric relation $\cos(\theta) = 1 - 2\sin^2(\theta/2)$, and the crystalline angle formula Eq. (2.7) we have

$$\sin\left(\frac{\theta}{2}\right) = \sqrt{\frac{1}{2}\left[1 - \frac{3m^2 + 3mr + r^2/2}{3m^2 + 3mr + r^2}\right]} = \frac{r}{2}\sqrt{\frac{1}{3m^2 + 3mr + r^2}}. \tag{2.34}$$

Thanks to the previous equation, it is easy to show that the ratio between the two moiré lattice parameters satisfy the following relation

$$\frac{\lambda_{\mathrm{M}}^{\mathrm{tb}}}{\lambda_{\mathrm{M}}^{\mathrm{c}}} = \frac{r}{\sqrt{\gcd(r,3)}}, \tag{2.35}$$

which is equal to 1 only if $r = 1$. The different periodicity between moiré patterns described in tight-binding and continuum models is explained by the fact that, at small twist angles, the general moiré lattices described by the tight-binding model are are almost periodic repetitions of the structures with $r = 1$ described by the continuum model and measured in scanning tunneling microscopy experiments [70, 71, 72, 73]. For a more in-depth discussion of these issues we refer to Ref. [64].

2.2 Electron-electron interactions and the Hartee approximation

In the preceding Sections, we presented one-particle models of TBG, i.e., models in which the Coulomb interaction between electrons is neglected. In many materials, the one-particle picture yields the correct qualitative description of the electronic properties and is modified only quantitatively if one includes the electron-electron interactions within perturbation theory. In Section 1.2, however, we have reviewed different experimental observations in TBG whose origin can be linked to the presence of strong electron-electron interactions in the case of twist angles close to the magic angle. For this reason, in the original work presented in Chapter 3, we have included the effects

of the electron-electron interactions in TBG making use of the Hartree approximation, which we now review.

Historically, the Hartree approximation provided the starting point for many-body theories of electronic systems. The basic idea behind the Hartree approach can be described as an attempt to approximate the ground-state wavefunction of the interacting system by that of an Hamiltonian where electrons move under the influence of an *effective* nonlocal potential. In reality each electron experiences the Coulomb potential created by all other electrons at a given point. This potential is in fact local but varies in time in an unpredictable manner. The Hartree approximation attempts to replace the time-dependent potential by a static one that gives a good description on the average. In this sense it is a *mean field* theory.

In the Hartree theory of N interacting electrons, the ground-state wavefunction of the many-body system $|\Psi\rangle$ is expressed as simple tensor product of orthonormalized one-electron orbitals $|\phi_i\rangle$

$$|\Psi\rangle = \otimes_{i=1}^{N} |\phi_i\rangle. \tag{2.36}$$

The many-body Hamiltonian of this system can be written as

$$\hat{H}_{ee} = \sum_{i=1}^{N} \hat{H}_i + \frac{1}{2} \sum_{i \neq j} \frac{e^2}{|\hat{\boldsymbol{r}}_i - \hat{\boldsymbol{r}}_j|}, \tag{2.37}$$

where $\hat{H}_i$ is the one-particle Hamiltonian of the i-th particle. For the sake of simplicity we assume that $\hat{H}_i = \hat{H}_0 \, \forall \; i = 1, \cdots, N$. The Hartree approximation consists in finding the orbitals $|\phi_i\rangle$ minimizing the expectation value $\langle\Psi|\hat{H}_{ee}|\Psi\rangle$. Now, suppose that $|\Psi\rangle_0 = \otimes_{i=1}^{N} |\phi_i\rangle_0$ is the minimizer, i.e. the product state for which the minimum $E_0 \equiv \; {}_0\langle\Psi|\hat{H}_{ee}|\Psi\rangle_0$ is reached. It is possible to show through standard variational techniques (see e.g. Ref. [17], Chapter 4) that the minimizer orbitals $|\phi_i\rangle_0$ are the solution of the following equation

$$\hat{H}_0 |\phi_i\rangle_0 + \left[\int d^D \boldsymbol{r} \frac{e^2}{|\hat{\boldsymbol{r}}_i - \boldsymbol{r}|} n(\boldsymbol{r}) \right] |\phi_i\rangle_0 = \epsilon_i |\phi_i\rangle_0, \tag{2.38}$$

where we have defined the particle density at position $\boldsymbol{r}$

$$n(\boldsymbol{r}) = \frac{1}{V} \sum_{j=1}^{N} \frac{1}{1 + \exp[(\epsilon_j - \mu)/k_{\mathrm{B}}T]} |\langle \boldsymbol{r}|\phi_j\rangle_0|^2, \tag{2.39}$$

with the assumption that the electron system is enclosed in a volume V and is in equlibrium at chemical potential μ and temperature T. Equation (2.38) appears as a simple eigenvalue equation depending on the particle density $n(\boldsymbol{r})$, Eq. (2.39). The particle density Eq. (2.39), on the other hand, depends on the solution of the Hartree relation Eq. (2.38). These two equations, i.e. the particle density in Eq. (2.39) and the Hartree relation in Eq. (2.38) are therefore coupled, and have to be solved simultaneously so that the solution is consistent. For this reason, the orbitals solving Eqs. (2.38) and (2.39) are known as "self-consistent" solutions of the Hartree approximation.

In a translationally invariant system described by the periodic Hamiltonian $\hat{H}_0$, we look for one-particle orbitals $|\boldsymbol{k}\nu\rangle$ of the Bloch form, so that the Hartree relation Eq. (2.38) to be solved is

$$\left(\hat{H}_0 + \hat{V}_{\rm H}\right)|\boldsymbol{k}\nu\rangle = \epsilon_{\boldsymbol{k}\nu}|\boldsymbol{k}\nu\rangle \ . \tag{2.40}$$

From Eq. (2.38) we have isolated the Hartree potential

$$V_{\rm H}(\boldsymbol{r}) \equiv \langle \boldsymbol{r}|\hat{V}_{\rm H}|\boldsymbol{r}\rangle = \int d^2\boldsymbol{r}' \frac{e^2}{|\boldsymbol{r}-\boldsymbol{r}'|} n(\boldsymbol{r}') \ . \tag{2.41}$$

The Fourier expansion of the Coulomb interaction reads as following

$$\frac{e^2}{|\boldsymbol{r}-\boldsymbol{r}'|} = \frac{1}{V}\sum_{\boldsymbol{q}} v_{\boldsymbol{q}} e^{i\boldsymbol{q}\cdot(\boldsymbol{r}-\boldsymbol{r}')} \ , \tag{2.42}$$

where, again, V is the volume of the electron system and

$$v_{\boldsymbol{q}} = \frac{2\pi e^2}{|\boldsymbol{q}|} \ . \tag{2.43}$$

Orbitals in the Bloch form depend on the crystal momentum $\boldsymbol{k}$ and band index ν, and can be expanded in a plane-waves basis as

$$\psi_\nu(\boldsymbol{r},\boldsymbol{k}) = \langle \boldsymbol{r}|\boldsymbol{k}\nu\rangle = \frac{1}{\sqrt{V}}\sum_{\boldsymbol{G}} u_{\boldsymbol{G}}(\boldsymbol{k},\nu) e^{i(\boldsymbol{k}+\boldsymbol{G})\cdot\boldsymbol{r}} \ , \tag{2.44}$$

$\boldsymbol{G}$ being a reciprocal lattice vector and $u_{\boldsymbol{G}}(\boldsymbol{k},\nu)$ being complex Fourier coefficients. The particle density $n(\boldsymbol{r})$ at position $\boldsymbol{r}$ is just the sum over the occupied states, namely

$$\begin{aligned} n(\boldsymbol{r}) &= \sum_{\boldsymbol{k}\nu} \frac{1}{1+\exp[(\epsilon_{\boldsymbol{k}\nu}-\mu)/k_{\rm B}T]} \psi^\dagger_\nu(\boldsymbol{r},\boldsymbol{k})\psi_\nu(\boldsymbol{r},\boldsymbol{k}) \\ &= \frac{1}{V}\sum_{\boldsymbol{k}\nu} \frac{1}{1+\exp[(\epsilon_{\boldsymbol{k}\nu}-\mu)/k_{\rm B}T]} \sum_{\boldsymbol{G},\boldsymbol{G}'} u^\dagger_{\boldsymbol{G}}(\boldsymbol{k},\nu) u_{\boldsymbol{G}'}(\boldsymbol{k},\nu) e^{i(\boldsymbol{G}'-\boldsymbol{G})\cdot\boldsymbol{r}} \\ &= \frac{1}{V}\sum_{\boldsymbol{k}\nu} \frac{1}{1+\exp[(\epsilon_{\boldsymbol{k}\nu}-\mu)/k_{\rm B}T]} \sum_{\boldsymbol{G},\boldsymbol{\mathcal{G}}} u^\dagger_{\boldsymbol{G}}(\boldsymbol{k},\nu) u_{\boldsymbol{G}+\boldsymbol{\mathcal{G}}}(\boldsymbol{k},\nu) e^{i\boldsymbol{\mathcal{G}}\cdot\boldsymbol{r}} \\ &\equiv \sum_{\boldsymbol{\mathcal{G}}} n_{\boldsymbol{\mathcal{G}}} e^{i\boldsymbol{\mathcal{G}}\cdot\boldsymbol{r}}, \end{aligned} \tag{2.45}$$

where we have introduced the quantity

$$n_{\boldsymbol{\mathcal{G}}} = \frac{1}{V}\sum_{\nu}\sum_{\boldsymbol{k}} \frac{1}{1+\exp[(\epsilon_{\boldsymbol{k}\nu}-\mu)/k_{\rm B}T]} \sum_{\boldsymbol{G}} u^\dagger_{\boldsymbol{G}}(\boldsymbol{k},\nu) u_{\boldsymbol{G}+\boldsymbol{\mathcal{G}}}(\boldsymbol{k},\nu) \ , \tag{2.46}$$

i.e. the Fourier component of the electron density at wave vector $\boldsymbol{\mathcal{G}}$. Now, substituting Eqs. (2.42), (2.43) and (2.45) into Eq. (2.41), and carrying out simple algebraic

manipulations, we find

$$\begin{aligned} V_{\mathrm{H}}(\boldsymbol{r}) &= \int d^2\boldsymbol{r}' \frac{e^2}{|\boldsymbol{r}-\boldsymbol{r}'|} n(\boldsymbol{r}') \\ &= \frac{1}{V}\sum_{\boldsymbol{q}} \int d\boldsymbol{r}' v_{\boldsymbol{q}} e^{i\boldsymbol{q}\cdot(\boldsymbol{r}-\boldsymbol{r}')} n(\boldsymbol{r}') \\ &= \frac{1}{V}\sum_{\boldsymbol{q}}\sum_{\boldsymbol{\mathcal{G}}} \int d\boldsymbol{r}' v_{\boldsymbol{q}} e^{i\boldsymbol{q}\cdot(\boldsymbol{r}-\boldsymbol{r}')} n_{\boldsymbol{\mathcal{G}}} e^{i\boldsymbol{\mathcal{G}}\cdot\boldsymbol{r}'} \\ &= \sum_{\boldsymbol{q}} e^{i\boldsymbol{q}\cdot\boldsymbol{r}} \sum_{\boldsymbol{\mathcal{G}}} v_{\boldsymbol{q}} n_{\boldsymbol{\mathcal{G}}} \delta_{\boldsymbol{q},\boldsymbol{\mathcal{G}}} \\ &= \sum_{\boldsymbol{\mathcal{G}}} v_{\boldsymbol{\mathcal{G}}} n_{\boldsymbol{\mathcal{G}}} e^{i\boldsymbol{\mathcal{G}}\cdot\boldsymbol{r}} \\ &= \sum_{\boldsymbol{\mathcal{G}}} \frac{2\pi e^2}{|\boldsymbol{\mathcal{G}}|} n_{\boldsymbol{\mathcal{G}}} e^{i\boldsymbol{\mathcal{G}}\cdot\boldsymbol{r}} \ , \end{aligned} \tag{2.47}$$

where we have used the equality

$$\frac{1}{V}\int d^2\boldsymbol{r} e^{-i\boldsymbol{q}\cdot\boldsymbol{r}} = \delta_{\boldsymbol{q},\boldsymbol{0}} \ . \tag{2.48}$$

To ensure overall charge neutrality due to the positively charged background [30], one has to exclude the term with $\boldsymbol{\mathcal{G}} = \boldsymbol{0}$ from the sum in the last term of Eq. (2.47). The last line of Eq. (2.47) shows that the Hartree potential in a translationally invariant system can be written as a sum over the reciprocal lattice vectors $\boldsymbol{\mathcal{G}}$ of the Fourier components of the particle density of wave vector $\boldsymbol{\mathcal{G}}$. Tipically, because the denominator in the last line of Eq. (2.47) grows with $|\boldsymbol{\mathcal{G}}|$, one can limit the sum over $\boldsymbol{G}$ to a small number of reciprocal lattice vectors $\boldsymbol{\mathcal{G}}$.

From a numerical point of view, in order to find the self-consistent solution to the Hartree approximation we have mainly worked with the variables $n_{\boldsymbol{\mathcal{G}}}$ for each of the reciprocal lattice vectors $\boldsymbol{\mathcal{G}}$ considered. Thanks to an iterative method, described in full detail in Section 2.4.2, we have updated the Fourier components of the particle density $n_{\boldsymbol{\mathcal{G}}}$ until the self-consistency was reached.

2.3 Linear Response Theory

In this section we are going to introduce the theoretical tools used in this Thesis to study optical and plasmonic properties of TBG. We are going to derive the theory for periodic systems, making extensive use of the fact that the single particle eigenstates of a periodic system are Bloch states, i.e. they can be labeled by two indexes $\boldsymbol{k}$ and ν, which are known as crystal momentum and band index, respectively. The crystal momentum $\boldsymbol{k}$ is a vector belonging the Brillouin zone of the system, whereas ν is a discrete index labelling the different electronic bands. A Bloch state $|\boldsymbol{k}\nu\rangle$ satisfy the relation

$$\langle \boldsymbol{r}|\boldsymbol{k}\nu\rangle = \frac{1}{V}\sum_{\boldsymbol{G}} u_{\boldsymbol{G}}(\boldsymbol{k},\nu) e^{i(\boldsymbol{k}+\boldsymbol{G})\cdot\boldsymbol{r}}, \tag{2.49}$$

where V is the electron system volume and the sum over $\boldsymbol{G}$ is a sum over the integer linear combinations of the reciprocal vectors' basis. The Bloch wavefunction can be therefore expanded as a sum of plane waves with wave vector $\boldsymbol{k}+\boldsymbol{G}$, where $\boldsymbol{k}$ belongs to the Brillouin Zone of the system and $\boldsymbol{G}$ is a reciprocal lattice vector. From now on, we assume that the electron system is inside a volume V in D spatial dimensions, and $d^D\boldsymbol{r}$ denote the integration measure in this D-dimensional space. Finally, in order to to simplify the notation, we define the Fermi-Dirac function calculated at the energy ϵ_m as

$$f_m \equiv \frac{1}{1+\exp[(\epsilon_m-\mu)/(k_{\mathrm{B}}T)]}, \tag{2.50}$$

where m is an arbitrary index.

2.3.1 Density-density response function in a periodic system

The density-density response function $\chi_{nn}(\boldsymbol{r},\boldsymbol{r}',t)$ describes how the expectation value of the particle density operator

$$\hat{n}(\boldsymbol{r}) = \sum_i \delta(\boldsymbol{r}-\hat{\boldsymbol{r}}_i), \tag{2.51}$$

at point $\boldsymbol{r}$ is affected by an external scalar potential $V_{\mathrm{ext}}(\boldsymbol{r}',t)$ that couples linearly to the density $\hat{n}(\boldsymbol{r}')$ at the point $\boldsymbol{r}'$. The density-density response function appears whenever one whishes to describe how the free carriers in a material are displaced by the presence of an electromagnetic field. See e.g. the case of collective excitations in Section 2.3.3, or the description of the dielectric behaviour of a material in Ref. [30], Chapter 5.

The Hamiltonian perturbed by the scalar potential $V_{\mathrm{ext}}(\boldsymbol{r}',t)$ is

$$\hat{H}_V(t) = \hat{H}_0 + \int V_{\mathrm{ext}}(\boldsymbol{r}',t)\hat{n}(\boldsymbol{r}')d^D\boldsymbol{r}', \tag{2.52}$$

where $\hat{H}_0$ is the unperturbed Hamiltonian. The density-density response function is defined as [30]

$$\chi_{nn}(\boldsymbol{r},\boldsymbol{r}',t) \equiv -\frac{i}{\hbar}\Theta(t)\langle[\hat{n}(\boldsymbol{r},t);\hat{n}(\boldsymbol{r}')]\rangle, \tag{2.53}$$

where $\Theta(t)$ is the Heaviside step function and $[\hat{X};\hat{Y}]=\hat{X}\hat{Y}-\hat{Y}\hat{X}$ is the commutator between the operators $\hat{X}$ and $\hat{Y}$. Denoting with $\langle\hat{X}\rangle$ the thermodynamical expectation value of the operator $\hat{X}$, it is possible to show [30] that the density-density response function is related to the time-dependent particle density induced by the perturbation

$$n_{\mathrm{ind}}(\boldsymbol{r},t) \equiv \langle\hat{n}(\boldsymbol{r})\rangle_V(t) - \langle\hat{n}(\boldsymbol{r})\rangle_0. \tag{2.54}$$

In particular, it holds that

$$n_{\mathrm{ind}}(\boldsymbol{r},t) = \int_0^\infty d\tau \int d^D\boldsymbol{r}'\chi_{nn}(\boldsymbol{r},\boldsymbol{r}',\tau)V_{\mathrm{ext}}(\boldsymbol{r}',t-\tau). \tag{2.55}$$

If electron-electron interactions are present in the system, the induced charge density creates an additional Coulomb field $V_{\text{ind}}(\boldsymbol{r}, t)$ which is superimposed to the external field. The total resulting potential seen by a test charge is referred to as the *screened scalar potential* and is given by

$$V_{\text{tot}}(\boldsymbol{r}, t) = V_{\text{ext}}(\boldsymbol{r}, t) + V_{\text{ind}}(\boldsymbol{r}, t), \tag{2.56}$$

where

$$V_{\text{ind}}(\boldsymbol{r}, t) = \int d\boldsymbol{r}' \frac{e^2 n_{\text{ind}}(\boldsymbol{r}', t)}{|\boldsymbol{r} - \boldsymbol{r}'|}. \tag{2.57}$$

Since the screened effective potential $V_{\text{tot}}(\boldsymbol{r}, t)$ experienced by a test charge is often quite different from the bare external potential, it makes sense to define a *proper* density–density response function, denoted by $\tilde{\chi}_{nn}(\boldsymbol{r}, \boldsymbol{r}', t)$, which gives the induced density $n_{\text{ind}}(\boldsymbol{r}, t)$ in terms of the total screened potential $V_{\text{tot}}(\boldsymbol{r}, t)$

$$n_{\text{ind}}(\boldsymbol{r}, t) = \int_0^\infty d\tau \int d^D\boldsymbol{r}' \tilde{\chi}_{nn}(\boldsymbol{r}, \boldsymbol{r}', \tau) V_{\text{tot}}(\boldsymbol{r}', t - \tau). \tag{2.58}$$

The density-density response can also be analysed in reciprocal space, by calculating its Fourier transform

$$\chi_{nn}(\boldsymbol{q}, \boldsymbol{q}', \omega) = \frac{1}{V} \int d^D\boldsymbol{r}\ e^{-i\boldsymbol{q}\cdot\boldsymbol{r}} \int d^D\boldsymbol{r}'\ e^{i\boldsymbol{q}'\cdot\boldsymbol{r}'} \int_0^\infty dt e^{i\omega t} \chi_{nn}(\boldsymbol{r}, \boldsymbol{r}', t). \tag{2.59}$$

From Eq. (2.55), it follows that the Fourier components of the induced particle density can be expressed as

$$n_{\text{ind}}(\boldsymbol{q}, \omega) = \sum_{\boldsymbol{q}'} \chi_{nn}(\boldsymbol{q}, \boldsymbol{q}', \omega) V_{\text{ext}}(\boldsymbol{q}', \omega), \tag{2.60}$$

where $V_{\text{ext}}(\boldsymbol{q}', \omega)$ is the Fourier transform of the external potential. With the help of Eq. (2.58), the induced particle density can be expressed in terms of the Fourier components of the *proper* density-density response function as

$$n_{\text{ind}}(\boldsymbol{q}, \omega) = \sum_{\boldsymbol{q}'} \tilde{\chi}_{nn}(\boldsymbol{q}, \boldsymbol{q}', \omega) V_{\text{tot}}(\boldsymbol{q}', \omega). \tag{2.61}$$

Density-density response of single particle systems

We now focus our attention to the case where electron-electron interactions are absent (or ignored). In this case the density-density response function is known as *Lindhard function*, and can be conveniently calculated starting from the Fourier transform in Eq. (2.59). In the following we also assume that the system is periodic.

Because of the periodicity of the lattice, the wave vectors $\boldsymbol{q}$ and $\boldsymbol{q}'$ can differ at most by a reciprocal lattice vector, and we can define

$$\chi_{nn}(\boldsymbol{q}, \boldsymbol{G}, \boldsymbol{G}', \omega) \equiv \chi_{nn}(\boldsymbol{q} + \boldsymbol{G}, \boldsymbol{q} + \boldsymbol{G}', \omega), \tag{2.62}$$

with $\boldsymbol{q} \in$ the Brillouin Zone, and $\boldsymbol{G},\ \boldsymbol{G}'$ reciprocal lattice vectors. By explicitating the thermodynamical expectation value in Eq. (2.53) as a sum over the Bloch eigenstates of a *periodic single particle Hamiltonian*, it is possible [30] to express Eq. (2.62) in the following form,

$$
\begin{aligned}
&\chi_{nn}(\boldsymbol{q},\boldsymbol{G},\boldsymbol{G}',\omega) = \\
&\quad = \frac{g}{V}\sum_{\nu,\nu'}\sum_{\boldsymbol{k},\boldsymbol{k}'}\frac{f_{\boldsymbol{k}\nu}-f_{\boldsymbol{k}'\nu'}}{\hbar\omega+\epsilon_{\boldsymbol{k}\nu}-\epsilon_{\boldsymbol{k}'\nu'}+i\eta} \\
&\qquad\qquad \times\left[\langle\boldsymbol{k}\nu|e^{-i(\boldsymbol{q}+\boldsymbol{G})\cdot\hat{\boldsymbol{r}}}|\boldsymbol{k}'\nu'\rangle\langle\boldsymbol{k}'\nu'|e^{i(\boldsymbol{q}+\boldsymbol{G}')\cdot\hat{\boldsymbol{r}}}|\boldsymbol{k}\nu\rangle\right] \\
&\quad = \frac{g}{V}\sum_{\nu,\nu'}\sum_{\boldsymbol{k}}\frac{f_{\boldsymbol{k}\nu}-f_{\boldsymbol{k}+\boldsymbol{q}-\boldsymbol{Q},\nu'}}{\hbar\omega+\epsilon_{\boldsymbol{k}\nu}-\epsilon_{\boldsymbol{k}+\boldsymbol{q}-\boldsymbol{Q},\nu'}+i\eta} \\
&\qquad\qquad \times\left[\langle\boldsymbol{k}\nu|e^{-i(\boldsymbol{q}+\boldsymbol{G})\cdot\hat{\boldsymbol{r}}}|\boldsymbol{k}+\boldsymbol{q}-\boldsymbol{Q},\nu'\rangle\langle\boldsymbol{k}+\boldsymbol{q}-\boldsymbol{Q},\nu'|e^{i(\boldsymbol{q}+\boldsymbol{G}')\cdot\hat{\boldsymbol{r}}}|\boldsymbol{k}\nu\rangle\right] \\
&\quad = \frac{g}{V}\sum_{\nu,\nu'}\sum_{\boldsymbol{k}}\frac{f_{\boldsymbol{k}\nu}-f_{\boldsymbol{k}+\boldsymbol{q}-\boldsymbol{Q},\nu'}}{\hbar\omega+\epsilon_{\boldsymbol{k}\nu}-\epsilon_{\boldsymbol{k}+\boldsymbol{q}-\boldsymbol{Q},\nu'}+i\eta} \\
&\qquad\qquad \times\left[\sum_{\boldsymbol{\Gamma}}u^{\dagger}_{\boldsymbol{\Gamma}}(\boldsymbol{k},\nu)u_{\boldsymbol{G}+\boldsymbol{\Gamma}+\boldsymbol{Q}}(\boldsymbol{k}+\boldsymbol{q}-\boldsymbol{Q},\nu')\sum_{\boldsymbol{\Gamma}}u^{\dagger}_{\boldsymbol{G}'+\boldsymbol{\Gamma}+\boldsymbol{Q}}(\boldsymbol{k}+\boldsymbol{q}-\boldsymbol{Q},\nu')u_{\boldsymbol{\Gamma}}(\boldsymbol{k},\nu)\right] \\
&\quad = \frac{g}{V}\sum_{\nu,\nu'}\sum_{\boldsymbol{k}}\frac{f_{\boldsymbol{k}\nu}-f_{\boldsymbol{k}+\boldsymbol{q}-\boldsymbol{Q},\nu'}}{\hbar\omega+\epsilon_{\boldsymbol{k}\nu}-\epsilon_{\boldsymbol{k}+\boldsymbol{q}-\boldsymbol{Q},\nu'}+i\eta} \\
&\qquad\qquad \times\left[\mathcal{M}(\boldsymbol{k},\boldsymbol{q},\boldsymbol{G},\nu,\nu')\mathcal{M}^{\star}(\boldsymbol{k},\boldsymbol{q},\boldsymbol{G}',\nu,\nu')\right] \\
&\quad = \frac{g}{V}\sum_{\nu,\nu'}\sum_{\boldsymbol{k}}\frac{f_{\boldsymbol{k}\nu}-f_{\boldsymbol{\kappa},\nu'}}{\hbar\omega+\epsilon_{\boldsymbol{k}\nu}-\epsilon_{\boldsymbol{\kappa},\nu'}+i\eta} \\
&\qquad\qquad \times\left[\mathcal{M}(\boldsymbol{k},\boldsymbol{q},\boldsymbol{G},\nu,\nu')\mathcal{M}^{\star}(\boldsymbol{k},\boldsymbol{q},\boldsymbol{G}',\nu,\nu')\right],
\end{aligned}
\tag{2.63}
$$

where η is a small positive infinitesimal (with dimensions of energy), g is the degeneracy factor, and the reciprocal lattice vector $\boldsymbol{Q}$, together with the vector $\boldsymbol{\kappa}$, satisfy the relation

$$\boldsymbol{\kappa} = \boldsymbol{k}+\boldsymbol{q}-\boldsymbol{Q} \tag{2.64}$$

with $\boldsymbol{\kappa}$ lying in the first Brillouin Zone. The relation $\boldsymbol{\kappa} = \boldsymbol{k}+\boldsymbol{q}-\boldsymbol{Q}$ implements the *folding* procedure needed when the vector $\boldsymbol{k}+\boldsymbol{q}$ lies outside the first Brillouin Zone. In last two equalities in Eq. (2.63), we have also defined

$$\mathcal{M}(\boldsymbol{k},\boldsymbol{q},\boldsymbol{G},\nu,\nu') \equiv \sum_{\boldsymbol{\Gamma}}u^{\dagger}_{\boldsymbol{\Gamma}}(\boldsymbol{k},\nu)u_{\boldsymbol{G}+\boldsymbol{\Gamma}+\boldsymbol{Q}}(\boldsymbol{k}+\boldsymbol{q}-\boldsymbol{Q},\nu'), \tag{2.65}$$

along with its complex conjugate. Notice also that we have used explicitly that the eigenstates of a periodic system are Bloch states $|\boldsymbol{k}\nu\rangle$ of the form given in Eq. (2.49).

The matrix elements in Eq. (2.63) are obtained by making use of the real-space representation of the Bloch states (2.49) and are given by

$$\begin{aligned}\langle \boldsymbol{k}\nu|e^{-i(\boldsymbol{q}+\boldsymbol{G})\cdot\hat{\boldsymbol{r}}}|\boldsymbol{k}'\nu'\rangle &= \frac{1}{V}\sum_{\boldsymbol{\Gamma},\boldsymbol{\Gamma}'} u^{\dagger}_{\boldsymbol{\Gamma}}(\boldsymbol{k},\nu)u_{\boldsymbol{\Gamma}'}(\boldsymbol{k}',\nu')\int d\boldsymbol{r}e^{-i(\boldsymbol{q}+\boldsymbol{G}+\boldsymbol{\Gamma}+\boldsymbol{k}-\boldsymbol{\Gamma}'-\boldsymbol{k}')\cdot\boldsymbol{r}} \\ &= \sum_{\boldsymbol{\Gamma},\boldsymbol{\Gamma}'} u^{\dagger}_{\boldsymbol{\Gamma}}(\boldsymbol{k},\nu)u_{\boldsymbol{\Gamma}'}(\boldsymbol{k}',\nu')\delta_{\boldsymbol{G}+\boldsymbol{\Gamma}+\boldsymbol{Q},\boldsymbol{\Gamma}'}\delta_{\boldsymbol{\kappa},\boldsymbol{k}'} \qquad (\boldsymbol{q}+\boldsymbol{k}\equiv\boldsymbol{\kappa}+\boldsymbol{Q}) \\ &= \sum_{\boldsymbol{\Gamma}} u^{\dagger}_{\boldsymbol{\Gamma}}(\boldsymbol{k},\nu)u_{\boldsymbol{G}+\boldsymbol{\Gamma}+\boldsymbol{Q}}(\boldsymbol{k}',\nu')\delta_{\boldsymbol{\kappa},\boldsymbol{k}'} \\ &= \delta_{\boldsymbol{\kappa},\boldsymbol{k}'}\mathcal{M}(\boldsymbol{k},\boldsymbol{q},\boldsymbol{G},\nu,\nu')\end{aligned} \tag{2.66a}$$

$$\begin{aligned}\langle \boldsymbol{k}'\nu'|e^{i(\boldsymbol{q}+\boldsymbol{G})\cdot\hat{\boldsymbol{r}}}|\boldsymbol{k}\nu\rangle &= \frac{1}{V}\sum_{\boldsymbol{\Gamma},\boldsymbol{\Gamma}'} u^{\dagger}_{\boldsymbol{\Gamma}'}(\boldsymbol{k}',\nu')u_{\boldsymbol{\Gamma}}(\boldsymbol{k},\nu)\int d\boldsymbol{r}e^{i(\boldsymbol{q}+\boldsymbol{G}+\boldsymbol{\Gamma}+\boldsymbol{k}-\boldsymbol{\Gamma}'-\boldsymbol{k}')\cdot\boldsymbol{r}} \\ &= \sum_{\boldsymbol{\Gamma},\boldsymbol{\Gamma}'} u^{\dagger}_{\boldsymbol{\Gamma}'}(\boldsymbol{k}',\nu')u_{\boldsymbol{\Gamma}}(\boldsymbol{k},\nu)\delta_{\boldsymbol{G}+\boldsymbol{\Gamma}+\boldsymbol{Q},\boldsymbol{\Gamma}'}\delta_{\boldsymbol{\kappa},\boldsymbol{k}'} \qquad (\boldsymbol{q}+\boldsymbol{k}\equiv\boldsymbol{\kappa}+\boldsymbol{Q}) \\ &= \sum_{\boldsymbol{\Gamma}} u^{\dagger}_{\boldsymbol{G}+\boldsymbol{\Gamma}+\boldsymbol{Q}}(\boldsymbol{k}',\nu')u_{\boldsymbol{\Gamma}}(\boldsymbol{k},\nu)\delta_{\boldsymbol{\kappa},\boldsymbol{k}'} \\ &= \delta_{\boldsymbol{\kappa},\boldsymbol{k}'}\mathcal{M}^{\star}(\boldsymbol{k},\boldsymbol{q},\boldsymbol{G}',\nu,\nu')\end{aligned} \tag{2.66b}$$

In the latter expressions we have used the "folding" relation, Eq. (2.64). The numerical calculations of the density-density response function of TBG presented in this Thesis are based upon Eq. (2.63), which is the *Lindhard* response function. We see that the last line of Eq. (2.63) is an expression where we require only the eigenvalue decomposition of the system's Hamiltonian expressed in the basis of plane waves, i.e. the set of functions $\{\boldsymbol{r}\mapsto e^{i\boldsymbol{G}\cdot\boldsymbol{r}}|\boldsymbol{G}$ is a reciprocal lattice vector$\}$.

Electron-electron interactions and the random phase approximation

The expression derived in Eq. (2.63) for the density-density response function is appropriate for a *non-interacting* crystal. Electron-electron interactions can be brought into the theory through different approaches [30, 120]. One of the most relevant among these is the Random Phase Approximation (RPA) [30]. In the RPA, the density-density response function of a periodic system *in presence of electron-electron interactions* is brutally approximated assuming that the response to the sum of the external potential $V_{\text{ext}}(\boldsymbol{q},\omega)$ and induced electrostatic potential $V_{\text{ind}}(\boldsymbol{q},\omega)$ is the (formally non-interacting) Hartree response function $\chi^{\text{H}}_{nn}(\boldsymbol{q},\boldsymbol{G},\boldsymbol{G}',\omega)$, i.e. Lindhard function Eq. (2.63) calculated in the appropriate basis of self-consistent Hartree orbitals (see Section 2.2). In the RPA, therefore, the the proper density-density response function of the interacting system is obtained by calculating the Hartree response function, and then using the relation

$$\tilde{\chi}^{\text{RPA}}_{nn}(\boldsymbol{q},\boldsymbol{G},\boldsymbol{G}',\omega)\equiv\chi^{\text{H}}_{nn}(\boldsymbol{q},\boldsymbol{G},\boldsymbol{G}',\omega). \tag{2.67}$$

2.3.2 Linear response theory of the conductivity in a periodic system

The electrical conductivity $\sigma_{\alpha\beta}(\boldsymbol{r}, \boldsymbol{r}', \omega)$ of an electron system is defined as the linear response function connecting the *electrical* current at position $\boldsymbol{r}$ to the *total* applied electric field at position $\boldsymbol{r}'$, i.e.

$$J^{\mathrm{el}}_{\alpha}(\boldsymbol{r}, \omega) = \int d^D \boldsymbol{r}' \sigma_{\alpha\beta}(\boldsymbol{r}, \boldsymbol{r}', \omega) E^{\mathrm{tot}}_{\beta}(\boldsymbol{r}', \omega) \ , \tag{2.68}$$

where $J^{\mathrm{el}}_{\alpha}(\boldsymbol{r}, \omega)$ is the α-th Cartersian component of the electrical current at position $\boldsymbol{r}$ and frequency ω, $E^{\mathrm{tot}}_{\beta}(\boldsymbol{r}', \omega)$ is the β-th Cartesian component of the *total* applied electric field at position $\boldsymbol{r}'$ and frequency ω. In this Section, Greek letters will denote Cartesian indices and the Einstein summation convention over repeated Greek indices is understood.

The condutivity of a material describes its response to electromagnetic fields and, as showed in the introductory Section 1.2.2, the measures carried out in the s-SNOM experiments can be directly linked to the conductivity of the 2D material. In this Section we review and derive the mathematical expressions of the conductivity used in the original works presented in Chapter 3.

By Fourier transforming both members of Eq. (2.68) we obtain

$$J^{\mathrm{el}}_{\boldsymbol{q}\alpha}(\omega) = \sum_{\boldsymbol{q}'} \sigma_{\alpha\beta}(\boldsymbol{q}, \boldsymbol{q}', \omega) E^{\mathrm{tot}}_{\boldsymbol{q}'\beta}(\omega) \ , \tag{2.69}$$

where we defined

$$J^{\mathrm{el}}_{\boldsymbol{q}\alpha}(\omega) = \int d^D \boldsymbol{r} \ e^{-i\boldsymbol{q}\cdot\boldsymbol{r}} J^{\mathrm{el}}_{\alpha}(\boldsymbol{r}, \omega) \ , \tag{2.70}$$

$$E^{\mathrm{tot}}_{\boldsymbol{q}\beta}(\omega) = \int d^D \boldsymbol{r} \ e^{-i\boldsymbol{q}\cdot\boldsymbol{r}} E^{\mathrm{tot}}_{\beta}(\boldsymbol{r}, \omega) \ , \tag{2.71}$$

$$\sigma_{\alpha\beta}(\boldsymbol{q}, \boldsymbol{q}', \omega) = \frac{1}{V} \int d^D \boldsymbol{r} \ e^{-i\boldsymbol{q}\cdot\boldsymbol{r}} \int d^D \boldsymbol{r}' \ e^{i\boldsymbol{q}'\cdot\boldsymbol{r}'} \sigma_{\alpha\beta}(\boldsymbol{r}, \boldsymbol{r}', \omega) \ , \tag{2.72}$$

and V is the electron system volume in D spatial dimensions.

We now consider a system of non-interacting electrons of mass m and charge $-e < 0$, whose dynamics is controlled by the Hamiltonian (in first quantization)

$$\hat{H}(t) = \sum_i \left[\frac{1}{2m} \left(\hat{\boldsymbol{p}}_i + \frac{e}{c} \boldsymbol{A}_1(\hat{\boldsymbol{r}}_i, t) \right)^2 - e\phi_0(\hat{\boldsymbol{r}}_i) \right] \ , \tag{2.73}$$

where $\hat{\boldsymbol{r}}_i$, and $\hat{\boldsymbol{p}}_i$ are the position and momentum operators of the i-th electron, respectively, $\phi_0(\boldsymbol{r})$ is an external, static, scalar electric potential, and $\boldsymbol{A}_1(\boldsymbol{r}, t)$ is a time-dependent vector potential perturbation. We note that any time-dependent scalar perturbation can be written as a vector potential using a gauge transformation [30].

In the spirit of linear response theory [30], we can expand the Hamiltonian with respect to the perturbation as

$$\hat{H}(t) = \hat{H}_0 + \hat{H}_1(t) + \mathcal{O}(A_1^2) \ , \tag{2.74}$$

where

$$\hat{H}_0 = \sum_i \left[\frac{1}{2m} \hat{\boldsymbol{p}}_i^2 - e\phi_0(\hat{\boldsymbol{r}}_i) \right] , \tag{2.75}$$

is the unperturbed Hamiltonian, and

$$\begin{aligned} \hat{H}_1(t) &= \sum_i \frac{e}{2mc} \{\hat{p}_{i,\alpha}; A_{1\alpha}(\hat{\boldsymbol{r}}_i, t)\} \\ &= \int d^D\boldsymbol{r}\ A_{1\alpha}(\boldsymbol{r}, t) \sum_i \frac{e}{2mc} \{\hat{p}_{i,\alpha}; \delta(\hat{\boldsymbol{r}}_i - \boldsymbol{r})\} \\ &= \int d^D\boldsymbol{r}\ \frac{e}{c} A_{1\alpha}(\boldsymbol{r}, t) \hat{J}^{\rm p}_\alpha(\boldsymbol{r}) \end{aligned} \tag{2.76}$$

is the perturbation Hamiltonian. Here, $\{\hat{X}; \hat{Y}\} = \hat{X}\hat{Y} + \hat{Y}\hat{X}$ is the anticommutator between the operators $\hat{X}$ and $\hat{Y}$, and $\hat{J}^{\rm p}_\alpha(\boldsymbol{r})$ is the *paramagnetic* current density operator

$$\hat{J}^{\rm p}_\alpha(\boldsymbol{r}) = \sum_i \left[\frac{1}{2m} \{\hat{p}_{i,\alpha}; \delta(\hat{\boldsymbol{r}}_i - \boldsymbol{r})\} \right] . \tag{2.77}$$

The physical *particle* current density operator at a position $\boldsymbol{r}$ is instead given by

$$\hat{J}_\alpha(\boldsymbol{r}) = \sum_i \left[\frac{1}{2m} \left\{ \hat{p}_{i,\alpha} + \frac{e}{c} A_{1,\alpha}(\boldsymbol{r}, t); \delta(\hat{\boldsymbol{r}}_i - \boldsymbol{r}) \right\} \right] = \hat{J}^{\rm p}_\alpha(\boldsymbol{r}) + \frac{e}{mc} A_{1,\alpha}(\boldsymbol{r}, t) \hat{n}(\boldsymbol{r}) , \tag{2.78}$$

where the particle density operator is given by

$$\hat{n}(\boldsymbol{r}) = \sum_i \delta(\hat{\boldsymbol{r}}_i - \boldsymbol{r}) . \tag{2.79}$$

The expectation value of the current operator is therefore

$$\begin{aligned} &J_\alpha(\boldsymbol{r}, t) \equiv \mathrm{Tr}[\hat{\rho}(t) \hat{J}_\alpha(\boldsymbol{r})] \\ &= \mathrm{Tr}[\hat{\rho}_0 \hat{J}^{\rm p}_\alpha(\boldsymbol{r})] + \int_0^\infty d\tau \int d^D\boldsymbol{r}' \frac{e}{c} A_{1\beta}(\boldsymbol{r}', t-\tau) \chi_{\hat{J}^{\rm p}_\alpha(\boldsymbol{r}), \hat{J}^{\rm p}_\beta(\boldsymbol{r}')}(\tau) + \frac{e}{mc} A_{1,\alpha}(\boldsymbol{r}, t)\, \mathrm{Tr}[\hat{\rho}_0 \hat{n}(\boldsymbol{r})] \\ &= \int_0^\infty d\tau \int d^D\boldsymbol{r}' \frac{e}{c} A_{1\beta}(\boldsymbol{r}', t-\tau) \chi_{\hat{J}^{\rm p}_\alpha(\boldsymbol{r}), \hat{J}^{\rm p}_\beta(\boldsymbol{r}')}(\tau) + \frac{e}{mc} A_{1,\alpha}(\boldsymbol{r}, t) n(\boldsymbol{r}). \end{aligned} \tag{2.80}$$

Here $\hat{\rho}(t)$ is the density operator of the many-body system, $\hat{\rho}_0$ is its equilibrium value, and we used the notation of Ref. [30].

By Fourier transforming with respect to space and time, making use of $J^{\rm el}_{\boldsymbol{q}\alpha}(\omega) = -eJ_{\boldsymbol{q}\alpha}(\omega)$, and $\boldsymbol{A} = -(ic/\omega)\boldsymbol{E}$, and comparing with (2.69), we finally find:

$$\sigma_{\alpha\beta}(\boldsymbol{q}, \boldsymbol{q}', \omega) = \frac{ie^2}{\omega V} \left[\chi_{\hat{J}^{\rm p}_{\boldsymbol{q}\alpha} \hat{J}^{\rm p}_{-\boldsymbol{q}'\beta}}(\omega) + \frac{\delta_{\alpha\beta}}{m} \langle \hat{n}_{\boldsymbol{q}-\boldsymbol{q}'} \rangle \right] , \tag{2.81}$$

where the Fourier transforms of the density and current density operators are give by, respectively,

$$\hat{n}_{\boldsymbol{q}} = \sum_i e^{-i\boldsymbol{q}\cdot\hat{\boldsymbol{r}}_i} \tag{2.82}$$

and

$$\hat{J}^{\rm p}_{\boldsymbol{q}\alpha} = \sum_i \frac{1}{2m} \left\{ \hat{p}_{i,\alpha}; e^{-i\boldsymbol{q}\cdot\hat{\boldsymbol{r}}_i} \right\} = \sum_i \frac{1}{2m} \left\{ \hat{p}_{i,\alpha}; \hat{n}_{\boldsymbol{q}} \right\} \ . \tag{2.83}$$

The paramagnetic current-current response function in Eq. (2.81) can be written, at the non-interacting level, as

$$\chi_{\hat{J}^{\rm p}_{\boldsymbol{q}\alpha}\hat{J}^{\rm p}_{-\boldsymbol{q}'\beta}}(\omega) = \sum_{mn} \frac{f_m - f_n}{\epsilon_m - \epsilon_n + \hbar\omega + i\eta} \langle m|\hat{J}^{\rm p}_{\boldsymbol{q}\alpha}|n\rangle\langle n|\hat{J}^{\rm p}_{-\boldsymbol{q}'\beta}|m\rangle \ , \tag{2.84}$$

where $\{|m\rangle\}$ is a complete set of eigenstates of $\hat{H}_0$ and ϵ_m are the corresponding energies, η is a small positive infinitesimal (with dimensions of energy).

Conductivity in periodic single particle systems

In a crystal, Bloch translational invariance implies that the wave vectors $\boldsymbol{q}$ and $\boldsymbol{q}'$ can differ at most by a reciprocal lattice vector: the conductivity can therefore be written as

$$\sigma^{\boldsymbol{G}\boldsymbol{G}'}_{\alpha\beta}(\boldsymbol{q},\omega) \equiv \sigma_{\alpha\beta}(\boldsymbol{q}+\boldsymbol{G}, \boldsymbol{q}+\boldsymbol{G}', \omega) \ , \tag{2.85}$$

with $\boldsymbol{q}$ in the first Brillouin zone and $\boldsymbol{G}$, $\boldsymbol{G}'$ reciprocal lattice vectors. If electron-electron interactions are neglected, the one particle eigenstates of $\hat{H}_0$ are in the Bloch form $|\boldsymbol{k}\nu\rangle$, and Eq. (2.81) can be recast in the form

$$\begin{aligned}\sigma^{\boldsymbol{G}\boldsymbol{G}'}_{\alpha\beta}(\boldsymbol{q},\omega) =& \frac{ie^2\hbar}{V} \sum_{\boldsymbol{k},\nu,\nu'} \left[-\frac{f_{\boldsymbol{k}\nu} - f_{\boldsymbol{k}+\boldsymbol{q}\nu'}}{\epsilon_{\boldsymbol{k}\nu} - \epsilon_{\boldsymbol{k}+\boldsymbol{q}\nu'}} \right] \frac{\langle \boldsymbol{k}\nu|\hat{J}^{\rm p}_{\boldsymbol{q}+\boldsymbol{G}\alpha}|\boldsymbol{k}+\boldsymbol{q}\nu'\rangle\langle \boldsymbol{k}+\boldsymbol{q}\nu'|\hat{J}^{\rm p}_{-\boldsymbol{q}-\boldsymbol{G}'\beta}|\boldsymbol{k}\nu\rangle}{\epsilon_{\boldsymbol{k}\nu} - \epsilon_{\boldsymbol{k}+\boldsymbol{q}\nu'} + \hbar\omega + i\eta} \\ &+ \frac{ie^2}{Vm\omega} T^{\boldsymbol{G},\boldsymbol{G}'}_{\alpha\beta}(\boldsymbol{q}) \ ,\end{aligned} \tag{2.86}$$

where

$$T^{\boldsymbol{G}\boldsymbol{G}'}_{\alpha\beta}(\boldsymbol{q}) = m \sum_{\boldsymbol{k},\nu,\nu'} \frac{f_{\boldsymbol{k}\nu} - f_{\boldsymbol{k}+\boldsymbol{q}\nu'}}{\epsilon_{\boldsymbol{k}\nu} - \epsilon_{\boldsymbol{k}+\boldsymbol{q}\nu'}} \langle \boldsymbol{k}\nu|\hat{J}^{\rm p}_{\boldsymbol{q}+\boldsymbol{G}\alpha}|\boldsymbol{k}+\boldsymbol{q}\nu'\rangle\langle \boldsymbol{k}+\boldsymbol{q}\nu'|\hat{J}^{\rm p}_{-\boldsymbol{q}-\boldsymbol{G}'\beta}|\boldsymbol{k}\nu\rangle + \delta_{\alpha\beta}\langle \hat{n}_{\boldsymbol{G}-\boldsymbol{G}'}\rangle \ . \tag{2.87}$$

To find Eqs. (2.86)-(2.87) we used the following mathematical identity:

$$\frac{1}{\epsilon_m - \epsilon_n + \hbar\omega + i\eta} = \frac{1}{\epsilon_m - \epsilon_n}\left[1 - \frac{\hbar\omega + i\eta}{\epsilon_m - \epsilon_n + \hbar\omega + i\eta}\right] \overset{\eta\to 0}{=} \frac{1}{\epsilon_m - \epsilon_n}\left[1 - \frac{\hbar\omega}{\epsilon_m - \epsilon_n + \hbar\omega + i\eta}\right] . \tag{2.88}$$

We now simplify the expression of the conductivity Eq. (2.86), by deriving its local approximation [17]. The local approximation is appropriate when one is interested in wavelengths much larger than the periodicity of the system, which in the case of TBG is the moiré wavelength. Using the relation

$$\hat{J}^{(0)}_{\boldsymbol{0}\alpha} = \frac{1}{m}\hat{p}_\alpha = \frac{i}{\hbar}\left[\hat{H}_0; \hat{r}_\alpha\right] \tag{2.89}$$

and the canonical commutator $[\hat{r}_\alpha; \hat{p}^{(0)}_\beta] = i\hbar\delta_{\alpha\beta}$, one can show that

$$\lim_{\boldsymbol{q}\to\boldsymbol{0}} T^{\boldsymbol{00}}_{\alpha\beta}(\boldsymbol{q}) = 0 \ . \tag{2.90}$$

The local conductivity, defined as

$$\sigma_{\alpha\beta}(\omega) \equiv \lim_{\boldsymbol{q}\to\boldsymbol{0}} \sigma^{\boldsymbol{00}}_{\alpha\beta}(\boldsymbol{q},\omega) \ , \tag{2.91}$$

can be therefore expressed as:

$$\begin{aligned}\sigma_{\alpha\beta}(\omega) =& \frac{ie^2 g}{\hbar}\sum_\nu \int \frac{d^D\boldsymbol{k}}{(2\pi)^D}[-f'_{\boldsymbol{k}\nu}]\frac{\langle \boldsymbol{k}\nu|\frac{\hbar}{m}\hat{p}_\alpha|\boldsymbol{k}\nu\rangle\langle\boldsymbol{k}\nu|\frac{\hbar}{m}\hat{p}_\beta|\boldsymbol{k}\nu\rangle}{\hbar\omega+i\eta} \\ &+\frac{ie^2 g}{\hbar}\sum_{\nu\neq\nu'}\int\frac{d^D\boldsymbol{k}}{(2\pi)^D}\left[-\frac{f_{\boldsymbol{k}\nu}-f_{\boldsymbol{k}\nu'}}{\epsilon_{\boldsymbol{k}\nu}-\epsilon_{\boldsymbol{k}\nu'}}\right]\frac{\langle \boldsymbol{k}\nu|\frac{\hbar}{m}\hat{p}_\alpha|\boldsymbol{k}\nu'\rangle\langle\boldsymbol{k}\nu'|\frac{\hbar}{m}\hat{p}_\beta|\boldsymbol{k}\nu\rangle}{\epsilon_{\boldsymbol{k}\nu}-\epsilon_{\boldsymbol{k}\nu'}+\hbar\omega+i\eta} \ .\end{aligned} \tag{2.92}$$

Here, we introduced a degeneracy factor g accounting for possible degeneracies in the electronic spectrum, we also separated the terms of the sum with $\nu = \nu'$ and used the limit $\lim_{\boldsymbol{q}\to\boldsymbol{0}} \frac{f_{\boldsymbol{k}\nu}-f_{\boldsymbol{k}+\boldsymbol{q}\nu}}{\epsilon_{\boldsymbol{k}\nu}-\epsilon_{\boldsymbol{k}+\boldsymbol{q}\nu}} = f'_{\boldsymbol{k}\nu}$. The local conductivity $\sigma_{\alpha\beta}(\omega)$, in the case $\omega \neq 0$ it is often also called *optical conductivity*. The matrix elements appearing in Eq. (2.92) can be conveniently expressed as

$$\langle \boldsymbol{k}\nu|\frac{\hbar}{m}\hat{p}_\alpha|\boldsymbol{k}\nu'\rangle = \langle u_{\boldsymbol{k}\nu}|\frac{\hbar}{m}[\hat{p}_\alpha+\hbar k_\alpha]|u_{\boldsymbol{k}\nu'}\rangle = \langle u_{\boldsymbol{k}\nu}|\partial_{\boldsymbol{k}_\alpha}\hat{H}(\boldsymbol{k})|u_{\boldsymbol{k}\nu'}\rangle \ , \tag{2.93}$$

where $|u_{\boldsymbol{k}\nu}\rangle$ are the periodic parts of the Bloch wavefunctions and $\hat{H}(\boldsymbol{k}) \equiv e^{-i\boldsymbol{k}\cdot\boldsymbol{r}}\hat{H}_0 e^{i\boldsymbol{k}\cdot\boldsymbol{r}}$. In the following we will analyse separately the intra-band and an inter-band contributions to conductivity,

$$\sigma_{\alpha\beta}(\omega) = \sigma^{\text{intra}}_{\alpha\beta}(\omega) + \sigma^{\text{inter}}_{\alpha\beta}(\omega) \ . \tag{2.94}$$

The intra-band contribution (i.e. the first line of Eq. (2.92)) has a simple Drude-type frequency dependence and is given by

$$\sigma^{\text{intra}}_{\alpha\beta}(\omega) = G_0\frac{i\mathcal{W}^{(0)}_{\alpha\beta}}{\hbar\omega+i\eta} \ , \tag{2.95}$$

where $G_0 \equiv 2e^2/h$ is the conductance quantum, and $\mathcal{W}^{(0)}_{\alpha\beta}$ can be calculated from

$$\mathcal{W}^{(p)}_{\alpha\beta} \equiv -\pi g\sum_\nu\int\frac{d^2\boldsymbol{k}}{(2\pi)^2}f'_{\boldsymbol{k}\nu}(\epsilon_{\boldsymbol{k}\nu}-\mu)^p\langle u_{\boldsymbol{k}\nu}|\partial_{k_\alpha}\hat{H}(\boldsymbol{k})|u_{\boldsymbol{k}\nu}\rangle\langle u_{\boldsymbol{k}\nu}|\partial_{k_\beta}\hat{H}(\boldsymbol{k})|u_{\boldsymbol{k}\nu}\rangle \ , \tag{2.96}$$

by setting $p = 0$. In Eq. (2.96), the factor $(\epsilon_{\boldsymbol{k}\nu}-\mu)^p$ with p a non-negative integer has been introduced for later convenience, $f'_{\boldsymbol{k}\nu}$ denotes the derivative of the Fermi distribution with respect to its argument. The quantity $\mathcal{W}^{(0)}_{\alpha\beta}$ is proportional to the Drude weight $\mathcal{D}_{\alpha\beta}$, i.e.

$$\mathcal{D}_{\alpha\beta} \equiv \int_{-\infty}^{\infty} d\omega\,\text{Re}[\sigma^{\text{intra}}_{\alpha\beta}(\omega)] = \frac{e^2}{\hbar^2}\mathcal{W}^{(0)}_{\alpha\beta} \ . \tag{2.97}$$

The inter-band contribution to the optical conductivity is given by

$$\sigma_{\alpha\beta}^{\text{inter}}(\omega) = -i\pi g G_0 \sum_{\nu\neq\nu'} \int \frac{d^2\boldsymbol{k}}{(2\pi)^2} \frac{f_{\boldsymbol{k}\nu} - f_{\boldsymbol{k}\nu'}}{\epsilon_{\boldsymbol{k}\nu} - \epsilon_{\boldsymbol{k}\nu'}} \frac{\langle u_{\boldsymbol{k}\nu}|\partial_{k_\alpha}\hat{H}(\boldsymbol{k})|u_{\boldsymbol{k}\nu'}\rangle\langle u_{\boldsymbol{k}\nu'}|\partial_{k_\beta}\hat{H}(\boldsymbol{k})|u_{\boldsymbol{k}\nu}\rangle}{\hbar\omega + i\eta + \epsilon_{\boldsymbol{k}\nu} - \epsilon_{\boldsymbol{k}\nu'}} \ . \tag{2.98}$$

Integrals of the type written in Eq. (2.96) are also useful to calculate the Seebeck coefficient S, which describes the electrical response to a thermal gradient. Indeed, the Seebeck coefficient can be written as [107]

$$S = -\frac{1}{eT}\frac{I^{(1)}}{I^{(0)}} \ , \tag{2.99}$$

where

$$\begin{aligned} I^{(p)} \ &\equiv \ -\frac{e^2}{\hbar^2} g \sum_{\nu} \int \frac{d^2\boldsymbol{k}}{(2\pi)^2} f'_{\boldsymbol{k}\nu} \tau_{\boldsymbol{k}\nu} (\epsilon_{\boldsymbol{k}\nu} - \mu)^p \\ &\times \ \langle u_{\boldsymbol{k}\nu}|\partial_{k_x}\hat{H}(\boldsymbol{k})|u_{\boldsymbol{k}\nu}\rangle\langle u_{\boldsymbol{k}\nu}|\partial_{k_x}\hat{H}(\boldsymbol{k})|u_{\boldsymbol{k}\nu}\rangle \ . \end{aligned} \tag{2.100}$$

Here, $\tau_{\boldsymbol{k}\nu}$ is the momentum-dependent relaxation time. In the Relaxation Time Approximation (RTA), where the dependence of $\tau_{\boldsymbol{k}\nu}$ on $\boldsymbol{k}$ is neglected by setting $\tau_{\boldsymbol{k}\nu} \equiv \tau$, Eq. (2.99) reduces to

$$S_{\text{RTA}} = -\frac{1}{eT}\frac{\mathcal{W}^{(1)}}{\mathcal{W}^{(0)}} \ . \tag{2.101}$$

The RTA neglects the energy and momentum dependence of the scattering time, but correctly captures the intrinsic (i.e. band structure) contribution to the Seebeck coefficient.

Conductivity in the random phase approximation

The RPA expression of the electrical conductivity $\sigma_{\alpha\beta}^{\text{RPA}}(\boldsymbol{q},\boldsymbol{q}',\omega)$ can be easily obtained noticing that, if $\rho_{\text{ind}}(\boldsymbol{q},\omega) \equiv -en_{\text{ind}}(\boldsymbol{q},\omega)$ is the induced *charge* density, and $\phi_{\text{tot}}(\boldsymbol{q},\omega) \equiv -V_{\text{tot}}(\boldsymbol{q},\omega)/e$ is the total *electric* potential, Eq. (2.61) is transformed to

$$\rho_{\text{ind}}(\boldsymbol{q},\omega) = e^2 \sum_{\boldsymbol{q}'} \tilde{\chi}_{nn}(\boldsymbol{q},\boldsymbol{q}',\omega)\phi_{\text{tot}}(\boldsymbol{q}',\omega). \tag{2.102}$$

Now, using the continuity equation

$$i\boldsymbol{q}\cdot\boldsymbol{J}_{\text{el}}(\boldsymbol{q},\omega) - i\omega\rho_{\text{ind}}(\boldsymbol{q},\omega) = 0, \tag{2.103}$$

and $\boldsymbol{E}_{\text{tot}} = -i\boldsymbol{q}\phi_{\text{tot}}(\boldsymbol{q},\omega)$ in Eq. (2.69) we obtain the following relationship between $\tilde{\chi}_{nn}(\boldsymbol{q},\boldsymbol{q}',\omega)$ and $\sigma_{\alpha\beta}(\boldsymbol{q},\boldsymbol{q}',\omega)$:

$$\tilde{\chi}_{nn}(\boldsymbol{q},\boldsymbol{q}',\omega) = \frac{-i}{e^2\omega} q_\alpha q'_\beta \sigma_{\alpha\beta}(\boldsymbol{q},\boldsymbol{q}',\omega) \ . \tag{2.104}$$

By virtue of the previous equation and the relationship $\tilde{\chi}_{nn}^{\text{RPA}}(\boldsymbol{q},\boldsymbol{G},\boldsymbol{G}',\omega) \equiv \chi_{nn}^{\text{H}}(\boldsymbol{q},\boldsymbol{G},\boldsymbol{G}',\omega)$, it is easy to verify that the RPA conductivity $\sigma_{\alpha\beta}^{\text{RPA}}(\omega)$ in the local approximation Eq. (2.91), corresponds to the non-interacting conductivity Eq. (2.92) calculated with the basis of self-consistent Hartree orbitals.

2.3.3 Energy loss function and plasmons

In this Section we conclude the review of the physical quantities derived through linear response theory which are going to be calculated for TBG in Chapter 3. The energy loss function (or, briefly, loss function) $\mathcal{L}(\boldsymbol{q},\omega)$ is proportional to the probability of exciting the 2D electron system by applying a scalar perturbation of wave vector $\boldsymbol{q}$ and energy $\hbar\omega$. The loss function can be directly measured e.g. via electron-energy-loss spectroscopy [108] and displays peaks where self-sustained charge oscillations—i.e. plasmons—can be excited. It also carries information on inter-band transitions and Landau damping. As mentioned in Section 1.1.3, collective excitations of 2D electron systems can also be probed by scattering-type near-field optical microscopy.

In a crystal, the loss function is formally defined by [58]

$$\mathcal{L}(\boldsymbol{q},\omega) = -\operatorname{Im}\left\{[\epsilon^{-1}(\boldsymbol{q},\omega)]_{\boldsymbol{G}=\boldsymbol{0},\boldsymbol{G}'=\boldsymbol{0}}\right\} \ . \tag{2.105}$$

Here, $\epsilon_{\boldsymbol{G}\boldsymbol{G}'}(\boldsymbol{q},\omega)$ is the dielectric function of the crystal [30] viewed as a matrix with indices $\boldsymbol{G}$, $\boldsymbol{G}'$ in the space of reciprocal lattice vectors, $\boldsymbol{q}$ lies inside the first Brillouin zone, and inversion has to be understood as *matrix* inversion.

In a generic, not-translationally-invariant, electronic system the dielectric function relates the externally applied electric potential with the total electric potential (i.e. the sum of the external potential and the Hartree potential)

$$-e\phi_{\text{ext}}(\boldsymbol{q},\omega) = -e\sum_{\boldsymbol{q}'}\epsilon(\boldsymbol{q},\boldsymbol{q}',\omega)\phi_{\text{tot}}(\boldsymbol{q}',\omega) \ . \tag{2.106}$$

The dielectric function $\epsilon(\boldsymbol{q},\boldsymbol{q}',\omega)$ can be related [30, 109] to the *proper* density-density response function $\tilde{\chi}_{nn}(\boldsymbol{q},\boldsymbol{q}',\omega)$

$$\epsilon(\boldsymbol{q},\boldsymbol{q}',\omega) = \delta_{\boldsymbol{q}\boldsymbol{q}'} - e^2 L_{\boldsymbol{q},\omega}\tilde{\chi}_{nn}(\boldsymbol{q},\boldsymbol{q}',\omega) \ , \tag{2.107}$$

where we have assumed that the Coulomb interaction potential $L_{\boldsymbol{q},\omega}$ does not couple different wave vectors (i.e. the dielectric environment, which alters the e-e interaction in vacuum, has translational invariance).

In a crystal, all the response functions can connect wave vectors that differ at most by a reciprocal lattice vector. We can therefore define

$$\begin{aligned}\epsilon_{\boldsymbol{G}\boldsymbol{G}'}(\boldsymbol{q},\omega) \equiv \epsilon(\boldsymbol{q}+\boldsymbol{G},\boldsymbol{q}+\boldsymbol{G}',\omega) &= \delta_{\boldsymbol{q}+\boldsymbol{G}\,\boldsymbol{q}+\boldsymbol{G}'} - e^2 L_{\boldsymbol{q}+\boldsymbol{G},\omega}\tilde{\chi}_{nn}(\boldsymbol{q}+\boldsymbol{G},\boldsymbol{q}+\boldsymbol{G}',\omega) = \\ &= \delta_{\boldsymbol{G}\boldsymbol{G}'} + L_{\boldsymbol{q}+\boldsymbol{G},\omega}\frac{i(\boldsymbol{q}+\boldsymbol{G})_\alpha(\boldsymbol{q}+\boldsymbol{G}')_\beta\sigma_{\alpha\beta}(\boldsymbol{q}+\boldsymbol{G},\boldsymbol{q}+\boldsymbol{G}',\omega)}{\omega} \ ,\end{aligned} \tag{2.108}$$

where $\boldsymbol{q}$ lies in the first Brillouin zone, $\boldsymbol{G}$, $\boldsymbol{G}'$ are reciprocal lattice vectors, and in the equality between the first and second line we have used Eq. (2.104). Using Eq. (2.85) in the previous equation we immediately get

$$\epsilon_{\boldsymbol{G}\boldsymbol{G}'}(\boldsymbol{q},\omega) = \delta_{\boldsymbol{G}\boldsymbol{G}'} + L_{\boldsymbol{q}+\boldsymbol{G},\omega}\frac{i(\boldsymbol{q}+\boldsymbol{G})_\alpha(\boldsymbol{q}+\boldsymbol{G}')_\beta\sigma^{\boldsymbol{G}\boldsymbol{G}'}_{\alpha\beta}(\boldsymbol{q},\omega)}{\omega} \ . \tag{2.109}$$

As done for the conductivity, we simplify the loss function by calculating its local approximation. This amounts to neglecting the off-diagonal $\boldsymbol{G} \neq \boldsymbol{G}'$ terms in the space of the reciprocal lattice vectors and taking the limit $\boldsymbol{q} \to \boldsymbol{0}$ in the non-local conductivity, i.e.

$$\epsilon_{\boldsymbol{G}\boldsymbol{G}'}(\boldsymbol{q},\omega) \approx \delta_{\boldsymbol{G}\boldsymbol{G}'}\left[1 + L_{\boldsymbol{q}+\boldsymbol{G},\omega} \times \frac{i(\boldsymbol{q}+\boldsymbol{G})_\alpha (\boldsymbol{q}+\boldsymbol{G})_\beta \lim_{\boldsymbol{q}\to\boldsymbol{0}} \sigma^{\boldsymbol{G}\boldsymbol{G}}_{\alpha\beta}(\boldsymbol{q},\omega)}{\omega}\right] . \tag{2.110}$$

By following this procedure and making use of the isotropy of the system, we can express $\mathcal{L}(\boldsymbol{q},\omega)$ solely in terms of the local conductivity $\lim_{\boldsymbol{q}\to\boldsymbol{0}} \sigma^{\boldsymbol{0}\boldsymbol{0}}_{\alpha\beta}(\boldsymbol{q},\omega) = \delta_{\alpha\beta}\sigma(\omega)$ and the interaction potential $L_{\boldsymbol{q},\omega}$:

$$\mathcal{L}(\boldsymbol{q},\omega) \approx -\operatorname{Im}\left\{\frac{1}{1 + iq^2 L_{\boldsymbol{q},\omega}\dfrac{\sigma(\omega)}{\omega}}\right\} . \tag{2.111}$$

In a 2D system sandwiched between two half-spaces filled with a dielectric with a frequency-dependent permittivity $\bar{\varepsilon}(\omega)$, the interaction potential appearing in Eq. (2.111) reads as following:

$$L_{\boldsymbol{q},\omega} = \frac{2\pi}{q\bar{\varepsilon}(\omega)} . \tag{2.112}$$

The RPA loss function is given by inserting the RPA conductivity in Eq. (2.111)

$$\mathcal{L}^{\mathrm{RPA}}(\boldsymbol{q},\omega) \approx -\operatorname{Im}\left\{\frac{1}{1 + iq^2 L_{\boldsymbol{q},\omega}\dfrac{\sigma^{\mathrm{RPA}}(\omega)}{\omega}}\right\} , \tag{2.113}$$

or, equivalently, inserting the RPA proper density-density response function $\tilde{\chi}^{\mathrm{RPA}}_{nn}(\boldsymbol{q},\boldsymbol{q}',\omega)$ in Eq. (2.107).

2.3.4 Electron-electron interactions beyond the random phase approximation

Despite its popularity, the RPA is one of the most basic techniques available to describe the linear response of an interacting electron system. The next degree of approximation would be the time-dependent Hartree-Fock (TDHF) approximation, which requires the calculations of the Hartree-Fock orbitals and the evaluation of the contributions arising from proper diagrams containing one interaction line. Electron-hole attraction effects (i.e. excitonic effects), which are missed by the RPA theory we are employing in this Thesis, may alter the results on inter-band plasmons presented in the next Chapter, even at relatively small values of q. Much more work is needed to quantify such excitonic effects in TBG, the minimal theory that captures these effects being the TDHF approximation.

A much more advanced technique is the "dual-boson approach" [118, 119], which extends the dynamical mean field theory paradigm [120] allowing the calculation of collective excitations in correlated systems. Within this paradigm, the Authors of Refs. [116, 117] calculated the plasmonic properties of a strongly interacting two-dimensional Hubbard model beyond the RPA approximation. For a realistic description of TBG properties, these advanced techniques are necessary in the low-temperature regime when the twist angle is close to the magic one and the Fermi energy lies in the manifold of flat bands.

In this Thesis we have taken a much more humble approach, as we were motivated by the s-SNOM measurements in Ref. [43]. In this case, RPA is expected to be reliable since the thermal energy $k_{\mathrm{B}}T$ at room temperature is of the same order of the flat bands bandwidth. RPA is also expected to be accurate when the Fermi energy *does not* cross the flat bands as, in this case, the one-particle description of TBG is accurate, as showed by the scanning tunneling spectroscopy experiments [70, 71, 72, 73] reviewed in the introductory Chapter 1.

2.4 Numerical methods

In this section we discuss the numerical methods used in this Thesis to compute the energy spectrum of twisted bilayer graphene and the self-consistent solutions of the Hartree approximation. Our numerical codes have been implemented in Python 3, require only standard numerical libraries such as Numpy and Scipy, and are available at the following url: `https://gitlab.com/itorre/bandstructure-calculation`. We will however try to keep the discussion on a very general level, independent on the specifics of the progamming language used for the implementation.

2.4.1 Energy spectrum and electronic bands

As already mentioned in the previous sections, a periodic model is characterized by a basis of primitive translation vectors[1] $\boldsymbol{t}_1$ and $\boldsymbol{t}_2$, whose integer linear combinations

$$\boldsymbol{t}_n = n_1\boldsymbol{t}_1 + n_2\boldsymbol{t}_2 \quad \text{with } n = (n_1, n_2) \in \mathbb{Z} \times \mathbb{Z} \tag{2.114}$$

span a Bravais lattice. Accordingly, it is important to consider also the reciprocal lattice in the dual (or reciprocal) space. Indeed, the propagation wavevector $\boldsymbol{k}$ of a general plane wave $\exp(i\boldsymbol{k}\cdot\boldsymbol{r})$ has reciprocal length dimension, and can be conveniently represented in the reciprocal space. The reciprocal lattice is spanned by integer linear combinations $\boldsymbol{G}_n$ of the vectors $\boldsymbol{G}_1$ and $\boldsymbol{G}_2$, which are obtained from the primitive translation vectors through the relation $\boldsymbol{t}_i \cdot \boldsymbol{G}_j = 2\pi\delta_{ij}$.

The Brillouin zone is the region of the reciprocal space with the property that any point included in the BZ is closer to a chosen lattice point (say $\boldsymbol{G}_n = \boldsymbol{0}$) than to any other. The energy eigenvalues of a translational invariant model are labeled by the crystal wave vector $\boldsymbol{k}$, which is inside the Brillouin zone.

[1] We explicitly work with two-dimensional systems, which are relevant for this Thesis.

To numerically compute the electronic states of a periodic model, one needs the matrix elements of its Hamiltonian for an orthonormal basis which is *explicitly dependent on the crystal wave vector* $\boldsymbol{k}$. Two basis explicitly depending on $\boldsymbol{k}$ are commonly considered: Bloch sums and plane waves. Concrete examples of the usage of Bloch sums and plane waves are going to be presented when discussing the numerical calculation of the energy spectrum of TBG for, respectively, the tight-binding and continuum model. For the moment let just assume to have an orthonormal basis

$$\{|\phi_1(\boldsymbol{k})\rangle, \cdots, |\phi_N(\boldsymbol{k})\rangle \} \text{ with } \boldsymbol{k} \in \text{BZ}, \text{ and } \langle\phi_i(\boldsymbol{k})|\phi_j(\boldsymbol{k}')\rangle = \delta_{ij}\delta_{\boldsymbol{k}\boldsymbol{k}'} \tag{2.115}$$

and to know the system's Hamiltonian $\hat{H}$ matrix elements on this basis

$$H_{ij}(\boldsymbol{k}) \equiv \langle\phi_i(\boldsymbol{k})|\hat{H}|\phi_j(\boldsymbol{k})\rangle. \tag{2.116}$$

The matrix whose elements are $H_{ij}(\boldsymbol{k})$ is Hermitian by construction, and the spectral theorem assure it has N real eigenvalues. Let us now call these eigenvalues $\epsilon_{\boldsymbol{k}\nu}$ and $(c_1(\boldsymbol{k},\nu),\ldots,c_N(\boldsymbol{k},\nu)) \in \mathbb{C}^N$ the corresponding eigenvectors, with $\nu = 1, \cdots, N$ indexing the different eigenvalues. The quantities $\epsilon_{\boldsymbol{k}\nu}$ and $(c_1(\boldsymbol{k},\nu),\ldots,c_N(\boldsymbol{k},\nu))$ are routinely obtained numerically thanks to standard diagonalization algorithms based on the "divide and conquer" approach, with a computational cost of the order of $\sim N^3$ floating-point operations. The Bloch eigenstate at crystal momentum $\boldsymbol{k}$ and (band) index ν is given simply by

$$|\boldsymbol{k}\nu\rangle = \sum_{i=1}^{N} c_i(\boldsymbol{k},\nu)|\phi_i(\boldsymbol{k})\rangle. \tag{2.117}$$

By knowing the matrix elements of a generic operator $\hat{O}$ on the basis Eq. (2.115),

$$O_{ij}(\boldsymbol{k},\boldsymbol{k}') = \langle\phi_i(\boldsymbol{k})|\hat{O}|\phi_j(\boldsymbol{k}')\rangle, \tag{2.118}$$

the matrix elements of the same operator on the Bloch eigenstates are readily obtained

$$\langle\boldsymbol{k}\nu|\hat{O}|\boldsymbol{k}\nu'\rangle = \sum_{i=1}^{N}\sum_{j=1}^{N} c_i(\boldsymbol{k},\nu)^* O_{ij}(\boldsymbol{k},\boldsymbol{k}')c_j(\boldsymbol{k},\nu), \tag{2.119}$$

which is just a vector-matrix-vector product. These remarks, albeit being rather trivial linear algebra facts, allow to actually compute the matrix elements appearing in the electrical conductivity Eq. (2.92), and density-density response function Eqs. (2.66).

Tight-binding model of TBG: numerical energy spectrum

In this Section we are going to discuss how to compute the energy spectrum of TBG in the tight-binding approximation. We remind that the intra-layer and inter-layer Hamiltonian in the tight-binding model, Eqs. (2.11) and (2.16), were derived in the basis of the localized atomic orbitals $|n,\ell,\tau\rangle$, where $n = (n_1, n_2) \in \mathbb{Z}\times\mathbb{Z}$ is the index

of the n-th site of the Bravais lattice of Carbon atoms of the τ-th sublattice in the ℓ-th layer. From these definitions follows that the Carbon atoms are at positions

$$\boldsymbol{R}_{n,\ell,\tau} = n_1\tilde{\boldsymbol{a}}_{1,\ell} + n_2\tilde{\boldsymbol{a}}_{2,\ell} + \boldsymbol{d}_{\tau,\ell} \quad \text{with } n = (n_1, n_2) \in \mathbb{Z}\times\mathbb{Z}\ , \tag{2.120}$$

where $\tilde{\boldsymbol{a}}_{i,\ell}$ and $\boldsymbol{d}_{\tau,\ell}$ are defined in Eqs. (2.4) and (2.5). The moiré superlattice has translation vectors (see Eq. (2.8))

$$\boldsymbol{t}_1 = \lambda_{\mathrm{M}}\,(0,\,1)\,, \qquad \boldsymbol{t}_2 = \lambda_{\mathrm{M}}\left(-\frac{\sqrt{3}}{2},\,\frac{1}{2}\right), \tag{2.121a}$$

$$\lambda_{\mathrm{M}} = ar\sqrt{\frac{3}{\gcd(r,3)}\left[\left(\frac{m}{r}\right)^2 + \frac{m}{r} + \frac{1}{3}\right]}, \tag{2.121b}$$

where m and r are coprime integers which identify the twist angle. We now show how to exploit the translational invariance of the model to construct a primitive super-cell for the moiré superlattice. This will allow the construction of the Bloch sums needed to get the energy spectrum numerically.

Because of translational invariance, if a Carbon atom of layer ℓ and sublattice τ is found at position $\boldsymbol{R}_{n,\ell,\tau}$, for every $N = (N_1, N_2) \in \mathbb{Z}\times\mathbb{Z}$ another atom of the same kind is going to be found at positions $\boldsymbol{R}_{n,\ell,\tau} + N_1\boldsymbol{t}_1 + N_2\boldsymbol{t}_2 \equiv \boldsymbol{R}_{n,\ell,\tau} + \boldsymbol{t}_N$, where $\boldsymbol{t}_N = N_1\boldsymbol{t}_1 + N_2\boldsymbol{t}_2$ is an arbitrary linear combination of the moiré primitive vectors Eq. (2.121). Now, because, as just said another carbon atom is going to be found at $\boldsymbol{R}_{n,\ell,\tau} + N\boldsymbol{t}_N$, then it exists n_N such that

$$\boldsymbol{R}_{n_N,\ell,\tau} = \boldsymbol{R}_{n,\ell,\tau} + \boldsymbol{t}_N. \tag{2.122}$$

Using the intuition that, starting from an arbitrary site, atomic orbitals of the same kind are found also at integer linear combinations $\boldsymbol{t}_N$, it is possible to introduce the definition of "primitive moiré super-cell". The primitive super-cell of the moiré superlattice is the smallest set of atomic orbitals which under translations by integer linear combinations of the moiré primitive vectors $\boldsymbol{t}_N$ span *every* site $\boldsymbol{R}_{n,\ell,\tau}$ of the superlattice. In particular, when a primitive super-cell is defined, we can decompose the index n appearing in $\boldsymbol{R}_{n,\ell,\tau}$ in the following way

$$n \in \mathbb{Z}\times\mathbb{Z} \mapsto (\nu, N) \quad \text{with } \nu \in \text{ primitive cell and } N \in \mathbb{Z}\times\mathbb{Z}, \tag{2.123a}$$

$$|n,\ell,\tau\rangle \mapsto |N,\nu,\ell,\tau\rangle \equiv |N,\alpha\rangle, \tag{2.123b}$$

where we have defined the multi-index $\alpha = (\nu,\ell,\tau)$ for notational convenience. With the new notation, an atomic orbital $|N,\alpha\rangle$ is centered at position

$$\boldsymbol{R}_{N,\alpha} \equiv \boldsymbol{R}_\alpha + \boldsymbol{t}_N. \tag{2.124}$$

It is important to remind that the index ν, found in $\alpha = (\nu,\ell,\tau)$ is now varying *only on a finite subset of* $\mathbb{Z}\times\mathbb{Z}$, corresponding on the integer coordinates of Carbon atoms

inside the moiré super-cell. This observation imply that, because ν, ℓ, and τ take values on sets of finite cardinality, then also the multi-index $\alpha = (\nu, \ell, \tau)$ takes values in a set $\mathcal{S}$ of finite cardinality:

$$\mathcal{S} \equiv \{\alpha = (\nu, \ell, \tau) \mid \nu \in \text{ primitive cell }, \ell = \pm 1, \tau = \pm 1\}. \tag{2.125}$$

Numerically, for each $\boldsymbol{k}$ one will have to diagonalize a matrix of dimension $\#(\mathcal{S})^2$. Thanks to the previous definitions, it is now possible to define the set of orthonormal states depending on the crystal wave vector $\boldsymbol{k}$ introduced in Eq. (2.115) as Bloch sums of the following type

$$|\boldsymbol{k}, \alpha\rangle = \frac{1}{\sqrt{\mathcal{N}}} \sum_n e^{i\boldsymbol{t}_N \cdot \boldsymbol{k}} |N, \alpha\rangle \ , \tag{2.126}$$

where $\mathcal{N}$ is the number of moiré supercells present in the sample. By leveraging the notation introduced above, the tight-binding Hamiltonian of TBG can now be written as

$$\hat{H} = \sum_{N,N' \in \mathbb{Z}\times\mathbb{Z}} \sum_{\alpha,\alpha' \in \mathcal{S}} h_{\alpha\alpha'}(N, N') |N, \alpha\rangle\langle N', \alpha'|, \tag{2.127}$$

where $h_{\alpha\alpha'}(N, N')$ is immediately obtained by substituting the corresponding expressions found in Eqs. (2.11) and (2.16). Now, one has

$$\begin{aligned}
\langle \boldsymbol{k}, \beta | \hat{H} | \boldsymbol{k}', \beta' \rangle &= \frac{1}{\mathcal{N}} \sum_{M,M'} \sum_{N,N'} \sum_{\alpha,\alpha' \in \mathcal{S}} e^{-i\boldsymbol{k}\cdot\boldsymbol{t}_M + i\boldsymbol{k}'\cdot\boldsymbol{t}_{M'}} h_{\alpha\alpha'}(N, N') \langle M, \beta | N, \alpha\rangle \langle N', \alpha' | M', \beta'\rangle \\
&= \frac{1}{\mathcal{N}} \sum_{M,M'} \sum_{N,N'} \sum_{\alpha,\alpha' \in \mathcal{S}} e^{-i\boldsymbol{k}\cdot\boldsymbol{t}_M + i\boldsymbol{k}'\cdot\boldsymbol{t}_{M'}} h_{\alpha\alpha'}(N, N') \delta_{MN} \delta_{M'N'} \delta_{\alpha\beta} \delta_{\alpha'\beta'} \\
&= \frac{1}{\mathcal{N}} \sum_{N,N'} e^{-i\boldsymbol{k}\cdot\boldsymbol{t}_N + i\boldsymbol{k}'\cdot\boldsymbol{t}_{N'}} h_{\beta\beta'}(N, N') \\
&= \frac{1}{\mathcal{N}} \sum_{N,N'} e^{-i(\boldsymbol{k}-\boldsymbol{k}')\cdot\boldsymbol{t}_N} e^{i\boldsymbol{k}'\cdot(\boldsymbol{t}_{N'}-\boldsymbol{t}_N)} h_{\beta\beta'}((0,0), N'-N) \\
&= \delta_{\boldsymbol{k}\boldsymbol{k}'} \sum_L e^{i\boldsymbol{k}'\boldsymbol{t}_L} h_{\beta\beta'}((0,0), L) \\
&\equiv \delta_{\boldsymbol{k}\boldsymbol{k}'} H_{\beta\beta'}(\boldsymbol{k}),
\end{aligned} \tag{2.128}$$

where we have defined $H_{\beta\beta'}(\boldsymbol{k}) \equiv \sum_L e^{i\boldsymbol{k}'\boldsymbol{t}_L} h_{\beta\beta'}((0,0), L)$, we have used the orthonormality of the atomic orbitals, the translational invariance of the Hamiltonian $h_{\alpha\alpha'}(N, N') = h_{\alpha\alpha'}((0,0), N'-N)$ as well as the following relations

$$\frac{1}{\mathcal{N}} \sum_N e^{i(\boldsymbol{k}-\boldsymbol{k}')\cdot\boldsymbol{t}_N} = \delta_{\boldsymbol{k},\boldsymbol{k}'}, \tag{2.129a}$$

$$\boldsymbol{t}_{N'} - \boldsymbol{t}_N = \boldsymbol{t}_{N'-N}, \tag{2.129b}$$

$$L \equiv N' - N = (N'_1 - N_1, N'_2 - N_2) \in \mathbb{Z} \times \mathbb{Z}. \tag{2.129c}$$

The matrix elements $\langle \boldsymbol{k}, \beta | \hat{H} | \boldsymbol{k}', \beta' \rangle$ are correctly diagonal with respect to the crystal momentum $\boldsymbol{k}$, thanks to the factor $\delta_{\boldsymbol{k}\boldsymbol{k}'}$.

We now discuss how to find the set $\mathcal{S}$ (see Eq. (2.125)) of (ν, ℓ, τ) indices defining the primitive moiré super-cell. A convenient way is to define the moiré supercell as the parallelogram spanned by the moiré primitive vectors $\boldsymbol{t}_1$ and $\boldsymbol{t}_2$, Eq. (2.114). If the super-cell is chosen according to this definition, it is obvious that the whole 2D space can be covered by rigidly translating the super-cell by integer linear combinations of the moiré primitive vectors. To find the set $\mathcal{S}$ one should thus select the atomic orbitals whose positions are *inside* the parallelogram spanned by $\boldsymbol{t}_1$ and $\boldsymbol{t}_2$. In our codes we did it by observing that, for each of the layers ℓ, it exists a 2×2 matrix of integers Λ_ℓ such that

$$\begin{pmatrix} \boldsymbol{t}_1 \\ \boldsymbol{t}_2 \end{pmatrix} = \Lambda_\ell \begin{pmatrix} \tilde{\boldsymbol{a}}_{1,\ell} \\ \tilde{\boldsymbol{a}}_{2,\ell} \end{pmatrix} = \begin{pmatrix} \lambda_{11,\ell} & \lambda_{12,\ell} \\ \lambda_{21,\ell} & \lambda_{22,\ell} \end{pmatrix} \begin{pmatrix} \tilde{\boldsymbol{a}}_{1,\ell} \\ \tilde{\boldsymbol{a}}_{2,\ell} \end{pmatrix}. \tag{2.130}$$

This means that the primitive moiré translation vectors can be written as an integer linear combination of the primitive translation vectors of graphene in layer ℓ. An explicit parametrization of the matrix Λ_ℓ as a function of the twist angle is given e.g. in Ref. [64]. By inverting the previous equation one has

$$\begin{pmatrix} \tilde{\boldsymbol{a}}_{1,\ell} \\ \tilde{\boldsymbol{a}}_{2,\ell} \end{pmatrix} = \Lambda_\ell^{-1} \begin{pmatrix} \boldsymbol{t}_1 \\ \boldsymbol{t}_2 \end{pmatrix} = \frac{1}{\det(\Lambda_\ell)} \begin{pmatrix} \lambda_{22,\ell} & -\lambda_{12,\ell} \\ -\lambda_{21,\ell} & \lambda_{11,\ell} \end{pmatrix} \begin{pmatrix} \boldsymbol{t}_1 \\ \boldsymbol{t}_2 \end{pmatrix}. \tag{2.131}$$

By hypothesis, $\lambda_{ij,\ell}$ are integers, so $\det(\Lambda_\ell)$ is an integer as well. Now, from the previous equation it is readily checked that an atom centered at $\nu_1 \tilde{\boldsymbol{a}}_{1,\ell} + \nu_2 \tilde{\boldsymbol{a}}_{2,\ell}$ is inside the parallelogram spanned by $\boldsymbol{t}_1$ and $\boldsymbol{t}_2$ if and only if both entries of the row vector

$$\frac{1}{\det(\Lambda_\ell)} \begin{pmatrix} \nu_1 & \nu_2 \end{pmatrix} \begin{pmatrix} \lambda_{22,\ell} & -\lambda_{12,\ell} \\ -\lambda_{21,\ell} & \lambda_{11,\ell} \end{pmatrix} = \left[\left[\Lambda_\ell^{-1} \right]^{\mathrm{T}} \begin{pmatrix} \nu_1 \\ \nu_2 \end{pmatrix} \right]^{\mathrm{T}} \tag{2.132}$$

are smaller than 1. This condition is equivalent to the following system of integer inequalities for ν_1 and ν_2

$$\begin{pmatrix} 0 \\ 0 \end{pmatrix} \leq \begin{pmatrix} \lambda_{22,\ell} & -\lambda_{21,\ell} \\ -\lambda_{12,\ell} & \lambda_{11,\ell} \end{pmatrix} \begin{pmatrix} \nu_1 \\ \nu_2 \end{pmatrix} < \begin{pmatrix} \det(\Lambda_\ell) \\ \det(\Lambda_\ell) \end{pmatrix}. \tag{2.133}$$

The solution to the latter inequalities yields the set of integers $\nu = (\nu_1, \nu_2)$ to be included in the set $\mathcal{S}$.

The algorithm to obtain the tight-binding spectrum of TBG can thus be synthesized as follows:

1. Input the integers `m` and `r`, which parametrize the twist angle as in Eq. (2.7).
2. From `m` and `r` construct the matrix Λ_ℓ, as e.g. in Ref. [64].
3. Solve the inequalities in Eq. (2.133) and obtain the set $\mathcal{S}$.
4. Select an ordering of the elements of the set $\mathcal{S}$, Eq. (2.125), through a map $\iota : \mathcal{S} \to \mathbb{N}$, so that $\forall \alpha \in \mathcal{S}$ one has $\alpha \mapsto \iota(\alpha) = i_\alpha$ with $0 \leq i_\alpha < \#(\mathcal{S})$.

5. Initialize an empty 2D complex array `H_k` of size $\#(\mathcal{S}) \times \#(\mathcal{S})$.

6. Populate `H_k` with the matrix elements in Eq. (2.128), obtained through Eqs. (2.11) and (2.16). Of course, the matrix element $\langle \boldsymbol{k}, \beta | \hat{H} | \boldsymbol{k}', \beta' \rangle = H_{\beta\beta'}(\boldsymbol{k})$ is going to populate the $[\iota(\beta), \iota(\beta')]$ element of `H_k`.

7. For each $\boldsymbol{k}$, numerically diagonalize `H_k` to obtain the eigenvalues $\epsilon_{\boldsymbol{k}\nu}$ and $(c_1(\boldsymbol{k}, \nu), \ldots, c_{\#(\mathcal{S})}(\boldsymbol{k}, \nu)) \in \mathbb{C}^{\#(\mathcal{S})}$.

Continuum model of TBG: numerical energy spectrum

The continuum model of TBG was derived in Section 2.1.2, and is compactly expressed in Eq. (2.30), Eq. (2.31) and Eq. (2.32), copied below for convenience.

$$\hat{H}_0 = \begin{pmatrix} \hat{H}^{(1)} & \hat{U} \\ \hat{U}^\dagger & \hat{H}^{(2)} \end{pmatrix} , \tag{2.134a}$$

$$\hat{H}^{(\ell)} = v_{\mathrm{F}} \left[R_\ell(\theta/2)(\hat{\boldsymbol{p}} - \hbar \boldsymbol{K}_\ell) \right] \cdot (\sigma_x, \sigma_y) , \tag{2.134b}$$

$$\begin{aligned} \hat{U} = \begin{pmatrix} u_0 & u_1 \\ u_1 & u_0 \end{pmatrix} + e^{-i\frac{2\pi}{3} + i\boldsymbol{G}_1 \cdot \hat{\boldsymbol{r}}} \begin{pmatrix} u_0 & u_1 e^{i\frac{2\pi}{3}} \\ u_1 e^{-i\frac{2\pi}{3}} & u_0 \end{pmatrix} + \\ + e^{i\frac{2\pi}{3} + i\boldsymbol{G}_2 \cdot \hat{\boldsymbol{r}}} \begin{pmatrix} u_0 & u_1 e^{-i\frac{2\pi}{3}} \\ u_1 e^{i\frac{2\pi}{3}} & u_0 \end{pmatrix} . \end{aligned} \tag{2.134c}$$

Here $\hat{H}_0$ is the Hamiltonian of the model, $\hat{H}^{(\ell)}$ is the intra-layer term, $\hat{U}$ is the inter-layer term, whereas $\hat{\boldsymbol{r}}$ and $\hat{\boldsymbol{p}}$ are the position and momentum operators, respectively. The energy spectrum of the continuum model is obtained numerically by calculating the matrix elements of the Hamiltonian Eq. (2.134a) in the following basis of plane waves

$$W_{\boldsymbol{k},\varepsilon} = \{ |\boldsymbol{k} + \boldsymbol{G}\rangle \mid \langle \boldsymbol{r} | \boldsymbol{k} + \boldsymbol{G} \rangle = \exp[i(\boldsymbol{k} + \boldsymbol{G}) \cdot \boldsymbol{r}], \text{ and } \boldsymbol{G} \in \mathcal{S}_\varepsilon \}, \tag{2.135a}$$

where

$$\mathcal{S}_\varepsilon = \{ \boldsymbol{G} \in \text{ reciprocal vectors} \mid \frac{\max(|u_0|, |u_1|)}{\hbar v_{\mathrm{F}} \|\boldsymbol{G}\|} > \varepsilon, \text{ with } \varepsilon \ll 1 \}. \tag{2.135b}$$

The set $W_{\boldsymbol{k},\varepsilon}$ contains plane waves of wave-vector $\boldsymbol{k} + \boldsymbol{G}$, where $\boldsymbol{k}$ is the crystal wave-vector and $\boldsymbol{G}$ is a reciprocal lattice vector of the moiré superlattice, i.e. an integer linear combination of the vectors in Eq. (2.29), belonging to the set $\mathcal{S}_\varepsilon$. The set $\mathcal{S}_\varepsilon$ is a finite set of reciprocal lattice vectors, satisfying the condition $\max(|u_0|, |u_1|)/(\hbar v_{\mathrm{F}} \|\boldsymbol{G}\|) > \varepsilon$, which we now justify. By calculating the matrix elements between the functions in $W_{\boldsymbol{k},\varepsilon}$, one gets a term of the order of $\approx \hbar v_{\mathrm{F}} \|\boldsymbol{k} + \boldsymbol{G}\| \approx \hbar v_{\mathrm{F}} \|\boldsymbol{G}\|$ from the momentum operator $\hat{\boldsymbol{p}}$ in the intra-layer term in Eq. (2.134b), i.e. a term growing with the norm of $\boldsymbol{G}$. The intra-layer matrix element is already *diagonal* on the basis $W_{\boldsymbol{k},\varepsilon}$. Conversely,

the inter-layer term in Eq. (2.134c) gives contributions of the order of $\max(|u_0|, |u_1|)$, which are *not diagonal* in the basis $W_{\boldsymbol{k},\varepsilon}$. Truncating the reciprocal lattice vectors to $\mathcal{S}_\varepsilon$, is thus equivalent to discart non-diagonal terms of magnitude (relative to the diagonal terms) $\lesssim \varepsilon$.

Now, by taking the expectation values of Eq. (2.134a) between the states $|\boldsymbol{k}+\boldsymbol{G}\rangle \otimes |\ell,\tau\rangle \equiv |\boldsymbol{k}+\boldsymbol{G},\ell,\tau\rangle$ with $|\boldsymbol{k}+\boldsymbol{G}\rangle \in W_{\boldsymbol{k},\varepsilon}$ and $|\ell,\tau\rangle$ being the basis of discrete degrees of freedom (layer and sublattice) which is used to express Eq. (2.134b) and Eq. (2.134c) in matrix form, one gets

$$\langle \boldsymbol{k}+\boldsymbol{G},\ell,\tau|\hat{H}^{(\ell)}|\boldsymbol{k}+\boldsymbol{G}',\ell,\tau'\rangle = \delta_{\boldsymbol{G},\boldsymbol{G}'}\hbar v_{\mathrm{F}}\left[R_\ell(\theta/2)(\boldsymbol{k}+\boldsymbol{G}-\boldsymbol{K}_\ell)\right]\cdot(\sigma_x,\sigma_y)\ , \quad (2.136a)$$

$$\begin{aligned}\langle \boldsymbol{k}+\boldsymbol{G},\ell,\tau|\hat{U}|\boldsymbol{k}+\boldsymbol{G}',\ell',\tau'\rangle =& \delta_{\boldsymbol{G},\boldsymbol{G}'}\begin{pmatrix} u_0 & u_1 \\ u_1 & u_0\end{pmatrix} + \\ & \delta_{\boldsymbol{G},\boldsymbol{G}'+\boldsymbol{G}_1}e^{-i\frac{2\pi}{3}}\begin{pmatrix} u_0 & u_1e^{i\frac{2\pi}{3}} \\ u_1e^{-i\frac{2\pi}{3}} & u_0\end{pmatrix} + \\ & \delta_{\boldsymbol{G},\boldsymbol{G}'+\boldsymbol{G}_2}e^{i\frac{2\pi}{3}}\begin{pmatrix} u_0 & u_1e^{-i\frac{2\pi}{3}} \\ u_1e^{i\frac{2\pi}{3}} & u_0\end{pmatrix}.\end{aligned} \quad (2.136b)$$

With the knowledge of the Hamiltonian matrix elements on the states $\in W_{\boldsymbol{k},\varepsilon}$, it is now possible to state the algorithm to obtain the energy bands of the continuum model of TBG.

1. Input the twist angle θ, the tunneling amplitudes u_0 and u_1, and the value ε needed to define the basis set $W_{\boldsymbol{k},\varepsilon}$.

2. Define the basis of reciprocal lattice vector $\boldsymbol{G}_1$ and $\boldsymbol{G}_2$ from Eq. (2.29).

3. Build the set $\mathcal{S}_\varepsilon$ defined in Eq. (2.135b) using the condition $\max(|u_0|, |u_1|)/(\hbar v_{\mathrm{F}}\|\boldsymbol{G}\|) > \varepsilon$.

4. Define a mapping $\iota : \mathcal{S}_\varepsilon \to \mathbb{N}$ to order the elements of $\mathcal{S}_\varepsilon$ such that $\boldsymbol{G} \in \mathcal{S}_\epsilon \mapsto \iota(\boldsymbol{G}) = i_{\boldsymbol{G}}$.

5. Initialize an empty 2D complex array `H_k` of size $4\#(\mathcal{S}_\varepsilon)\times 4\#(\mathcal{S}_\varepsilon)$. The additional factor of 4 accounts for the layer and sub-lattice degrees of freedom.

6. Populate `H_k` with the matrix elements in Eqs. (2.136), which for the layer and sublattice degrees of freedom are ordered in the following way $\{|1A\rangle, |1B\rangle, |2A\rangle, |2B\rangle\}$. `H_k` should thus be populated in the following way
   $\texttt{H\_k}[4i_{\boldsymbol{G}}{:}4(i_{\boldsymbol{G}'}+1)] = \langle \boldsymbol{k}+\boldsymbol{G},\ell,\tau|\begin{pmatrix}\hat{H}^{(1)} & \hat{U} \\ \hat{U}^\dagger & \hat{H}^{(2)}\end{pmatrix}|\boldsymbol{k}+\boldsymbol{G}',\ell',\tau'\rangle$.

7. For each $\boldsymbol{k}$, numerically diagonalize `H_k` to obtain the eigenvalues $\epsilon_{\boldsymbol{k}\nu}$ and $(c_1(\boldsymbol{k},\nu),\ldots,c_{4\#(\mathcal{S}_\varepsilon)}(\boldsymbol{k},\nu)) \in \mathbb{C}^{4\#(\mathcal{S}_\varepsilon)}$.

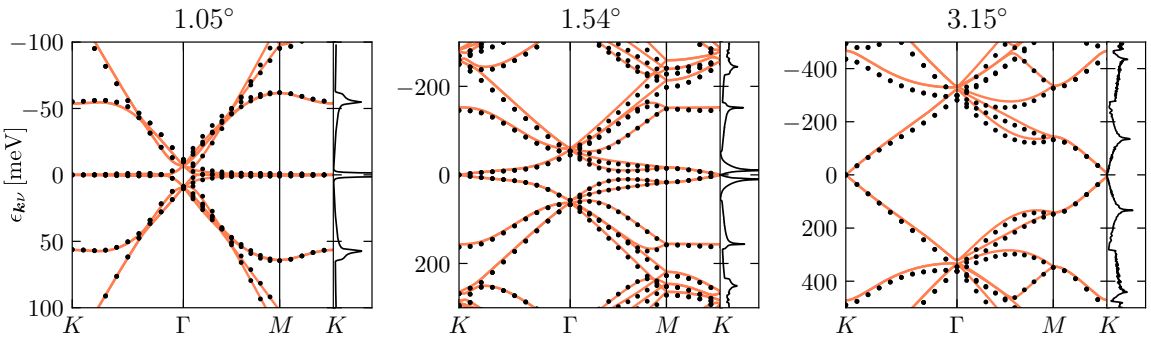

Figure 2.3: Numerical solutions of the tight-binding (black dots) and continuum model (solid red lines) of twisted bilayer graphene at different twist angles along the $K-\Gamma-M-K$ path of the moiré Brillouin zone. The density of states calculated with the eigenstates of the continuum model is showed in the immediate right of the band structure. For the continuum model it was set $u_0 = u_1 = 110\,\text{meV}$ (see Ref. [3]) corresponding, for the tight-binding model, to the inter-layer hopping parametrized as in Ref. [103].

The numerical solutions of the tight-binding and continuum models of TBG are compared in Fig. 2.3 at three different twist angles. For the three twist angles considered, the low-energy tight-binding and continuum eigenenergies are virtually the same, justifying the use of the continuum model as a low-energy expansion of the tight-binding model. As discussed in Section 2.1.2, however, the continuum model of TBG is valid only for small twist angles. At large twist angles, the tight-binding model should be preferred. Conversely, when the twist angle is small, the numerical solution of the continuum model is obtained remarkably faster than the tight-binding solution. For example, when the twist angle is $\theta = 1.05°$, the tight-binding solution requires the diagonalization of a matrix of dimension $\approx 10^4$ for each crystal wavevector $\boldsymbol{k}$, whereas the continuum model requires the diagonalization of a matrix of dimension $\lessapprox 10^3$. Recalling that the numerical diagonalization needs a number of floating point operations scaling as the third power of the dimension of the matrix, it follows that the solution of the continuum model is obtained roughly three orders of magnitude faster than the tight-binding solution.

2.4.2 Numerical solution of the Hartree equations

In this Section we discuss how to numerically obtain self-consistent Hartree orbitals of a given periodic model. As a first step it is necessary to lay down some hypothesis on the symmetry of the self-consistent orbitals. Firstly, we will assume that e-e interactions do not break the discrete translational symmetry of the original problem defined by $\hat{H}_0$. In addition, it is possible to simplify the problem even more by imposing that the point-group symmetry of $\hat{H}_0$ is not modified by the presence of e-e interactions. The latter hypothesis in practice allows to reduce the dimension of the space over which the optimization procedure inherent to the Hartree problem is carried out.

As showed in Section 2.2, a necessary (but not sufficient) condition for a set of one-particle (Bloch) orbitals to solve the variational Hartree problem, i.e. the minimization

of the energy operator over the product states, is that they satisfy Eq. (2.40), i.e.

$$\left(\hat{H}_0 + \hat{V}_{\mathrm{H}}[n_{\boldsymbol{G}}]\right)|\boldsymbol{k}\nu\rangle = \epsilon_{\boldsymbol{k}\nu}|\boldsymbol{k}\nu\rangle \ , \tag{2.137}$$

where $\hat{H}_0$ is the one-particle Hamiltonian of the model and $\hat{V}_{\mathrm{H}}$ is the Hartree potential

$$\hat{V}_{\mathrm{H}}[n_{\boldsymbol{G}}] = \sum_{\boldsymbol{G}\neq\boldsymbol{0}} \frac{2\pi e^2}{\bar{\varepsilon}\|\boldsymbol{G}\|} n_{\boldsymbol{G}} e^{i\boldsymbol{G}\cdot\hat{\boldsymbol{r}}} \ . \tag{2.138}$$

Here, $\bar{\varepsilon}$ is an appropriate dielectric constant, and the Fourier components of the particle density $n_{\boldsymbol{G}}$ at wave-vector $\boldsymbol{G}$ are

$$n_{\boldsymbol{G}} = \frac{1}{V}\sum_{\nu}\sum_{\boldsymbol{k}} \frac{1}{1+\exp[(\epsilon_{\boldsymbol{k}\nu}-\mu)/k_{\mathrm{B}}T]} \sum_{\boldsymbol{\mathcal{G}}} u^{\dagger}_{\boldsymbol{\mathcal{G}}}(\boldsymbol{k},\nu) u_{\boldsymbol{\mathcal{G}}+\boldsymbol{G}}(\boldsymbol{k},\nu) \ . \tag{2.139}$$

Equation (2.137), together with Eq. (2.139) are equivalent to ask that the product of the Bloch self-consistent orbitals $|\boldsymbol{k}\nu\rangle$ satisfying Eq. (2.137) is a stationary point of the energy functional $\langle\Psi|\hat{H}_{ee}|\Psi\rangle$ (see Section 2.2).

We now show that the problem of finding the self-consistent orbitals numerically is equivalent to find the root of a vectorial function. The variables of interest for the numerical calculations are going to be the (complex) Fourier components of the particle density $n_{\boldsymbol{G}}$. The Hartree potential Eq. (2.138) is indeed a sum of these Fourier components, weighted by the inverse 2-norm of the reciprocal lattice vector $\boldsymbol{G}$. Because of this weighting factor, the sum over the reciprocal lattice vectors in Eq. (2.138) is usually truncated only to reciprocal lattice vectors of norm smaller than a given threshold. For the sake of concreteness, let the number of terms retained in Eq. (2.138) be N, and let us collect these terms $n_{\boldsymbol{G}}$ in a vector $\boldsymbol{n} \equiv (n_{\boldsymbol{G}_1}, n_{\boldsymbol{G}_2}, \ldots, n_{\boldsymbol{G}_N}) \in \mathbb{C}^N$. Let us now define the vector function $\boldsymbol{f} : \mathbb{C}^N \to \mathbb{C}^N$ taking a vector of Fourier components for the particle density as input $\boldsymbol{n}_{\mathrm{in}} \in \mathbb{C}^N$, and outputting another vector $\boldsymbol{n}_{\mathrm{out}} \in \mathbb{C}^N$ of Fourier components for the particle density. The output $\boldsymbol{n}_{\mathrm{out}}$ is obtained by diagonalizing Eq. (2.137) with the input components $\boldsymbol{n}_{\mathrm{in}}$, and using the computed spectrum to calculate $\boldsymbol{n}_{\mathrm{out}}$ from Eq. (2.139). It is immediate to verify that the self-consistency condition is attained when $\boldsymbol{n}_{\mathrm{out}} = \boldsymbol{n}_{\mathrm{in}}$ i.e. when

$$\boldsymbol{n}_{\mathrm{out}} - \boldsymbol{n}_{\mathrm{in}} = \boldsymbol{f}(\boldsymbol{n}_{\mathrm{in}}) - \boldsymbol{n}_{\mathrm{in}} = \boldsymbol{0}, \tag{2.140}$$

which is equivalent to look for the roots of the function $\boldsymbol{n} \mapsto \boldsymbol{f}(\boldsymbol{n}) - \boldsymbol{n}$.

Numerically, the root-finding problems are usually solved by iterative algorithms of the following type

1. Start with an initial guess for the the Fourier components of the particle density $\boldsymbol{n}_0 \in \mathbb{C}^N$.

2. Compute $\boldsymbol{f}(\boldsymbol{n}_0)$.

3. From $\boldsymbol{n}_0$ and $\boldsymbol{f}(\boldsymbol{n}_0)$ update the input to $\boldsymbol{n}_1$, and compute $\boldsymbol{f}(\boldsymbol{n}_1)$.

4. Iterate until $\|\boldsymbol{f}(\boldsymbol{n}_i) - \boldsymbol{n}_i\| < \varepsilon$, where ε is the chosen tolerance and $\|\cdot\|$ is any chosen norm. Usual choices are $\|\cdot\|_2$ and $\|\cdot\|_\infty$.

The critical step of the previous algorithm is the update step, i.e. obtaining $\boldsymbol{n}_{i+1}$ from $\boldsymbol{n}_i$ and $\boldsymbol{f}(\boldsymbol{n}_i)$ in a way that the difference $\|\boldsymbol{f}(\boldsymbol{n}_i) - \boldsymbol{n}_i\|$ goes to 0 as the number of iterations grows. This can be accomplished by various strategies, some of which require the knowledge of $\boldsymbol{f}(\,\cdot\,)$ as well as its Jacobian. For the problems interesting for this Thesis, the Jacobian of $\boldsymbol{f}(\,\cdot\,)$ is not available analytically and it can only be evaluated numerically. Its evaluation, however, is computationally too expensive, as for the Jacobian there are required many evaluations of the function $\boldsymbol{f}(\,\cdot\,)$ itself, and already for a single point $\boldsymbol{n} \in \mathbb{C}^N$, the calculation of $\boldsymbol{f}(\boldsymbol{n})$ requires the diagonalization of Eq. (2.137) for a large number of $\boldsymbol{k}$ values, needed in the corresponding sum in Eq. (2.139). For this reason we will present two mixing schemes designed to minimize the number of function evaluations.

The most simple update scheme is known as "Simple mixing" and is just a weighted combination of $\boldsymbol{n}_i$ and $\boldsymbol{f}(\boldsymbol{n}_i)$

$$\boldsymbol{n}_{i+1} = \alpha \boldsymbol{n}_i + (1-\alpha)\boldsymbol{f}(\boldsymbol{n}_i) \quad \text{with } \alpha \in \mathbb{R}. \tag{2.141}$$

The drawback of this iteration scheme is that its convergence *strongly* depends on the properties of the function $\boldsymbol{f}$. For example, if the function $\boldsymbol{f}$ is Lipschitz continuous, i.e. it exists a constant constant L satisfying

$$\|\boldsymbol{f}(\boldsymbol{x}) - \boldsymbol{f}(\boldsymbol{y})\| \leq L\|\boldsymbol{x} - \boldsymbol{y}\| \quad \forall\, \boldsymbol{x}, \boldsymbol{y} \in \mathbb{C}^N, \tag{2.142}$$

it follows that

$$\begin{aligned}
\|\boldsymbol{f}(\boldsymbol{n}_{i+1}) - \boldsymbol{n}_{i+1}\| &= \|\boldsymbol{f}(\boldsymbol{n}_{i+1}) - \alpha\boldsymbol{n}_i - (1-\alpha)\boldsymbol{f}(\boldsymbol{n}_i)\| \\
&= \|\boldsymbol{f}(\boldsymbol{n}_{i+1}) - \boldsymbol{f}(\boldsymbol{n}_i) + \alpha\left(\boldsymbol{f}(\boldsymbol{n}_i) - \boldsymbol{n}_i\right)\| \\
&\leq \|\boldsymbol{f}(\boldsymbol{n}_{i+1}) - \boldsymbol{f}(\boldsymbol{n}_i)\| + \|\alpha\left(\boldsymbol{f}(\boldsymbol{n}_i) - \boldsymbol{n}_i\right)\| \\
&\leq L\,\|\boldsymbol{n}_{i+1} - \boldsymbol{n}_i\| + \alpha\,\|\boldsymbol{f}(\boldsymbol{n}_i) - \boldsymbol{n}_i\| \\
&= L\,\|\alpha\boldsymbol{n}_i + (1-\alpha)\boldsymbol{f}(\boldsymbol{n}_i) - \boldsymbol{n}_i\| + \alpha\,\|\boldsymbol{f}(\boldsymbol{n}_i) - \boldsymbol{n}_i\| \\
&= L(1-\alpha)\,\|\boldsymbol{f}(\boldsymbol{n}_i) - \boldsymbol{n}_i\| + \alpha\,\|\boldsymbol{f}(\boldsymbol{n}_i) - \boldsymbol{n}_i\| \\
&= \left[L(1-\alpha) + \alpha\right]\|\boldsymbol{f}(\boldsymbol{n}_i) - \boldsymbol{n}_i\|\,.
\end{aligned} \tag{2.143}$$

From the latter equation it easily follows that self-consistency is assured if α is chosen in the following way

$$\frac{L}{L-1} < \alpha < 1 \quad \text{if } L < 1, \tag{2.144a}$$

$$1 < \alpha < \frac{L}{L-1} \quad \text{if } L > 1. \tag{2.144b}$$

In real scenarios, however, the regularity properties of $\boldsymbol{f}$ are often not known a priori, and the convergence of the simple mixing algorithm may be hard to reach if not impossible at all.

An alternative to the simple mixing scheme described above is the "Broyden mixing" scheme [110, 111], treating the density update as an appoximate inversion procedure. The goal, in the Broyden scheme, is to minimize the residual

$$\boldsymbol{r}(\boldsymbol{n}) \equiv \boldsymbol{f}(\boldsymbol{n}) - \boldsymbol{n}. \tag{2.145}$$

The exact minimization of $\boldsymbol{r}$ is, of course, not possible as this would amount to the solution of the original problem. However, an alternative and approximate solution may be devised if an initial point sufficiently close to the true solution is feeded to the algorithm. The Broyden algorithm is a generalization of the one-dimensional Newton's method, replacing the derivative with the Jacobian of the residual $= \frac{\partial r_i(\boldsymbol{n})}{\partial n_j}$ for $i, j = 1, \ldots, N$. The Jacobian is going to be obtained only in an approximate form, to reduce the number of function evaluations. The Broyden mixing scheme reads

$$\boldsymbol{n}_{i+1} = \boldsymbol{n}_i - J_i^{-1}\boldsymbol{r}(\boldsymbol{n}_i), \tag{2.146}$$

where J_i^{-1} is the approximate Jacobian inverse at the i-th iteration, and is defined as

$$J_i^{-1} = J_{i-1}^{-1} + \frac{\Delta\boldsymbol{n}_i - J_{i-1}^{-1}\Delta\boldsymbol{r}_i}{\Delta\boldsymbol{n}_i^T J_{i-1}^{-1}\Delta\boldsymbol{r}_i}\Delta\boldsymbol{n}_i^T J_{i-1}^{-1}, \tag{2.147}$$

where the following definitions were made

$$\Delta\boldsymbol{r}_i = \boldsymbol{r}(\boldsymbol{n}_i) - \boldsymbol{r}(\boldsymbol{n}_{i-1}), \tag{2.148a}$$

$$\Delta\boldsymbol{n}_i = \boldsymbol{n}_i - \boldsymbol{n}_{i-1}. \tag{2.148b}$$

The approximate inverse Jacobian in Eq. (2.147) is obtained by taking the current estimate of the Jacobian matrix J_{i-1} and improving it obtaining the *unique* J_i which solve the "secant condition"

$$J_i\Delta\boldsymbol{n}_i \approx \Delta\boldsymbol{r}_i, \tag{2.149}$$

and which is closest to J_{i-1} in Frobenius norm. The secant condition is just a finite-difference expansion of $\boldsymbol{r}(\boldsymbol{n})$, used to obtain an approximation of the Jacobian. Since the correction $J_i - J_{i-1}$ turns out to be a rank-one matrix, knowing J_{i-1}^{-1} it is possible to obtain J_i^{-1} thanks to the Sherman-Morrison formula [110]. Usually, the Broyden iterative method is initialized with $J_0 \propto \mathbb{1}_{N\times N}$.

It is worth to mention that with the recent wide spread interest in machine learning, a tremendous amount of efforts are now directed to devise cheap and efficient optimization algorithms. As we have argued above, finding the self-consistent solution of the Hartree problem is equivalent to minimize the norm of the residual

$$\boldsymbol{r}(\boldsymbol{n}) \equiv \boldsymbol{f}(\boldsymbol{n}) - \boldsymbol{n}. \tag{2.150}$$

The new optimization algorithms forged by the machine learning community may therefore be leveraged to solve the Hartree self-consistency equations Eq. (2.137). For example, an interesting optimization scheme suited for large parameter spaces is Bayesian

optimization [112, 113]. The idea of Bayesian optimization is showed in Fig. 2.4 and can be described as follows. Consider an unknown, multidimensional function such as $\boldsymbol{r}(\boldsymbol{n})$. The relationship between $\boldsymbol{n}$ and $\boldsymbol{r}(\,\cdot\,)$ does not need to be analytic. The goal of Bayesian optimization is to find the global extremum of $\|\boldsymbol{r}(\boldsymbol{n})\|$ with as few evaluations of $\boldsymbol{r}(\boldsymbol{n})$ as possible and without computing the gradient of $\boldsymbol{r}(\boldsymbol{n})$. Bayesian optimization begins with a few random evaluations of $\boldsymbol{r}(\boldsymbol{n})$ at a few random points of the N-dimensional space. The results of the evaluation are used to obtain an approximate model of $\boldsymbol{r}(\boldsymbol{n})$ and a Bayesian uncertainty of this model. This model is then used to inform the subsequent evaluation of $\boldsymbol{r}(\boldsymbol{n})$ with the aim of minimizing $\|\boldsymbol{r}(\boldsymbol{n})\|$. The benefits of Bayesian optimization are twofold: firstly, the function to be optimized does not need to have any special regularity properties. Second, the results of Bayesian optimization are naturally endowed with a measure of their uncertainty, which is useful to estimate the intrinsic error given by the numerical procedures.

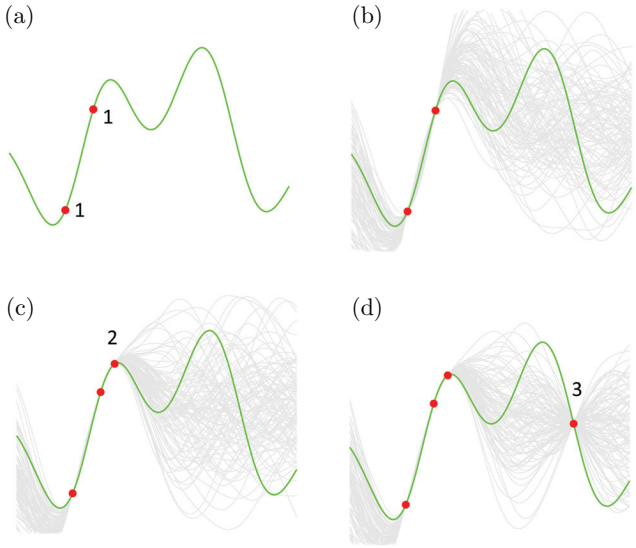

Figure 2.4: Panel (a), Bayesian optimization of a function (shown by solid green curve) by the iterative evaluation of the function. Panel (b), a new model of the function (grey curves) is constructed at each iteration and the subsequent evaluation of the function (Panels (c) and (d)) is informed by the mean and the uncertainty of the most recent model. The symbols depict the results of the function evaluation and the numbers label the iteration order. Each function evaluation reduces the uncertainty of the model in some part of the variable space, which forces the algorithm to evaluate the function elsewhere. This ensures that the optimization algorithm does not get trapped in local extrema. Figure adapted from Ref. [113].

Hartree self-consistency in twisted bilayer graphene

For our calculations of the self-consistent Hartree orbitals of TBG — which we now review — the Simple mixing iterative procedure did not converge to any solution, and we therefore used the Broyden iterations[110, 111]. The one-particle model $\hat{H}_0$

appearing in Eq. (2.137), used for TBG is the Continuum model Eq. (2.134a) diagonalized as explained in Section 2.4.1. For the diagonalization of the continuum model, a basis of 271 plane waves lying in the first 10 hexagonal shells spanned by the moiré reciprocal lattice vectors was used. The total number of states in the basis was thus $271 \times 4 = 1084$, where the factor of 4 is coming from sublattice and layer indexes. We have computed the full spectrum but retained only half of it, i.e. ≈ 500 energy bands around the charge neutrality point because, as a rule of thumb, a plane-wave expansion gives a good approximation only for half of the computed spectrum around the charge neutrality point [17].

The self-consistent Hartree orbitals have been obtained setting absolute tolerance $\|\boldsymbol{f}(\boldsymbol{n})-\boldsymbol{n}\|_\infty < \varepsilon_a = 10^{-8}$ and a relative tolerance of $\|\boldsymbol{f}(\boldsymbol{n})-\boldsymbol{n}\|_\infty / \min(\|\boldsymbol{f}(\boldsymbol{n})\|_2, \|\boldsymbol{n}\|_2) < \varepsilon_r = 10^{-5}$. The integrals over the moiré Brillouin zone were performed over a mesh of $60 \times 60 = 3600$ equally spaced points.

The space of parameters over which the Broyden iterations are carried on can be reduced with the following observations. From the definition of the Fourier components of the density, Eq. (2.139) it holds

$$\begin{aligned} n_{-\boldsymbol{G}} &= \frac{1}{V}\sum_\nu \sum_{\boldsymbol{k}} \frac{1}{1+\exp[(\epsilon_{\boldsymbol{k}\nu}-\mu)/k_\mathrm{B}T]} \sum_{\boldsymbol{\mathcal{G}}} u^\dagger_{\boldsymbol{\mathcal{G}}}(\boldsymbol{k},\nu) u_{\boldsymbol{\mathcal{G}}-\boldsymbol{G}}(\boldsymbol{k},\nu) \\ &= \frac{1}{V}\sum_\nu \sum_{\boldsymbol{k}} \frac{1}{1+\exp[(\epsilon_{\boldsymbol{k}\nu}-\mu)/k_\mathrm{B}T]} \sum_{\boldsymbol{\mathcal{G}}} u^\dagger_{\boldsymbol{\mathcal{G}}+\boldsymbol{G}}(\boldsymbol{k},\nu) u_{\boldsymbol{\mathcal{G}}}(\boldsymbol{k},\nu) \\ &= n^*_{\boldsymbol{G}}, \end{aligned} \tag{2.151}$$

i.e. the density at $-\boldsymbol{G}$ is just the complex-conjugate of the density at $\boldsymbol{G}$. Furthermore, enforcing the point-group symmetry of the non-interacting model for the Hartree orbitals as well, i.e. the D_3 point group for TBG[104], it holds that:

$$u^\dagger_{\boldsymbol{G}} u_{\boldsymbol{G}'} = u^\dagger_{R(\pm 2\pi/3)\boldsymbol{G}} u_{R(\pm 2\pi/3)\boldsymbol{G}'}, \tag{2.152}$$

where $R(\theta)$ is the rotation matrix of angle θ. This follows from the fact that when a symmetry is present, the Hamiltonian commutes with the element of the symmetry group. Inserting the previous relation into Eq. (2.139) it readily follows that

$$n_{R(\pm 2\pi/3)\boldsymbol{G}} = n_{\boldsymbol{G}}. \tag{2.153}$$

When the sum over the reciprocal vectors in Eq. (2.139) is performed over *the first hexagonal shell spanned by the moiré reciprocal lattice vectors*, these vectors can be written as $\pm\boldsymbol{G}$, $\pm R(2\pi/3)\boldsymbol{G}$ and $\pm R(-2\pi/3)\boldsymbol{G}$, with $\boldsymbol{G}$ being one of the two vectors in the basis of reciprocal vectors of TBG. Using the relations derived previously, it is easy to see that one ought compute only $n_{\boldsymbol{G}}$, while the others (i.e. the density at vectors $-\boldsymbol{G}$, $\pm R(2\pi/3)\boldsymbol{G}$ and $\pm R(-2\pi/3)\boldsymbol{G}$) are just equal to $n_{\boldsymbol{G}}$ or its complex-conjugate.

These observations entail that if the point-group symmetry of the self-consistent states is actually D_3, and using the symmetry relations just discussed, the space where the self-consistency algorithm is run is only two-dimensional, and the degrees of freedom can be parametrized by $\mathrm{Re}[n_{\boldsymbol{G}}]$ and $\mathrm{Im}[n_{\boldsymbol{G}}]$.

3

Optical and plasmonic properties of twisted bilayer graphene

The unique features of the low-energy spectrum of TBG also manifest in its optical properties, as showed experimentally e.g. in Refs. [43, 114]. As discussed in Section 1.2.2, Ref. [43] unveiled the crucial role of the inter-layer tunneling amplitude in the determination of the optical and plasmonic properties of TBG. Comparing theoretical results with experimental data [43], it was suggested that u_0 can be much smaller than u_1 in significant areas of real samples. u_0 and u_1 are the two energy scales entering the continuum model of TBG and defined in Eq. (2.27). For the sake of clarity, we remind the reader that in the literature the cases $u_0 = u_1$ or $u_0 \lesssim u_1$ are often studied. In the seminal work by Bistrizer and MacDonald (Ref. [3]), the authors took $u_0 = u_1 = 110$ meV, while the authors of Ref. [104] took $u_0 = 79.7$ meV and $u_1 = 97.5$ meV. Extensive density functional theory simulations including lattice relaxation [106, 115] suggest $u_0 = 78$ meV and $u_1 = 98$ meV for a range of twist angles $1.08° \leq \theta \leq 3.89°$. Finally, the authors of Ref. [78] considered a greatly simplified continuum model for TBG, which has $u_0 = 0$. In this so-called "chirally-symmetric" continuum model, the low-energy bands near the CNP are rigorously flat (i.e. they have zero bandwidth) at the magic angle. As we show below, the values of u_0 and u_1 strongly influence the optical properties of TBG. Optical experiments are therefore a very useful tool to measure these parameters.

In this Chapter we present a thorough investigation of two main physical quantities introduced in the previous Chapter, namely the *local* optical conductivity $\sigma(\omega)$ and energy loss function $\mathcal{L}(\boldsymbol{q}, \omega)$ of TBG for different filling factors and twist angles. These investigations are complemented by the results, presented on the last Section of this Chapter, about the static density-density response function of TBG. With reference to the mean-field theory of linear response (see, for example, Sect. 4.7 of Ref. [30]), we perform our calculations at the level of the RPA, discussed in Section 2.3. This requires

to calculate eigenstates and eigenenergies according to the self-consistent Hartree mean-field theory presented in Section 2.2 and then feed these results to the Kubo formula in Eq. (2.92).

The optical conductivity is a *proper* linear response function relating the electrical current to the *total* electric field (i.e. the sum of the external electric field and the average electric field generated by the electron themselves) applied to an electron system. It encodes the response of the electron system to a spatially-uniform oscillating field and is therefore of primary importance to interpret far-field optical experiments. When e-e interactions are neglected, once the single-particle eigenstates and eigenenergies of the system are known, it can be calculated as a sum over allowed transitions according to Kubo formula [30], as showed in Section 2.3.2. Interactions modify this result in essentially two ways. First, they modify the set of eigenstates that one should use. Indeed, one should add to the non-interacting Hamiltonian a potential that takes into account the impact on one electron of the presence of all the other electrons. Second, they add new contributions to the response function stemming from *dynamical* exchange and correlation effects. In the framework of many-body diagrammatic perturbation theory [30], these can be viewed as arising from *irreducible* diagrams containing at least one interaction line. (Since $\sigma(\omega)$ is a proper response function reducible diagrams do not contribute to the perturbative series.)

The energy loss function $\mathcal{L}(\boldsymbol{q},\omega)$ measures the amount of energy that the system is able to absorb from an external scalar perturbation with wave vector $\boldsymbol{q}$ and angular frequency ω. It is particularly useful to identify collective modes that couple to the charge density, since these appear as well defined peaks in the energy loss function. As explained in Section 2.3.3, its calculation requires, in principle, the knowledge of the *non-local* conductivity $\sigma_{\alpha\beta}^{\boldsymbol{GG'}}(\boldsymbol{q},\omega)$. Here we resort to the local approximation that is appropriate for wavelengths much larger than the moiré periodicity and only requires the knowledge of the *local* conductivity $\sigma_{\alpha\beta}(\omega) \equiv \lim_{\boldsymbol{q}\to\boldsymbol{0}} \sigma_{\alpha\beta}^{\boldsymbol{00}}(\boldsymbol{q},\omega)$ (see Section 2.3.2).

As a natural byproduct of the calculation of the intra-band contribution to $\sigma(\omega)$, we obtain an approximate expression for the Seebeck coefficient (or thermopower) S. The latter measures the coupling between electrical and thermal phenomena in TBG. Our approximation captures the band structure contribution to S, while neglecting the largely unknown energy dependence of the scattering mechanisms in TBG.

We will focus on the impact of *two* key physical effects on $\sigma(\omega)$ and $\mathcal{L}(\boldsymbol{q},\omega)$ for TBG with varying filling factor:

i) As discussed above, recent experiments have highlighted the fact that u_0 needs not to be equal or comparable to u_1. In this Chapter, we fix u_1, and study the role of u_0 in the range $0 \leq u_0 \leq u_1$;

ii) It has been emphasized [121, 122] that *intrinsic* (i.e. not due to e.g. Coulomb impurities) spatial inhomogeneities are important in magic-angle TBG. In other words, due to the moiré periodicity, the ground-state electron density $n(\boldsymbol{r})$ is not homogeneous in space. Technically speaking, therefore, the results of the single-particle band models introduced e.g. in Refs. [3, 104] need to be iterated self-consistently in the Hartree approximation [30] to see how they are altered by e-e interactions, as functions of the filling factor. Here, we therefore compute

the corresponding "Hartree conductivity" by using the self-consistently calculated bands and eigenstates for a range of filling factors and different twist angles. As discussed in Section 2.3.2, this is equivalent to include electron-electron interactions at the level of the RPA theory. These calculations take into account the role of static screening in reshaping the bare bands and rearranging in space the single-particle Bloch eigenstates of electrons moving in TBG.

Moreover, starting from the magic angle, we will study the role of the twist angle θ in the window $\theta^\star \lesssim \theta \lesssim 2^\circ$, where the physics of TBG is dominated by the moiré modulations of the inter-layer tunneling amplitudes. This regime (and not only the regime $\theta \approx \theta^\star$) is interesting in its own right [123] since it displays a markedly different behavior with respect to standard single-layer graphene.

We will show that, at zero filling, the optical conductivity and loss function are strongly dependent on θ and u_0, while they are insensitive to Hartree self-consistency. Conversely, away from zero filling, the Hartree potential gives strong corrections to both optical conductivity and loss function, especially in the low-frequency domain.

The optical and plasmonic properties of TBG have been investigated also in a number of previous pioneering works [77, 123, 124, 125, 126, 127]. The local optical conductivity has been previously calculated by the authors of Refs. [123, 124, 125] for twist angles $\theta \gtrsim 1.5^\circ$. These calculations have been carried out by means of the non-interacting continuum model introduced in Ref. [3]. (The optical response of TBG beyond the linear-response approximation has been recently calculated in Ref. [126] for large twist angles.) The loss function of TBG has been calculated in Refs. [77, 125, 127], for angles near the magic one, and by means of the non-interacting band models introduced in Refs. [3, 104]. These works did not take into account neither Hartree self-consistency nor the inter-layer tunnelling asymmetry $u_0 \neq u_1$.

Throughout the Chapter we will set the inter-sublattice hopping energy to $u_1 = 97.5$ meV. Most of our calculations below have been carried out at a twist angle $\theta = 1.05^\circ$, which is close to the magic angle [78, 104, 121]. Furthermore, we work at temperatures $T > T_c$, where T_c is the maximum critical temperature at which any of the aforementioned exotic phases occurs [5, 6, 65, 66, 67, 68, 69, 70, 71, 72, 73, 75], and we set $\bar{\varepsilon}(0) = 4.9$.

Dependencies on the twist angle are presented in Section 3.3 below. We have also relied on symmetry simplifications. Indeed, for 2D systems, the optical conductivity is in general a 2×2 matrix with respect to the Cartesian indices α, β, as showed in Eq. (2.94). Since the continuum Hamiltonian of TBG, in Eq. (2.30), has a D_3 point group [104], which we assume to be unbroken also when e-e interactions are taken into account in the Hartree approximation, it follows that $\sigma_{\alpha\beta}(\omega) = \sigma(\omega)\delta_{\alpha\beta}$, where $\sigma(\omega) \equiv \sigma_{xx}(\omega) = \sigma_{yy}(\omega)$ and $\delta_{\alpha\beta}$ is the Kronecker symbol. The same holds for all the other relevant properties, i.e. the intra-band optical conductivity Eq. (2.95) $\sigma^{\rm intra}_{\alpha\beta}(\omega) = \sigma^{\rm intra}(\omega)\delta_{\alpha\beta}$, the inter-band optical conductivity Eq. (2.98) $\sigma^{\rm inter}_{\alpha\beta}(\omega) = \sigma^{\rm inter}(\omega)\delta_{\alpha\beta}$, the spectral weight Eq. (2.96) $\mathcal{W}^{(p)}_{\alpha\beta} = \mathcal{W}^{(p)}\delta_{\alpha\beta}$ and the Drude weight Eq. (2.97) $\mathcal{D}_{\alpha\beta} = \mathcal{D}\delta_{\alpha\beta}$.

Finally, we stess that whenever the single-particle optical conductivities and loss functions presented in the following Sections are calculated with the self-consistent

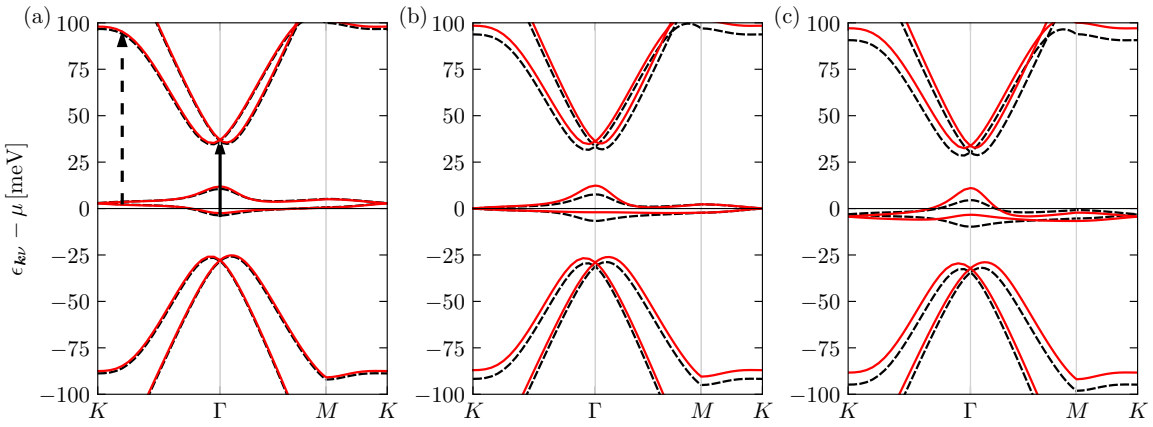

FIGURE 3.1: TBG energy bands for different filling factors are plotted along the K-Γ-M-K path in the moiré Brillouin zone (see Fig. 2.2). Data in this figure refer to $\theta = 1.05°$, $u_0 = 79.7$ meV, $u_1 = 97.5$ meV, $T = 5$ K, and $\bar{\varepsilon}(0) = 4.9$. Solid red and dashed black lines are the energy bands calculated by including e-e interactions in the Hartree self-consistent approach discussed in Section 2.2 and with the single-particle Hamiltonian (2.30), respectively. Different panels refer to different values of the filling factor ξ. Panel (a) Hole doping: $\xi = -3/4$. The vertical arrows mark the optical transitions responsible for the peaks in the optical conductivity, as discussed in Sections 3.1, 3.2 and 3.3. Panel (b) CNP: $\xi = 0$. Panel (c) Electron doping: $\xi = +3/4$.

Hartree orbitals of TBG, the electron-electron interactions are automatically included at the level of the RPA, as discussed in Section 2.3.

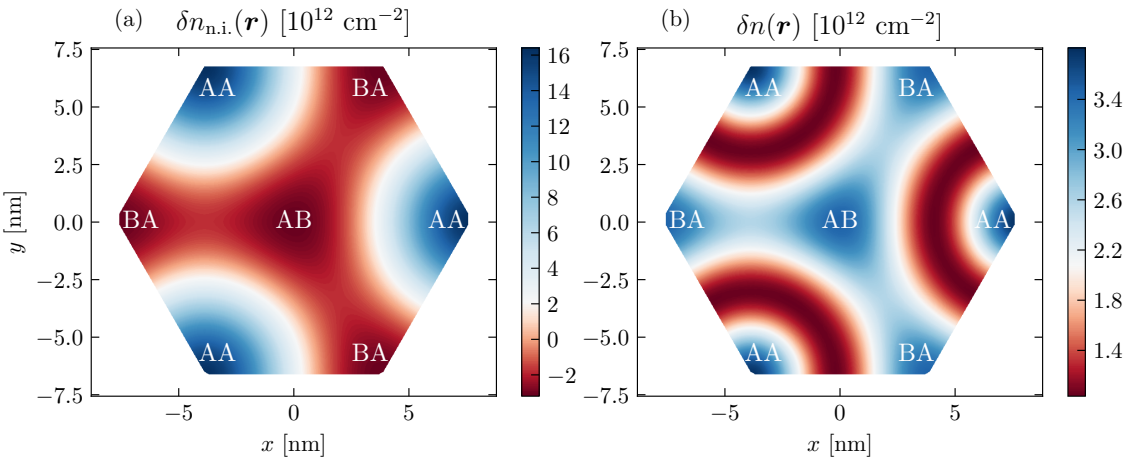

FIGURE 3.2: Deviations $\delta n(\boldsymbol{r})$ of the ground-state density $n(\boldsymbol{r})$ from the density n_0 at the CNP. The quantity in Eq. (3.5) is plotted for filling factor $\xi = +3/4$. Data in this figure refer to $\theta = 1.05°$, $u_0 = 79.7$ meV, $u_1 = 97.5$ meV, $T = 5$ K, and $\bar{\varepsilon}(0) = 4.9$. Panel (a) Results for non-interacting electrons. Panel (b) Results calculated by taking into account the Hartree potential (2.47). In both panels the density value corresponding to the white color is set to $\delta n_{\text{n.i.}} = \delta n \simeq 2.07 \times 10^{12}$ cm^{-2}, corresponding to the average value of the density throughout the primitive cell. We have annotated the regions of the unit cell where local AB, AA, and BA stacking occurs between the two layers.

3.1 Dependence on the filling factor

We now discuss dependencies of the various quantities introduced in Section 2.3.2 on the filling factor. Here, we set the intra-sublattice hopping energy at the value [104] $u_0 = 79.7$ meV.

In Fig. 3.1 we plot the moiré bands of TBG for three values of the filling factor. In the absence of the Hartree potential, the band structure (black dashed lines) is independent of the filling and is composed of flat bands close to zero energy and higher energy dispersive bands with positive (conduction bands) and negative (valence bands) energy, in agreement with the results of Ref. [104]. At zero temperature and zero filling ($\mu = 0$), the valence flat band and lower-energy valence bands are fully occupied. The conduction flat band and higher-energy bands, on the other hand, are completely empty.

When the Hartree potential is taken into account, all the energy bands (solid red lines in Fig. 3.1) exhibit a filling-factor-dependent distortion with respect to the bare bands. In the corners of the moiré Brillouin zone, i.e. in the vicinity of the K points, the distortion due to the Hartree potential is negligible and virtually filling independent, whereas it becomes prominent in the neighbourhood of the moiré Brillouin zone's center, i.e. the Γ point. When $\xi = -3/4$ [see Fig. 3.1(a)], the bands' distortion is moderate throughout the moiré Brillouin zone (this is valid also for higher and lower energy bands). At zero filling ($\xi = 0$) [see Fig. 3.1(b)] and for $\xi = +3/4$ [see Fig. 3.1(c)], however, the flat bands display a substantial upward bending, up a value larger than

~ 5 meV at the Γ point (see Fig. 3.1(c)). We point out that such distortion is of the same order of the flat-band bandwidth. The strong impact of Hartree corrections on the flat bands of TBG was already highlighted in Ref. [121]. Higher and lower energy bands are also affected by the Hartree potential by a virtually rigid upward energy shift, with little shape distortion.

At a given temperature T, the chemical potential can be found by the usual equation ensuring particle-number conservation:

$$\delta n + n_0 = g \sum_{\nu} \int_{\mathrm{MBZ}} \frac{d^2\boldsymbol{k}}{(2\pi)^2} f_{\boldsymbol{k}\nu} \ . \tag{3.1}$$

Here, "MBZ" stands for moiré Brillouin zone, the electron (hole) density $\delta n > 0$ ($\delta n < 0$) is simply the electron density measured from the CNP, i.e. $\delta n = 0$ at CNP, and the quantity n_0 is the total electron density at CNP. The latter can be conveniently expressed in units of the following "elementary density", corresponding to the contribution to the total density coming from a fully occupied energy band:

$$n_{\mathrm{b}} = \frac{g}{\Omega_{\mathrm{u.c.}}} \ , \tag{3.2}$$

where

$$\Omega_{\mathrm{u.c.}} = \frac{\sqrt{3}}{2} \left[\frac{a}{2\sin(\theta/2)} \right]^2 \tag{3.3}$$

is the area of the moiré unit cell. The low-energy continuum model predicts the existence of an infinite number of moiré mini-bands above and below the CNP. If we retain a number N_{bands} of energy bands above the CNP and N_{bands} energy bands below the CNP, the density at the CNP is $n_0 = N_{\mathrm{bands}} n_{\mathrm{b}}$. The "filling factor" is therefore given by the dimensionless ratio:

$$\xi \equiv \frac{\delta n}{n_{\mathrm{b}}} \ . \tag{3.4}$$

At zero filling, $\delta n = 0$ and $\mu \approx 0$ (μ is not exactly zero at zero filling because particle-hole symmetry is not exact). In particular, the chemical potential is within the flat bands when $|\xi| < 1$ and temperature is small. In Fig. 3.2 we show how the real space density $n(\boldsymbol{r})$ deviates from the density n_0 at the CNP, i.e. we plot the quantity

$$\delta n(\boldsymbol{r}) \equiv n(\boldsymbol{r}) - n_0 \ , \tag{3.5}$$

where n_0 was defined in Eq. (3.1) and

$$n(\boldsymbol{r}) \equiv \sum_{\boldsymbol{G}} n_{\boldsymbol{G}} e^{i\boldsymbol{G}\cdot\boldsymbol{r}} \ . \tag{3.6}$$

The sum over $\boldsymbol{G}$ in the Eq. (3.6) runs over the vectors in the first hexagonal shell spanned by the primitive vectors in Eq. (2.29), whereas $n_{\boldsymbol{G}}$ was defined in Eq. (2.46). For a full derivation of Eq. (3.6) we refer the reader to Section 2.2. Numerical results in Fig. 3.2 refer to $\xi = +3/4$.

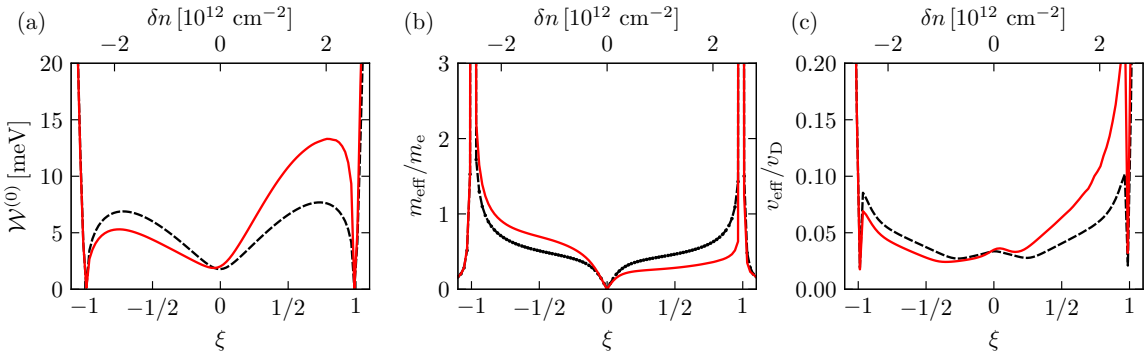

FIGURE 3.3: Drude weight and related physical quantities as functions of the carrier density δn (upper horizontal axis) and filling factor ξ (lower horizontal axis), for $\theta = 1.05°$, $u_0 = 79.7$ meV, $u_1 = 97.5$ meV, $T = 5$ K, and $\bar{\varepsilon}(0) = 4.9$. Data represented by solid red (dashed black) lines have been calculated with the eigenvalues and eigenvectors of the self-consistent Hartree (bare) Hamiltonian Eq. (2.40) (Eq. (2.30)). Panel (a) The quantity $\mathcal{W}^{(0)}$, i.e. the Drude weight $\mathcal{D}$ in units of $e^2/\hbar^2$. Panel (b) Ratio between the effective mass m_{eff} defined in Eq. (3.9) and the electron mass in vacuum m_{e}. (c) Ratio between the effective velocity v_{eff} defined in Eq. (3.10) and the Fermi velocity in monolayer graphene v_{D}.

In panel (a) of Fig. 3.2 we plot the non-interacting density profile $\delta n_{\mathrm{n.i.}}(\boldsymbol{r})$, which is calculated by neglecting the Hartree potential. It displays spatial fluctuations across the primitive cell on the order of $\lesssim 20 \times 10^{12}$ cm^{-2}. On the other hand, when the Hartree potential (i.e. screening) is taken into account as in panel (b), the amplitude of density oscillations is significantly reduced to $\lesssim 3 \times 10^{12}$ cm^{-2}. In the two panels we have set the center of the diverging color map (i.e. the value corresponding to the white color) to $\delta n_{\mathrm{n.i.}} = \delta n \simeq 2.07 \times 10^{12}$ cm^{-2}, corresponding to the average value of the density throughout the primitive cell. Indeed, a simple integration of Eq. (3.5) over the unit cell of TBG yields

$$\frac{1}{\Omega_{\mathrm{u.c.}}} \int_{\mathrm{u.c.}} d\boldsymbol{r}\ \delta n(\boldsymbol{r}) = \delta n = \xi n_{\mathrm{b}}, \tag{3.7}$$

where δn was defined in Eq. (3.1) and the last equality follows from Eq. (3.4).

The effect of the Hartree potential on the optical conductivity originates from the distortion of both energy bands and wavefunction amplitudes, through the matrix elements of the velocity operator (i.e. $v_{\alpha,\nu\nu'} = \hbar^{-1}\langle u_{\boldsymbol{k}\nu}|\partial_{k_\alpha}\hat{H}(\boldsymbol{k})|u_{\boldsymbol{k}\nu'}\rangle$) in Eqs. (2.96) and (2.98). Figure 3.3(a) shows the dependence of $\mathcal{W}^{(0)}$—the Drude weight in units of $e^2/\hbar^2$—on the filling factor, with (solid red lines) and without (dashed black lines) Hartree self-consistency. If the chemical potential is within the flat bands, i.e. if $|\xi| < 1$, the value of $\mathcal{W}^{(0)}$ is strongly modified by the Hartree potential. $\mathcal{W}^{(0)}$ is nearly particle-hole symmetric when the Hartree corrections are neglected, but becomes strongly asymmetric when Hartree corrections are accounted for. In particular,

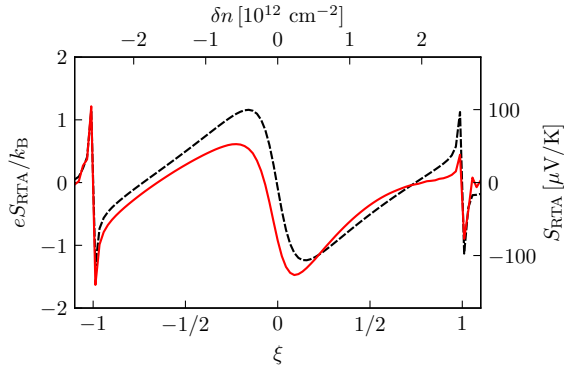

FIGURE 3.4: Same as in Fig. 3.3—$\theta = 1.05°$, $u_0 = 79.7$ meV, $u_1 = 97.5$ meV, $T = 5$ K, and $\bar{\varepsilon}(0) = 4.9$—but for the Seebeck coefficient S_{RTA} defined in Eq. (2.101). We performed the same calculations by using the less general Mott formula and found qualitative agreement with the results in this plot.

$\mathcal{W}^{(0)}$ reaches its local maxima at filling factors $\xi \simeq \pm 0.7$, with a value of ~ 7 meV, in the absence of Hartree corrections. When the Hartree potential is accounted for, the maximum for electron doping (at $\xi \simeq +0.7$) is $\mathcal{W}^{(0)} \simeq 13$ meV, and for hole doping (at $\xi \simeq -0.7$) is $\mathcal{W}^{(0)} \simeq 5$ meV. Close to the CNP, $\mathcal{W}^{(0)} \simeq 2$ meV both if the Hartree corrections are accounted for or neglected. Note that $\mathcal{W}^{(0)}$ is finite at the CNP because of finite-T effects. As we shall see later, close to charge neutrality, the Hartree potential only yields modest corrections to the optical properties of TBG.

To give a better physical picture of our results, and to help the comparison with other electronic systems, we can express the Drude weight in the following alternative forms

$$\mathcal{D} \equiv \frac{\pi e^2 |\delta n|}{m_{\mathrm{eff}}} \equiv \frac{\pi e^2 v_{\mathrm{eff}}^2 N(\mu)}{2} \ , \tag{3.8}$$

where m_{eff} and v_{eff} are an effective mass and velocity, respectively, and $N(\mu)$ is the density of states per unit area, evaluated at the chemical potential. Comparing Eq. (3.8) with the formulas in Section 2.3.2 we get

$$m_{\mathrm{eff}} = \frac{\pi \hbar^2 |\delta n|}{\mathcal{W}^{(0)}} \tag{3.9}$$

and

$$v_{\mathrm{eff}} = \sqrt{\frac{2\mathcal{W}^{(0)}}{\pi \hbar^2 N(\mu)}} \ . \tag{3.10}$$

In Fig. 3.3 we show plots of these quantities as functions of carrier density. As expected, we clearly see that $v_{\mathrm{eff}} \ll v_{\mathrm{D}}$ in a wide range of carrier densities.

Figure 3.4 shows the Seebeck coefficient calculated in the RTA from Eq. (2.101), as a function of the filling factor. Results obtained from the self-consistent Hartree theory (red curve) are compared with non-interacting results (black dashed curve). The thermoelectric effect, quantified by the Seebeck coefficient, is one of the main photocurrent generation mechanism in monolayer graphene at room temperature [128], and played an

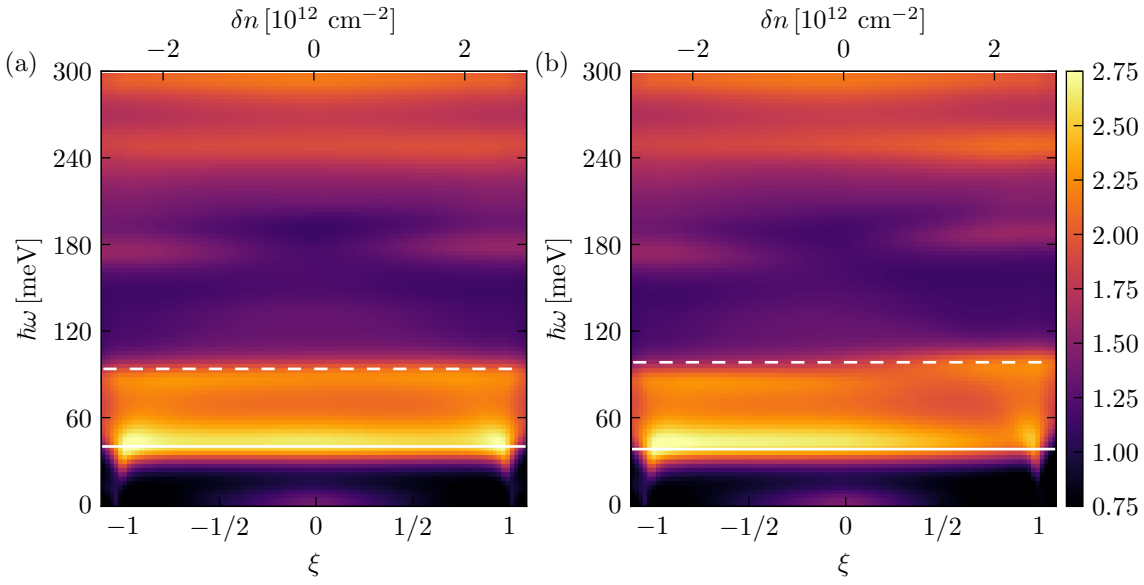

FIGURE 3.5: The inter-band contribution $\mathrm{Re}[\sigma^{\mathrm{inter}}(\omega)]$ (in units of G_0) to the real part of the optical conductivity, which is related to optical absorption, is plotted as a function of the photon energy $\hbar\omega$ and carrier density δn (or, equivalently, filling factor ξ). Data in this plot refer to $\theta = 1.05°$, $u_0 = 79.7$ meV, $u_1 = 97.5$ meV, $T = 5$ K, and $\bar{\varepsilon}(0) = 4.9$. Solid and dashed white lines are placed at energies equal to the gap between the valence flat band and the first non-flat conduction band at the points Γ and K in the moiré Brillouin zone, respectively. These energies are associated to the optical transitions marked in panel (a) of Fig. 3.1. Panel (a) $\mathrm{Re}[\sigma^{\mathrm{inter}}(\omega)]$ as calculated from Eq. (2.98) with $\hat{H}(\boldsymbol{k})$ taken as the non-interacting Hamiltonian (2.30). Panel (b) $\mathrm{Re}[\sigma^{\mathrm{inter}}(\omega)]$ as calculated by taking into account the self-consistent Hartree potential, i.e. by using Eq. (2.98) with $\hat{H}(\boldsymbol{k})$ as in Eq. (2.40).

important role in both the study of fundamental phenomena in graphene[129] and the realization of graphene-based photodetectors [128, 130]. Our calculations (see Fig. 3.4) demonstrate that, due to the much slower carrier velocity, TBG maintains a significant thermoelectric effect even at cryogenic temperatures $\approx$ 5K, making low-temperature photocurrent spectroscopy a useful technique to study TBG close to the transition to correlated states.

In Fig. 3.5 we display the real part of the inter-band optical conductivity as calculated from Eq. (2.98). The imaginary part can be straightforwardly obtained from the Kramers-Kronig relation [30].

The quantity $\mathrm{Re}[\sigma^{\mathrm{inter}}(\omega)]$ is related to the inter-band optical absorption at an incident photon energy $\hbar\omega$. If the matrix elements $v_{\alpha,\nu\nu'}$ are non-zero for symmetry reasons, peaks are expected in $\mathrm{Re}[\sigma^{\mathrm{inter}}(\omega)]$ when the photon energy matches a vertical inter-band transition, i.e. when $\epsilon_{\boldsymbol{k}\nu} - \epsilon_{\boldsymbol{k}\nu'} + \hbar\omega \approx 0$ in Eq. (2.98). Multiple distinct peaks of $\mathrm{Re}[\sigma^{\mathrm{inter}}(\omega)]$ are visible in Fig. 3.5, two of which are highlighted explicitly. At the very bottom of the two panels, for $\hbar\omega \lesssim 10$ meV, the lighter spot close to the CNP stems from a weak inter-flat-band contribution to the optical conductivity. Increasing ω, $\mathrm{Re}[\sigma^{\mathrm{inter}}(\omega)]$ decreases until $\hbar\omega \simeq 40$ meV, where it reaches its absolute

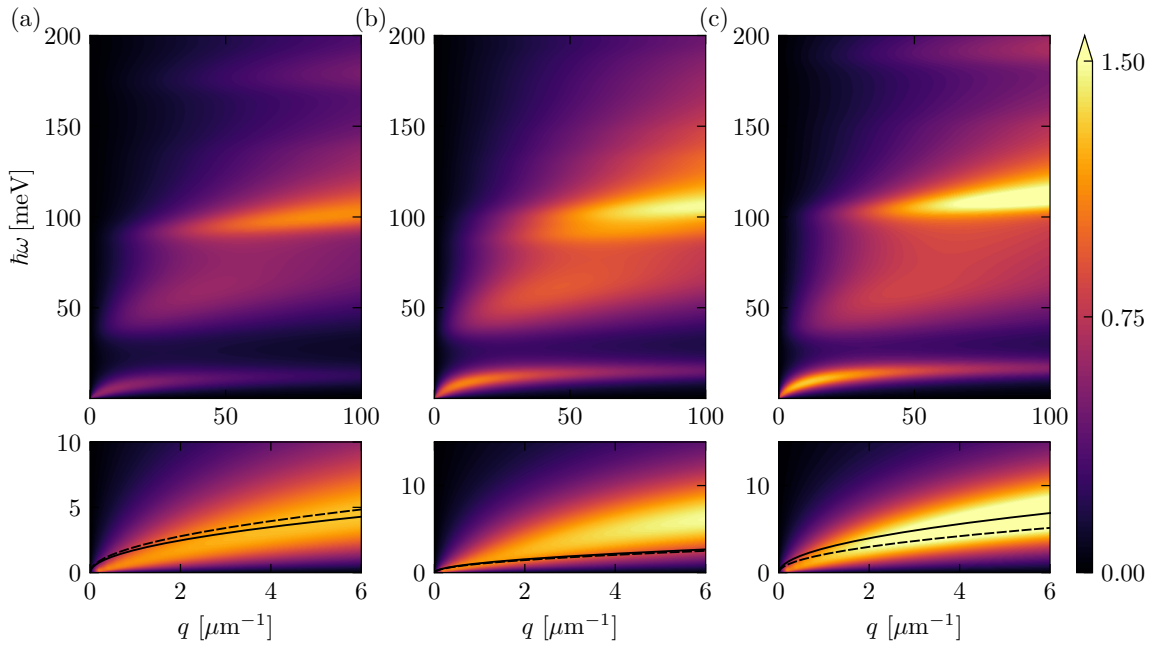

FIGURE 3.6: 2D plots of the energy loss function $\mathcal{L}(\boldsymbol{q},\omega)$, for different values of the filling factor ξ at $\theta = 1.05°$, $u_0 = 79.7$ meV, $u_1 = 97.5$ meV, $T = 5$ K, and $\bar{\varepsilon}(0) = 4.9$: (a) hole doping, $\xi = -3/4$; (b) CNP, $\xi = 0$; (c) electron doping, $\xi = +3/4$. In all the panels, the lower sub panels zoom in on a smaller region of the energy-momentum plane. All 2D plots displayed in this figure have been obtained by using the self-consistent Hartree approximation. The black solid (dashed) lines are the analytical intra-band plasmon dispersions calculated through Eq. (3.11), making use of eigenvalues and eigenvectors of the self-consistent Hartree (bare) Hamiltonian in Eq. (2.40) (Eq. (2.30)), respectively.

maximum. The position of this peak is pretty much identical and filling-independent in both panels, whereas its intensity is slightly different in the two panels, with a filling-dependent intensity for the case of the results obtained with the Hartree self-consistency, panel b). The optical transitions associated with this peak are due to electrons with momenta close to the Γ point in the moiré Brillouin zone that are excited by photons from the valence flat band to the first non-flat conduction band. This optical transition is highlighted with a solid arrow in panel (a) of Fig. 3.1. Part of the spectral weight of this peak is also due to transitions from the first non-flat valence band to the conduction flat band. The second notable peak in $\mathrm{Re}[\sigma^{\mathrm{inter}}(\omega)]$ occurs at $\hbar\omega \simeq 95$ meV and is associated to optical transitions between the same bands involved in the previously discussed peak, albeit for electrons in the vicinity of the corners of the moiré Brillouin zone, as showed by the dashed arrow in panel (a) of Fig. 3.1.

The effect of the Hartree self-consistency on the inter-band contribution $\mathrm{Re}[\sigma^{\mathrm{inter}}(\omega)]$ to the optical conductivity is mostly appreciable in the vicinity of its peaks. The intensity of the strongest peak becomes filling-dependent when the Hartree corrections are taken into account, with higher intensity at negative values of ξ, i.e. for hole doping. The second most-intense peak, which, as stated above, originates from transitions

occurring near the K point in the moiré Brillouin zone, is not affected in its intensity by the Hartree corrections. Nonetheless, switching from negative to positive filling factors, the energy at which the peak occurs varies slightly. This can be understood by recalling that, as discussed above, the non-flat bands are rigidly shifted by the Hartree potential, whereas the flat bands are unaffected by $V_{\rm H}$ in the vicinity of the K point in the moiré Brillouin zone.

In Fig. 3.6 we illustrate the dependence of the loss function on the filling factor, for the same values of ξ as in Fig. 3.1 and for the same parameters u_0, θ, and T. $\mathcal{L}(\boldsymbol{q},\omega)$ encodes both inter- and intra-band contributions, as already discussed for the conductivity $\sigma(\omega)$. The color plots in Fig. 3.6 have been obtained by employing the fully self-consistent Hartree model, Eq. (2.40). For each of the columns in Fig. 3.6, the upper panel displays $\mathcal{L}(\boldsymbol{q},\omega)$ in a range of energies and wave vectors where inter-band plasmons are excited [77]. Conversely, the lower panels are a zoom at small ω and q. In the latter, ordinary intra-band plasmons [30] are clearly visible, whose dispersion relation admits a simple analytical description. The plasmon peaks, indeed, stem from zeroes of the longitudinal dielectric function, Eq. (2.109). Plasmon dispersions originating from intra-band processes are easily extracted by plugging the value of the intra-band optical conductivity (2.95) into Eq. (2.109). After straightforward manipulations, we reach the usual [30] 2D intra-band plasmon dispersion relation

$$\hbar\omega_{\rm pl}(q\to 0)=\sqrt{\frac{2e^2\mathcal{W}^{(0)}q}{\bar{\varepsilon}(0)}}\ . \tag{3.11}$$

In the lower panels of Fig. 3.6 we have also plotted the previous equation using the values of $\mathcal{W}^{(0)}$ computed both with and without Hartree corrections. Away from the CNP—panels (a) and (c) of Fig. 3.6—the loss function has a clearly distinguishable peak dispersing as predicted by Eq. (3.11). The two analytical dispersion relations are different because they depend on the value of $\mathcal{W}^{(0)}$, which, as we have seen before, is modified by the Hartree potential with respect to the bare value when TBG is doped away from the CNP. Recalling that the color plots refer to the fully self-consistent Hartree theory, it is no surprise to see that the intra-band plasmon mode observed as a peak in $\mathcal{L}(\boldsymbol{q},\omega)$ at small q and ω is centered around the dispersion relation calculated with the fully self-consistent Hartree value of $\mathcal{W}^{(0)}$, i.e. around the solid black line.

A completely different behavior is observed at the CNP. In this case the loss function displays a well defined plasmon branch which, however, does not follow the approximate analytic plasmon dispersion in Eq. (3.11). This is readily explained by remembering that the analytic plasmon dispersion presented above describes collective excitations arising from intra-band processes. At the CNP, the Fermi surface shrinks down to a single point, and intra-band collective modes can originate only from finite-temperature effects (i.e. thermally-excited quasiparticles). Albeit the present calculations are carried out at a finite temperature, $T = 5$ K, the intra-flat-band plasmon branch due to thermally excited quasiparticles is not a clearly distinguishable component of the low-energy loss function. Rather, the low-energy plasmon branch visible at the CNP stems from optical transitions between the flat bands. This follows from simple energetic considerations. Since the characteristic energy scale of this plasmon is $\lesssim 20$ meV, the

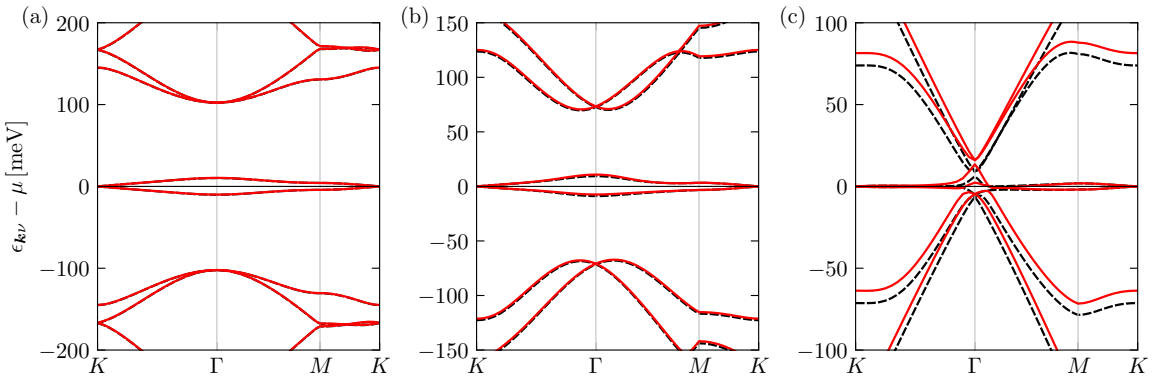

FIGURE 3.7: TBG energy bands for different values of u_0 are plotted along the K-Γ-M-K path in the moiré Brillouin zone. Data in this figure refer to $\theta = 1.05°$, $u_1 = 97.5$ meV, $T = 5$ K, $\xi = 0$, and $\bar{\varepsilon}(0) = 4.9$. Color coding and line styles have the same meaning as in Fig. 3.1. Different panels refer to different values of the intra-sublattice inter-layer tunneling energy u_0. Panel (a) $u_0 = 0$ meV (as in Ref. [69]). Panel (b) $u_0 = 48.2$ meV. Panel (c) $u_0 = u_1 = 97.5$ meV (as in Ref. [3]).

inter-band processes from which it originates are bound to occur in the manifold of nearly-flat bands. This is justified by observing that exciting electrons onto the higher energy bands would require an energy $\hbar\omega > 20$ meV. We note that at $\xi = 0$ the two analytical dispersion relations shown at the bottom of panel (b) are almost identical. This is because $\mathcal{W}^{(0)}$—as previously mentioned—is unaffected by the Hartree potential at the CNP.

For any of the values of the filling factor, there is also another quite noticeable peak in $\mathcal{L}(\boldsymbol{q}, \omega)$ at energies $\hbar\omega \approx 100$ meV. This an inter-band plasmon, analogous to the one measured in Ref. [43] at $\theta = 1.35°$. It starts off at a finite wave vector ≈ 5 μm^{-1} and its position in the ω-q plane is just weakly affected by the filling factor ξ.

The optical transitions responsible for this inter-band plasmon are the ones occurring at the energy highlighted by the dashed white line in panel (b) of Fig. 3.5. At $\theta = 1.05°$ and for the values of the parameter u_0 chosen in this Section, this inter-band plasmon originates from processes occurring near the corners of the moiré Brillouin zone.

3.2 Dependence on the intra-sublattice inter-layer tunneling energy u_0

We now present numerical results for $\sigma(\omega)$ and $\mathcal{L}(\boldsymbol{q}, \omega)$ obtained by changing the intra-sublattice inter-layer hopping energy u_0. As in Sect. 3.1, the inter-sublattice inter-layer hopping energy has been fixed at $u_1 = 97.5$ meV, the twist angle at $\theta = 1.05°$, and the temperature at $T = 5$ K. We here study the dependence on u_0 only at the CNP, i.e. at $\xi = 0$.

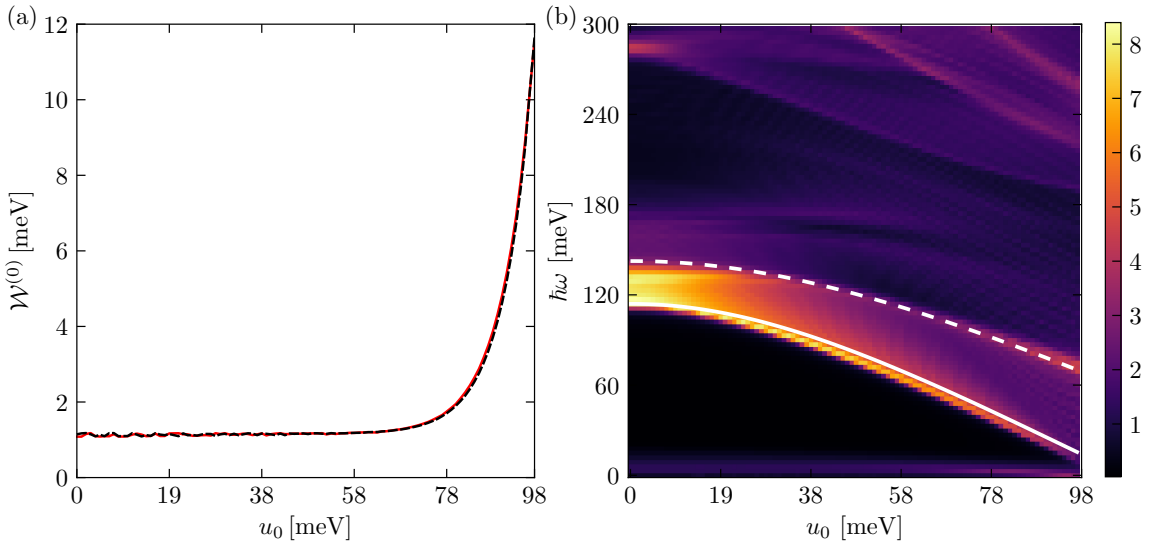

FIGURE 3.8: Panel (a) Drude weight in units of $e^2/\hbar^2$ as a function of u_0, for $\theta = 1.05°$, $u_1 = 97.5$ meV, $T = 5$ K, $\xi = 0$, and $\bar{\varepsilon}(0) = 4.9$. Color coding and line styles have the same meaning as in panel (a) of Fig. 3.3. Panel (b) The quantity $\mathrm{Re}[\sigma^{\mathrm{inter}}(\omega)]$ (in units of G_0), related to the optical absorption, is plotted as a function of $\hbar\omega$ and u_0. Results in this panel have been obtained by employing the Hartree self-consistent approximation and refer to $\theta = 1.05°$, $u_1 = 97.5$ meV, $T = 5$ K, and $\xi = 0$. Solid and dashed white lines are placed at energies equal to the gap between the valence flat band and the first non-flat conduction band at the point Γ and K in the moiré Brillouin zone, respectively. These lines are associated to the optical transitions marked in Fig. 3.1(a).

It is known [69] that for, $u_0 = 0$, the flat bands' bandwidth at the magic angle is exactly zero throughout the whole moiré Brillouin zone. Since $\theta = 1.05°$ is close to but not exactly the magic angle, the flat bands' bandwidth is non-zero even at $u_0 = 0$. It is also known [69] that TBG at small values of u_0 hosts large (i.e. on the order of ≈ 100 meV) energy gaps between the flat bands and the "remote" conduction/valence bands. These gaps therefore provide a rough estimate of the energy scales at which optical transitions occur. This is going to be quite evident both in the optical conductivity and loss function calculated at $u_0 = 0$.

In Fig. 3.7 we display the energy bands of TBG at different values of u_0. At $u_0 = 0$ meV, the Hartree corrections on the band structure are negligible and the energy gap between the flat bands and the adjacent bands is on the order of ≈ 100 meV. At $u_0 = 48.2$ meV, again, the Hartree potential leaves the bare energy bands almost unchanged. In this case, however, the energy gap between the flat bands and the adjacent bands is ≈ 120 meV near the K point and ≈ 75 meV near the Γ point. Finally, at $u_0 = u = 97.5$ meV, the Hartree potential manifests as an upward bending of the flat bands, most noticeably near the Γ point, whereas the energy gap between flat bands and adjacent bands is $\lesssim 5$ meV at the Γ point and ≈ 75 meV at the K point. We remind the reader that TBG bands at $u_0 = 79.7$ meV, which is the value predicted

for corrugated TBG [104, 106], and $\xi = 0$ can be found in panel (b) of Fig. 3.1.

An important remark is now in order. Even though the Hartree contribution distorts the bare bands, the energy gaps between flat bands and adjacent conduction/valence bands are virtually the same as in the case of the bare bands. This is another manifestation of the previously noted fact that, close to zero filling, the optical properties are qualitatively unaffected by the Hartree potential. Conversely, the value of u_0 dramatically alters the energies at which optical transitions with large spectral weight occur.

In Fig. 3.8 we show $\mathcal{W}^{(0)}$, i.e. the Drude weight in units of $e^2/\hbar^2$, and the real part $\mathrm{Re}[\sigma^{\mathrm{inter}}(\omega)]$ of the inter-band optical conductivity. We note that $\mathcal{W}^{(0)}$ is an increasing function of u_0. This follows from the fact that $\mathcal{W}^{(0)}$, whose microscopic expression can be obtained from Eq. (2.96) by setting $\alpha = \beta$, depends on the derivative of the bands with respect to $\boldsymbol{k}$, i.e. on $|\langle \boldsymbol{k}\nu|\partial_{k_\alpha}\hat{H}(\boldsymbol{k})|\boldsymbol{k}\nu\rangle|^2 = |\partial_{k_\alpha}\epsilon_{\boldsymbol{k}\nu}|^2$. Now, as shown in Fig. 3.7, the flat bands at $u_0 = 0$ vary more smoothly throughout the moiré Brillouin zone with respect to the bands evaluated at finite u_0. In the latter case, we note a sudden variation of the band dispersion in the vicinity of the Γ point. Once again, since we are at the CNP, the quantity $\mathcal{W}^{(0)}$ calculated in the fully self-consistent Hartree approximation is practically indistinguishable with respect to the bare result, as evident from panel (a) of Fig. 3.8. In panel (b) of Fig. 3.8 we therefore plot the real part $\mathrm{Re}[\sigma^{\mathrm{inter}}(\omega)]$ of the inter-band contribution to the optical conductivity calculated in the Hartree approximation. We clearly see that $\mathrm{Re}[\sigma^{\mathrm{inter}}(\omega)]$ shows a very interesting dependence on u_0, with its peaks shifting sensibly with it. As in Fig. 3.5, the solid white line is the energy separation between the valence flat band and the first non-flat conduction band at the Γ point, whereas the dashed white line is the energy separation between the same pairs of bands, albeit evaluated at the K point in the moiré Brillouin zone. The position of the peak corresponding to the optical transition at the Γ point decreases monotonically with u_0 from a maximum of $\hbar\omega \simeq 120$ meV at $u_0 = 0$ meV to a minimum of $\hbar\omega \simeq 5$ meV at $u_0 = u = 97.5$ meV. These energy values are recovered also by looking at the band structures in Fig. 3.7. A similar, monotonically decreasing behavior is followed by the peaks associated to the optical transitions near the K point in the moiré Brillouin zone. In this case, the position of the peak is $\hbar\omega \simeq 150$ meV at $u_0 = 0$ meV and $\hbar\omega \simeq 70$ meV at $u_0 = 97.5$ meV. As a final note on the inter-band optical conductivity, we stress that the intra-sublattice hopping energy scale u_0 is responsible also for sensible shifts in the position of optical transitions at higher energies, up to hundreds of meV (see Fig. 3.8).

The loss function, evaluated for different values of u_0, is showed in Fig. 3.9. As before, the upper panels display $\mathcal{L}(\boldsymbol{q}, \omega)$ at energy scales which are suited to inspect collective excitations originating from inter-band processes. Inter-band plasmon branches are clearly visible at energies $\hbar\omega > 50$ meV and are analogous to the ones experimentally measured in Ref. [43]. The position of these branches in the ω-q plane is fairly sensitive to the value of the parameter u_0. An inter-band plasmon with characteristic excitation energy $\hbar\omega \approx 140$ meV at $u_0 = 0$ meV drops down in energy to $\hbar\omega \approx 80$ meV at $u_0 = 97.5$ meV. As before, at excitation energies $\lesssim 20$ meV there is a quite evident plasmon branch, which originates from inter-flat-band optical transitions. Starting from $u_0 = 0$, the corresponding peak in the loss function is well defined up

to $u_0 = 48.2$ meV, whereas it rapidly broadens in the limit $u_0 = u_1 = 97.5$ meV, as shown in the corresponding upper panel. The lower panels of Fig. 3.9 illustrate the loss function at small q and ω. The analytical plasmon dispersion Eq. (3.11) is not shown because, as discussed in the previous Section, it is suited to describe intra-band plasmons. At charge neutrality, such intra-band excitations can arise only from finite-temperature effects, and in the present case ($T = 5$ K) it is pratically impossible to clearly identify their contribution to the loss function.

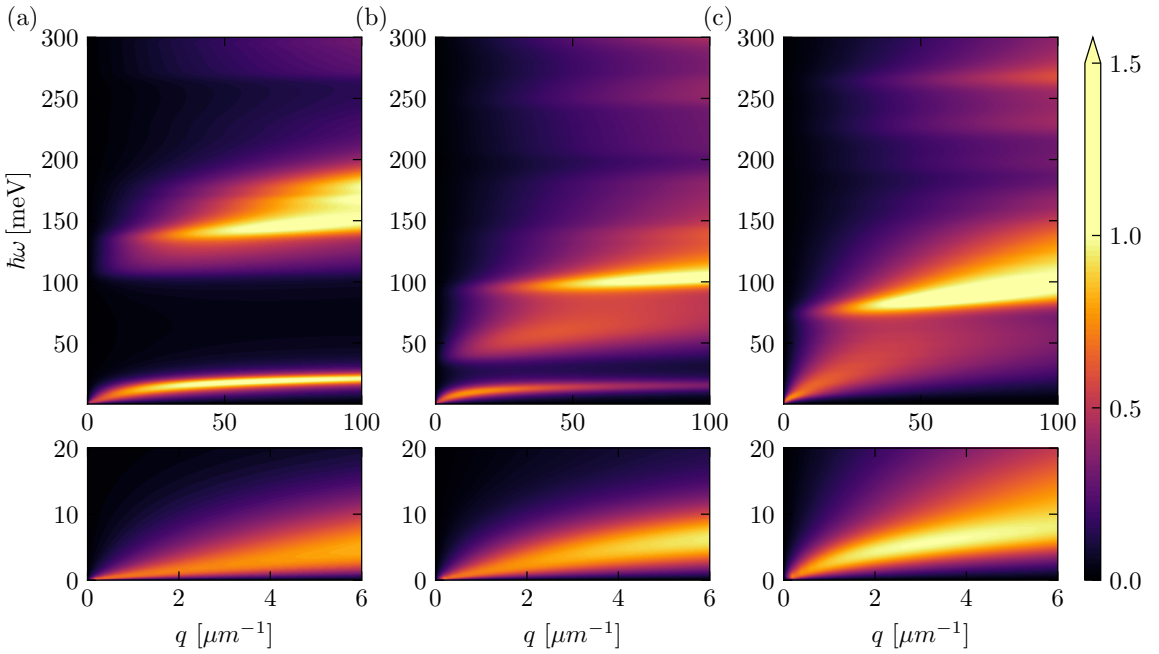

FIGURE 3.9: 2D plots of the loss function $\mathcal{L}(\boldsymbol{q}, \omega)$ for different values of the intra-sublattice hopping energy u_0 at $\theta = 1.05°$, $u_1 = 97.5$ meV, $T = 5$ K, $\xi = 0$, and $\bar{\varepsilon}(0) = 4.9$: (a) $u_0 = 0$ as in Ref. [69]; (b) $u_0 = 48.2$ meV; (c) $u_0 = u_1 = 97.5$ meV as in Ref. [3]. In all the panels, the lower sub panels zoom in on a smaller region of the energy-momentum plane. Data displayed in this figure have been obtained by employing the self-consistent Hartree approximation at the CNP ($\xi = 0$).

3.3 Dependence on the twist angle

We now move on to discuss the optical conductivity and loss function of TBG as functions of the twist angle θ. It is known [3, 64] that, for a fraction of their bandwidth, TBG's low-energy bands disperse linearly, akin to the ones of monolayer graphene, albeit with a renormalized Fermi velocity. The linear energy dispersion of TBG, however, extends over a fraction of the low-energy bands' bandwidths that decreases very rapidly as a function of θ.

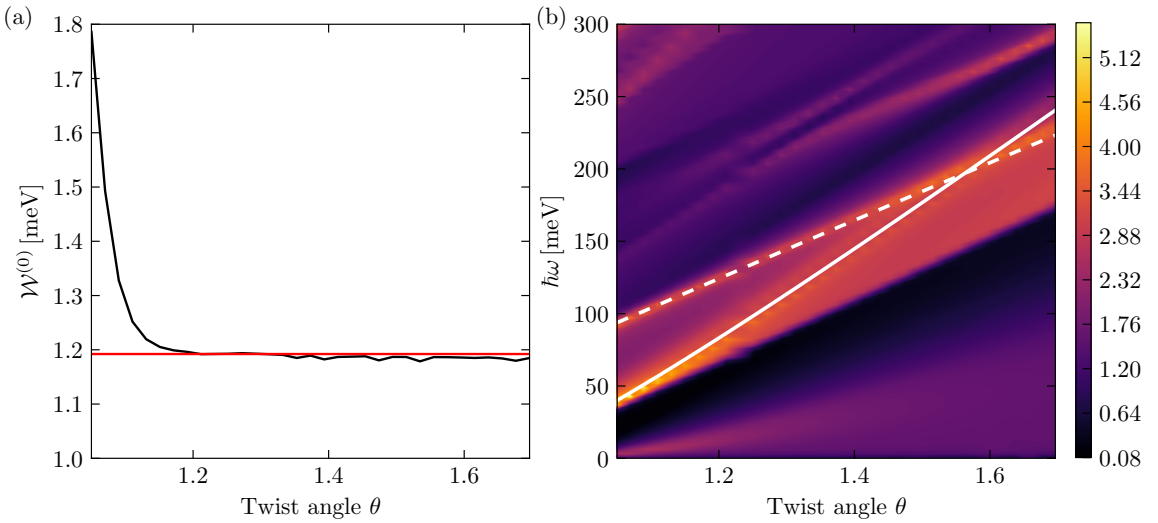

FIGURE 3.10: (a) The Drude weight (in units of $e^2/\hbar^2$) is plotted as a function of the twist angle θ. The solid black trace denotes data calculated via Eq. (2.96) at $\xi = 0$, $u_0 = 79.7$ meV, $u_1 = 97.5$ meV, $T = 5$ K, and $\bar{\varepsilon}(0) = 4.9$, and obtained by making use of the eigenvalues and eigenvectors of self-consistent Hartree Hamiltonian (2.40). The solid red line is the value of $\mathcal{W}^{(0)}$ calculated analytically for a linear energy dispersion relation. (b) The quantity $\mathrm{Re}[\sigma^{\mathrm{inter}}(\omega)]$ (in units of G_0) is plotted as a function of $\hbar\omega$ and θ. Data in this plot have been obtained by setting $\xi = 0$, $u_0 = 79.7$ meV, $u_1 = 97.5$ meV, and $T = 5$ K, and calculated from Eq. (2.98) with the fully self-consistent Hamiltonian (2.40). Solid and dashed white lines are placed at energies equal to the gap between the valence flat band and the first non-flat conduction band at the point Γ and K in the moiré Brillouin zone, respectively. These lines are associated to the optical transitions marked in Fig. 3.1(a).

The dependence of $\sigma(\omega)$ on θ, down to $\theta \gtrsim 2.0°$, has been studied in Ref. [123]. For this reason, we will focus on $\theta \lesssim 2.0°$. We set $\xi = 0$, $u_1 = 97.5$ meV, and $u_0 = 79.7$ meV. As in the previous Sections, $T = 5$ K.

The dependence of the band structure of TBG on θ has been extensively discussed in the literature [3, 64, 131]. The bandwidth of the "flat bands", i.e. the bands closer to the CNP at 1.05°, increases very rapidly with θ, becoming [123] ≈ 500 meV at $\theta \approx 2.5°$, i.e. the two "flat" bands extend over a total energy range of ≈ 1 eV. In light of this, from now on we will refer to these bands as first conduction and valence bands.

In Fig. 3.10 we show the Drude weight in units of $e^2/\hbar^2$, i.e. $\mathcal{W}^{(0)}$, and the real part $\mathrm{Re}[\sigma^{\mathrm{inter}}(\omega)]$ of the inter-band optical conductivity as functions of θ. The quantity $\mathcal{W}^{(0)}$ is a monotonically decreasing function of the twist angle, approaching an asymptotic value at large θ, which can be calculated analytically. A straightforward calculation, indeed, shows that, at the CNP, the value of $\mathcal{W}^{(0)}$ for linear energy bands is $\mathcal{W}^{(0)} = g k_{\mathrm{B}} T \log(2)$, independent of the Fermi velocity. The value of $k_{\mathrm{B}}T \approx 0.4$ meV, chosen in our numerical calculations, is much smaller than the bandwidth of the valence and conduction bands, especially so for the case of $\theta \gtrsim 1.2°$ (see Fig. 3.10). The quantity $\mathcal{W}^{(0)}$, thus, converges to the asymptotic limit $g k_{\mathrm{B}} T \log(2)$ when the value of $k_{\mathrm{B}}T$ is much smaller than the energy scale over which the bands are linear. On the other

hand, at smaller twist angles—and generally speaking when $k_{\mathrm{B}}T$ is larger than or comparable to the energy range over which the first valence and conduction bands are linear—$\mathcal{W}^{(0)}$ increases. In panel (a) of Fig. 3.10, it is evident that already at $T = 5$ K, the Drude weight of TBG (in units of $e^2/\hbar^2$) has values that are quite different from the ones expected for a material with linearly-dispersing energy bands. This effect is expected to be enhanced by temperature, i.e. for higher T, the value of $\mathcal{W}^{(0)}$ is expected to converge to $gk_{\mathrm{B}}T\log(2)$ at larger twist angles.

As we discussed earlier, $\mathrm{Re}[\sigma^{\mathrm{inter}}(\omega)]$ shows peaks at energies $\hbar\omega$ at which the denominator in Eq. (2.98) is minimal, i.e. when $\hbar\omega + \epsilon_{\boldsymbol{k}\nu} - \epsilon_{\boldsymbol{k}\nu'} \approx 0$. The energies at which those peaks occur increase monotonically with the twist angle. In panel (b) of Fig. 3.10 we have marked with solid and dashed white lines the excitation energies of the optical transitions occurring near the Γ and K points of the moiré Brillouin zone, respectively. Around $\theta \approx 1.55°$ these lines cross, meaning that the energy distance between the valence band and the second conduction band is wider at Γ than at K. As in the case of variable intra-sub-lattice hopping energy, the positions of the peaks of the optical conductivity change with θ, in a wide range of energies. Fig. 3.10(b) shows that these modifications occur up to energies $\hbar\omega \simeq 300$ meV.

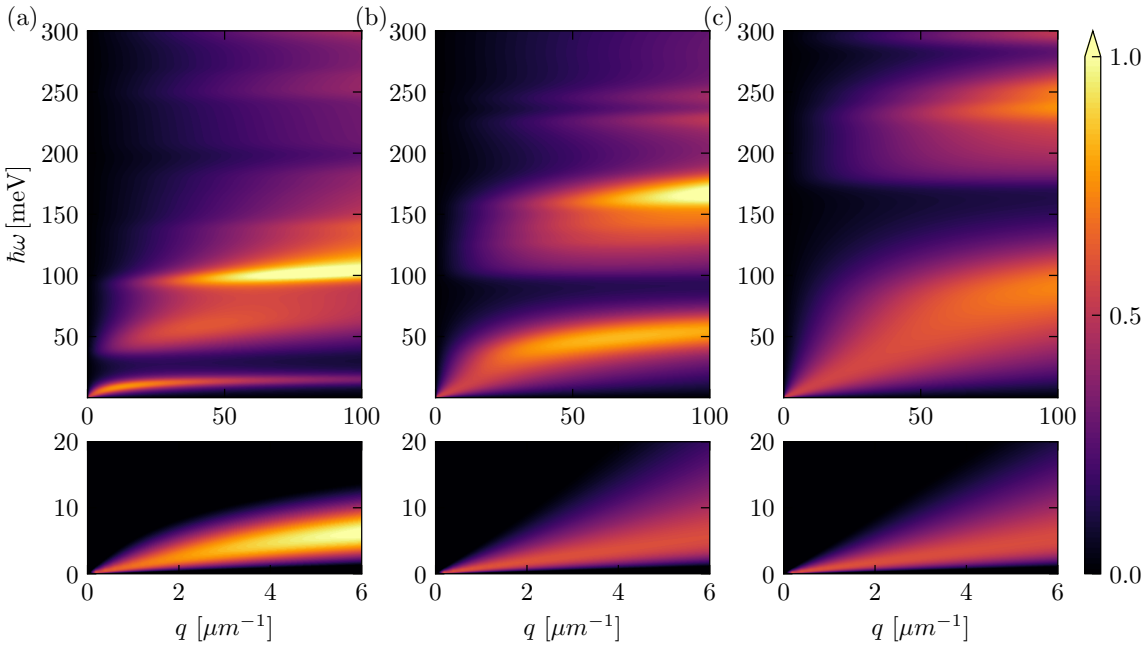

Figure 3.11: 2D plots of the loss function $\mathcal{L}(\boldsymbol{q},\omega)$ for different values of the twist angles θ at $\xi = 0$, $u_0 = 79.7$ meV, $u_1 = 97.5$ meV, $T = 5$ K, and $\bar{\varepsilon}(0) = 4.9$. In all the panels, the lower sub panels zoom in on a smaller region of the energy-momentum plane. Data displayed in this figure have been obtained by employing the self-consistent Hartree approximation at the CNP ($\xi = 0$). Panel (a) $\theta = 1.05°$. Panel (b) $\theta = 1.35°$. Panel (c) $\theta = 1.65°$.

The loss function of TBG at three different twist angles is shown in Fig. 3.11.

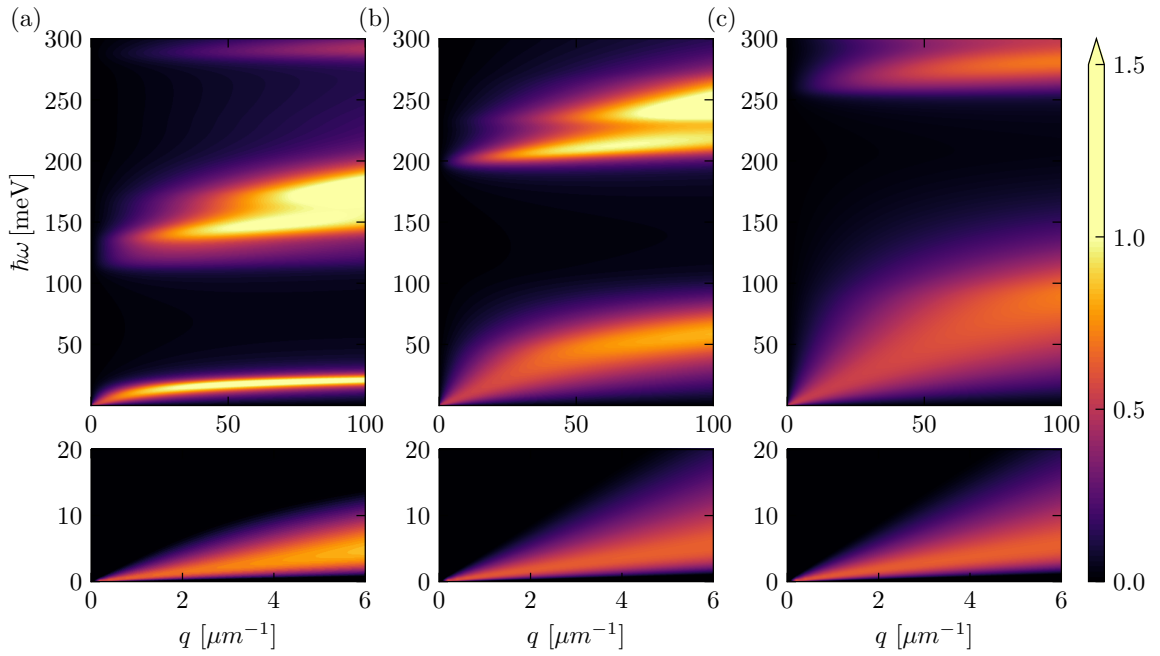

FIGURE 3.12: 2D plots of the loss function $\mathcal{L}(\boldsymbol{q},\omega)$ for different values of the twist angles θ at $\xi = 0$, $u_0 = 0$ meV, $u_1 = 97.5$ meV, $T = 5$ K, and $\bar{\varepsilon}(0) = 4.9$. In all the panels, the lower sub panels zoom in on a smaller region of the energy-momentum plane. Data displayed in this figure have been obtained by employing the self-consistent Hartree approximation at the CNP ($\xi = 0$). Panel (a) $\theta = 1.05°$. Panel (b) $\theta = 1.35°$. Panel (c) $\theta = 1.65°$.

In its lower panels, a low-energy, low-momentum plasmon branch can be identified. Once again, this originates from inter-band transitions because, at the CNP and at $T = 5$ K, intra-band plasmon modes are practically absent. This inter-band plasmon branch appears however as a rather broad peak in the loss function, i.e. it is strongly damped. With the help of the upper panels, we see that it is found at excitation energies $\hbar\omega \lesssim 20$ meV in the case of $\theta = 1.05°$. For $\theta = 1.35°$ and $\theta = 1.65°$, on the other hand, the low-energy, low-momentum branch does not extend to large momenta and energies, progressively disappearing as q and ω increase. At higher energies, various peaks in the loss function can be identified. The clearest ones are: 1) one at $\hbar\omega \approx 100$ meV for $\theta = 1.05°$, 2) one at $\hbar\omega \approx 50$ meV and one at $\hbar\omega \approx 170$ meV for $\theta = 1.35°$, and, finally, 3) one at $\hbar\omega \approx 250$ meV for $\theta = 1.65°$.

In Figure 3.12 we show again the twist-angle dependence of the loss function, but in this case for $u_0 = 0$ meV, corresponding to the idealized chirally-symmetric continuum model [78]. It is evident that reducing u_0 leads to a much stronger and more dispersive (and therefore propagating) inter-band plasmon mode, in the energy range $\approx$ 150-250 meV. This suggests that one can gain information about the value of u_0 by measuring the inter-band plasmon dispersion. The energy of the inter-band plasmon shifts towards higher energies with increasing angle, in agreement with the upward shift observed for all the optical transitions in panel (b) of Fig. 3.10. Also its intensity seems to decrease monotonically with increasing angle.

Since plasmon modes delicately depend on θ, u_0, and ξ, care needs to be exercised when color plots of the loss function referred to different sets of parameters are compared with each other. For example, as showed in Ref. [43], for $\theta = 1.35^\circ$ and $u_0 = 0$, a clear inter-band plasmon mode emerges at energy $\hbar\omega \gtrsim 100$ meV.

3.4 Loss function of TBG encapsulated in hexagonal Boron Nitride

In a 2D system sandwiched between two half-spaces filled with a dielectric with a frequency-dependent permittivity $\bar{\varepsilon}(\omega)$, the interaction potential appearing in Eq. (2.111) reads as following

$$L_{\boldsymbol{q},\omega} = \frac{2\pi}{q\bar{\varepsilon}(\omega)} \ . \tag{3.12}$$

Since high-quality samples of TBG are always encapsulated in hBN, which is an hyperbolic uniaxial dielectric [45], we here take

$$\bar{\varepsilon}(\omega) = \sqrt{\varepsilon_z(\omega)\varepsilon_x(\omega)} \ , \tag{3.13}$$

where $\varepsilon_z(\omega)$ and $\varepsilon_x(\omega)$ are the out-of-plane and in-plane dielectric permittivities of hBN. As anticipated in Section 1.1.4, these have the following frequency dependence [45] ($i = x, z$)

$$\epsilon_i(\omega) = \epsilon_i(\infty) + \frac{s_i\hbar^2\omega_i^2}{\hbar^2\omega_i^2 - i\hbar^2\gamma_i\omega - \hbar^2\omega^2} \ , \tag{3.14}$$

with parameters given in Table 3.1. Note that with the parametrization (3.14) of the frequency dependence of the permittivities $\epsilon_i(\omega)$, we have $\bar{\varepsilon}(0) = 4.9$, in agreement with the value used in the previous Sections.

In writing Eq. (3.13) we have neglected finite-thickness effects and assumed that TBG is encapsulated between two semi-infinite hBN crystal slabs. Finite-thickness effects can be accounted for by introducing suitable q-dependent form factors [43, 132] in Eq. (3.12).

The loss function of TBG encapsulated in hBN evaluated for different values of ξ, u_0 and θ is shown in Figs. 3.13, 3.14, and 3.15, respectively. As before, the upper panels display $\mathcal{L}(\boldsymbol{q},\omega)$ at energy scales which are suited to inspect collective excitations originating from inter-band processes. Inter-band plasmon branches are clearly visible at energies $\hbar\omega > 50$ meV in any of the three figures, and are analogous to the ones experimentally measured in Ref. [43]. Qualitatively, the inter-band plasmons of hBN-encapsulated TBG have similar features with respect to those calculated by neglecting the frequency dependence of $\bar{\varepsilon}(\omega)$, as in the previous Sections. For the most part, the filling factor ξ leaves their position in the ω-q plane unaltered. Conversely, both the inter-layer hopping amplitude and the twist angle have a higher impact on the inter-band plasmons. The inter-layer hopping amplitude, in particular, shifts the characteristic frequency of the inter-band plasmon from $\hbar\omega \approx 140$ meV at $u_0 = 0$ down to $\hbar\omega \approx 80$ meV at $u_0 = 97.5$ meV.

	$i = x$	$i = z$
s_i	2.001	0.5262
$\epsilon_i(\infty)$	4.9	2.95
$\hbar\omega_i$ (meV)	168.6	94.2
$\hbar\gamma_i$ (meV)	0.87	0.25

Table 3.1: The parameters entering the bulk hBN dielectric functions in Eq. (3.13). These values have been extracted from Ref. [45].

In Figs. 3.13, 3.14 and 3.15 we have clearly highlighted the hBN reststrahlen bands in the energy intervals 94 meV $\leq \hbar\omega \leq$ 102 meV (lower reststrahlen band) and 170 meV $\leq \hbar\omega \leq$ 200 meV (upper reststrahlen band). These bounds can be easily found by looking at the (four) frequencies at which the product $\varepsilon_x(\omega)\varepsilon_z(\omega)$ changes sign. Inside the reststrahlen bands $\varepsilon_x(\omega)\varepsilon_z(\omega) < 0$. Since we have considered semi-infinite hBN crystal slabs, no Fabry-Pérot hyperbolic phonon polariton modes [133] appear in the energy loss function inside the reststrahlen bands.

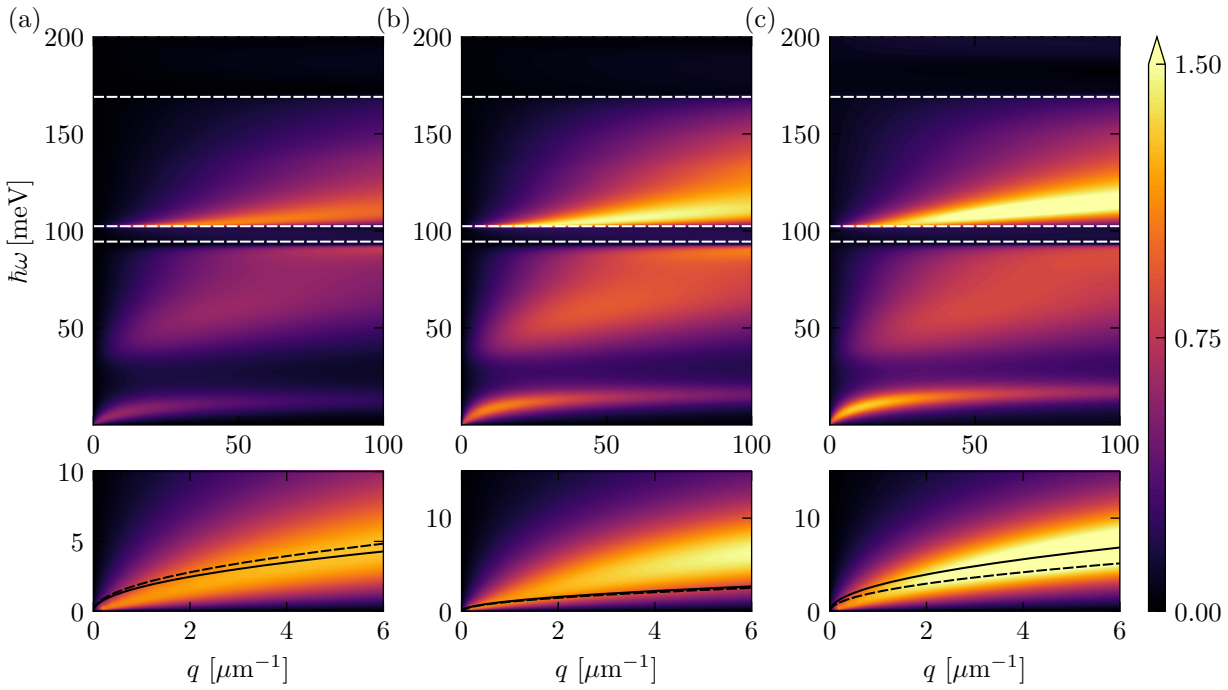

Figure 3.13: 2D plots of the energy loss function $\mathcal{L}(\boldsymbol{q},\omega)$ of TBG encapsulated in hBN, for different values of the filling factor ξ at $\theta = 1.05°$, $u_0 = 79.7$ meV, $u_1 = 97.5$ meV, and $T = 5$ K: (a) hole doping, $\xi = -3/4$; (b) CNP, $\xi = 0$; (c) electron doping, $\xi = +3/4$. In all the panels, the lower sub panels zoom in on a smaller region of the energy-momentum plane. All 2D plots displayed in this figure have been obtained by using the self-consistent Hartree approximation. The black solid (dashed) lines are the analytical intra-band plasmon dispersions calculated through Eq. (3.11), making use of eigenvalues and eigenvectors of the self-consistent Hartree (bare) Hamiltonian in Eq. (2.40) (Eq. (2.30)), respectively. The white dashed lines denote the bounds of the hBN reststrahlen bands. The upper edge of the upper reststrahlen band is outside of the range of values of $\hbar\omega$ shown in this figure.

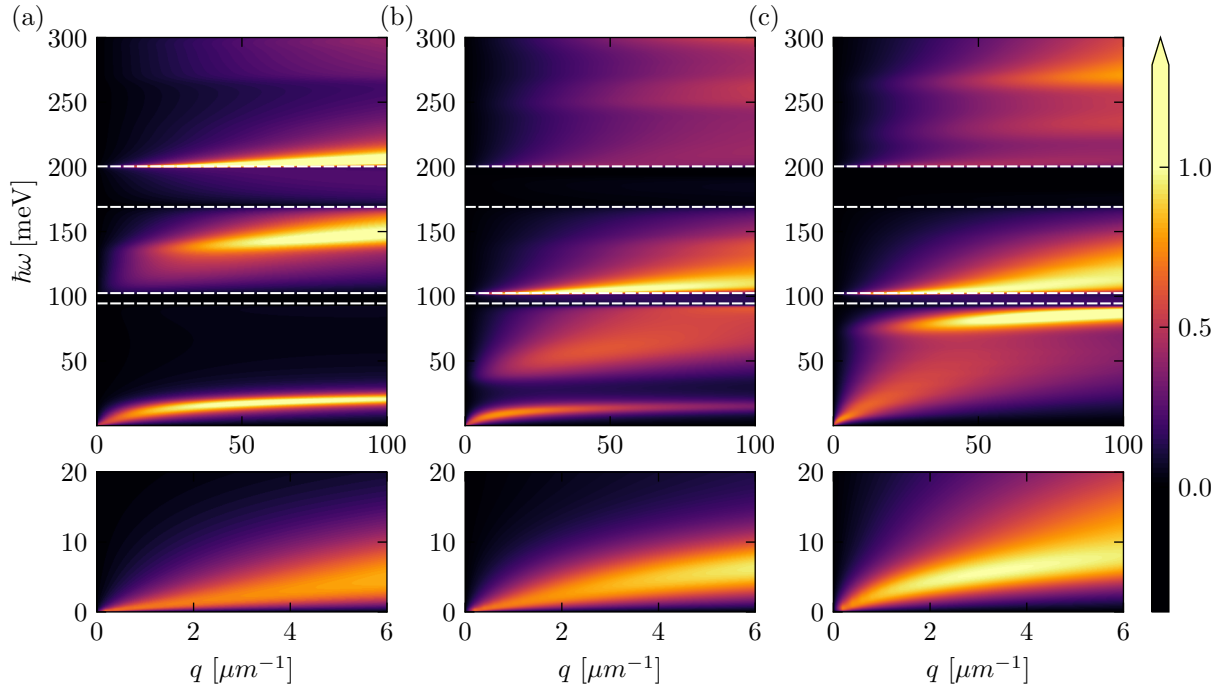

FIGURE 3.14: 2D plots of the loss function $\mathcal{L}(\boldsymbol{q},\omega)$ of TBG encapsulated in hBN, for different values of the intra-sublattice hopping energy u_0 at $\theta = 1.05°$, $u_1 = 97.5$ meV, $\xi = 0$, and $T = 5$ K: (a) $u_0 = 0$ as in Ref. [69]; (b) $u_0 = 48.2$ meV; (c) $u_0 = u_1 = 97.5$ meV as in Ref. [3]. In all the panels, the lower sub panels zoom in on a smaller region of the energy-momentum plane. Data displayed in this figure have been obtained by employing the self-consistent Hartree approximation at the CNP ($\xi = 0$). The white dashed lines denote the bounds of the hBN reststrahlen bands.

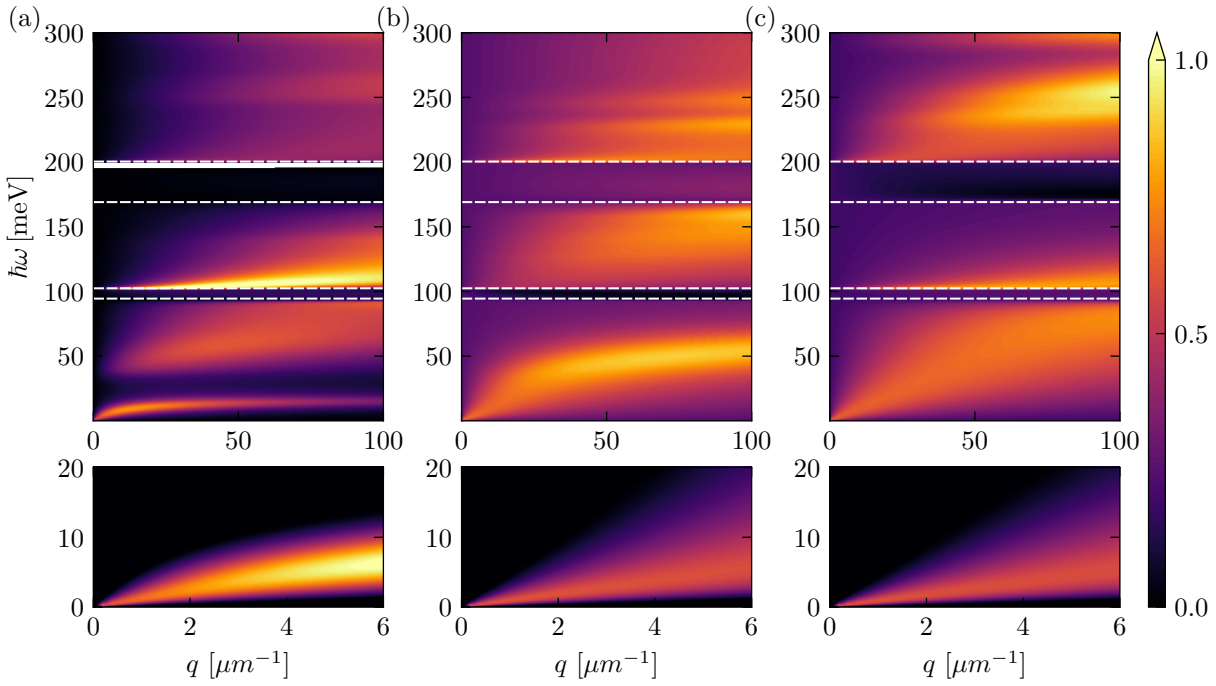

Figure 3.15: 2D plots of the loss function $\mathcal{L}(\boldsymbol{q},\omega)$ of TBG encapsulated in hBN, for different values of the twist angles θ at $\xi = 0$, $u_0 = 79.7$ meV, $u_1 = 97.5$ meV, and $T = 5$ K. In all the panels, the lower sub panels zoom in on a smaller region of the energy-momentum plane. Data displayed in this figure have been obtained by employing the self-consistent Hartree approximation at the CNP ($\xi = 0$). Panel (a) $\theta = 1.05°$. Panel (b) $\theta = 1.35°$. Panel (c) $\theta = 1.65°$. The white dashed lines denote the bounds of the hBN reststrahlen bands.

3.5 Static density-density response function of twisted bilayer graphene

We conclude the Chapter showing unpublished results on the Lindhard function of TBG. The derivation of the density-density response function for a single-particle periodic system was presented in full generality in Section 2.3.1, and the results reported here are based on the continuum model of TBG, derived in Section 2.1.2 and numerically solved as explained in Section 2.4.1.

The calculation of the *non-interacting* density-density response of TBG presented in this Section is an introductory step toward the description of the *interacting* response within the RPA. Furthermore, once the RPA response is calculated, the dielectric properties of TBG are given for free, as the dielectic function is given by [30, 54]

$$\epsilon^{\mathrm{RPA}}(\boldsymbol{q},\boldsymbol{G},\boldsymbol{G}',\omega) = \delta_{\boldsymbol{G},\boldsymbol{G}'} - v_{\boldsymbol{q}+\boldsymbol{G}}\tilde{\chi}^{\mathrm{RPA}}_{nn}(\boldsymbol{q},\boldsymbol{G},\boldsymbol{G}',\omega). \tag{3.15}$$

The calculation of $\tilde{\chi}^{\mathrm{RPA}}_{nn}(\boldsymbol{q},\boldsymbol{G},\boldsymbol{G}',\omega)$ is also useful to go beyond the local approximation for the optical conductivity and loss function thanks to Eq. (2.104).

For TBG, in particular, it is interesting to decouple the contribution of the low-energy flat bands from the contribution of the remote bands in the density-density response. This can be accomplished by dividing the sum over the bands in Eq. (2.63) in three terms, namely

$$\sum_{\nu,\nu'} = \sum_{\nu,\nu'\in\text{flat bands}} + \sum_{\nu,\nu'\in\text{remote bands}} + \left[\sum_{\substack{\nu\in\text{flat bands}\\ \nu'\in\text{remote bands}}} + \sum_{\substack{\nu\in\text{remote bands}\\ \nu'\in\text{flat bands}}}\right]. \tag{3.16}$$

In the following we will denote the first term in the right hand side of Eq. (3.16) as $\chi_{\mathrm{flat}}(\boldsymbol{q},\boldsymbol{G},\boldsymbol{G}',\omega)$, i.e. the flat bands component of the density-density response. In the same fashion, the second term of the right hand side of Eq. (3.16), i.e. the remote bands component of the density-density response corresponding to transition between valence and conduction bands not belonging to the manifold of flat bands, is going to be denoted $\chi_{\mathrm{remote}}(\boldsymbol{q},\boldsymbol{G},\boldsymbol{G}',\omega)$. The third term of Eq. (3.16) accounts for the transitions between flat bands and remote bands. We will not attach any special notation to this contribution, and when needed it is going to be obtained as the difference $\chi_{nn}(\boldsymbol{q},\boldsymbol{G},\boldsymbol{G}',\omega) - \chi_{\mathrm{remote}}(\boldsymbol{q},\boldsymbol{G},\boldsymbol{G}',\omega) - \chi_{\mathrm{flat}}(\boldsymbol{q},\boldsymbol{G},\boldsymbol{G}',\omega)$.

The results presented below have been obtained fixing the twist angle to $\theta = 1.05°$, the temperature to $k_{\mathrm{B}}T = 0.0004\,\mathrm{eV}$, corresponding to $\approx 5\,\mathrm{K}$, and $u_1 = 97.5$ meV. The intra-sublattice hopping energy u_0 was set either to $u_0 = 0.0797\,\mathrm{eV}$ as in Ref. [104] or to $u_0 = 0\,\mathrm{eV}$ as in Ref. [78]. We have also analysed different filling factors (as defined in Section 3.1), namely $\xi \in \{0, 0.25, 0.5, 0.75\}$. The results showed below are not within the RPA, as they are calculated in the absence of the Hartree corrections. These corrections, however, are going to be included future works.

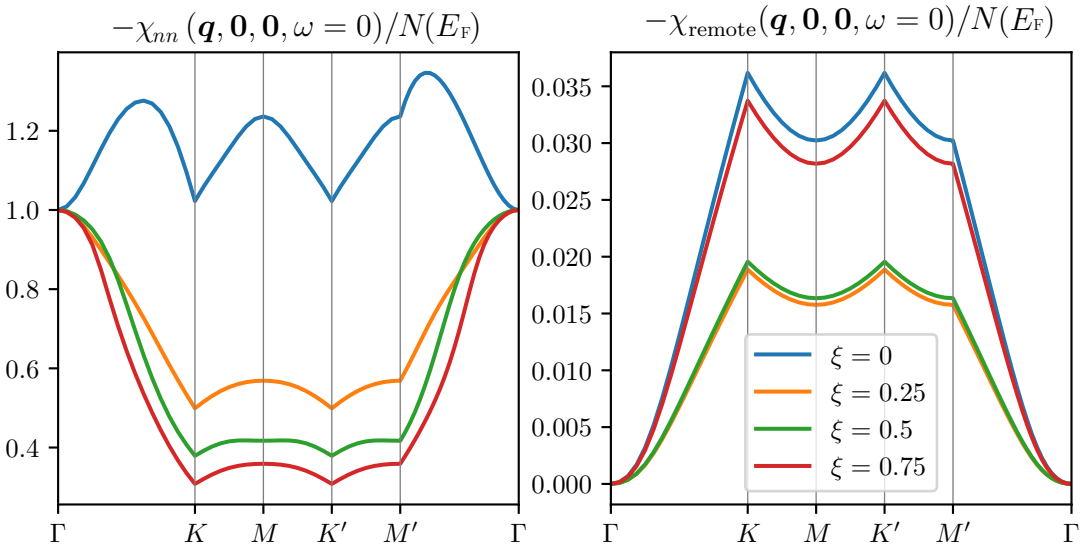

Figure 3.16: Dimentionles static density-density response function for the case $u_0 = 0.0797\,\text{eV}$, as in Ref. [104]. Left panel: full density-density response. Right panel: contributions of the remote bands to the density-density response.

3.5.1 The static density-density response of TBG

The "static limit" of the density-density response function is obtained by letting $\omega \to 0$. A general property of the static density-density response function is that, using the notation of Ref. [30],

$$\lim_{\boldsymbol{q}\to\mathbf{0}} \chi_{nn}(q,\mathbf{0},\mathbf{0},\omega=0) = -N(E_F), \tag{3.17}$$

where $N(E_F)$ is the "thermal density of states" at the Fermi energy.

$$N(E_F) = -\frac{g}{L^D}\sum_{\boldsymbol{k},\nu}\frac{\partial f_{\boldsymbol{k},\nu}}{\partial \epsilon_{\boldsymbol{k},\nu}} \overset{T\to 0}{=} \frac{g}{L^D}\sum_{\boldsymbol{k},\nu}\delta(E_F-\epsilon_{\boldsymbol{k},\nu}). \tag{3.18}$$

In Figures 3.16 and 3.17 we show the dimentionless static density-density response function $-\chi_{nn}(q,\mathbf{0},\mathbf{0},\omega=0)/N(E_F)$ for the case $u_0 = 0.0797\,\text{eV}$ and $u_0 = 0\,\text{eV}$, respectively. In both figures, the left panel shows the *full* density-density response whereas the right panel shows the *remote-bands-only* response. Qualitatively, the intra-sublattice hopping amplitudes $u_0 = 0.0797\,\text{eV}$ and $u_0 = 0\,\text{eV}$ give similar results in the case of nonzero filling factor. When $\xi = 0$, on the other hand, the amplitude of $-\chi_{nn}(q,\mathbf{0},\mathbf{0},\omega=0)/N(E_F)$ at $u_0 = 0\,\text{eV}$ reach higher values than its counterpart at $u_0 = 0.0797\,\text{eV}$. Furthermore, at $u_0 = 0.0797\,\text{eV}$, $-\chi_{nn}(q,\mathbf{0},\mathbf{0},\omega=0)/N(E_F)$ approaches 1 at the K and K' point in the moiré Brillouin zone, whereas when $u_0 = 0\,\text{eV}$ this does not happen.

The limit Eq. (3.17) is respected in our numerical calculations, and the full dimentionless density-density response function $-\chi_{nn}(q,\mathbf{0},\mathbf{0},\omega=0)/N(E_F)$ approaches 1 for

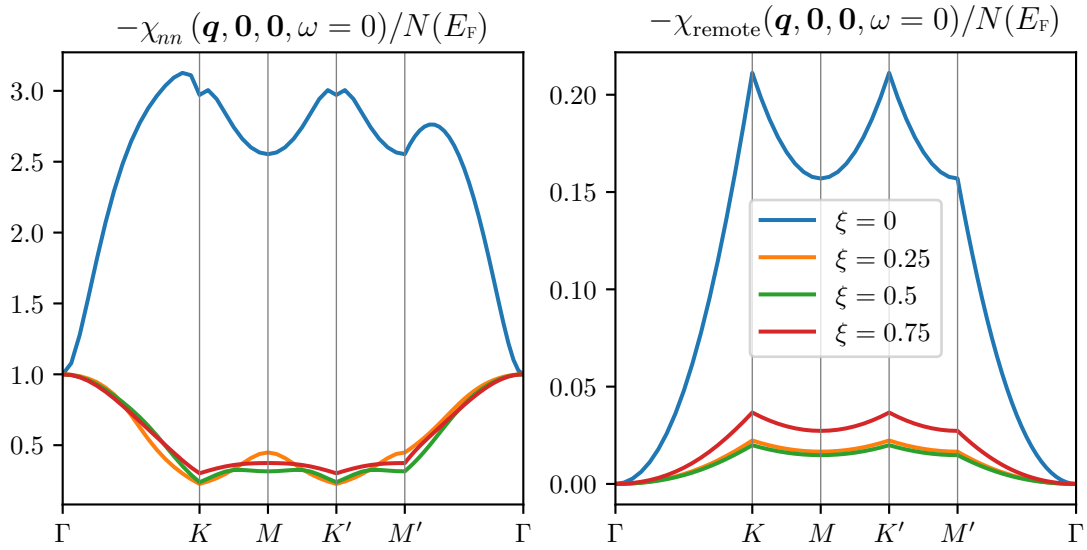

FIGURE 3.17: Dimentionles static density-density response function for the case $u_0 = 0\,\text{eV}$, as in Ref. [78]. Left panel: full density-density response. Right panel: contributions of the remote bands to the density-density response.

wavevectors $\boldsymbol{q} \to \mathbf{0}$, i.e. $\boldsymbol{q}$ close to the Γ point of the Brillouin zone. In both cases, $u_0 = 0.0797\,\text{eV}$ in Fig. 3.16 and $u_0 = 0\,\text{eV}$ in Fig. 3.17, the response at half-filling, i.e. $\xi = 0$ is markedly different with respect to the response at $\xi \in \{0.25, 0.5, 0.75\}$. At half filling, $-\chi_{nn}(q,\mathbf{0},\mathbf{0},\omega=0)/N(E_F) \geq 1$, whereas $-\chi_{nn}(q,\mathbf{0},\mathbf{0},\omega=0)/N(E_F) \leq 1$ when $\xi \in \{0.25, 0.5, 0.75\}$.

Physically, two important quantities to be calculated are the static density-density response function due to transitions between remote valence bands and remote conduction bands $\chi_{\text{remote}}(q,\mathbf{0},\mathbf{0},\omega=0)$, and the static density-density response function between flat bands and remote bands

$$\chi_{nn}(q,\mathbf{0},\mathbf{0},\omega=0) - \chi_{\text{remote}}(q,\mathbf{0},\mathbf{0},\omega=0) - \chi_{\text{flat}}(q,\mathbf{0},\mathbf{0},\omega=0).$$

These response functions are physically relevant as they could be used to calculate the dielectric function through Eq. (3.15). The dielectric functions can, in turn, be incorporated directly into mean-field or exact-diagonalization calculations for the flat bands. The static approximation (i.e. neglecting terms at $\omega \neq 0$) would be justified by the fact that the flat band physics is on an energy scale smaller than any of the transitions between remote bands. The dielectric function associated with the contributions coming from transitions between the flat bands, however, are less likely to be meaningful at low energies and very close to the magic angle, as the many-body interactions totally reshape the bands. In this respect, we also refer to the discussion of scanning tunneling microscopy and scanning tunneling spectroscopy experiments on TBG in the introductory Section 1.2.

The remote-bands-only contributions to the density-density response of TBG are showed in the right panels of Figures 3.16 and 3.17. By comparing the left and right

ξ	a_1	a_2	a_3	a_4
-0.75	-0.0173 ± 0.001	0.8097 ± 0.0169	-1.823 ± 0.0875	1.281 ± 0.143
-0.5	-0.0105 ± 0.0006	0.4929 ± 0.0103	-1.1096 ± 0.0532	0.7797 ± 0.0871
-0.25	-0.0107 ± 0.0006	0.4982 ± 0.0104	-1.1216 ± 0.0538	0.7881 ± 0.088
0	-0.0207 ± 0.0012	0.9682 ± 0.0202	-2.1799 ± 0.1046	1.5318 ± 0.171
0.25	-0.0108 ± 0.0006	0.5049 ± 0.0105	-1.1368 ± 0.0546	0.7988 ± 0.0892
0.5	-0.0112 ± 0.0007	0.5235 ± 0.0109	-1.1786 ± 0.0566	0.8282 ± 0.0925
0.75	-0.0193 ± 0.0011	0.9028 ± 0.0188	-2.0324 ± 0.0975	1.4282 ± 0.1595

Table 3.2: Least squares fit parameters for the polynomial approximation of the remote-bands contribution to the density-density response function $-\chi_{\text{remote}}(\boldsymbol{q}, \mathbf{0}, \mathbf{0}, \omega = 0)/N(E_{\text{F}}) \approx \sum_{j=1}^{4} a_j \|\boldsymbol{q}\|_2^j$. These parameters are suited for $u_0 = 0.0797\,\text{eV}$, as in Ref. [104].

ξ	a_2
-0.75	0.3726 ± 0.0009
-0.5	0.2021 ± 0.0005
-0.25	0.2267 ± 0.0005
0	2.145 ± 0.0049
0.25	0.2267 ± 0.0005
0.5	0.2021 ± 0.0005
0.75	0.3726 ± 0.0009

Table 3.3: Least squares fit parameters for the polynomial approximation of the remote-bands contribution to the density-density response function $-\chi_{\text{remote}}(\boldsymbol{q}, \mathbf{0}, \mathbf{0}, \omega = 0)/N(E_{\text{F}}) \approx a_2 \|\boldsymbol{q}\|_2^2$. These parameters are suited for $u_0 = 0\,\text{eV}$, as in Ref. [78].

panel of Fig. 3.16 it is seen that the static density-density response function of TBG is dominated by the contributions of the flat bands. The remote-bands contributions $-\chi_{\text{remote}}(q, \mathbf{0}, \mathbf{0}, \omega = 0)/N(E_{\text{F}})$ plotted in the right panel are, indeed, more than one order of magnitude smaller than the full response $-\chi_{nn}(q, \mathbf{0}, \mathbf{0}, \omega = 0)/N(E_{\text{F}})$. The same is also true for Fig. 3.17.

Leveraging the idea to include the static dielectric function due to transitions between the remote bands in exact diagonalization and mean field calculations, it is interesting to give an effective desciption of $-\chi_{\text{remote}}(q, \mathbf{0}, \mathbf{0}, \omega = 0)/N(E_{\text{F}})$ by means of a polynomial fit of the following form

$$-\frac{\chi_{\text{remote}}(\boldsymbol{q}, \mathbf{0}, \mathbf{0}, \omega = 0)}{N(E_{\text{F}})} \approx \sum_j a_j \|\boldsymbol{q}\|_2^j. \tag{3.19}$$

For the case $u_0 = 0.0797\,\text{eV}$, showed in the right panel of Fig. 3.16, a good polynomial approximation is attained by truncating at the fourth order. The fit parameters are summarized in Table 3.2. Conversely, for the $u_0 = 0.0797\,\text{eV}$, showed in the right panel of Fig. 3.17, a simple quadratic approximation $-\chi^{(0)}_{\text{remote}}(\boldsymbol{q}, \mathbf{0}, \mathbf{0}, \omega = 0)/N(0) \approx a_2 \|\boldsymbol{q}\|_2^2$ is sufficient. The fit parameters in this case are summarized in Table 3.3.

3.6 Concluding remarks

We have calculated the optical conductivity, energy loss function and static density-density response function of twisted bilayer graphene, for a wide range of microscopic parameters. In particular, we have focussed on the dependence of these properties on the intra-sublattice inter-layer tunneling rate u_0 and ground-state charge density inhomogeneity.

Away from the charge neutrality point, we have showed that the low-frequency components of the optical conductivity, i.e. the ones governed by the Drude weight $e^2\mathcal{W}^{(0)}/\hbar^2$, are sensibly modified by the Hartree potential in Eq. (2.41). In particular, we found a significant enhancement of the particle-hole asymmetry of $\mathcal{W}^{(0)}$. Conversely, the high-frequency components of the optical conductivity are pretty much unaffected by the Hartree potential, and their dependence on the filling factor is also very weak. The loss function reflects all these facts. The low-frequency peaks are well described, away from the charge neutrality point, by the result in Eq. (3.11) and depend directly on $\mathcal{W}^{(0)}$. Conversely, the high-frequency peaks arising from inter-band transitions are virtually independent of the filling factor.

As a byproduct of our calculations, we obtained the Seebeck coefficient in the relaxation time approximation. Our result suggests that a strong thermoelectric effect should persist down to temperatures of ≈ 5 K. In the near future, therefore, photocurrent mapping techniques at cryogenic temperatures may prove to be valid tools to study the onset of the transition to broken symmetry states.

At filling factor $\xi = 0$, i.e. at the charge neutrality point, we have evaluated $\sigma(\omega)$ and $\mathcal{L}(\boldsymbol{q},\omega)$ for different values of the intra-sublattice inter-layer tunneling energy u_0. The Drude weight $e^2\mathcal{W}^{(0)}/\hbar^2$ is a monotonically increasing function of u_0, which is practically insensitive to the Hartree potential (2.41). The (real part of the) inter-band contribution to the optical conductivity is not affected by the Hartree potential as well, whereas it shows a very interesting dependence on u_0. The position of the peaks in $\mathrm{Re}[\sigma^{\mathrm{inter}}(\omega)]$ associated to optical transitions between flat bands and neighbouring bands decreases monotonically with u_0. It is important to keep in mind that u_0 can be modified by extrinsic factors such as strain present in the samples, resulting in a sensible alteration of the optical properties of TBG. Similarly, the peaks in the energy loss function that are related to inter-band optical transitions are strongly affected by the value of the intra-sublattice inter-layer hopping energy. This is agreement with recent experimental work [43]. Indeed, the authors of Ref. [43] noted that a good match between experimental results and theory was possibile only when the value of u_0 used for theoretical predictions was substantially smaller than that reported in the literature [104, 131].

We have also studied the dependence of $\sigma(\omega)$ and $\mathcal{L}(\boldsymbol{q},\omega)$ on the twist angle θ, again at the charge neutrality point. We have showed that the low-frequency $\omega \simeq 0$ component of the optical conductivity, determined by $\mathcal{W}^{(0)}$, can be approximated by the value obtained for linear-dispersing energy bands only if the value of $k_{\mathrm{B}}T$ is much smaller than the energy range over which the valence and conduction bands are linear. This condition does not hold true in TBG with $\theta \lesssim 1.2^\circ$ already at $T = 5$ K, showing that a description of TBG based on a linear approximation of the energy bands in not

sufficient at angles close to the magic one. The (real part of the) inter-band optical conductivity has peaks at energies which increase monotonically with the twist angle.

Finally, we have analysed the static density-density response function of twisted bilayer graphene at different filling factors and intra-sublattice hopping energies u_0. The calculation of the static density-density response function is the first step toward an RPA description of twisted bilayer graphene. We have also shown that the contribution of the remote bands to the density-density response can be conveniently parametrized as a polynomial function of the wavevector $\boldsymbol{q}$.

We conclude mentioning that in *all* of our results we have shown that the behaviour of twisted bilayer graphene at half-filling is markedly different with respect to the case of nonzero filling factor. Special care should therefore be deserved to the study of the configuration $\xi = 0$.

4

Two-dimensional topological insulators

The notion of topological phases of matter was introduced in Section 1.3, with a particular focus on their experimental observation. In this Chapter, we will introduce and discuss the *theoretical* tools needed for a mathematical description of two-dimensional phases of matter. As anticipated in the experimental introduction, the main focus of this Thesis is on *insulating* topological phases realised in two-dimensional materials. Among these, we will present theoretical models for Chern insulators and $\mathbb{Z}_2$ topological insulators. The latter are also known simply as 2D topological insulators or 2DTIs, and we will adhere to this naming convention. The models for these materials are one-particle tight-binding Hamiltonians. These Hamiltonians are often not intended to be faithful models for real topological materials, whose quantitative descriptions are usually accomplished via density functional techniques. On the other hand, the simple tight-binding models presented in this Chapter can be casted to mathematical forms which make the inspection of topological phase transitions — and their onset as the parameters of the model are changed — very convenient.

The physical observables encoding the vast majority of the topological properties of such phases, are related to the electron transport. This Chapter, therefore, contains also a Section where the Landauer-Büttiker theory of phase-coherent transport [24] is presented and discussed. According to the Landauer-Büttiker theory, the electronic transport in mesoscopic conducting systems can be described with the help of a corresponding quantum-mechanical scattering problem. The Landauer-Büttiker theory of transport is a purely quantum mechanical theory which, is valid only in the absence of inelastic collisions. In any event, the validity of the Landauer-Büttiker theory do not pose any concern for the materials considered in this Thesis, as the real experiments (presented in Section 1.3) are always in regimes where the electronic transport can be satisfactory described with a ballistic theory.

The Chapter is organized as follows: the Landauer-Büttiker theory in presented immediately in Section 4.1, the main goal of this Section being to show how to obtain

the physical quantities relevant to transport, such as resistances and conductances, in the Landauer-Büttiker framwork. Next, in Section 4.2, we present the general theory of Chern insulators and 2DTIs, as well as the Haldane model [83] of Chern insulator, introduced in 1988, and the Kane-Mele model [85, 86] of 2DTIs, introduced in 2005. Both these models are defined on an hexagonal lattice and are closely related one another.

4.1 Landauer-Büttiker theory of ballistic transport

The Landauer-Büttiker theory of transport deals with mesoscopic systems and treats the electron transport problem as a scattering problem. The problem of calculating transport characteristics as, for example, electrical conductance or thermal conductance is therefore reduced to solving a quantum-mechanical scattering problem whose scattering potential defines the conductor under investigation. In its traditional form, the Landauer-Büttiker theory applies to non-interacting systems in the stationary regime [24, 134, 135]. The theory presented in the following deals with two-terminal devices, i.e. mesoscopic systems with two leads from which electrical and thermal currents can flow through, as schematically showed in Fig. 4.1. The leads are connected to the mesoscopic system in one side, and are supposed to be attached to large electron reservoirs to the other. The reservoirs are assumed to be at the thermodynamical equilibrium, with temperature T_α and chemical potential μ_α, with the index $\alpha = 1, 2$ labelling the reservoirs. The derivation of the Landauer-Büttiker theory is pivoted in the calculation of the electric current operator within the second quantization framework. The central idea of the derivation, however, is that electrons ejected by the reservoirs traverse the lead and undergo to a scattering process mediated by the potential defining the mesoscopic sample. After the scattering process, the electrons flow back into the reservoirs through the leads. The "scattering matrix", which is a quantity of central interest in the Landauer-Büttiker theory, enters at this stage by relating the incident and scattered electronic states. Indeed, let us define the "incident states", i.e. the states describing electrons ejected from the α-th reservoir and *incident* in the sample at energy ϵ, as $\psi^{(in)}_{\alpha,n}(\epsilon)/\sqrt{\hbar v_{\alpha,n}(\epsilon)}$ and the "scattered states" as $\psi^{(out)}_{\alpha,n}(\epsilon)/\sqrt{\hbar v_{\alpha,n}(\epsilon)}$. The incident and scattered states are normalized to $\sqrt{\hbar v_{\alpha,n}(\epsilon)}$, where $v_{\alpha,n}(\epsilon)$ is the group velocity of the electrons at energy ϵ, in order to carry unit flux [135]. Within the second quantization frameowrk, it is customary to define creation and destruction operators for sets of one-particle quantum states. Here, we will denote these operators as $\hat{a}^\dagger_{\alpha,n}(\epsilon)$ and $\hat{a}_{\alpha,n}(\epsilon)$ for the set of *incident* states, whereas $\hat{b}^\dagger_{\alpha,n}(\epsilon)$ and $\hat{b}_{\alpha,n}(\epsilon)$ create (or destroy) electrons in the *scattered* states.

The power of the scattering approach — in the context of electronic transport — is that any information concerning the flowing of electrons through the mesoscopic sample is synthetically encoded in a single mathematical object: the scattering matrix. Thanks to the scattering matrix (and the principle of superposition) it is possible to know how an incident electronic state will look like after the scattering event. In particular, the scattering matrix $S(\epsilon)$ is defined as the linear operator mapping the vector of creation

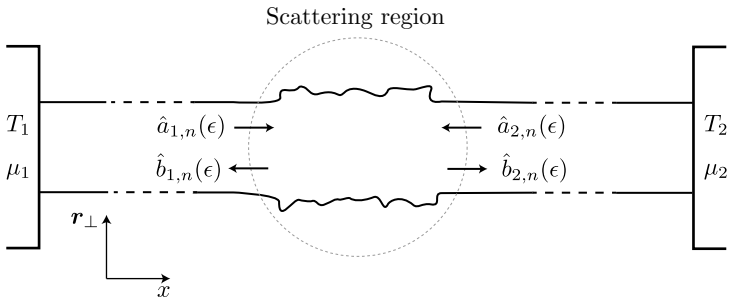

Figure 4.1: Typical geometry studied within the Landauer-Büttiker formalism. A central scattring region is connected to two electronic reservoirs through metallic leads. The electronic reservoirs are at the termodynamical equilibrium, and each leads host a superposition of incident $\hat{a}_{\alpha,n}(\epsilon)$ and scattered $\hat{b}_{\alpha,n}(\epsilon)$ states.

(and destruction) operators of the incident states at energy ϵ to the vector of creation and destruction operators of the scattered states at the same energy

$$\begin{pmatrix} \hat{b}_{1,1}(\epsilon) \\ \hat{b}_{1,2}(\epsilon) \\ \vdots \\ \hat{b}_{1,N_1}(\epsilon) \\ \hat{b}_{2,1}(\epsilon) \\ \hat{b}_{2,2}(\epsilon) \\ \vdots \\ \hat{b}_{2,N_2}(\epsilon) \end{pmatrix} = S(\epsilon) \begin{pmatrix} \hat{a}_{1,1}(\epsilon) \\ \hat{a}_{1,2}(\epsilon) \\ \vdots \\ \hat{a}_{1,N_1}(\epsilon) \\ \hat{a}_{2,1}(\epsilon) \\ \hat{a}_{2,2}(\epsilon) \\ \vdots \\ \hat{a}_{2,N_2}(\epsilon) \end{pmatrix} \iff \hat{b}_{\alpha,n} = \sum_{\beta=1,2} \sum_{m=1}^{N_\beta} S_{\alpha\beta,nm}(\epsilon) \hat{a}_{\beta,m}, \tag{4.1}$$

where we supposed that the Hilbert space describing the electronic states in the α-th lead has dimension N_α. The dimension of the scattering matrix $S(\epsilon)$ at energy ϵ is therefore $N_1 \times N_2$. For later convenience, it is interesting to introduce the following partition of the scattering matrix

$$S(\epsilon) \equiv \begin{pmatrix} r(\epsilon) & t(\epsilon) \\ t'(\epsilon) & r'(\epsilon) \end{pmatrix}, \tag{4.2}$$

where $r(\epsilon)$ and $r'(\epsilon)$ are blocks concerning the reflection of electrons into the original reservoir, whereas $t(\epsilon)$ and $t'(\epsilon)$ concern the transmission on the other lead.

The creation operators for the incident and scattered states, are related by an equation analogous to Eq. (4.1) where $S(\epsilon)$ is replaced by its conjugate $S^*(\epsilon)$. Now, because the scattering matrix relates states with the same energy ϵ, it is understood that the scattering approach is suited to describe *elastic* scattering events. A basic property of the scattering matrix is its unitarity $S^\dagger(\epsilon)S(\epsilon) = \mathbb{1}$. The unitarity of the scattering matrix easily follows from the conservation, during the scattering process, of the total current.

Arguably the most important application of the Landauer-Büttiker approach for the problem of electronic transport is the calculation of the mean electric current flowing

through the mesoscopic sample. In the second quantization formalism this is done by first writing down the current operator for the α-th lead [134, 135]

$$\hat{I}_\alpha(x,t) = \frac{i\hbar e}{2m}\int d\boldsymbol{r}_\perp \left\{ \frac{\partial\hat{\Psi}^\dagger_\alpha(\boldsymbol{r},t)}{\partial x}\hat{\Psi}_\alpha(\boldsymbol{r},t) - \hat{\Psi}^\dagger_\alpha(\boldsymbol{r},t)\frac{\partial\hat{\Psi}_\alpha(\boldsymbol{r},t)}{\partial x}\right\}, \tag{4.3}$$

where x and $\boldsymbol{r}_\perp$ are the longitudinal and transverse coordinates (see Fig. 4.1), and we supposed that the particles have mass m and carry charge e. The operator $\hat{\Psi}_\alpha(\boldsymbol{r},t)$ is the field operator for electrons in lead α

$$\begin{aligned}\hat{\Psi}_\alpha(\boldsymbol{r},t) &= \frac{1}{\sqrt{2\pi}}\int_0^\infty d\epsilon\; e^{-i\epsilon t/\hbar}\sum_{n=1}^{N_\alpha}\left\{\hat{a}_{\alpha,n}(\epsilon)\frac{\psi^{(in)}_{\alpha,n}(\epsilon)}{\sqrt{\hbar v_{\alpha,n}(\epsilon)}} + \hat{b}_{\alpha,n}(\epsilon)\frac{\psi^{(out)}_{\alpha,n}(\epsilon)}{\sqrt{\hbar v_{\alpha,n}(\epsilon)}}\right\}\\ &= \frac{1}{\sqrt{2\pi}}\int_0^\infty d\epsilon\; e^{-i\epsilon t/\hbar}\sum_{n=1}^{N_\alpha}\frac{\xi_{\alpha,n}(\boldsymbol{r}_\perp)}{\sqrt{\hbar v_{\alpha,n}(\epsilon)}}\left\{\hat{a}_{\alpha,n}(\epsilon)e^{-ik_{\alpha,n}(\epsilon)x} + \hat{b}_{\alpha,n}(\epsilon)e^{ik_{\alpha,n}(\epsilon)x}\right\},\end{aligned} \tag{4.4}$$

where in the second line we have used the assumption that $\psi^{(in)}_{\alpha,n}(\epsilon)$ and $\psi^{(out)}_{\alpha,n}(\epsilon)$ are separable products of transverse and longitudinal components

$$\psi^{(in)}_{\alpha,n}(\epsilon,\boldsymbol{r}) \equiv \xi_{\alpha,n}(\boldsymbol{r}_\perp)e^{-ik_{\alpha,n}(\epsilon)x}, \tag{4.5a}$$

$$\psi^{(out)}_{\alpha,n}(\epsilon,\boldsymbol{r}) \equiv \xi_{\alpha,n}(\boldsymbol{r}_\perp)e^{ik_{\alpha,n}(\epsilon)x}. \tag{4.5b}$$

Substituting the field operator Eq. (4.4) and its hermitian conjugate into the expression for the current operator Eq. (4.3), it is possible to arrive at the following expression for the current operator

$$\hat{I}_\alpha(t) = \frac{e}{h}\int_0^\infty d\epsilon\int_0^\infty d\epsilon'\;\exp\left(i\frac{\epsilon-\epsilon'}{\hbar}t\right)\sum_{n=1}^{N_\alpha}\left\{\hat{b}^\dagger_{\alpha,n}(\epsilon)\hat{b}_{\alpha,n}(\epsilon') - \hat{a}^\dagger_{\alpha,n}(\epsilon)\hat{a}_{\alpha,n}(\epsilon')\right\}. \tag{4.6}$$

The latter expression is obtained by basic algebraic manipulations, the normalization of the transverse wavefunction $\int d\boldsymbol{r}_\perp\; \xi^*_{\alpha,n}(\boldsymbol{r}_\perp)\xi_{\alpha,n'}(\boldsymbol{r}_\perp) = \delta_{n,n'}$, and the following approximations

$$v_{\alpha,n}(\epsilon) \approx v_{\alpha,n}(\epsilon'), \tag{4.7a}$$

$$k_{\alpha,n}(\epsilon) \approx k_{\alpha,n}(\epsilon'). \tag{4.7b}$$

The justification of Eqs. (4.7) relies in the observation that for all observable quantities (average current, noise, or higher moments of the current distribution) people are usually interested in voltage biases much smaller than the Fermi energy E_F. Therefore, in all these observables the main contributions come from energies included in an interval much smaller than the energy itself $|\epsilon-\epsilon'| \ll \epsilon \sim E_\mathrm{F}$, and this justifies the approximation in Eqs. (4.7). These approximations are responsible for an algebraic

cancellation of any quantity depending on the longitudinal component x. For a full derivation of Eq. (4.6) from Eq. (4.3) we refer to Ref. [135].

The average current $\langle \hat{I}_\alpha(t) \rangle$ is obtained by taking the thermodynamical expectation value of the operators $\hat{a}^\dagger_{\alpha,n}(\epsilon)\hat{a}_{\alpha,n}(\epsilon')$ and $\hat{b}^\dagger_{\alpha,n}(\epsilon)\hat{b}_{\alpha,n}(\epsilon')$. For the operator concerning the incident states, the averaging procedure is quite easy, as these states are supposed to arrive from an electronic reservoir at the thermodynamical equilibrium

$$\begin{aligned} \langle \hat{a}^\dagger_{\alpha,n}(\epsilon)\hat{a}_{\alpha',n'}(\epsilon') \rangle &= \delta_{\alpha,\alpha'}\delta_{n,n'}\delta(\epsilon-\epsilon') \left[1+\exp(\frac{\epsilon-\mu_\alpha}{k_B T_\alpha})\right]^{-1} \\ &\equiv \delta_{\alpha,\alpha'}\delta_{n,n'}\delta(\epsilon-\epsilon') f_\alpha(\epsilon). \end{aligned} \tag{4.8}$$

In the last term, $f_\alpha(\epsilon)$ is the Fermi-Dirac distribution function for the α-th reservoir calculated at energy ϵ. The operators concerning scattered states, however, are not coming from a reservoir at the thermodynamical equilibrium, and their thermodynamical average is calculated by first expressing $\hat{b}^\dagger_{\alpha,n}(\epsilon)\hat{b}_{\alpha,n}(\epsilon')$ as a combination of the operator for the incident states, for which we know the average Eq. (4.8). At this stage, the relation in Eq. (4.1) can be leveraged to obtain

$$\begin{aligned} \langle \hat{b}^\dagger_{\alpha,n}(\epsilon)\hat{b}_{\alpha,n'}(\epsilon') \rangle &= \sum_{\beta,\beta'}\sum_{m,m'} S^*_{\alpha\beta,nm}(\epsilon) S_{\alpha\beta',n'm'}(\epsilon') \langle \hat{a}^\dagger_{\beta,m}(\epsilon)\hat{a}_{\beta',m'}(\epsilon') \rangle \\ &= \delta(\epsilon-\epsilon') \sum_{\beta,\beta'}\sum_{m,m'} S^*_{\alpha\beta,nm}(\epsilon) S_{\alpha\beta',n'm'}(\epsilon') \delta_{\beta,\beta'}\delta_{m,m'} f_\beta(\epsilon) \\ &= \delta(\epsilon-\epsilon') \sum_{\beta}\sum_{m} S^*_{\alpha\beta,nm}(\epsilon) S_{\alpha\beta,n'm}(\epsilon') f_\beta(\epsilon). \end{aligned} \tag{4.9}$$

Thanks to the expression in Eqs. (4.8) and (4.9) it is possible to calculate the thermodynamical average $\langle \hat{I}_\alpha(t) \rangle$ of Eq. (4.6), which is given by

$$\langle \hat{I}_\alpha(t) \rangle = \langle \hat{I}_\alpha \rangle = \frac{e}{h}\int_0^\infty d\epsilon \sum_\beta f_\beta(\epsilon) \sum_{n=1}^{N_\alpha}\sum_{m=1}^{N_\beta} \left\{ |S_{\alpha\beta,nm}(\epsilon)|^2 - \delta_{n,m}\delta_{\alpha,\beta} \right\}. \tag{4.10}$$

The case of two terminals simplify the previous expression even more. Thanks to the unitarity of the scattering matrix, it is easy to show that in a two terminal setup, the average current is written as

$$\langle \hat{I}_\alpha \rangle = \frac{e}{h}\int_0^\infty d\epsilon\ \mathcal{T}(\epsilon) \left[f_\beta(\epsilon) - f_\alpha(\epsilon) \right], \tag{4.11}$$

where here it is understood $\alpha \neq \beta$ and the "transmission function" $\mathcal{T}(\epsilon)$ is defined as

$$\mathcal{T}(\epsilon) = \mathrm{Tr}\left[t(\epsilon) t^\dagger(\epsilon) \right] = \sum_{n=1}^{N_\alpha}\sum_{m=1}^{N_\beta} S_{\alpha\beta,nm}(\epsilon) S^*_{\alpha\beta,nm}(\epsilon), \qquad \text{for } \alpha \neq \beta. \tag{4.12}$$

In the second term we have used the notation of the sub-blocks decomposition Eq. (4.2), to point out that the transmission function $\mathcal{T}(\epsilon)$ depends on the block of the scattering matrix concerned with the transmission amplitudes.

We conclude mentioning that the previous equations were derived for the case of spinless particles. If any degeneracy due to discrete degrees of freedom such as spin (but also e.g. valley, sublattice) are present, the current in Eq. (4.11) should be multiplied by the appropriate factor g.

4.2 Topology of two-dimensional insulators: theory and models

4.2.1 Bloch insulators and their topology

The insulating state of matter, i.e. a state where the flow of electrons through the material is prohibited, is ubiquitous in nature. Insulators owe their physical properties to many different factors, ranging from the chemical properties of the constitutive elements (see e.g. closed-shell insulators), to the properties of the electronic bonds (as in many band insulators) or to the presence of strong electron-electron interactions for the case of Mott insulators. For crystalline insulating materials whose physical properties are well captured by a one-particle theory, the band theory of solids [17] provides a powerful language to describe the electronic structure of such states. The band theory of solids makes use of the Bloch theorem in order to classify and describe the electronic states of periodic systems. Indeed, the electronic states of a periodic model are labelled by the crystal wavevector $\boldsymbol{k}$ and the discrete band index ν. Now, if the Fermi energy E_{F} lies in an energy gap, i.e. it lies between two bands $\tilde{\nu}$ and $\tilde{\nu}+1$ for which the Hamiltonian eigenvalues satisfy $\max_{\boldsymbol{k}\in\mathrm{BZ}}(\epsilon_{\boldsymbol{k},\tilde{\nu}}) < E_{\mathrm{F}} < \min_{\boldsymbol{k}\in\mathrm{BZ}}(\epsilon_{\boldsymbol{k},\tilde{\nu}+1})$, no states are available for the electronic transport at energies close to E_{F} and the system is therefore insulating. These insulating phases of matter are often referred to as "Bloch insulators", and theirs topology is actually the topology of the band structures associated to such phases.

The crystal wavevector $\boldsymbol{k}$ lies in the first Brillouin zone, which is a finite region of the reciprocal space. Because of the translational symmetry of such models, the opposite edges of the Brillouin zone can be identified one another, making the Brillouin zone equivalent to a torus. The "band structure" of a crystal is defined as the mapping from the crystal wavevector[1] $\boldsymbol{k} \in \mathbb{T}_2$, to the Bloch Hamiltonian $\hat{H}(\boldsymbol{k})$ which is an Hermitian operator, defined below, derived from the main Hamiltonian of the system. Band structures where the eigenvalues of $\hat{H}(\boldsymbol{k})$ show an energy gap, can be classified topologically by considering the equivalence classes of Bloch Hamiltonians $\hat{H}(\boldsymbol{k})$ that can be continuously deformed into one another without closing the energy gap. These classes are characterized by a topological invariant $n \in \mathbb{Z}$, called the Chern invariant. The theory of the Chern invariant is rooted in the mathematics of fiber bundles [136], but it can be understood physically in terms of the Berry curvature [137, 138] associated with the Bloch wave functions.

The concepts of Barry phase and Berry curvature were introduced by Sir Michael

[1] For the sake of concreteness, in this Chapter we suppose to work in two-dimensions, so that the Brillouin zone is isomorphic to the 2-torus $\mathbb{T}_2$.

Berry in a seminal paper [137] concerning the adiabatic evolution of an eigenenergy state when some external parameters are changed slowly and cyclically, i.e. so that they describe a closed loop in the parameter space. In the absence of degeneracy, the eigenstate will come back to itself at the end the loop, but there will be a phase difference equal to the time integral of the energy (divided by $\hbar$) plus an extra, which is now commonly known as the Berry phase.

Thanks to the Bloch theorem [17], the eigenstates $|\boldsymbol{k}\nu\rangle$ of a periodic Hamiltonian $\hat{H}_0$ satisfy the eigenvalue equation

$$\hat{H}_0|\boldsymbol{k}\nu\rangle = \epsilon_{\boldsymbol{k}\nu}|\boldsymbol{k}\nu\rangle. \tag{4.13}$$

Thanks to the translational invariance of the Hamiltonian, the Bloch eigenvalues can be written as

$$\langle \boldsymbol{r}|\boldsymbol{k}\nu\rangle = e^{i\boldsymbol{k}\cdot\boldsymbol{r}}\langle \boldsymbol{r}|u_{\boldsymbol{k}\nu}\rangle = e^{i\boldsymbol{k}\cdot\boldsymbol{r}}u_{\boldsymbol{k}\nu}(\boldsymbol{r}), \tag{4.14}$$

where $|u_{\boldsymbol{k}\nu}\rangle$ are the periodic parts of the Bloch wavefunctions. Thanks to the previous decomposition of the eigenstates, and defining the Bloch Hamiltonian as

$$\hat{H}(\boldsymbol{k}) \equiv e^{-i\boldsymbol{k}\cdot\boldsymbol{r}}\hat{H}_0 e^{i\boldsymbol{k}\cdot\boldsymbol{r}}, \tag{4.15}$$

it is immediate to show that the eigenvalue equation Eq. (4.13) is equivalent to

$$\hat{H}(\boldsymbol{k})|u_{\boldsymbol{k}\nu}\rangle = \epsilon_{\boldsymbol{k}\nu}|u_{\boldsymbol{k}\nu}\rangle. \tag{4.16}$$

The Berry curvature for the Bloch wavefunctions $|u_{\boldsymbol{k}\nu}\rangle$ is defined as [138]

$$\Omega^{\nu}_{\alpha\beta}(\boldsymbol{k}) = i\sum_{\nu'\neq\nu}\frac{\langle u_{\boldsymbol{k}\nu}|\partial_{\boldsymbol{k}_\alpha}\hat{H}(\boldsymbol{k})|u_{\boldsymbol{k}\nu'}\rangle\langle u_{\boldsymbol{k}\nu'}|\partial_{\boldsymbol{k}_\beta}\hat{H}(\boldsymbol{k})|u_{\boldsymbol{k}\nu}\rangle - (\alpha\leftrightarrow\beta)}{(\epsilon_{\boldsymbol{k}\nu}-\epsilon_{\boldsymbol{k}\nu'})^2}, \tag{4.17}$$

where α and β are cartesian indexes. The Berry curvature is a gauge invariant vector field whose flux through the Brillouin zone gives topological classification of the band structure [136, 138]. The Chern invariant $n \in \mathbb{Z}$, characterizing classes of equivalence of insulating Bloch Hamiltonians, is given by the following expression

$$n = \sum_{\nu\in \text{ occupied bands}}\frac{1}{2\pi}\int_{\text{BZ}} dk_\alpha dk_\beta \Omega^{\nu}_{\alpha\beta}(\boldsymbol{k}). \tag{4.18}$$

In general, the Berry curvature integrated over a closed manifold is *always* quantized in the units of 2π, as showed e.g. in Ref. [8], Chapter 3. If a Bloch Hamiltonian $\hat{H}(\boldsymbol{k})$ is in an equivalence class whose Chern invariant, i.e. the integral of the Berry curvature over the Brillouin zone, is different from 0 is said to be topologically non-trivial. From a mathematical perspective, a nonzero Chern number is a manifestation of the impossibility to choose a global gauge that is continuous and single valued over the entire Brillouin zone [8].

A topologically non-trivial class of insulating band structures is thus characterized by a nonzero Chern number, and as long as the energy gap is not closed, the Bloch Hamiltonian can be freely perturbed without changing its topological classification.

Quite remarkably, it turns out that the Chern number, Eq. (4.18) is strongly related with an observable quantity, being the Hall conductance. The Hall conductance of a two-dimensional material is the off-diagonal term of the conductivity tensor Eq. (2.94). From the Kubo formula of the conductivity, Eqs. (2.95) and (2.98), it is quite easy to check that in the static limit $\omega \to 0$, the intra-band contribution to the conductivity vanishes (if the Fermi energy is within the energy gap), whereas the inter-band contributions is equal to (for $\alpha \neq \beta$)

$$\sigma^{\text{inter}}_{\alpha\beta}(\omega = 0) = -g\frac{e^2}{h}\frac{1}{2\pi}\sum_{\nu\in \text{ occupied bands}}\int_{\text{BZ}} dk_\alpha dk_\beta \Omega^\nu_{\alpha\beta}(\boldsymbol{k}) = -g\frac{e^2}{h}n, \tag{4.19}$$

where g is the degeneracy factor and the small temperature limit $T \to 0$ is understood. The Hall conductivity is therefore proportional to the Chern number, where the proportionality constant depends only on fundamental constants. Let us insist on the observation that any perturbation or disorder added to the Hamiltonian which, however, does not close the energy gap, leaves the Chern number (and so the Hall conductivity) unaltered. This is the mathematical explaination of the exceptionally flat plateaus of the Hall conductivity observed in quantum Hall effect experiments, as discussed in Section 1.3.

To gather more insight, it is interesting to note that a necessary condition to have topologically non-trivial band structures is to have broken time-reversal symmetry. Indeed, it is easy to show that if the system is time-reversal symmetric, it follows that [138] $\Omega^\nu_{\alpha\beta}(-\boldsymbol{k}) = -\Omega^\nu_{\alpha\beta}(\boldsymbol{k})$ and the integral in Eq. (4.19) vanishes trivially. In addition to this, if the system is also symmetric under spatial inversion, the Berry curvature satisfy $\Omega^\nu_{\alpha\beta}(-\boldsymbol{k}) = \Omega^\nu_{\alpha\beta}(\boldsymbol{k})$. Therefore, for crystals with simultaneous time-reversal and spatial inversion symmetry the Berry curvature vanishes identically throughout the Brillouin zone.

The previous discussion on the symmetry of the Berry curvature entails that any time-reversal symmetric Bloch insulator is in the topologically trivial Chern class. For these time-reversal invariant models, however, it exists a different topological classification proposed in 2005 by Kane and Mele [85, 86]. The key to understand this new topological class is to examine the role of time-reversal symmetry for spin 1/2 particles.

Time-reversal symmetry is represented by an antiunitary operator

$$\hat{\Theta} = \exp(i\hat{\sigma}_y/\hbar)\hat{K} \tag{4.20}$$

where $\hat{S}_y$, is the spin operator along the y direction, whose matrix elements are given by the Pauli matrix σ_y if the spin quantization axis is chosen along z, and $\hat{K}$ is the complex conjugation. For spin 1/2 electrons, $\hat{\Theta}$ has the property $\hat{\Theta}^2 = -\mathbb{1}$. A time-reversal invariant Bloch Hamiltonian must satisfy

$$\hat{\Theta}\hat{H}(\boldsymbol{k})\hat{\Theta}^{-1} = \hat{H}(-\boldsymbol{k}), \tag{4.21}$$

and, as in the case of Chern insulators, it is possible to classify the equivalence classes of Hamiltonians satisfying this constraint and that can be smoothly deformed without

closing the energy gap. The Chern number, as said, is $n = 0$, but there is an additional $\mathbb{Z}_2$ topological invariant with two possible values[2], $\nu = 0$ or 1 [85, 86].

The calculation of the topological invariant ν is quite simple if the 2D system conserves the perpendicular spin $\hat{S}_z$. In this case the up and down spins have independent Chern numbers $n_\uparrow$ and $n_\downarrow$. Time-reversal symmetry requires $n_\uparrow + n_\downarrow = 0$, but the difference $n_\uparrow - n_\downarrow$ defines a quantized spin Hall conductivity. The $\mathbb{Z}_2$ topological invariant ν is then simply

$$\nu = [(n_\uparrow - n_\downarrow)/2] \bmod 2. \tag{4.22}$$

More general definitions of ν are available when $\hat{S}_z$ nonconserving terms are added to the Bloch Hamiltonian (see e.g. Ref. [7]).

Akin to the Chern number n, the $\mathbb{Z}_2$ topological invariant ν is related to physical observables connected to the electronic transport. In particular, as briefly mentioned before, with an argument analogous to the case of the Chern number, and using the definition in Eq. (4.22), it is possible to show that ν is proportional to the spin Hall conductivity. More details on this subject, however, are postponed to the next section where edge states and the concept of bulk-boundary correspondance are introduced.

Let us now conclude the section clarifying some basic nomenclature. Two-dimensional insulating electron systems which show non-trivial topology in the Chern sense, i.e. $n \neq 0$ are called "Chern insulators". On the other hand, time-reversal symmetric insulators displaying a non-zero $\mathbb{Z}_2$ topological classification are often referred to as "quantum spin Hall insulators" (owing to the aforementioned quantized spin Hall conductivity), or more simply "two-dimensional topological insulators" (2DTIs). We will stick to the latter choice, which is arguably the most common in literature.

Edge states and bulk boundary correspondance

A fundamental consequence of the topological classification of gapped band structures is the existence of gapless conducting states at interfaces where the topological invariant changes. The existence of such edge states is deeply related to the topology of the bulk electronic state. The existence of edge states in topologically non-trivial crystal is readily explained imagining an interface where the Bloch Hamilltonian slowly interpolates between a topologically non-trivial insulator (n or $\nu \neq 0$) and a trivial insulator $n = \nu = 0$. Somewhere along the way the energy gap has to vanish because otherwise it would be impossible for the topological invariant to change. There will therefore be low energy electronic states bound to the region where the energy gap passes through zero. This interplay between topology and gapless modes is ubiquitous in physics and has appeared in many contexts.

For Chern insulators, the topological invariant n can be showed to be the number of edge states at the interface with topologically trivial insulators. The edge states of Chern insulators are said to be *chiral*, i.e. they can flow along the edge only in one of the two possible directions, as showed in Fig. 4.2. This observation can be leveraged to

[2]The $\mathbb{Z}_2$ topological invariant should not be confused with a band index. The meaning of the symbol ν, however, should be self-evident from the context.

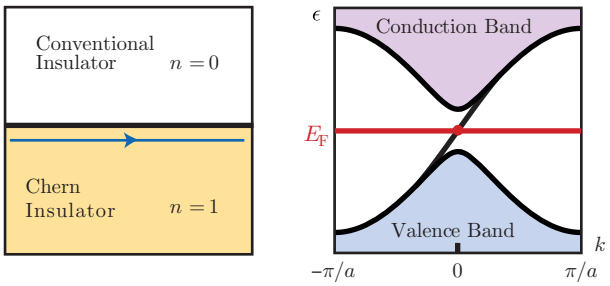

FIGURE 4.2: Illustration the chiral edge modes of Chern insulators. On the left, a Chern insulator with $n = 1$ is interfaced with a trivial insulator ($n = 0$). At the interface, where the energy gap closes, a chiral edge mode is established. On the right panel, a schematic of the band structure of this system. The system is periodic in the direction parallel to the interface, and Bloch theorem can be used. The bulk conduction and valence bands, are joined by an edge mode traversing the energy gap. Figure adapted from Ref. [7].

explain the perfect quantization of the Hall conductance. Indeed, an electron moving along the edge of the Chern insulator, cannot be scattered in the direction opposite to his current motion simply because, due to the chirality of the edge mode, there are no available states for transport in the opposite direction, and perfect quantization follows. The chiral edge states in Chern insulators can be seen explicitly by solving the Haldane model (presented in the following section) in a semi-infinite geometry. We mention that the quantized Hall conductance and its related edge states were observed for the first time in Ref. [82]. The quantum Hall effect is observed in the presence of a magnetic field, whereas our review of the Chern insulators is based only on the intrinsic band structure of the sample. Although the theoretical description of quantum Hall systems and Chern insulators is apparently different, it is indeed possible to introduce "magnetic Bloch bands" to describe the electronic states of a 2D electron system threaded by a perpendicular magnetic fields. Thanks to this technique, due to Peierls, it is seen that quantum Hall systems and Chern insulators share the same topological classification.

Edge states are also present in 2DTIs, and their existence is guaranteed by the topological invariant ν itself. The $\mathbb{Z}_2$ invariant ν, indeed, is the number of pairs of edge states modulo 2. In the case of 2DTIs, edge states are always originated in pairs. In each pair there are two counter-propagating modes, one for each spin direction. The fact that in $\mathbb{Z}_2$ topological insulators opposite spins propagate in opposite directions it is called "spin-momentum locking", and the edge states are said to be *helical* (as opposed to the chiral states of Chern insulators), and are schematically showed in Fig. 4.3. Thanks to simple symmmetry arguments it is also possible to show a conductance quantization in 2DTIs, akin to the one in Chern insulators. For spinful time-reversal invariant insulators where many-particle effects are absent, it is possible to show that the eigenstates are at least twofold degenerate. This results is known as Kramers' theorem, and follows from the relation $\hat{\Theta}^2 = -\mathbb{1}$ valid in for spin 1/2 particles. Indeed, suppose that $|\phi\rangle$ is an eigenstate of the Hamiltonian $\hat{H}_0|\phi\rangle = \epsilon_\phi|\phi\rangle$. It is evident that

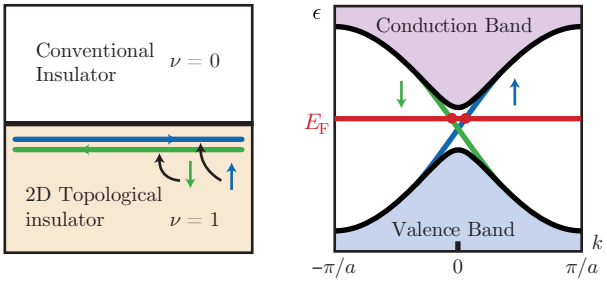

Figure 4.3: Illustration the helical edge modes of 2DTIs. On the left, a 2DTI with $\nu = 1$ is interfaced with a trivial insulator ($\nu = 0$). At the interface, where the energy gap closes, a couple of counterpropagating edge modes is established. On the right panel, a schematic of the band structure of this system. The system is periodic in the direction parallel to the interface, and Bloch theorem can be used. The bulk conduction and valence bands, are joined by the two helical edge modes traversing the energy gap. Because they have opposite velocity $\sim d\epsilon(k)/dk$, their slope on the $\epsilon - k$ plane is opposite. Figure adapted from Ref. [7].

$|\phi\rangle$ and $\hat{\Theta}|\phi\rangle$ belong to the same energy eigenvalue ϵ_ϕ, because the Hamiltonian is time-reversal symmetric, and hence commutes with $\hat{\Theta}$. If $|\phi\rangle$ and $\hat{\Theta}|\phi\rangle$ are not degenerate, they have to represent the *same* state. In the degenerate case one will have $\hat{\Theta}|\phi\rangle = c|\phi\rangle$ for some constant c. This mean $\hat{\Theta}^2|\phi\rangle = |c|^2|\phi\rangle$, which is impossible necause $|c|^2 \neq -1$. The helical modes of 2DTIs are Kramers pairs, and we now show through the Landauer-Büttiker formalism that if time-reversal symmetry is ensured and $\nu = 1$, i.e. there is an odd number of pairs of helical edge states, then there is always going to be at least a single mode that is transmitted with unit probability. In particular, if there is only one pair of helical modes, then it follows that the conductivity will be quantized to $2e^2/h$.

Now, suppose that there are N pairs of helical edge modes in the 2DTI. We label the incident states (i.e. the ones created by the operators $\hat{a}_{\alpha,n}$ in Section 4.1) as $|m, \alpha\rangle$, with $m = 1, \ldots, N$. The scattered states are the time-reversed partners of the incoming states, so they are given by $\hat{\Theta}|m, \alpha\rangle$. The electronic state in the lead α are superpositions of incoming and scattered states,

$$|\psi, \alpha\rangle = \sum_{m=1}^{N} a_{\alpha,m}|m, \alpha\rangle + b_{\alpha,m}\hat{\Theta}|m, \alpha\rangle. \tag{4.23}$$

The coefficients $a_{\alpha,m}$ and $b_{\alpha,m}$ are related by the scattering matrix, as in Eq. (4.1). There are a total of $2N$ incoming and $2N$ scattered modes, so the scattering matrix is a $2N \times 2N$ matrix. As explained in Section 4.1, the scattering matrix is also unitary, and it is conveniently splitted into reflection and transmission blocks of dimension $N \times N$,

$$S \equiv \begin{pmatrix} r & t \\ t' & r' \end{pmatrix}. \tag{4.24}$$

In order to distrupt the electron transport along the edges of the 2DTI, one can try to add disorder in the Hamiltonian. If the electron transport is affected by the disorder,

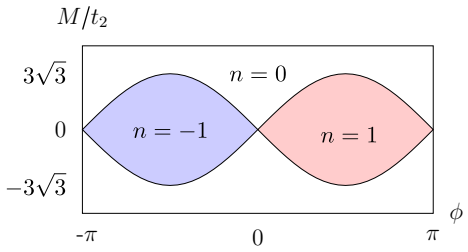

FIGURE 4.4: Topological phase diagram of the Haldane model, Eq. (4.27). Figure adapted from Ref. [139].

then in the limiting case of strong disorder one should be able to achieve the situation where there is no transmission at all, $t = t' = 0$. In this case, all modes must be reflected back, so the reflection blocks of the scattering matrix become unitary, $rr^\dagger = r'r'^\dagger = \mathbb{1}_{N\times N}$. Thanks to the fact that the electronic states in the α-th lead, Eq. (4.23), are linear combinations of Kramers partners, and applying to them the time-reversal operator $\hat{\Theta}$, it is easy to show that the scattering matrix has to be antisymmetric $S = -S^{\mathrm{T}}$. However, if $S = -S^{\mathrm{T}}$ and the electronic transport is disrupted so that $t = t' = 0$, then the $N \times N$ reflection matrix must be both unitary, $rr^\dagger = \mathbb{1}_{N\times N}$, and antisymmetric, $r = -r^{\mathrm{T}}$. When the 2DTI is topologically non-trivial $\nu = 1$, the pairs of edge modes are odd, and therefore N is odd. In the case of odd N the two conditions on the unitarity and antisymmetry of r cannot be satisfied simultaneously, since any odd-dimensional antisymmetric matrix must have a single zero eigenvalue, while unitary matrices only have eigenvalues with unit norm. Now, because $r = -r^{\mathrm{T}}$ is enforced by time-reversal symmetry, which we assume by hypothesis, the unitarity condition $rr^\dagger = \mathbb{1}_{N\times N}$ must be released. In this case, it is impossible to have $t = 0$. Furthermore, this zero eigenvalue of r means that there is always a single mode that is transmitted with unit probability, proving our statement. To conclude, Kramers theorem implies that Anderson disorder in a 2DTI cannot induce back-scattering at a 2DTI edge, yielding conductance quantization against elastic disorder [7, 8, 87, 88, 89, 90].

4.2.2 The Haldane model

In 1988, D. Haldane proposed a tight-binding model [83] which realises a Chern insulator. In the Haldane model the time-reveral symmetry breaking necessary to have nonzero Chern number is realised thanks to second-neighbour hopping between the sites of an hexagonal lattice. The building block of the Haldane model is the tight-binding Hamiltonian of single-layer graphene, Eq. (1.5), presented in the first Chapter and reported here for convenience

$$\mathcal{H}(\boldsymbol{k}) = t \begin{pmatrix} 0 & f(\boldsymbol{k}) \\ f^*(\boldsymbol{k}) & 0 \end{pmatrix}. \tag{4.25}$$

The Haldane model can be constructed by adding terms to Eq. (4.25) on the basis of straightforward symmetry arguments. First, the model in Eq. (4.25) is not an insulator,

and a gap should be opened. It is fairly simple to do that by adding "mass" term, i.e. an on-site term whose sign is opposite for different sublattices. If $M > 0$ is the magnitude of the mass term, then Eq. (4.25) becomes

$$\mathcal{H}(\boldsymbol{k}) = t \begin{pmatrix} 0 & f(\boldsymbol{k}) \\ f^*(\boldsymbol{k}) & 0 \end{pmatrix} + M\sigma_z, \tag{4.26}$$

where σ_z is the third Pauli matrix. The previous Hamiltonian, however, is still time-reversal symmetric and thus is in the trivial topological Chern class. To break time-reversal symmetry it is sufficient to add a complex second neighbour hopping term $\sim t_2 e^{i\phi}$, where $e^{i\phi}$ can be interpreted as the Aharonov-Bohm phase generated by the presence of an effective perpendicular magnetic field. For the sites of an hexagonal lattice the second neighbours belong to the same sublattice of the starting site. Therefore, calculating the matrix elements of the second neighbour hopping term with energy $\sim t_2 e^{i\phi}$ on the basis of Bloch states Eq. (1.3) adds diagonal contributions to Eq. (4.26), which becomes

$$\begin{aligned} \mathcal{H}_{\mathrm{H}}(\boldsymbol{k}) =& t \begin{pmatrix} 0 & f(\boldsymbol{k}) \\ f^*(\boldsymbol{k}) & 0 \end{pmatrix} + 2t_2 \cos(\phi) \sum_{i=1}^{3} \cos(\boldsymbol{k}\cdot\boldsymbol{b}_i) \mathbb{1}_{2\times 2} + \\ &+ \left[M - 2t_2 \sin(\phi) \sum_{i=1}^{3} \sin(\boldsymbol{k}\cdot\boldsymbol{b}_i) \right] \sigma_z. \end{aligned} \tag{4.27}$$

Here, the vectors $\pm\boldsymbol{b}_i$ with $i = 1, 2, 3$ identify the second-neighbours of a site in the hexagonal lattice considered. With the choice of primitive translation vectors as in Eq. (1.1a), one has

$$\boldsymbol{b}_1 = \boldsymbol{a}_1, \tag{4.28a}$$

$$\boldsymbol{b}_2 = -\boldsymbol{a}_2, \tag{4.28b}$$

$$\boldsymbol{b}_3 = \boldsymbol{a}_2 - \boldsymbol{a}_1. \tag{4.28c}$$

The Chern number of the Haldane model can be calculated analytically (see e.g. Ref. [83, 139]), and is given by

$$n = \frac{1}{2} \left[\mathrm{sign}\left(\frac{M}{t_2} + 3\sqrt{3}\sin(\phi) \right) - \mathrm{sign}\left(\frac{M}{t_2} - 3\sqrt{3}\sin(\phi) \right) \right]. \tag{4.29}$$

From the analytical expression of the Chern number given in the previous equation, it follows the phase diagram showed in Fig. 4.4. We conclude the Section mentioning that Hamiltonians analogous to the one of the Haldane model can also be designed for different Bravais lattices. An example for the square lattice is given e.g. in Ref. [8], Chapter 8.

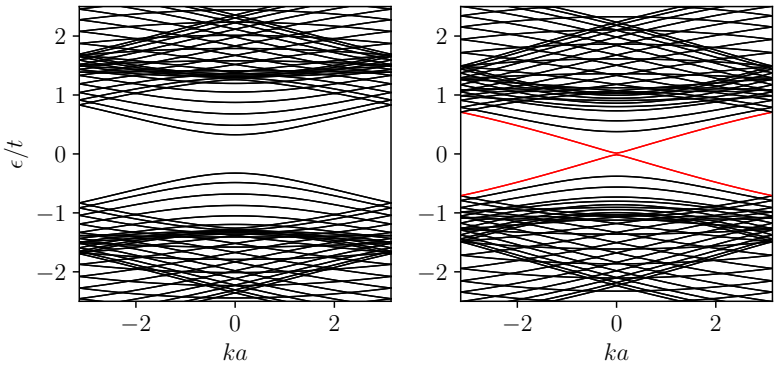

FIGURE 4.5: Band structure of the Kane-Mele model implemented in a zig-zag nanoribbon (see Section 1.1.2) of width $W = 10a$, a being the lattice parameter. The Kane-Mele Hamiltonian is given in Eqs. (4.32) and (4.33). Left panel: $M/t_2 = \frac{3}{2}3\sqrt{3}$, corresponding to the trivial insulator. Right panel: $M/t_2 = \frac{1}{2}3\sqrt{3}$ corresponding to the $\mathbb{Z}_2$ topological insulating phase.

4.2.3 The Kane-Mele model

Research on spin-orbit coupling in graphene led Kane and Mele [85, 86] to propose a model consisting in two time-reversed copies of the Haldane model. In the Kane-Mele model the spin degree of freedom is taken into account, and the overall model is time-reversal symmetric. Taken separately, however, the Hamiltonians for the two spins polarizations violate time reversal symmetry and are equivalent to Haldane's model Eq. (4.27) for spinless electrons. Following Ref. [85], it is convenient to work with a basis where the sublattice and spin degrees of freedom are ordered as such:

$$\{|A\uparrow\rangle, |A\downarrow\rangle, |B\uparrow\rangle, |B\downarrow\rangle\}. \tag{4.30}$$

In the above basis, the Kane-Mele model may be written in terms of the identity matrix, 5 Dirac matrices Γ_a and their 10 commutators $\Gamma_{ab} = [\Gamma_a, \Gamma_b]/(2i)$. The Dirac matrices are chosen according to the following convention

$$\Gamma_{(1,2,3,4,5)} = (\sigma_x \otimes I, \sigma_z \otimes I, \sigma_y \otimes \tau_x, \sigma_y \otimes \tau_y, \sigma_y \otimes \tau_z), \tag{4.31}$$

where the Pauli matrices σ_k and τ_k represent the sublattice and spin indices. In the sublattice-spin basis Eq. (4.30), the time-reversal operator is is given by $\Theta|u\rangle = i(\mathbb{1}_{2\times2}\otimes \tau_y)|u\rangle^*$. The five Dirac matrices are even under time-reversal $\Theta\Gamma^a\Theta^{-1} = \Gamma^a$ while the 10 commutators are odd, $\Theta\Gamma^{ab}\Theta^{-1} = -\Gamma^{ab}$.

With the definitions above, the Kane-Mele Hamiltonian is written as

$$\mathcal{H}_{\mathrm{KM}}(\boldsymbol{k}) = \sum_{a=1}^{5} d_a(\mathbf{k})\Gamma_a + \sum_{a<b=1}^{5} d_{ab}(\boldsymbol{k})\Gamma_{ab}, \tag{4.32}$$

where the non-zero $d(\boldsymbol{k})$'s are given by

$$\begin{aligned} d_1 &= t[1 + 2\cos(q_x)\cos(q_y)], \\ d_{12} &= -2t\cos(q_x)\sin(q_y), \\ d_2 &= M, \\ d_{15} &= t_2[2\sin(2q_x) - 4\sin(q_x)\cos(q_y)]. \end{aligned} \tag{4.33}$$

Here, $q_x \equiv k_x a/2$, $q_y \equiv \sqrt{3}k_y a/2$ and a is the lattice parameter of the hexagonal lattice. In Eq. (4.33), we employ the same notation used in the previous section for the Haldane model, so M is the mass term, and t_2 is the second-neighbour hopping amplitude. With respect to the Haldane model, Eq. (4.27), the Kane-Mele Hamiltonian above is written by setting the phase ϕ to $\phi = \pi/2$. The time-reversal invariance of $\mathcal{H}_{\rm KM}(\boldsymbol{k})$ is reflected in the symmetry (antisymmetry) of d_a (d_{ab}) under $\mathbf{k} \to -\mathbf{k}$.

Kane and Mele showed [85] that their Hamiltonian Eq. (4.32) is topologically *non-trivial* when $M/t_2 < 3\sqrt{3}$, i.e. the $\mathbb{Z}_2$ topological invariant is $\nu = 1$. In Fig. 4.5 we show the energy bands of the Kane-Mele model implemented in a zig-zag nanoribbon (see Section 1.1.2). The left panel shows the trivial case $M/t_2 > 3\sqrt{3}$, which is obviously a Bloch insulator. The right panel, on the other hand, shows the topological case $M/t_2 < 3\sqrt{3}$, where a pair of conducting edge modes (highlighted in red) connect the bulk valence bands with the bulk conduction bands. The modes highlighted in red are localized at the edges of the nanoribbon, and are a manifestation of the topological phase transition occurring at the interface between the Kane-Mele nanoribbon and the vacuum.

We conclude this Section with two remarks. First, as for the case of the Haldane model, an Hamiltonian analogous to the one by Kane-Mele can be realised for square lattices [8]. The implementation on the square lattice corresponds to the so-called "Bernevig-Hughes-Zhang model" introduced in Ref. [88]. The BHZ model is relevant for $\mathbb{Z}_2$ topological insulators realised in semiconducting heterostructures. As a final remark we also mention that a recent work [140] has shown that a naturally occurring layered mineral (jacutingaite) realizes the Kane-Mele model.

5

Failure of conductance quantization in 2DTIs due to magnetic impurities

In this Chapter we discuss a mechanism mediated by electron-electron interactions which breaks the topological protection of 2DTI edge modes discussed in Section 4.2.1. The proposal of this mechanism is motivated by the fact that all experimental measurements on 2DTIs show deviations from the expected quantized value of conductance $2e^2/h$. These deviations are observed particularly in small-gap semiconductor heterostructures such as HgTe/CdHgTe and InAs/GaSb quantum wells [84, 91, 92, 95, 96], but also in atomically-thin crystals such as WTe_2 [52, 53]. On the other hand, the existence of conducting edge modes was clearly demonstrated via non-local measurements in Refs. [91, 92, 95, 96]. Semiconducting heterostructures were extensively studied in the low-temperature regime (below 4 K) [84, 96] because of their small energy gap. For channel lengths L shorter than ~ 1 μm, fluctuations of the conductance around the quantized value $2e^2/h$ were observed as a function of the back gate voltage. For longer channels, even the average conductance was found to deviate from $2e^2/h$ and even totally suppressed [97], when the edge was perturbed by a scanning tip. Among the 2DTIs realized by semiconducting heterostructures, the best results were obtained thanks to Si doping [96]. In these samples, conductance is quantized up to 1-2% at very low temperatures. Monolayers of WTe_2 exhibit [52] conductance quantization up to 100 K, making them the 2DTIs existing at the highest temperatures up to date, though displaying quantization only in short channels ($L \lesssim 100$ nm). The cause of the breakdown of conductance quantization is still poorly understood. Clearly, one possibility is the presence of an external magnetic field [52, 84] or of magnetic impurities [141, 142, 143], which induce spin-flip scattering (thus back-scattering). Magnetic impurities, however, are rare both in materials grown by molecular beam epitaxy [84, 91, 92, 95, 96] and in mechanically-exfoliated crystals [52, 53], but explain

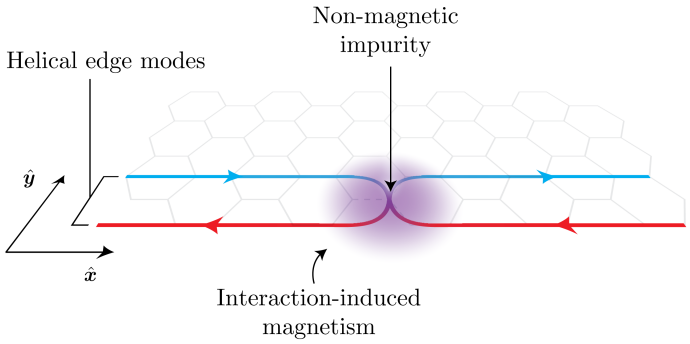

FIGURE 5.1: A cartoon of the physical process introduced and analyzed in this chapter. At an edge of a 2DTI, a non-magnetic short-range impurity can effectively act as a magnetic one due to its dressing via onsite electron-electron interactions. The latter favor the formation of a local magnetic moment with non-zero in-plane components. These cause spin mixing and hence back-scattering.

experimental data in the "extrinsic" case in which magnetic dopants are deliberately added to pristine three-dimensional TI samples [144, 145]. Coupling between opposite edges, in very narrow samples or in purposely fabricated point contacts, can also induce back-scattering [146, 147, 148], with no need of time-reversal symmetry breaking. Importantly, the breakdown of conductance quantization could arise from two-body interactions, because the Kramers theorem is valid only for one-particle electronic states. In Ref. [87] it was suggested that electron-electron (electron-electron) interactions in 2DTIs can cause back-scattering through a third-order perturbation-theory scattering process, while the spontaneous breaking of time-reversal symmetry due to interactions was studied in Ref. [149]. Interactions are also at the core of other mechanisms proposed to explain the spoiling of conductance quantization in 2DTIs. Back-scattering resulting from weak electron-electron interactions and an impurity potential, in the absence of axial spin symmetry, was considered in Ref. [150]. Deviations from $2e^2/h$ were found to scale like T^4, at low temperatures T. The coupling of edge modes to charge puddles, naturally present in real samples, was accounted for in Refs. [151, 152] and found to lead to a correction to the conductance scaling like T^4 at low temperatures. In contrast, recent experiments [52] show nearly temperature-independent conductance in 2DTIs. Another mechanism that leads to the breakdown of conductance quantization is related to the edge reconstruction [153], which can occur when the confining potential of the 2DTIs edges is not sufficiently sharp. Finally, the effects of Rashba spin-orbit coupling [154, 155], phonons [156], nuclear spins [157, 158], disordered probes [159], coupling to external baths [160], and noise [161] have also been analyzed.

The simple mechanism proposed in this Chapter is based on the interplay between non-magnetic scatterers and electron-electron interactions, which leads to the breakdown of conductance quantization in 2DTIs even at zero temperature, and can result in the total suppression of the conductance. Starting from the single-particle Kane-Mele Hamiltonian [85, 86] describing a 2DTI ribbon, we consider the presence of short-range non-magnetic impurities at its edges (see Fig. 5.1). As expected, this leads to an enhancement of the local DOS, as in the case of midgap states in graphene [2] and

three-dimensional TIs [162, 163, 164]. In the presence of Hubbard-like electron-electron interactions, using the self-consistent unrestricted Hartree-Fock method, we show that these short-range defects favor the formation of local magnetic moments, leading to the spontaneous breakdown of time-reversal symmetry and back-scattering.

5.1 Model

We consider the Kane-Mele model of 2DTI, Eq. (4.32). We write the Hamiltonian on the basis of the atomic orbitals localized at the sites of an Hexagonal lattice [8, 85, 86]. The "real space representation" is employed in order to add an Hubbard term [165, 166] to include electron-electron interactions in the model,

$$\hat{\mathcal{H}}_{\mathrm{KM}} = t \sum_{\langle ij\rangle,\alpha} \hat{c}^{\dagger}_{i\alpha}\hat{c}_{j\alpha} + it_2 \sum_{\langle\langle ij\rangle\rangle,\alpha,\beta} \nu_{ij}\hat{c}^{\dagger}_{i\alpha}\tau_z^{\alpha\beta}\hat{c}_{j\beta} + U\sum_i \hat{c}^{\dagger}_{i\uparrow}\hat{c}_{i\uparrow}\hat{c}^{\dagger}_{i\downarrow}\hat{c}_{i\downarrow} \,. \tag{5.1}$$

In Eq. (5.1), $\hat{c}^{\dagger}_{i\alpha}$ ($\hat{c}_{i\alpha}$) creates (destroys) an electron of spin α on the i-th site of a honeycomb lattice and τ_z is a 2×2 Pauli matrix acting on spin space. The sums over $\langle ij\rangle$ ($\langle\langle ij\rangle\rangle$) are intended between i and j being first (second) neighbours. The parameters t and t_2 are hopping energies between first and second neighboring sites, respectively. The second term in Eq. (5.1) is the term added by Kane and Mele [85, 86] as a time-reversal invariant version of the Haldane model [83], and is responsible for the existence of helical edge modes, as discussed in Section 4.2.3. The factor ν_{ij} is equal to ± 1, with $\nu_{ji} = -\nu_{ij}$, depending on the orientation of the two nearest-neighbor bonds the electron traverses in going from site j to i: $\nu_{ij} = -1(+1)$ if the electron reaches the second neighbour going (anti-)clockwise. The last term accounts for local electron-electron repulsive interactions. Such a two-body term will be treated within mean-field theory. The key point here is that we are not interested in dealing accurately with strong correlations in 2DTIs [166]. Our aim is to utilize the simplest approach that enables us to capture an important effect stemming from local electron-electron interactions in the weak-coupling $U/t < 1$ regime. In this regime, mean-field theory is expected to be accurate and allows us to obtain an effective single-particle Hamiltonian, which can be used in combination with Landauer-Büttiker theory (see Ref. [24] and Section 4.1) to compute transport properties.

We consider a ribbon extending in the region $0 \le x \le L$, $0 \le y \le W$, with armchair edges and periodic boundary conditions in the $\hat{\boldsymbol{x}}$-direction (see Fig. 5.1). In order to investigate the effect of atomic-scale defects, we assume the presence of one or two vacancies, which can be accounted for by dropping from the sums in Eq. (5.1) terms involving the lattice sites where the atoms are missing. The case of many vacancies can be tackled in a straightforward manner but lies beyond the scope of this work. Our main point, here, is to demonstrate the importance of local electron-electron interactions in dressing short-range non-magnetic impurities in a magnetic fashion.

Using the usual Hartree-Fock decoupling [30], we can express (5.1) in the unrestricted Hartree-Fock approximation [167, 168] as

$$\begin{aligned}\hat{\mathcal{H}}_{\rm KM} \simeq t\sum_{\langle ij\rangle,\alpha}\hat{c}^{\dagger}_{i\alpha}\hat{c}_{j\alpha} + it_2\sum_{\langle\langle ij\rangle\rangle,\alpha,\beta}\nu_{ij}\hat{c}^{\dagger}_{i\alpha}\tau_z^{\alpha\beta}\hat{c}_{j\beta} + \\ \frac{U}{2}\sum_{i,\alpha,\beta}\hat{c}^{\dagger}_{i\alpha}(n_i\mathbb{1}^{\alpha\beta} - \boldsymbol{m}_i\cdot\boldsymbol{\tau}^{\alpha\beta})\hat{c}_{i\beta} - \frac{U}{4}\sum_i(n_i^2 - |\boldsymbol{m}_i|^2)\ ,\end{aligned} \tag{5.2}$$

where $\mathbb{1}$ is the 2×2 identity matrix, $\boldsymbol{\tau} = (\tau_x, \tau_y, \tau_z)$ is a vector of 2×2 Pauli matrices acting on spin space, and we have defined the local mean electron density

$$n_i = \langle\sum_{\alpha} c^{\dagger}_{i\alpha}c_{i\alpha}\rangle \tag{5.3}$$

and the local mean spin polarization $\boldsymbol{s}_i = \hbar\boldsymbol{m}_i/2 = \hbar(m_i^x, m_i^y, m_i^z)/2$ with

$$\boldsymbol{m}_i = \langle\sum_{\alpha,\beta} c^{\dagger}_{i\alpha}\boldsymbol{\tau}^{\alpha\beta}c_{i\beta}\rangle\ , \tag{5.4}$$

which must be determined self-consistently. In order to do so, we use an iterative algorithm [169] which involves the exact diagonalization of the Hamiltonian (5.2). Our calculations were performed at temperature $T = 0$, but can easily be extended to finite temperature. For $t_2 = 0$, i.e. when the second neighbour hopping term is neglected, the lattice is bipartite in the sense of Ref. [170] and Lieb theorem holds, so that a non-zero ground-state spin polarization rigorously follows from sublattice imbalance (i.e. different number of sites in the two sublattices). As we will see below, a ground-state spin polarization occurs even for $t_2 \neq 0$—i.e. in the topological phase of (5.1) with gap $\delta_{\rm g} = |6\sqrt{3}t_2|$ [85]—where Lieb theorem does not apply. All numerical results below refer to a rectangular sample with $L = 45(\sqrt{3}/2)a$ and width $W = 25a$.

5.2 Breakdown of conductance quantization in 2DTIs

In Fig. 5.2 we plot the spatial profile of the three components—m_i^x, top panel, m_i^y, central panel, and m_i^z, bottom panel—of the dimensionless spin polarization (5.4), calculated at half filling for $t_2/t = 0.09$ and $U/t = 0.1$, when a single vacancy is placed at $x = 23(\sqrt{3}/2)a$ and $y = a$, where a is the lattice parameter. The ground-state electron density n_i turns out to be nearly uniform.

The results show that spin polarization occurs around the vacancy, being vanishing elsewhere with the exception of asymmetric tails extending throughout the edge. This nicely agrees with the Stoner criterion, stating that a ground-state magnetization can occur in presence of a peak in the DOS. Indeed, a short-range defect generally hosts bound states localized around it, leading to an enhancement of the local DOS in proximity of the defect.

It is interesting to note that a finite spin polarization is bound to atomic-scale imperfections. Away from the vacancy the sample displays zero spin polarization. We

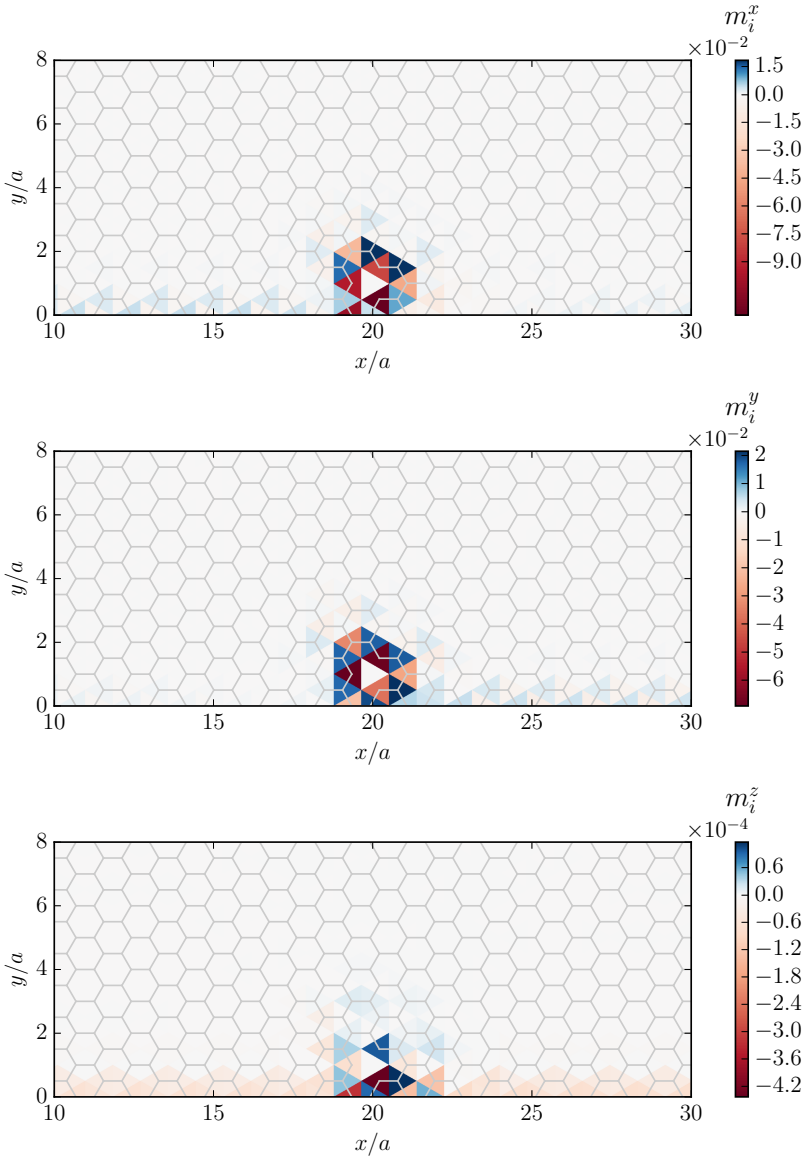

Figure 5.2: Interaction-induced spin polarization near a vacancy. Color plot of the three components of the spatial profile of the dimensionless spin polarization $\boldsymbol{m}_i$ around a vacancy located at $x = 23(\sqrt{3}/2)a$ and $y = a$. Top panel: m_i^x. Central panel: m_i^y. Bottom panel: m_i^z. From Eq. (5.2) it is clear that the components of $\boldsymbol{m}_i$ lying on the $\hat{\boldsymbol{x}}$-$\hat{\boldsymbol{y}}$ plane are those leading to spin-mixing and hence back-scattering. Numerical results in this figure have been obtained by setting $t_2/t = 0.09$ and $U/t = 0.1$.

thus expect that short-range edge roughness, which naturally occurs e.g. in atomically-thin crystals [52, 53], as well can in general lead to interaction-induced spin polarization. We now move to analyze its effects on the transport properties of the system.

Due to spin-momentum locking, back-scattering is induced by spin-flip events, which, in turn, are induced by the terms proportional to m_i^x and m_i^y in Eq. (5.2). Once

the mean-field theory parameters n_i and $\boldsymbol{m}_i$ are obtained, the conductance of the sample in a two-terminal setup (where one lead is attached to the left and the other to the right) can be calculated within the Landauer-Büttiker formalism [24]. In particular, at zero temperature, the differential conductance G is given by $G = (2e^2/h)\mathcal{T}(E_{\rm F})$, $\mathcal{T}(E_{\rm F})$ being the transmission coefficient at the Fermi energy. Quantization of conductance is a consequence of $\mathcal{T}(E_{\rm F})$ being an integer number. We have calculated the transmission as a function of energy ϵ for the mean-field Hamiltonian (5.2)—with n_i and $\boldsymbol{m}_i$ calculated self-consistently—by utilizing the toolkit "KWANT" [171]. The leads are defined by the same Hamiltonian (5.2) with $\boldsymbol{m}_i = \boldsymbol{0}$ and n_i uniform and equal to 1 (corresponding to half filling) for every i.

Figs. 5.3 and 5.8 show the transmission coefficient $\mathcal{T}(\epsilon)$ as a function of energy ϵ ($\epsilon = 0$ denotes the energy at which the edge-mode dispersions cross in the leads), in the presence of one and two vacancies, respectively, and for different values of U/t. According to Fig. 5.3, relative to a single vacancy placed at $x = 23(\sqrt{3}/2)a$ and $y = a$, $\mathcal{T} < 2$ (thus conductance quantization is spoiled) for $\epsilon \approx 0$. In particular, pairs of sharp dips appear where back-scattering is maximum and $\mathcal{T}(\epsilon)$ takes its minimum value, i.e. $\mathcal{T}(\epsilon) \simeq 1$ due to the presence of an unperturbed propagating mode on the opposite edge of the sample. The main effect of increasing U from $0.1t$ to $0.5t$ is an enhancement of the separation between the dips, while the value of $\mathcal{T}(\epsilon)$ between the dips is slightly suppressed (by a few percent) with respect to $\mathcal{T}(\epsilon) = 2$, virtually independently of U. For larger values of U, for example at $U = 0.8t$, $\mathcal{T}(\epsilon)$ is much more affected presenting, apart from the pairs of dips, a sensible suppression in a larger range of energies. A few remarks are in order here. First, due to the approximate particle-hole symmetry of the model (5.1) at $t_2/t \ll 1$, the transmission is a nearly perfectly even function of ϵ. As already noted, the transmission is never below 1 because the unperturbed edge mode on the opposite side of the ribbon is perfectly conducting. Notice that at the energies where the dips occur the transmission relative to one edge mode nearly vanishes. Nearly total suppression of the conductance in a 2DTI was experimentally observed in Ref. [97]. Since the sample displays a finite spin polarization only around the impurity and the edge-mode wavefunctions decay exponentially away from the edge, the detrimental effects of a vacancy on the conductance G rapidly vanish as this is moved towards the center of the sample. As the impurity is moved away from the edge into the center of the sample, the suppression of the transmission $\mathcal{T}$ becomes negligible. This is shown in Fig. 5.4, where the three curves refer to three different positions of a single vacancy. The main panel shows that when $y = (3/2)a$ and $y = 2a$ the corresponding transmissions are virtually energy-independent. A zoom of the data in the main panel is reported in the inset. For $y = 2a$, the transmission deviates from 2 by less than 0.1%. This behavior is easily explained by remembering that the edge-mode wavefunctions decay exponentially away from the edge over a length scale on the order of the lattice parameter a (see Fig. 5.7). If the distance between the edge and the vacancy is larger than a, their overlap decreases exponentially, strongly reducing the chances of back-scattering events.

The behavior of $\mathcal{T}(\epsilon)$ for $U/t \ll 1$ can be understood by solving the problem of a

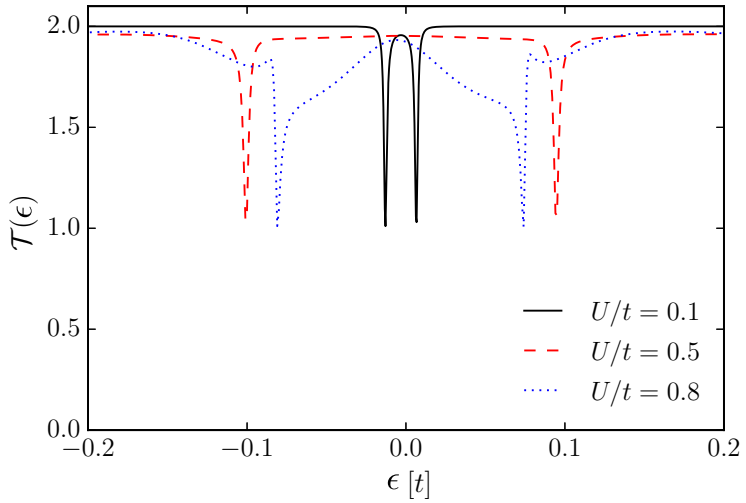

Figure 5.3: Breakdown of conductance quantization for a single vacancy at the edge of a 2DTI. The transmission $\mathcal{T}(\epsilon)$ is plotted as a function of energy ϵ (in units of t) at half filling and for energies lying in the gap δ_g. Different curves refer to different values of U/t. Numerical results in this figure have been obtained by setting $t_2/t = 0.09$ ($\delta_g \simeq 0.93t$). Since on-site electron-electron interactions produce a spin polarization with in-plane components near the vacancy, back-scattering events occur at the same 2DTI edge and lead to the breakdown of conductance quantization, i.e. $\mathcal{T}(\epsilon) < 2$.

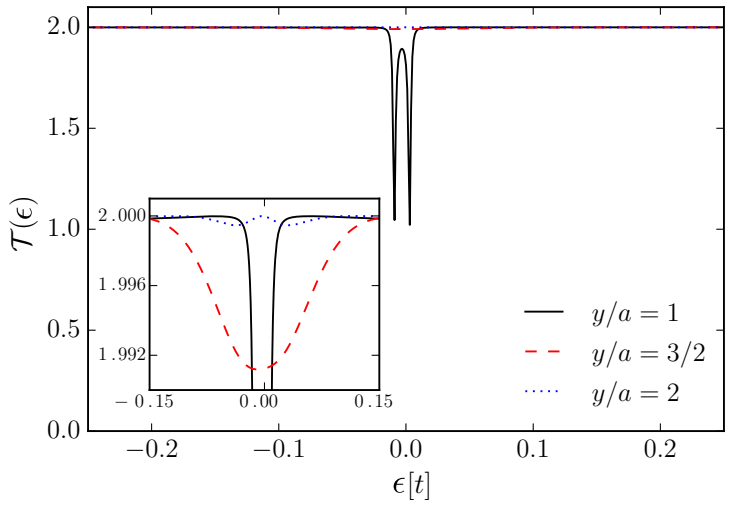

Figure 5.4: Transmission $\mathcal{T}(\epsilon)$ as a function of energy ϵ (in units of t) in the presence of a single vacancy, at half filling and for energies lying in the gap δ_g. Different curves refer to different values of the distance y of the vacancy from the edge, located at $y = 0$. Numerical results in this figure have been obtained by setting $\lambda/t = 0.09$ and $U/t = 0.1$. Inset: zoom of the data in the main panel.

magnetic δ-like impurity [172, 173] at a single edge. In this regime, the dips in $\mathcal{T}(\epsilon)$ can be parametrized by a Breit-Wigner dependence on ϵ. Accordingly, such dips can be explained as anti-resonances resulting from the localization of an electron around the impurity. Our numerical data, in the weak-coupling $U/t \ll 1$ regime, are well fitted by the simple model proposed in Ref. [172], which describes a single edge of a 2DTI in which a pair of helical edge modes is coupled to a δ-like magnetic impurity. According to Ref. [172], the transmission $\mathcal{T}_{\rm SE}(\epsilon)$ relative to a single edge is given by

$$\mathcal{T}_{\rm SE}(\epsilon) = 1 - (1-\alpha^2)\frac{\tilde{\gamma}^2}{(\epsilon^2 - E_{\rm a}^2)^2 + \tilde{\gamma}^2} \ . \tag{5.5}$$

Here, $\pm E_{\rm a}$ with $E_{\rm a} = \sqrt{\Delta^2 - \gamma^2}/2$ are the positions of the dips. The parameter γ describes coupling between the edge mode and the magnetic impurity and Δ is the strength of the magnetic impurity, while $\tilde{\gamma} = \gamma\Delta/2$ is related to the dips' width, which in the limit $\tilde{\gamma}/E_{\rm a}^2 \ll 1$ is given by $\tilde{\gamma}/E_{\rm a}$. The quantity α, which take values in the range $-1 \leq \alpha \leq 1$, controls the depth of the dips and is given by $\alpha = \cos(\theta)$, where θ is the angle formed by the magnetization of the impurity with a vector normal to the plane of the 2DTI.

A least-square minimization procedure shows that Eq. (5.5) fits very well our numerical data in the weak coupling regime $U/t \ll 1$. For example, Fig. 5.5 shows a comparison between the numerical data $\mathcal{T}_{\rm SE}(\epsilon) = \mathcal{T}(\epsilon) - 1$ relative to a single edge for one vacancy and $U/t = 0.1$, as reported in Fig. 5.3, and Eq. (5.5) with $\gamma = 0.0021$, $\Delta = 0.0196$, $E_{\rm a} = 0.0033$, and $\cos(\theta) = 0.0362$.

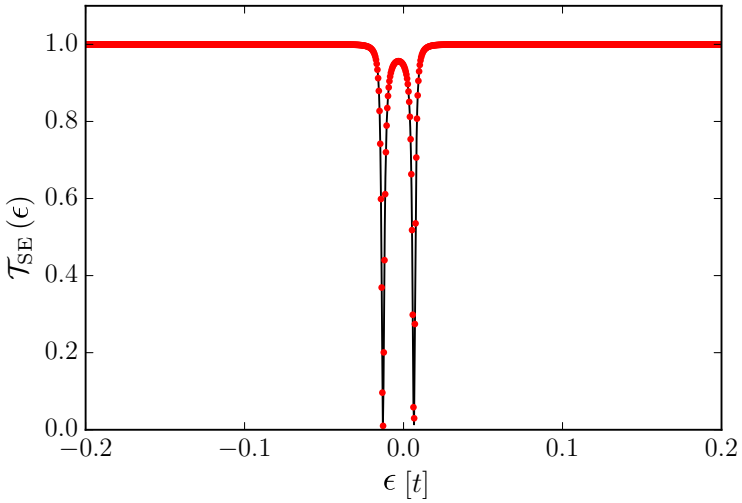

FIGURE 5.5: Numerical (red dots) and analytical (solid black line) results for the transmission $\mathcal{T}_{\rm SE}(\epsilon)$ relative to a single edge, as a function of energy ϵ (in units of t). Numerical results have been obtained for the same parameters relative to Fig. 5.3, and $U/t = 0.1$.

Local DOS calculations show that at the energy $\epsilon = \pm E_{\rm a}$ of the dips the local DOS peaks around the impurity. This suggests that an electron with energy $\epsilon = \pm E_{\rm a}$ traversing the sample gets localized in the bound state around the impurity and scattered back

after a waiting time, which is inversely proportional to the width of the Breit-Wigner function. The local density of states $D(\epsilon, \boldsymbol{r})$ at two different representative values of energy ϵ is showed in Figs. 5.6 and 5.7.

Fig. 5.6 shows $D(\epsilon, \boldsymbol{r})$ at $E = -0.013t$, which matches the energy of one of the dips for the case of a single vacancy and parameters as in Fig. 5.3, with $U/t = 0.1$. It is clear that $D(\epsilon, \boldsymbol{r})$ is localized around the position of the vacancy, where the local ground-state spin polarization is also finite (see Fig. 5.2). On the other hand, by choosing a value of energy far from the dip in the transmission, one finds that the corresponding states are delocalized along the edge (see Fig. 5.7), and support transport.

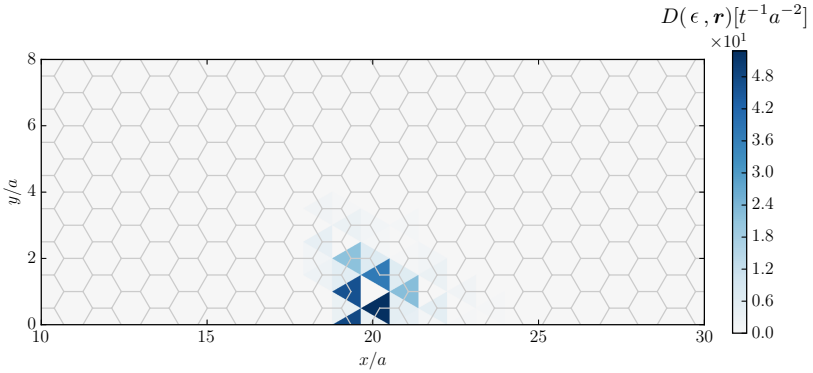

Figure 5.6: Local density of states $D(\epsilon, \boldsymbol{r})$ (in units of $t^{-1}a^{-2}$) for a single vacancy, at the energy where the dip occurs in $\mathcal{T}(\epsilon)$ in Fig. 5.3, i.e. $\epsilon = -0.013t$. All parameters are the same as in Fig. 5.3 and $U/t = 0.1$.

Fig. 5.8 shows the transmission calculated in the presence of two vacancies. We clearly see that $\mathcal{T}(\epsilon)$ is much more affected by the vacancies with respect to the case of a single vacancy, being suppressed in larger ranges of energy even in the weak-coupling regime. Moreover, for $U = 0.8t$ the transmission relative to one edge mode is suppressed to zero for $-0.1t < \epsilon < 0.1t$.

The Kane-Mele Hamiltonian [85] can be enriched by adding a Rashba term of the form

$$\hat{\mathcal{H}}_{\mathrm{R}} = i\lambda_{\mathrm{R}} \sum_{\langle i,j \rangle} \sum_{\alpha,\beta} \hat{c}^{\dagger}_{i\alpha} (\boldsymbol{\tau}^{\alpha\beta} \times \boldsymbol{d}_{ij})_z \hat{c}_{j\beta} \ , \tag{5.6}$$

which preserves the topological phase [85] for not too large values of λ_{R}, with respect to λ. $\boldsymbol{d}_{ij}$ in the equation above is the vector connecting site i to site j. Even in the presence of such term, a ground-state spin polarization still develops around a vacancy. Fig. 5.9 shows the resulting transmission as a function of energy, calculated for $t_2/t = 0.09$, $\lambda_{\mathrm{R}}/t = 0.15$, and $U/t = 0.5$. Despite the large value of λ_{R}/t, along with the dips broadening, the main difference with respect to the case where the Rashba term is absent (see Fig. 5.3) is that now $\mathcal{T}(\epsilon)$ exhibits a sizable asymmetry with respect to $\epsilon = 0$, as a consequence of the enhanced particle-hole asymmetry.

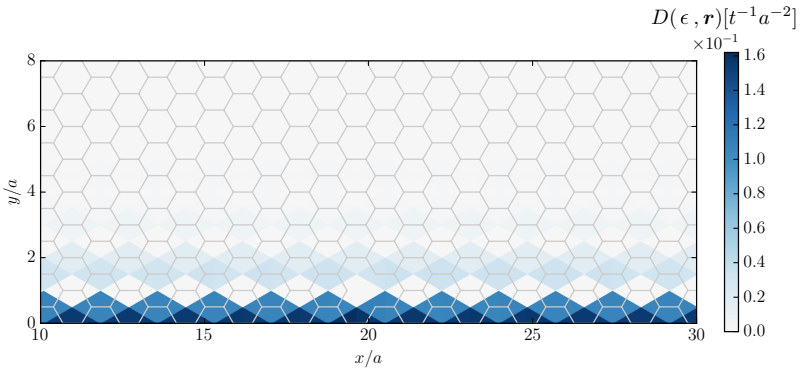

FIGURE 5.7: Same as in Fig. 5.6 but for an energy $\epsilon = -0.2t$, i.e. far from the one relative to the transmission dip.

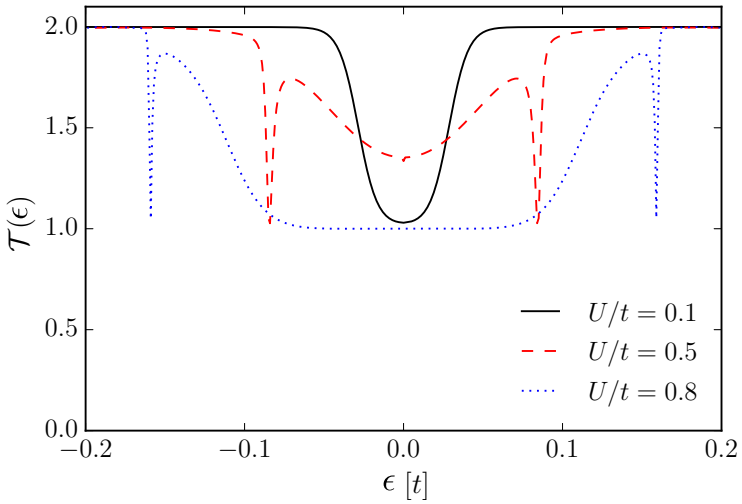

FIGURE 5.8: Same as in Fig. 5.3 but for the case of two vacancies placed at $x = 23(\sqrt{3}/2)a$, $y = (3/2)a$ and $x = 26(\sqrt{3}/2)a$, $y = (1/2)a$.

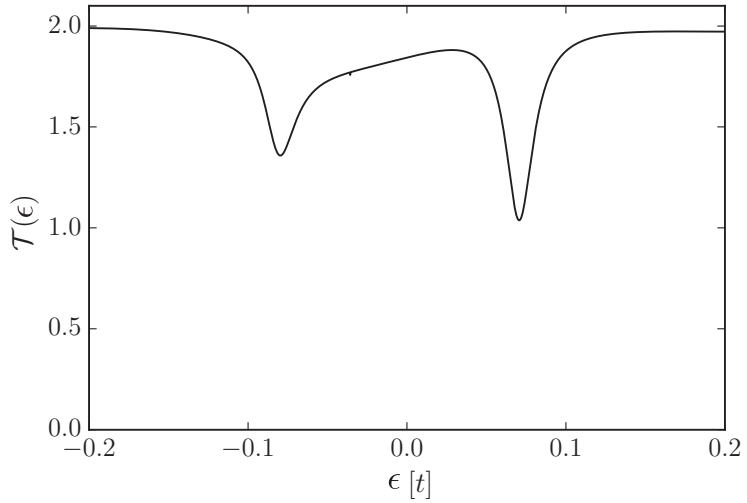

Figure 5.9: Transmission $\mathcal{T}(\epsilon)$ as a function of energy ϵ (in units of t) for a single vacancy, obtained in presence of Rashba spin-orbit coupling. Numerical results in this figure have been obtained by setting $t_2/t = 0.09$, $\lambda_{\mathrm{R}}/t = 0.15$, and $U/t = 0.5$. The position of the vacancy is as in the case of Fig. 5.3.

5.3 Conclusions

We have shown that the combined action of short-range non-magnetic impurities and onsite electron-electron interactions in two-dimensional topological insulators leads to strong back-scattering.

Strong deviations from quantization occur even in the zero-temperature limit. In contrast, all other theories [149, 150, 151, 152] including electron-electron interactions yield deviations of the conductance from its quantized value, which vanish rapidly (i.e. like T^α with $\alpha \geq 4$) as a function of temperature T in the low-temperature limit. These deviations, scaling as power-laws of T, arise because of scattering processes induced by electron-electron interactions. With the present mechanism, on the other hand, we have shown that the ground state of the Kane-Mele-Hubbard model displays a $T = 0$ quantum phase transition from a paramagnetic to a magnetic state if short-range impurities and onsite electron-electron interactions are taken into account. It is because of this ground-state quantum phase transition that our corrections to conductance quantization do not scale to zero in the $T \to 0$ limit. Ground-state edge reconstruction due to electron-electron interactions [153] also operates down to $T = 0$ but applies only to samples with smooth confining potentials. For example, for a BHZ model applied to a HgTe/CdHgTe quantum well [88], edge reconstruction occurs [153] for confining potentials that decay slower than 13 meV/nm. While certainly relevant for samples with smooth edges, the scenario of edge reconstruction is not expected to apply to atomically-thin crystals [52, 53], which possess sharp edges either created naturally by mechanical exfoliation or deliberately by etching.

In our theory, large deviations from quantization occur also in the weak-coupling $U/t < 1$ regime, where our mean-field theory is expected to be accurate. In this case, the suppression of transmission as a function of energy can be interpreted in terms of anti-resonances stemming from the time spent by an electron in the bound states formed near short-range impurities, before is back-scattered due to spin-flipping terms in Eq. (5.2).

The formation of local magnetic moments in the presence of short-range impurities and onsite electron-electron interactions is a general feature of bipartite lattices [2, 170], for which the spectrum is particle-hole symmetric. Deep in the gap, any topological insulator possesses approximate particle-hole symmetry around the energy at which the edge modes cross. We have shown that small deviations from exact particle-hole symmetry (e.g. due to $t_2 \neq 0$ in our model) do not spoil the formation of local magnetic moments near short-range impurities. Furthermore, the same happens with the addition of Rashba spin-orbit coupling, which introduces extra terms breaking the exact particle-hole symmetry of (5.1) at $t_2 = 0$. We therefore expect that the spontaneous formation of local magnetic moments near short-range impurities induced by onsite electron-electron interactions is a general feature of 2D topological insulators.

Future research

We conclude with a brief comment on some research paths to pursue starting from the original works presented in this Thesis.

In Chapter 3 we have addressed many of the important optical, plasmonic and dielectric properties of twisted bilayer graphene. In our calculations, the electron-electron interactions have been included at the level of the Random Phase Approximation [30] (RPA), which is justified in the limit of weak coupling. As previously commented, if one is interested in the room-temperature physics of twisted bilayer graphene, as in the case of the s-SNOM measurements in Ref. [43], the RPA is sufficient. Nevertheless, it would be very interesting to extend our work to regimes where the twisted bilayer graphene is strongly correlated, i.e. at low temperatures and when the twist angle is close to the magic angle. The simplest way to go beyond the RPA is to carry out a time-dependent Hartree-Fock approximation, which includes contributions arising from proper diagrams containing one interaction line. A second possibility is to employ the dual-boson approach, as e.g. done in Refs. [116, 117]. In addition to approximations beyond the RPA, we mention that our calculations heavily relied on the local approximation (see Section 2.3). It is therefore very interesting to compute the full (i.e. non-local) optical, plasmonic and dielectric properties of twisted bilayer graphene. This is the subject of a future work, whose preliminary results have been presented in Section 3.5.

In Chapter 5 we have presented an original result on the interplay between electron-electron interactions and localized defects in two-dimensional topological insulators. Our calculations were performed with the Kane-Mele model, which is an idealized model. Although Ref. [140] has shown that a naturally occurring layered mineral (jacutingaite) realizes the Kane-Mele model, many other realistic two-dimensional topological insulators are not accurately described by the Kane-Mele model. A natural follow up to our work is therefore the extension of our calculation to other models, especially in the case of atomically thin topological insulators such as WTe_2.

References

[1] A. H. Castro Neto, F. Guinea, N. M. R. Peres, K. S. Novoselov, and A. K. Geim, Rev. Mod. Phys. **81**, 109 (2009).

[2] M.I. Katsnelson, *Graphene: Carbon in Two Dimensions* (Cambridge University Press, Cambridge, 2012).

[3] R. Bistritzer and A. H. MacDonald, Proc. Natl. Acad. Sci. (USA) **108**, 12233 (2011).

[4] J. M. B. Lopes dos Santos, N. M. R. Peres, and A. H. Castro Neto, Phys. Rev. Lett. **99**, 256802 (2007).

[5] Y. Cao, V. Fatemi, S. Fang, K. Watanabe, T. Taniguchi, E. Kaxiras, and P. Jarillo-Herrero, Nature **556**, 43 (2018).

[6] Y. Cao, V. Fatemi, A. Demir, S. Fang, S. L. Tomarken, J. Y. Luo, J. D. Sanchez-Yamagishi, K. Watanabe, T. Taniguchi, E. Kaxiras, R. C. Ashoori, and P. Jarillo-Herrero, Nature **556**, 80 (2018).

[7] M.Z. Hasan and C.L. Kane, Rev. Mod. Phys. **82**, 3045 (2010).

[8] B.A. Bernevig and T.L. Hughes, *Topological Insulators and Topological Superconductors* (Princeton University Press, Princeton and Oxford, 2013).

[9] K. S. Novoselov, A. K. Geim, S. V. Morozov, D. Jiang, Y. Zhang, S. V. Dubonos, I. V. Grigorieva, and A. A. Firsov, Science **306**, 666 (2004).

[10] A. K. Geim and I. V. Grigorieva, Nature **499**, 419 (2013).

[11] K. S. Novoselov, A. Mishchenko, A. Carvalho, and A. H. Castro Neto, Science **353**, aac9439 (2016).

[12] L. A. Falkovsky and S. S. Pershoguba, Phys. Rev. B 76, 153410 (2007).

[13] L. A. Falkovsky, Optical properties of graphene, Journal of Physics: Conference Series **129**, 012004 (2008).

[14] D. S. L. Abergel and V. I. Fal'ko, Phys. Rev. B 75, 155430 (2007).

[15] A. A. Balandin, S. Ghosh, W. Bao, I. Calizo, D. Teweldebrhan, F. Miao, and C. N. Lau, Nano Letters **8**, 902 (2008).

[16] C. Lee, X. Wei, J. W. Kysar, and J. Hone, Science **321**, 385 (2008).

[17] G. Grosso and G. P. Parravicini, *Solid State Physics (Second Edition)* (Academic Press, Amsterdam, 2014).

[18] S. Reich, J. Maultzsch, C. Thomsen, and P. Ordejón, Phys. Rev. B **66**, 035412 (2002).

[19] M. O. Goerbig Rev. Mod. Phys. **83**, 1193 (2011).

[20] K. Nakada, M. Fujita, G. Dresselhaus, and M. S. Dresselhaus, Phys. Rev. B **54**, 17954 (1996).

[21] L. Brey and H. A. Fertig, Phys. Rev. B **73**, 235411 (2006).

[22] X. Wang, Y. Ouyang, X. Li, H. Wang, J. Guo, and H. Dai, Phys. Rev. Lett. **100**, 206803 (2008).

[23] J. Li, I. Martin, M. Büttiker, and A. F. Morpurgo, Nature Physics **7**, 38 (2011).

[24] S. Datta, *Electronic Transport in Mesoscopic Systems.* (Cambridge University Press, Cambridge, 1995).

[25] R. Krishna Kumar, D. A. Bandurin, F. M. D. Pellegrino, Y. Cao, A. Principi, H. Guo, G. H. Auton, M. Ben Shalom, L. A. Ponomarenko, G. Falkovich, K. Watanabe, T. Taniguchi, I. V. Grigorieva, L. S. Levitov, M. Polini, and A. K. Geim, Nature Physics **13**, 1182 (2017).

[26] B. Wunsch, T. Stauber, F. Sols, and F. Guinea, New Journal of Physics **8**, 318 (2006).

[27] A. Principi, M. Polini, and G. Vignale, Phys. Rev. B **80**, 075418 (2009).

[28] A. Grigorenko, M. Polini, and K. Novoselov, Nature Photonics **6**, 749 (2012).

[29] R. R. Nair, P. Blake, A. N. Grigorenko, K. S. Novoselov, T. J. Booth, T. Stauber, N. M. R. Peres, and A. K. Geim, Science **320**, 1308 (2008).

[30] G.F. Giuliani and G. Vignale, *Quantum Theory of the Electron Liquid* (Cambridge University Press, Cambridge, 2005).

[31] D. Pines and P. Nozières, *The Theory of Quantum Liquids.* (W. A. Benjamin Inc., New York, 1963).

[32] A. Sommerfeld, Ann. Phys. **303**, 233 (1899).

[33] R. H. Ritchie, Phys. Rev. **106**, 874 (1957).

[34] J. N. Anker, W. P. Hall, O. Lyandres, N. C. Shah, J. Zhao, and R. P. Van Duyne, Nature Materials **7**, 442 (2008).

[35] R. F. Oulton, V. J. Sorger, T. Zentgraf, R.-M. Ma, C. Gladden, L. Dai, G. Bartal, and X. Zhang, Nature **461**, 629 (2009).

[36] A. V. Akimov, A. Mukherjee, C. L. Yu, D. E. Chang, A. S. Zibrov, P. R. Hemmer, H. Park, and M. D. Lukin, Nature **450**, 402 (2007).

[37] S. Thongrattanasiri, F. H. L. Koppens, and F. J. García de Abajo, Phys. Rev. Lett. **108**, 047401 (2012).

[38] A. Y. Nikitin, F. Guinea, F. J. Garcia-Vidal, and L. Martin-Moreno, Phys. Rev. B **85**, 081405 (2012).

[39] A. Woessner, Y. Gao, I. Torre, M. B. Lundeberg, C. Tan, K. Watanabe, T. Taniguchi, R. Hillenbrand, J. Hone, M. Polini, and F. H. L. Koppens, Nat. Photon. **11**, 421 (2017).

[40] A. Woessner, M. B. Lundeberg, Y. Gao, A. Principi, P. Alonso-González, M. Carrega, K. Watanabe, T. Taniguchi, G. Vignale, M. Polini, J. Hone, R. Hillenbrand, and F. H. L. Koppens, Nature Materials **14**, 421 (2014).

[41] J. Chen, M. Badioli, P. Alonso-Gonzalez, S. Thongrattanasiri, F. Huth, J. Osmond, M. Spasenovic, A. Centeno, A. Pesquera, P. Godignon, A. Zurutuza Elorza, N. Camara, F. J. G. de Abajo, R. Hillenbrand, and F. H. L. Koppens, Nature **487**, 77 (2012).

[42] Z. Fei, A. S. Rodin, G. O. Andreev, W. Bao, A. S. McLeod, M. Wagner, L. M. Zhang, Z. Zhao, M. Thiemens, G. Dominguez, M. M. Fogler, A. H. C. Neto, C. N. Lau, F. Keilmann, and D. N. Basov, Nature **487**, 82 (2012).

[43] N. C. H. Hesp, I. Torre, D. Rodan-Legrain, P. Novelli, Y. Cao, S. Carr, S. Fang, P. Stepanov, D. Barcons-Ruiz, H. Herzig-Sheinfux, K. Watanabe, T. Taniguchi, D. K. Efetov, E. Kaxiras, P. Jarillo-Herrero, M. Polini, and F. H. L. Koppens, arXiv:1910.07893.

[44] K. Watanabe, T. Taniguchi, and H. Kanda, Nature Materials **3**, 404 (2004).

[45] J. D. Caldwell, A. V. Kretinin, Y. Chen, V. Giannini, M. M. Fogler, Y. Francescato, C. T. Ellis, J. G. Tischler, C. R. Woods, A. J. Giles, M. Hong, K. Watanabe, T. Taniguchi, S. A. Maier, and K. S. Novoselov, Nature Commun. **5**, 5221 (2014).

[46] L. Wang, I. Meric, P. Y. Huang, Q. Gao, Y. Gao, H. Tran, T. Taniguchi, K. Watanabe, L. M. Campos, D. A. Muller, J. Guo, P. Kim, J. Hone, K. L. Shepard, and C. R. Dean, Science **342**, 614 (2013).

[47] C. Dean, A. F. Young, I. Meric, C. Lee, L. Wang, S. Sorgenfrei, K. Watanabe, T. Taniguchi, P. Kim, K. Shepard, and J. Hone, Nature Nanotechnology **5**, 722 (2010).

[48] X. Qian, J. Liu, L. Fu, and J. Li, Science **346**, 1344 (2014).

[49] S. Manzeli, D. Ovchinnikov, D. Pasquier, O. V. Yazyev, and A. Kis, Natutre Rev. Materials **2**, 17033 (2017).

[50] B. Sipos, A. Kusmartseva, A. Akrap, H. Berger, L. Forró, and E. Tutiš, Nature Materials **7**, 960 (2008).

[51] A. Splendiani, L. Sun, Y. Zhang, T. Li, J. Kim, C.-Y. Chim, G. Galli, and F. Wang, Nano Lett. **10**, 1271 (2010).

[52] S. Wu, V. Fatemi, Q.D. Gibson, K. Watanabe, T. Taniguchi, R.J. Cava, and P. Jarillo-Herrero, Science **359**, 76 (2018).

[53] Y. Shi, J. Kahn, B. Niu, Z. Fei, B. Sun, X. Cai, B. A. Francisco, D. Wu, Z.-X. Shen, X. Xu, D. H. Cobden, and Y.-T. Cui, Science Advances **5**, eaat8799 (2019).

[54] A. Tomadin, M. Polini, and J. Jung, Phys. Rev. B **99**, 035432 (2019).

[55] M. Yankowitz, J. Xue, and B. J. LeRoy, J. Phys.: Condens. Matter **26**, 303201 (2014).

[56] J. Xue, J. Sanchez-Yamagishi, D. Bulmash, P. Jacquod, A. Deshpande, K. Watanabe, T. Taniguchi, P. Jarillo-Herrero, and B. J. LeRoy, Nature Materials **10**, 282 (2011).

[57] M. Yankowitz, J. Xue, D. Cormode, J. D. Sanchez-Yamagishi, K. Watanabe, T. Taniguchi, P. Jarillo-Herrero, P. Jacquod, and Brian J. LeRoy, Nature Physics **8**, 382 (2012).

[58] A. Tomadin, F. Guinea, and M. Polini, Phys. Rev. B **90**, 161406 (2014).

[59] S. Shallcross, S. Sharma, and O. A. Pankratov, Phys. Rev. Lett. **101**, 056803 (2008).

[60] E. J. Mele, Phys. Rev. B **81**, 161405(R) (2010).

[61] S. Shallcross, S. Sharma, E. Kandelaki, and O. A. Pankratov, Phys. Rev. B **81**, 165105 (2010).

[62] G. Li, A. Luican, J. M. B. Lopes dos Santos, A. H. Castro Neto, A. Reina, J. Kong, and E. Y. Andrei, Nature Phys. **6**, 109 (2010).

[63] R. Bistritzer and A. H. MacDonald, Phys. Rev. B **81**, 245412 (2010).

[64] J. M. B. Lopes dos Santos, N. M. R. Peres, and A. H. Castro Neto, Phys. Rev. B **86**, 155449 (2012).

[65] M. Yankowitz, S. Chen, H. Polshyn, Y. Zhang, K. Watanabe, T. Taniguchi, D. Graf, A. F. Young, and C. R. Dean, Science **363**, 1059 (2019).

[66] X. Lu, P. Stepanov, W. Yang, M. Xie, M. A. Aamir, I. Das, C. Urgell, K. Watanabe, T. Taniguchi, G. Zhang, A. Bachtold, A. H. MacDonald, and D. K. Efetov, Nature **574**, 653 (2019).

[67] A. L. Sharpe, E. J. Fox, A. W. Barnard, J. Finney, K. Watanabe, T Taniguchi, M. A. Kastner, and D. Goldhaber-Gordon, Science **365**, 605 (2019).

[68] M. Serlin, C. L. Tschirhart, H. Polshyn, Y. Zhang, J. Zhu, K. Watanabe, T. Taniguchi, L. Balents, and A. F. Young, Science **367**, 900 (2020).

[69] S. L. Tomarken, Y. Cao, A. Demir, K. Watanabe, T. Taniguchi, P. Jarillo-Herrero, and R. C. Ashoori, Phys. Rev. Lett. **123**, 046601 (2019).

[70] Y. Choi, J. Kemmer, Y. Peng, A. Thomson, H. Arora, R. Polski, Y. Zhang, H. Ren, J. Alicea, G. Refael, F. von Oppen, K. Watanabe, T. Taniguchi, and S. Nadj-Perge, Nature Phys. **15**, 1174 (2019).

[71] A. Kerelsky, L. J. McGilly, D. M. Kennes, L. Xian, M. Yankowitz, S. Chen, K. Watanabe, T. Taniguchi, J. Hone, C. Dean, A. Rubio, and A. N. Pasupathy, Nature **572**, 95 (2019).

[72] Y. Xie, B. Lian, B. Jäck, X. Liu, C.-L. Chiu, K. Watanabe, T. Taniguchi, B. A. Bernevig, and A. Yazdani, Nature **572**, 101 (2019).

[73] Y. Jiang, X. Lai, K. Watanabe, T. Taniguchi, K. Haule, J. Mao, and E. Y. Andrei, Nature **573**, 91 (2019).

[74] A. Uri, S. Grover, Y. Cao, J. A. Crosse, K. Bagani, D. Rodan-Legrain, Y. Myasoedov, K. Watanabe, T. Taniguchi, P. Moon, M. Koshino, P. Jarillo-Herrero, and E. Zeldov, Nature **581**, 47 (2020).

[75] P. Stepanov, I. Das, X. Lu, A. Fahimniya, K. Watanabe, T. Taniguchi, F. H. L. Koppens, J. Lischner, L. Levitov, and D. K. Efetov, Nature **583**,375 (2020).

[76] H. S. Arora, R. Polski, Y. Zhang, A. Thomson, Y. Choi, H. Kim, Z. Lin, I. Z. Wilson, X. Xu, J.-H. Chu, K. Watanabe, T. Taniguchi, J. Alicea, and S. Nadj-Perge, Nature **583**,379 (2020).

[77] T. Stauber and H. Kohler, Nano Lett. **16**, 6844 (2016).

[78] G. Tarnopolsky, A. J. Kruchkov, and A. Vishwanath, Phys. Rev. Lett. **122**, 106405 (2019).

[79] C. Nayak, S. H. Simon, A. Stern, M. Freedman, and S. Das Sarma, Rev. Mod. Phys. **80**, 1083 (2008).

[80] A. Y. Kitaev, Annals Phys. **303**, 2 (2003).

[81] K. S. Novoselov, A. K. Geim, S. V. Morozov, D. Jiang, M. I. Katsnelson, I. V. Grigorieva, S. V. Dubonos, and A. A. Firsov, Nature **438**, 197 (2005).

[82] K. v. Klitzing, G. Dorda, and M. Pepper, Phys. Rev. Lett. **45**, 494 (1980).

[83] F.D.M. Haldane, Phys. Rev. Lett. **61**, 2015 (1988).

[84] M. König, S. Wiedmann, C. Brüne, A. Roth, H. Buhmann, L.W. Molenkamp, X.-L. Qi, and S.-C. Zhang, Science **318**, 5851 (2007).

[85] C.L. Kane and E.J. Mele, Phys. Rev. Lett. **95**, 146802 (2005).

[86] C.L. Kane and E.J. Mele, Phys. Rev. Lett. **95**, 226801 (2005).

[87] C. Xu and J.E. Moore, Phys. Rev. B **73**, 045322 (2006).

[88] B.A. Bernevig, T.L. Hughes, and S.-C. Zhang, Science **314**, 1757 (2006).

[89] X.-L. Qi and S.-C. Zhang, Rev. Mod. Phys. **83**, 1057 (2011).

[90] Y. Ren, Z. Qiao, and Q. Niu, Rep. Prog. Phys. **79**, 066501 (2016).

[91] A. Roth, C. Brüne, H. Buhmann, L.W. Molenkamp, J. Maciejko, X.-L. Qi, and S.-C. Zhang, Science **325**, 5938 (2009).

[92] G. Grabecki, J. Wróbel, M. Czapkiewicz, Ł. Cywiński, S. Gierałtowska, E. Guziewicz, M. Zholudev, V. Gavrilenko, N.N. Mikhailov, S.A. Dvoretski, F. Teppe, W. Knap, and T. Dietl, Phys. Rev. B **88**, 165309 (2013).

[93] C. Liu, T. L. Hughes, X.-L. Qi, K. Wang, and S.-C. Zhang, Phys. Rev. Lett. **100**, 236601 (2008).

[94] I. Knez, R.-R. Du, and G. Sullivan, Phys. Rev. Lett. **107**, 136603 (2011).

[95] K. Suzuki, Y. Harada, K. Onomitsu, and K. Muraki, Phys. Rev. B **87** 235311 (2013).

[96] L. Du, I. Knez, G. Sullivan, and R.R. Du, Phys. Rev. Lett. **114**, 096802 (2015).

[97] M. König, M. Baenninger, A.G.F. Garcia, N. Harjee, B.L. Pruitt, C. Ames, P. Leubner, C. Brüne, H. Buhmann, L.W. Molenkamp, and D. Goldhaber-Gordon, Phys. Rev. X **3**, 021003 (2013).

[98] S. Tang, C. Zhang, D. Wong, Z. Pedramrazi, H.-Z. Tsai, C. Jia, B. Moritz, M. Claassen, H. Ryu, S. Kahn, J. Jiang, H. Yan, M. Hashimoto, D. Lu, R. G. Moore, C.-C. Hwang, C. Hwang, Z. Hussain, Y. Chen, M. M. Ugeda, Z. Liu, X. Xie, T. P. Devereaux, M. F. Crommie, S.-K. Mo, and Z.-X. Shen, Nat. Phys. **13**, 683 (2017).

[99] S. J. Ahn, P. Moon, T.-H. Kim, H.-W. Kim, H.-C. Shin,E. H. Kim, H. W. Cha, S.-J. Kahng, P. Kim, M. Koshino,Y.-W. Son, C.-W. Yang, and J. R. Ahn, Science **361**, 782 (2018).

[100] Y. Takesaki, K. Kawahara, H. Hibino, S. Okada, M. Tsuji, and H. Ago, Chem. Mater. **28**, 4583 (2016).

[101] W. Yao, E. Wang, C. Bao, Y. Zhang, K. Zhang, K. Bao,C. K. Chan, C. Chen, J. Avila, M. C. Asensio, J. Zhu, and S. Zhou, Proc. Natl. Acad. Sci. (USA) **115**, 6928 (2018).

[102] P. Moon, M. Koshino, and Y.-W. Son, Phys. Rev. B **99**, 165430 (2019).

[103] G. Trambly de Laissardière, D. Mayou, and L. Magaud, Nano Lett. **10**, 804 (2010).

[104] M. Koshino, N. F. Q. Yuan, T. Koretsune, M. Ochi, K. Kuroki, and L. Fu, Phys. Rev. X **8**, 031087 (2018).

[105] M. Koshino, New J. Phys. **17**, 015014 (2015).

[106] P. Lucignano, D. Alfè, V. Cataudella, D. Ninno, and G. Cantele, Phys. Rev. B **99**, 195419 (2019).

[107] N. W. Ashcroft and N. D. Mermin, *Solid State Physics* (Saunders College, New York, 1976).

[108] R. F. Egerton, Rep. Prog. Phys. **72**, 016502 (2009).

[109] I. Torre, M. I. Katsnelson, A. Diaspro, V. Pellegrini, and M. Polini, Phys. Rev. B **96**, 035433 (2017).

[110] W. H. Press, S. A. Teukolsky, W. T. Vetterling, and B. P Flannery, *Numerical Recipes 3rd Edition: The Art of Scientific Computing*(Cambridge University Press, Cambridge, 2007)

[111] D. D. Johnson, Phys. Rev. B **38**, 12807 (1988).

[112] B. Shahriari, K. Swersky, Z. Wang, R. P. Adams and N. de Freitas, Proceedings of the IEEE **104**, 148 (2016).

[113] R. V. Krems, Phys. Chem. Chem. Phys. **21**, 13392 (2019).

[114] M. I. B. Utama, R. J. Koch, K. Lee, N. Leconte, H. Li, S. Zhao, L. Jiang, J. Zhu, K. Watanabe, T. Taniguchi, P. D. Ashby, A. Weber-Bargioni, A. Zettl, C. Jozwiak, J. Jung, E. Rotenberg, A. Bostwick, and F. Wang, Nature Phys. (2020).

[115] G. Cantele, D. Alfè, F. Conte, V. Cataudella, D. Ninno, and P. Lucignano, arXiv:2004.14323.

[116] E. G. C. P. van Loon, H. Hafermann, A. I. Lichtenstein, A. N. Rubtsov, and M. I. Katsnelson, Phys. Rev. Lett. **113**, 246407 (2014).

[117] H. Hafermann, E. G. C. P. van Loon, M. I. Katsnelson, A. I. Lichtenstein, and O. Parcollet Phys. Rev. B **90**, 235105 (2014).

[118] A. N. Rubtsov, M. I. Katsnelson, and A. I. Lichtenstein, Annals of Physics **327**, 1320 (2012).

[119] E. A. Stepanov, E. G. C. P. van Loon, A. A. Katanin, A. I. Lichtenstein, M. I. Katsnelson, and A. N. Rubtsov, Phys. Rev. B **93**, 045107 (2016).

[120] A. Georges, G. Kotliar, W. Krauth, and M. J. Rozenberg, Rev. Mod. Phys. **68**, 13 (1996).

[121] F. Guinea and N. R. Walet, Proc. Natl. Acad. Sci. USA **115**, 13174 (2018).

[122] M. Xie and A. H. MacDonald, Phys. Rev. Lett. **124**, 097601 (2020).

[123] P. Moon and M. Koshino, Phys. Rev. B **87**, 205404 (2013).

[124] C. J. Tabert and E. J. Nicol, Phys. Rev. B **87**, 121402(R) (2013).

[125] T. Stauber, P. San-Jose, and L. Brey, New J. Phys. **15**, 113050 (2013).

[126] T. N. Ikeda, Phys. Rev. Research **2**, 032015 (2020).

[127] L. Lewandowski and L. Levitov, Proc. Natl. Acad. Sci. USA **116**, 20869 (2019).

[128] F. H. L. Koppens, T. Mueller, Ph. Avouris, A. C. Ferrari, M. S. Vitiello, and M. Polini, Nature Nanotech. **9**, 780 (2014).

[129] M. B. Lundeberg, Y. Gao, A. Woessner, C. Tan, P. Alonso-González, K. Watanabe, T. Taniguchi, J. Hone, R. Hillenbrand, and F. H. L. Koppens, Nature Materials **16**, 204 (2017).

[130] S. Castilla, B. Terrés, M. Autore, L. Viti, J. Li, A.Y. Nikitin, I. Vangelidis, K. Watanabe, T. Taniguchi, E. Lidorikis, M. S. Vitiello, R. Hillenbrand, K.-J. Tielrooij, and F. H. L. Koppens, Nano Lett. **19**, 2765 (2019).

[131] S. Carr, S. Fang, Z. Zhu, and E. Kaxiras, Phys. Rev. Research **1**, 013001 (2019).

[132] P. Alonso-González, A. Y. Nikitin, Y. Gao, A. Woessner, M. B. Lundeberg, A. Principi, N. Forcellini, W. Yan, S. Vélez, A. J. Huber, K. Watanabe, T. Taniguchi, F. Casanova, L. E. Hueso, M. Polini, J. Hone, F. H. L. Koppens, and R. Hillenbrand, Nature Nanotech. **12**, 31 (2017).

[133] A. Tomadin, A. Principi, J. C. W. Song, L. S. Levitov, and M. Polini, Phys. Rev. Lett. **115**, 087401 (2015).

[134] Y. M. Blanter and M. Büttiker, Physics Reports **336**, 1 (2000).

[135] M. V. Moskalets, *Scattering matrix approach to non-stationary quantum transport.* (Imperial College Press, London, 2012).

[136] M. Nakahara, *Geometry, Topology and Physics (Second Edition).* (Hilger, Bristol, 1990).

[137] M. V. Berry, Proc. R. Soc. London, Ser. A **392**, 45 (1984).

[138] D. Xiao, M.-C. Chang, and Q. Niu, Rev. Mod. Phys. **82**, 1959 (2010).

[139] Michel Fruchart and David Carpentier, Comptes Rendus Physique **14**, 779 (2013).

[140] A. Marrazzo, M. Gibertini, D. Campi, N. Mounet, and N. Marzari, Phys. Rev. Lett. **120**, 117701 (2018).

[141] Y. Tanaka, A. Furusaki, and K.A. Matveev, Phys. Rev. Lett. **106** 236402 (2011).

[142] J. Maciejko, C. Liu, Y. Oreg, X.L. Qi, C. Wu, and S.-C. Zhang, Phys. Rev. Lett. **102**, 256803 (2009).

[143] B.L. Altshuler, I.L. Aleiner, and V.I. Yudson, Phys. Rev. Lett. **111**, 086401 (2013).

[144] Y.L. Chen, J.-H. Chu, J.G. Analytis, Z.K. Liu, K. Igarashi, H.-H. Kuo, X.L. Qi, S.K. Mo, R.G. Moore, D.H. Lu, M. Hashimoto, T. Sasagawa, S.-C. Zhang, I.R. Fisher, Z. Hussain, and Z.X. Shen, Science **329**, 5992 (2010).

[145] L.A. Wray, S.-Y. Xu, Y. Xia, D. Hsieh, A.V. Fedorov, Y.S. Hor, R.J. Cava, A. Bansil, H. Lin, and M.Z. Hasan, Nature Phys. **7**, 3237 (2011).

[146] A. Ström and H. Johannesson, Phys. Rev. Lett. **102**, 096806 (2009).

[147] T.L. Schmidt, Phys. Rev. Lett. **107**, 096602 (2011).

[148] C.-Y. Hou, E.-A. Kim, and C. Chamon, Phys. Rev. Lett. **102**, 076602 (2009).

[149] C. Wu, B.A. Bernevig, and S.-C. Zhang, Phys. Rev. Lett. **96**, 106401 (2006).

[150] T.L. Schmidt, S. Rachel, F. von Oppen, and L.I. Glazman, Phys. Rev. Lett. **108**, 156402 (2012).

[151] J.I. Väyrynen, M. Goldstein, and L.I. Glazman, Phys. Rev. Lett. **110**, 216402 (2013).

[152] J.I. Väyrynen, M. Goldstein, Y. Gefen, and L.I. Glazman, Phys. Rev. B **90** 115309 (2014).

[153] J. Wang, Y. Meir, and Y. Gefen, Phys. Rev. Lett. **118**, 046801 (2017).

[154] A. Ström, H. Johannesson, and G.I. Japaridze, Phys. Rev. Lett. **104**, 256804 (2010).

[155] F. Crépin, J. C. Budich, F. Dolcini, P. Recher, and B. Trauzettel, Phys. Rev. B **86**, 121106(R) (2012).

[156] J.C. Budich, F. Dolcini, P. Recher, and B. Trauzettel, Phys. Rev. Lett. **108**, 086602 (2012).

[157] C.-H. Hsu, P. Stano, J. Klinovaja, and D. Loss, Phys. Rev. B **96**, 081405 (2017).

[158] C.-H. Hsu, P. Stano, J. Klinovaja, and D. Loss, Phys. Rev. B **97**, 125432 (2018).

[159] A. Mani and C. Benjamin, Phys. Rev. Applied **6**, 014003 (2016).

[160] A.A. Bagrov, F. Guinea, and M.I. Katsnelson, arXiv:1805.11700.

[161] J.I. Väyrynen, D.I. Pikulin, and J. Alicea, arXiv:1803.01021.

[162] A.M. Black-Schaffer and D. Yudin, Phys. Rev. B **90**, 161413 (2014).

[163] A.M. Black-Schaffer and A.V. Balatsky, Phys. Rev. B **85**, 121103 (2012).

[164] A.M. Black-Schaffer and A.V. Balatsky, Phys. Rev. B **86**, 115433 (2012).

[165] S. Rachel and K. Le Hur, Phys. Rev. B **82**, 075106 (2010).

[166] S. Rachel, arXiv:1804.10656.

[167] J.A. Vergés, E. Louis, P.S. Lomdahl, F. Guinea, and A.R. Bishop, Phys. Rev. B **43**, 6099 (1991).

[168] J.A. Vergés, F. Guinea, and E. Louis, Phys. Rev. B **46**, 3562 (1992).

[169] H. Feldner, Z.Y. Meng, A. Honecker, D. Cabra, S. Wessel, and F.F. Assaad, Phys. Rev. B **81**, 115416 (2010).

[170] E.H. Lieb, Phys. Rev. Lett. **62**, 1201 (1989).

[171] C.W. Groth, M. Wimmer, A.R. Akhmerov, and X. Waintal, New J. Phys. **16**, 063065 (2014).

[172] X. Dang, J.D. Burton, and E.Y. Tsymbal, J. Phys.: Condens. Matter **28**, 38LT01 (2016).

[173] J.-H. Zheng and M.A. Cazalilla, Phys. Rev. B **97**, 235402 (2018).